Effect of Electrochemical Promotion and Metal-Support Interaction on Catalytic Performance of Nano-catalysts

Yasmine Hajar

Thesis submitted
in partial fulfillment of the requirements for the
Doctorate in Philosophy degree in Chemical Engineering

Department of Chemical and Biological Engineering
Faculty of Engineering
University of Ottawa

Abstract

In heterogeneous catalysis, promoting the activity of the catalytic metals is long known as an important method to make a process more efficient and viable. Noble metals have been promoted classically by a chemical coverage of an ionic solution on the surface of the catalyst or using inert support, e.g., silica or alumina, allowing an increase of the dispersion of the catalyst. Therefore, new methods of promotion needed to be better explored to improve the efficiency of metal and metal oxide catalysts. One way of enhancing the catalyst's activity is to disperse the noble metal at the nanoscale using an active type of support that is ion-conducting. Not only lattice ions can be exchanged with the surface of the nanoparticles but it can also engage in the oxidation reaction on the surface, resulting in what is known as metal-support interaction (MSI). Another method of improving the catalytic activity is to polarize the catalyst, allowing ions to migrate from a solid electrolyte to the gas-exposed surface, in a phenomenon known as electrochemical promotion of catalysis (EPOC). The change in the ions concentration on the surface would change the adsorption energy of the gaseous reactants and enhance or supress the catalytic rate.

In this thesis, the effect of supporting nanoparticles of noble and non-noble metal (oxides) (Pt, Ru, Ir, Ni) was studied for the case of ionic and ionic-electronic conducting supports (CeO_2, TiO_2, YSZ). The enhancement in their catalytic rate was found and correlated to an electrochemical property, the exchange current density. Then, using isotopically-labeled oxygen, the oxygen exchange ability of the conductive oxides was evaluated when supporting Ir and Ru nanoparticles and correlated with the results from C_3H_8 isotopic oxidation reaction, which showed the extent of involvement of oxygen from the support as carried by the isotopically-labeled CO_2 produced.

Following this, electrochemical promotion of catalysis experiments were performed for different reactant/catalyst systems (C_2H_4 - Pt, Ru; C_3H_8 - Pt; CH_4 - Pd, Ni_9Pd). In the first system, the main outcome was the functional equivalence found for the MSI and EPOC effect in promoting the catalysts as experiments were performed at different temperatures, reactants partial pressures and polarization values. In the case of C_3H_8/Pt, the novel dispersion of Pt on an intermediate supporting layer (LSM/GDC) was found as a feasible method to obtain long stability of the catalyst while electrochemically promoting the rate of reaction. For CH_4 oxidation, the polarization of the Pd nanoparticles showed continuous oxidation of the bulk of the catalyst resulting in a continuous

increase of the catalytic rate. The Ni_9Pd synthesized in a way to form a core/double-shell layer of Ni/Pd resulted in an enhanced catalytic rate and enhanced stability compared to stand-alone Pd.

And lastly, to comprehend the ions' effect in the electrochemical promotion and the non-Faradaic nature of the phenomena, density-functional theory (DFT) modeling was used to demonstrate the increase of the heat of adsorption of reactants depending on their electronegative/positive nature.

Résumé

Dans le sujet de catalyse hétérogène, la promotion de l'activité des métaux catalytiques est reconnue depuis longtemps comme une méthode importante pour rendre un processus plus efficace et plus viable. Les métaux nobles ont été stimulés classiquement par une déposition chimique d'une solution ionique sur la surface du catalyseur et/ou en utilisant un support inerte, par exemple de l'oxyde de silicium ou d'aluminium, permettant une augmentation de la dispersion du catalyseur. Pour cela, de nouvelles méthodes de promotion doivent être mieux explorées pour améliorer l'efficacité des catalyseurs à base de métaux et d'oxydes métalliques. L'un des moyens de renforcer l'activité du catalyseur consiste à disperser le métal noble à l'échelle nanométrique à l'aide d'un type de support actif à conduction ionique. Non seulement les ions du réseau peuvent être échangés avec la surface des nanoparticules, mais ils peuvent également participer à la réaction d'oxydation à la surface, ce qui entraîne une interaction dite interaction métal-support (MSI). Une autre méthode d'amélioration de l'activité catalytique consiste à polariser le catalyseur, ce qui permet aux ions de migrer d'un électrolyte solide vers la surface exposée aux gaz, dans un phénomène connu sous le nom de promotion électrochimique de la catalyse (EPOC). La modification de la concentration en ions à la surface modifierait l'énergie d'adsorption des réactifs gazeux et augmenterait ou supprimerait la vitesse catalytique.

Dans cette thèse, l'effet du support de nanoparticules de métaux nobles et non nobles (oxydes) (Pt, Ru, Ir, Ni) a été étudié dans le cas des supports conducteurs ioniques et électro-ioniques (CeO_2, TiO_2, YSZ). L'amélioration de leur taux catalytique a été trouvée et corrélée à une propriété électrochimique, la densité de courant d'échange. Ensuite, en utilisant de l'oxygène marqué isotopiquement, l'aptitude à l'échange d'oxygène des oxydes conducteurs a été évaluée lors du support de nanoparticules d'Ir et de Ru et corrélée aux résultats de la réaction d'oxydation isotopique de C_3H_8 ; ce qui a montré l'engagement de l'oxygène contenu dans le support tel que le CO_2 isotopique était produit.

Après cela, des expériences de promotion de la catalyse électrochimique ont été réalisées pour différents systèmes réactifs / catalyseurs (C_2H_4 - Pt, Ru; C_3H_8 - Pt; CH_4 - Pd, Ni_9Pd). Dans le premier système, le résultat principal était l'équivalence fonctionnelle trouvée pour les effets MSI et EPOC dans la promotion des catalyseurs, les expériences étant effectuées à différentes températures, pressions partielles de réactifs et valeurs de polarisation. Dans le cas de C_3H_8 / Pt,

la nouvelle dispersion de Pt sur une couche de support intermédiaire (LSM / GDC) s'est révélée être une méthode réalisable pour obtenir une longue stabilité du catalyseur tout en améliorant électrochimiquement la vitesse de réaction. Pour l'oxydation du CH_4, la polarisation des nanoparticules de Pd montrait une oxydation continue de la masse du catalyseur, ce qui entraînait une augmentation continue de la vitesse catalytique. Le Ni_9Pd synthétisé de manière à former une couche noyau / double enveloppe de Ni / Pd a entraîné une vitesse catalytique accrue et une stabilité accrue par rapport au Pd autonome.

Enfin, pour comprendre l'effet des électrons et la nature non faradique de la promotion électrochimique, une modélisation par la théorie de la densité fonctionnelle (DFT) a été utilisée pour démontrer l'augmentation de la chaleur d'adsorption des réactifs en fonction de leur potentiel électronégatif/positif.

Statement of Contributions of Collaborators and Co-Authorship

I hereby declare that I am the first author of all the chapters written in this thesis.

I acknowledge the supervision of Dr. Elena Baranova on the work described in this thesis, her editorial comments in each chapter, and scientific guidance in performing lab experiments at the University of Ottawa.

Chapter 1, 2 and 10 are solely written by me under the editorial comments of Dr. Elena Baranova.

Chapter 3 is written by me and had editorial contribution from Dr. Holly Dole (University of Ottawa), Ph.D. student Mohamed Houache (University of Ottawa), Dr. Vernoux and Dr. Baranova. The synthesis, experimental and interpretation work was solely done by me at University of Ottawa. The TEM characterization was performed by Dr. Martin Couillard (NRC). The synthesis of stand-alone nickel was performed by M. Houache. The experimental work related to Ni was assisted by Ubaidullah Tariq. The rest of the synthesis and interpretation work was solely done by me.

Chapter 4 is written by me and had editorial contribution from Dr. Antoinette Boréave, Dr. Angel Caravaca, Dr. Philippe Vernoux (IRCELYON) and Dr. Baranova. I solely conducted the synthesis, experimental and interpretation work, at IRCELYON under the supervision of Dr. Boréave and Dr. Vernoux and at University of Ottawa under the supervision of Dr. Baranova. XRF characterization was performed by Bob Whitehead (RMC).

Chapter 5 is written by me and had editorial contribution from Dr. Baranova. The synthesis and interpretation work was solely conducted by me. The experimental work was assisted by co-op student Kiran Patel and M.Eng. student U. Tariq at University of Ottawa.

Chapter 6 is co-first authored between me and Valerio Di Palma. I conducted all the EPOC experiments, data interpretation, analysis and interpretation at IRCELYON. Di Palma (DIFFER) carried the Pt atomic layer deposition and characterized the Pt size distribution. M.A. Verheijen prepared the sample lamellas and carried the TEM characterization. Dr. Vasileios Kyriakou (DIFFER) drafted the manuscript and Dr. Michel Tsampas (DIFFER) conceived the intellectual concept. Each of Dr. Baranova, Dr. Vernoux (IRCELYON), Dr. M. Creatore and Dr. van de Sanden had critical suggestions and writing feedback on the EPOC and/or characterization experiments.

Chapter 7 is written by me and had editorial contributions from Dr. Baranova. The synthesis, preparation and interpretation work was solely performed by me. The experimental work was assisted by M.Eng. student Balaji Venkatesh.

Chapter 8 is written by me and had editorial contribution from Dr. Gianluigi Botton (McMaster) and Dr. Baranova. The synthesis of Ni and Ni_9Pd was performed by M. Houache. The experimental

work was assisted by B. Venkatesh. TEM imaging and EDS mapping were performed by Reza Safari (McMaster), the HAADF-EELS imaging was performed by Sagar Prabhudev (McMaster) and EDS analyses with aberration-corrected TEM were performed by Hanshuo Liu (McMaster). The rest of the synthesis, preparation, interpretation work was solely done by me.

Chapter 9 is written by me and had editorial contribution from Dr. Stephan Steinmann and Dr. Carine Michel (ENS de Lyon) and Dr. Baranova. Initial surface model and calculation was performed with help from Laureline Treps (ENS de Lyon). Subsequent calculation and interpretation work was solely performed by me.

Acknowledgements

First and foremost, I would like to express my sincere gratitude and appreciation to my thesis supervisor Dr. Elena A. Baranova who guided me along the years and offered me numerous opportunities. Her guidance, advice and innovative ideas made this work branch into a bigger scope through successful collaborations.

I would like to express my thankfulness to Dr. Philippe Vernoux and Dr. Antoinette Boréave who welcomed me in the Institute of Research on Catalysis and Environment in Lyon, France. They offered tremendous guidance on isotopic oxygen exchange method and gave me access to their equipment and characterization facilities. They also opened to me the opportunity to collaborate with Dr. Mihalis Tsampas from the Fundamental Energy Research Institution in the Netherlands.

My gratitude is tremendous to Dr. Carine Michel and Dr. Stephan Steinmann who taught me how to perform density functional theory (DFT) modeling at École Normale Supérieure (ENS) de Lyon. It was terrifically rewarding to work with them and Laureline Treps at their institution.

I am thankful to Dr. Holly Dole who shared with me her knowledge on electrochemical promotion and catalysis. Thank you as well to each of Kiran Patel, Ubaidullah Tariq and Balaji Venkatesh for helping me in running experiments. Evans Monyoncho, Mohamed Houache, Chris Panaritis, Emily Cossar, Niloofar Aligholizadeh and Najmeh Ahledel, thank you for all the discussions and learning we had from each other in the lab.

I would like to recognise the Chemical and Biological engineering department as a whole, its professors, administrative staff (Sylvie and Francine) and technical staff (Louis, Gérard, Franco, and James). Each have helped me in their own way.

I would like to express also my gratitude to Dr. Gianluigi Botton (and his team), Dr. Yun Liu, Dr. Martin Couillard, Dr. Bulat Gabidullin and Bob Whitehead for the distinguished characterization tests each have presented.

I am humbled by the honor of receiving the Vanier Canada Graduate scholarship. The financial lift it removed came with a heavier responsibility that I held high and proud. I am also thankful for the Michael Smith award, PALSE and the international scholarship.

I am grateful for the wonderful friends I have made in the D218 office and our endless discussions about our different research work. We pushed and motivated each other and made the long days and nights in the office bearable. Therefore, Charbel, Fahad, Dean, Shaz, Tolu, Shidan, Marie, Vida, Emily, Géraldine, Farhad, Mohamed, Sean, Khoi, Chris P., Niloofar, Milad, Ali, Katrina, Chris M., and Curtis, I wish you the best in your professional endeavors.

I am forever indebted to my parents for the infinite and selfless love they have shown to me, my sister and brother. They paved the way for our move to Canada even though it meant being away from them and home. Therefore, I am forever grateful for their support in every step I take.

I love you, mom and dad. This thesis is for you.

Table of contents

List of Figures

List of Tables

Nomenclature

List of Acronyms and Abbreviations

AC	Alternating current
ADF	Angular dark field
ALD	Atomic layer deposition
BSCF	Cobalt doped strontium barium ferrite
CE	Counter electrode
CPD	Contact potential difference
CV	Cyclic voltammetry
CZO	Ceria-zirconia
CZY	Ceria-zirconia-yttria
DAQ	Data acquisition
DFT	Density functional theory
DLS	Dynamic light scattering
EDX/EDS	Energy dispersive X-ray spectroscopy
EELS	Electron energy loss spectroscopy
EPOC	Electrochemical promotion of catalysis
ESD	Electrostatic spray deposition
FIB	Focus ion beam
FS	Final state
FTIR	Fourier Transform infrared
FWHM	Full-width at half maximum
GC	Gas Chromatography
GDC	Gadolinium doped ceria
GWP	Global warming potential
HAADF	High-angle annular dark field
ICP-OES	Inductively-coupled plasma optical emission spectrometry
IOE	Isotopic oxygen exchange
IS	Initial state
LHHW	Langmuir-Hinshelwood-Hougen-Watson
LSCF	Cobalt doped strontium lanthanum ferrite
LSM	Lanthanum- Samarium
MEP	Minimum energy pathway
MIEC	Mixed ionic-electronic conductor
MSI	Metal-support interaction
MvK	Mars and van Krevelen
NDIR	Non-dispersive infrared
NEMCA	Non-Faradaic electrochemical modification of catalytic activity
NEB	Nudged Elastic Band
NG	Natural Gas
NGV	Natural gas vehicles
NP	Nano-particle
OMME	Oxametallacycle
OSC	Oxygen storage capacity
PAW	Projector Augmented Wave
PGM	Platinum group metals
QN	Quasi-Newton
RE	Reference electrode

RWGS	Reverse water-gas shift
SEM	Scanning electron microscopy
SFE	Surface free energy
SHE	Standard hydrogen electrode
SMSI	Strong metal-support interaction
SOE	Standard oxygen electrode
SOEC	Solid oxide electrolyte cell
SSA	Specific surface area
SSCR	Single–chamber capsule reactor
SSCR2G	Second generation single–chamber capsule reactor
STEM	Scanning transmission electron microscopy
TEM	Transmission electron microscopy
TEPOC	Thermoelectric promotion of catalysis
TOF	Turnover frequency (s^{-1})
TPD	Temperature programmed desorption
TPIOE	Temperature-programmed isotopic oxygen exchange
TPO	Temperature-programmed oxidation
UPS	Ultraviolet photoelectron spectroscopy
US-PP	Ultra-soft pseudopotentials
VASP	Vienna Ab ignition Simulation Package
VOC	Volatile organic compound
WE	Working electrode
WF	Work function
XPS	X-ray photoelectron spectroscopy
XRD	X-ray diffraction
XRF	X-ray fluorescence
YSZ	Yttria-stabilized zirconia

List of Symbols or Abbreviations

Symbol	**Meaning**
A	Pre-exponential factor
a	Adsorbed
ads	Adsorption
a_M	Atomic surface area of the metal
amu	Atomic mass unit
at	Atomic
br	Bridge
cus	Coordinatively unsaturated
D	Dispersion
d	Average particle size (diameter)
E	Energy
e	Electron charge equal to $1.6.10^{-19}$
E_a	Activation energy
E_{ads}	Adsorption energy
E_n	Energy level of the system
F	Faraday's constant equal to 96 485
fcc	Face centered cubic
G	Gibb's free energy
$G_{cut\text{-}off}$	Cut-off energy
$\vec{g}$	Wave vector
H	Enthalpy

$\hat{H}$	Time-independent Hamiltonian
$\hbar$	Reduced Planck's constant
K	Dimensionless shape factor
k	Kinetic constant
$\vec{k}$	Vector of reciprocal space
k_b	Boltzmann constant equal to 1.38. 10^{-23} J/K
I	Current
i	Current density
i_0	Exchange current density
M	Metal
M_W	Molecular weight
N	Number
N_A	Avogadro's number equal to 6.022 x 10^{23}
NC_K	Cavity size
N_G	Gas-exposed catalyst surface
N_M	Atomic surface density
n	Number of moles
ocp	Open-circuit potential
P	Dipole moment
P	Total pressure
p	Partial pressure
R	Universal gas constant equal to 8.314 J/mol K
$\vec{R}$	Spatial coordinates of nuclei
r	Catalytic rate
$\vec{r}$	Spatial coordinates of electrons
r_o	Rate at open-circuit condition
r_u	Catalytic rate for unpromoted catalyst
Δr	Change in catalytic rate
S	Surface
T	Temperature
t	Time
$\hat{T}$	Kinetic energy operator
tpb	Three-phase boundary
U	Potential
U_{cell}	Cell potential
u	Cell periodic function
$\dot{V}$	Volumetric flow rate
$\hat{V}$	Potential energy operator
vac	Vacuum
$\widehat{W}$	Electron-electron repulsion
wt	weight

List of Greek Symbols

Symbol	**Meaning**
α_H	NEMCA coefficient
α-Al_2O_3	Alpha-alumina
β	Line broadening at FWHM
γ	Surface free energy
γ-Al_2O_3	Gamma-alumina

ε_0	Dielectric constant or electric permeability of vacuum equal to 8.85. 10^{-12}
ε_d	D-band center
ε_r	Relative permittivity
θ	Chemisorption surface coverage term
θ	Bragg angle
k	Adsorption coefficient
Λ	Faradaic efficiency
λ	X-ray wavelength equal to 1.5418 x 10^{-10}
μ	Chemical potential
σ	Conductivity
ρ	Rate enhancement ratio
ρ	Electronic density
ρ_M	Metal density
$\rho(\vec{r})$	Specific electron density
τ	Relaxation constant
Φ	Work function
ψ_n	n-particle wave function

Subscripts

o	Open-circuit
A	Acceptor
ads	Adsorption
D	Donor
i	Species i
p	Promoter
WR	Working-reference

Superscripts

o	Standard conditions
δ^-	Partial Negative Charge
δ^+	Partial Positive Charge

Chapter 1 General Introduction

1.1. Introduction

Catalysis is a key technology for the development of a sustainable society: catalysts are responsible for lowering the energy required to activate a reaction pathway as well as influencing the selectivity of a chemical process [1–3]. 85 % of chemicals produced have been in contact with a catalyst [3,4]; therefore, one can be aware of how catalysts have shaped the chemical industry. An important sector where catalysts play a vital role is car exhaust systems where catalysts reduce the emission of air pollutants. Ambient levels of carbon monoxide, nitrogen dioxide, sulfur dioxide and volatile organic compounds (VOCs) play an exacerbating role on the human respiratory and cardiovascular diseases [5–10]; therefore, improving the efficiency of heterogeneous catalysts is necessary to enhance the control of these emissions. Many heterogeneous catalysts and supports, including metal oxides [11], noble metals supported by metal oxides or carbon [12], and noble metals supported by a mixture of metal oxides [13] have been extensively studied to control VOC emissions. Research that focuses on improving catalytic technology has included using less-expensive catalyst materials (compared to the conventional use of noble metals films), increasing their catalytic performance and achieving higher efficiency [14–17].

Enhancing the activity of the catalyst requires adding a promoting factor. The classical method to do so is through a chemical promotion that requires covering the catalyst surface with a promoting additive (e.g., Cl^- ions) when preparing a catalyst [18]. The addition of such species results in the modification of the electronic or crystal structure of the catalyst's surface with an objective of improving the activity/selectivity of the catalyst [19–23]. A sophisticated way to promote the same catalyst is through in-situ electrochemical modification of the catalyst electronic and surface structure using a small current or potential stimulus at the catalyst working electrode. This is known as Non-Faradaic Electrochemical Modification of Catalytic Activity (NEMCA) or Electrochemical Promotion of Catalysis (EPOC). In such a phenomenon, promoting ionic species (e.g., $O^{\delta-}$, $Na^{\delta+}$) intercalate from the ionically conductive solid electrolyte to the metal when the circuit is closed. This in-situ back-spillover of promoting species can alter the catalytic performance of the catalysts; depending on the properties of the

ionic species that migrate to the surface; the adsorption strength of the catalyst may be enhanced, affecting the activation energies of the reaction and/or product selectivity [19,20,32,33,24–31].

Another type of promotion known in the field is metal-support interaction (MSI). The support plays a promoting role due to the interaction that occurs at the ionic and/or electronic level between the metal catalyst and the support without an electrical stimulus [34]. When supporting a metal on an active support, migration of promoting species (e.g. $O^{\delta-}$) from the support to the metal occurs, resulting in modification of the reaction mechanism. Two factors allow this phenomenon: 1- the support with a finite ionic conductivity rather than an insulating property such as SiO_2. 2- the metal catalyst used is nano-dispersed providing a short distance for the promoting species to migrate between the support and the metal, spontaneously [19,34].

1.2. Research objectives

The principal objective of this research was to investigate different methods of catalytic promotion to enhance the catalytic rate per mass used. Using the knowledge of electrochemical promotion and metal-support interaction methods [19], noble and non-noble metallic nanoparticles were promoted by means of these two methods to enhance the catalytic oxidation of volatile organic compounds (VOCs): methane, ethylene, and propane. These unreacted VOCs emitted to our atmosphere have a higher global warming potential than CO_2 and consequently enhancing the catalytic efficiency and increasing their conversion help us save the environment from their notorious effect.

The basis of this thesis is a fundamental hypothesis which goes as follows:

"*Promoting unsupported nano-catalysts by applying an electrical field is functionally equivalent to the catalytic enhancement that results from metal-support interaction"*

To understand better each of EPOC and MSI and the closeness in their functionality, the following detailed objectives were met:

- Synthesis of nanoparticle catalysts of noble, non-noble metals or bimetallics then depositing them on ionic and mixed ionic-electronic conductive supports.
- Characterization of physical and chemical properties of the nano-size catalysts using x-ray diffraction (XRD), scanning electron microscopy (SEM), transmission electron microscopy

(TEM), high-angle annular dark field (HAADF), scanning transmission electron microscopy (STEM) with elemental mapping using electron energy loss spectroscopy (EELS), and Energy Dispersive X-ray Spectroscopy (EDS). Additional characterization tests using dynamic light scattering (DLS), X-ray Fluorescence (XRF) and inductively-coupled plasma optical emission spectrometry (ICP-OES) were also performed.

- Enhance the design of the heterogeneous catalysis reactor, electrochemical cell, and setup, as well as the data-acquisition (DAQ) method using thermocouples, flow meters, temperature controller, infrared (IR) analyzer for CO_2 concentration, mass spectroscopy (MS), micro-gas chromatography (micro-GC), DAQ hardware and LabView® program.
- Evaluate and compare the catalytic efficiency of supported noble metals for the oxidation reactions, test the effect of changing the metal-oxide support used as well as the effect of the metal's class: noble, non-noble, or bimetallic.
- Assess the oxygen exchange capacity from the lattice structure of metal oxides using temperature-programmed and isothermal isotopic oxygen exchange tests.
- Perform polarization measurements for the catalysts using a potentiostat/galvanostat under different conditions of temperature, pressure, and feed gas composition and obtain the exchange current densities of the catalyst.
- Assess the effect of the electric field applied on the catalytic performance of stand-alone catalysts and compare the catalytic performance of supported metals to the electrochemical promotion of the metals.
- Compare the electrochemical promotion effect on the catalytic performance of non-noble metal alone and in their noble/non-noble bi-metallic form.
- Comprehend at the atomistic level the effect of an electrical field (change of the catalyst work function) on the rate-limiting reaction step: adsorption of reactants and dissociation of intermediates.
- Relate the findings of the ab-initio theoretical calculations to the experimental findings of electrochemical promotion.

1.3. Thesis structure and organization

This dissertation comprises ten chapters.

Chapter 1 A general introduction to this dissertation is given along with the objectives and motivations behind this work.

Chapter 2 A literature review of heterogeneous catalysis and the promotion methods used are elaborated, along with detailed background research about electrochemical promotion of catalysis (EPOC), metal-support interaction (MSI) and density functional theory (DFT).

Chapter 3 Heterogeneous catalysis experiments were performed for the ethylene oxidation reaction on iridium and nickel-based catalysts resulting in finding a direct correlation between the heterogeneous catalytic activity of the catalysts, and their electrochemical characteristics, specifically their intrinsic exchange current density.

Chapter 4 Another method of characterizing the active support property is using isotopic oxygen exchange measurements. Isothermal and temperature-programmed isotopic oxygen exchange experiments were conducted to fundamentally understand the engagement of the ionically and mixed ionic-electronic conductive active supports (CeO_2, TiO_2 and YSZ) in an oxidation reaction and hence affect the catalytic rate of propane oxidation reaction. This work was complemented with an ethylene *titration* measurement under oxygen deficient conditions.

Chapter 5 This chapter comes as a direct comparison study between EPOC and MSI influence on the catalytic rate enhancement of Pt and Ru by electrochemically promoting them vs supporting the nanoparticles on the aforementioned active supports.

Chapter 6 Synthesis method and morphology of the catalysts are key for the catalyst's activity. Therefore, Pt deposited by atomic layer deposition was investigated for its catalytic activity and ability to be electrochemically promoted for the case of propane oxidation.

Chapter 7 Another important volatile organic compound to be tested is methane, which is a more challenging and thermally demanding reactant (given its highest H/C ratio). Therefore, in this chapter, we shed light on the electrochemical promotion of methane using palladium nanoparticles synthesized with the polyol method.

Chapter 8 Similarly to the case of ethylene oxidation, it was important to test non-noble metals for the case of methane oxidation. Therefore, nickel alone, as well as various ratios of Ni/Pd, were tested for their catalytic activity and electrochemical promotion ability. Ni_9Pd was

the most efficient, therefore, its enhanced activity was showed here in comparison to Pd and Ni alone.

Chapter 9 The last research chapter was about ab-initio atomistic modeling of electrochemical promotion. Using the Vienna ab-initio simulation package (VASP) and density functional theory (DFT), we modeled the surface of ruthenium oxide (110) and its most stable surface termination as a function of temperature and potential. We then studied the adsorption energy of an ethylene molecule on the surface and the effect of charge removal/addition on this energy as a simulation of oxygen migration to the surface that occurs during electrochemical promotion. The model's findings were directly related to the experimental work of ethylene oxidation on ruthenium catalyst. A further step was taken to demonstrate the effect of electron addition/removal on the dissociation of an ethylene molecule as well as on a gaseous oxygen molecule passing by transition state calculation.

Chapter 10 And finally, this chapter includes final conclusions, contributions and recommendations for future work.

Appendices The appendices at the end include supplementary information for Chapters 4, 5, 8 and 9, as well as a list of the publications, conference meetings and poster presentations related to this work.

References

[1] G. Ertl, H. Knozinger, J. Weitkamp, Handbook of Heterogeneous Catalysis, Wiley-VCH, Weinheim, 1997.

[2] J.M. Thomas, W.J. Thomas, Principles and Practice of Heterogenous Catalysis, VCH, Weinheim, 1997.

[3] B. Cornils, W.A. Herrmann, R. Schlogl, C.H. Wong, eds., Catalysis from A to Z, a concise encyclopedia, Wiley-VCH, Weinheim, 2000.

[4] J. Hagen, Industrial Catalysis, a practical approach, Wiley-VCH, Weinheim, 1999.

[5] R.T. Burnett, S. Cakmak, M.E. Raizenne, D. Stieb, R. Vincent, D. Krewski, J.R. Brook, O. Philips, H. Ozkaynak, The association between ambient carbon monoxide levels and daily mortality in Toronto, Canada., J. Air Waste Manage. Assoc. 48 (1998) 689–700.

[6] R.T. Burnett, J. Brook, A. Environment, E. Canada, T. Dann, C. Delocla, O. Philips, S. Canada, S. Cakmak, R. Vincent, Association between particulate- and gas-phase components of urban air pollution and daily mortality in eight canadian cities, Inhal. Toxicol. 12 (2000) 15–39.

[7] K.Y. Fung, I.N. Luginaah, K.M. Gorey, Impact of air pollution on hospital admissions in Southwestern Ontario, Canada: generating hypotheses in sentinel high-exposure places, Environ. Heal. 6 (2007) 18–25.

[8] S. Cakmak, R. Dales, J. Leech, L. Liu, The influence of air pollution on cardiovascular and pulmonary function and exercise capacity: Canadian Health Measures Survey (CHMS)., Environ. Res. 111 (2011) 1309–1312.

[9] H. Chen, M.S. Goldberg, R.T. Burnett, M. Jerrett, A.J. Wheeler, P.J. Villeneuve, Long-term exposure to traffic-related air pollution and cardiovascular mortality, Epidemiology. 24 (2013) 35–43.

[10] L. Liu, R. Poon, L. Chen, A.-M. Frescura, P. Montuschi, G. Ciabattoni, A. Wheeler, R. Dales, Acute effects of air pollution on pulmonary function, airway inflammation, and oxidative stress in asthmatic children., Environ. Health Perspect. 117 (2009) 668–74.

[11] S.C. Kim, W.G. Shim, Catalytic combustion of VOCs over a series of manganese oxide catalysts, Appl. Catal. B Environ. 98 (2010) 180–185.

[12] N. Kamiuchi, T. Mitsui, N. Yamaguchi, H. Muroyama, T. Matsui, R. Kikuchi, K. Eguchi, Activation of Pt/SnO2 catalyst for catalytic oxidation of volatile organic compounds, Catal. Today. 157 (2010) 415–419.

[13] Z. Abbasi, M. Haghighi, E. Fatehifar, S. Saedy, Synthesis and physicochemical characterizations of nanostructured Pt/Al2O3-CeO2 catalysts for total oxidation of VOCs., J. Hazard. Mater. 186 (2011) 1445–54.

[14] S. Bensaid, F. a. Deorsola, D. Fino, N. Russo, After-treatment of household wood-fired stove emissions: From catalyst formulation to full-scale system, Catal. Today. 197 (2012) 76–89.

[15] P. Gawade, A.-M.C. Alexander, R. Clark, U.S. Ozkan, The role of oxidation catalyst in dual-catalyst bed for after-treatment of lean burn natural gas exhaust, Catal. Today. 197 (2012) 127–136.

[16] J.R. Theis, R.W. McCabe, The effects of high temperature lean exposure on the subsequent HC conversion of automotive catalysts, Catal. Today. 184 (2012) 262–270.

[17] M.F. Weilenmann, P. Soltic, S. Hausberger, The cold start emissions of light-duty-vehicle fleets: A simplified physics-based model for the estimation of CO2 and pollutants., Sci. Total Environ. 444 (2013) 161–176.

[18] A. de Lucas-Consuegra, New Trends of Alkali Promotion in Heterogeneous Catalysis: Electrochemical Promotion with Alkaline Ionic Conductors, Catal. Surv. from Asia. 19 (2015) 25–37.

[19] C.G. Vayenas, S. Bebelis, C. Pliangos, S. Brosda, D. Tsiplakides, Electrochemical Activation of Catalysis: Promotion, Electrochemical Promotion, and Metal-Support Interactions, Springer, New York, 2001. http://link.springer.com/10.1007/b115566.

[20] C.G. Vayenas, S. Bebelis, S. Ladas, Dependence of catalytic rates on catalyst work function, Nature. 343 (1990) 625–627.
[21] S. Brosda, C.G. Vayenas, J. Wei, Rules of chemical promotion, Appl. Catal. B Environ. 68 (2006) 109–124.
[22] S. Brosda, C.G. Vayenas, Rules and Mathematical Modeling of Electrochemical and Classical Promotion 2. Modeling, J. Catal. 208 (2002) 38–53.
[23] C.G. Vayenas, S. Brosda, C. Pliangos, Rules and Mathematical Modeling of Electrochemical and Classical Promotion 1. Reaction Classification and Promotional Rules, J. Catal. 203 (2001) 329–350.
[24] I.V. V. Yentekakis, C.G.G. Vayenas, The effect of electrochemical oxygen pumping on the steady-state and oscillatory behavior of CO oxidation on polycrystalline Pt, J. Catal. 111 (1988) 170–188.
[25] S. Bebelis, C.G. Vayenas, Non-faradaic electrochemical modification of catalytic activity. 1. The case of ethylene oxidation on Pt, J. Catal. 118 (1989) 125–146.
[26] C.A. Cavalca, G. Larson, C.G. Vayenas, G.L. Haller, Electrochemical Modification of CH3OH Oxidation Selectivity and Activity on a Pt Single-Pellet Catalytic Reactor, J. Phys. Chem. 97 (1993) 6115–6119.
[27] S.G. Neophytides, C.G. Vayenas, TPD and Cyclic Voltammetric Investigation of the Origin of Electrochemical Promotion in Catalysis, J. Phys. Chem. 99 (1995) 17063–17067.
[28] G. Pacchioni, F. Illas, S. Neophytides, C.G. Vayenas, Quantum-Chemical Study of Electrochemical Promotion in Catalysis, J. Phys. Chem. 100 (1996) 16653–16661.
[29] C.G. Vayenas, S. Bebelis, Electrochemical promotion of heterogeneous catalysis, Catal. Today. 51 (1999) 581–594.
[30] C. Vayenas, S. Brosda, C. Pliangos, The double-layer approach to promotion, electrocatalysis, electrochemical promotion, and metal–support interactions, J. Catal. 216 (2003) 487–504.
[31] A. Piram, X. Li, F. Gaillard, C. Lopez, A. Billard, P. Vernoux, Electrochemical promotion of environmental catalysis, Ionics (Kiel). 11 (2005) 327–332.
[32] A. de Lucas-Consuegra, F. Dorado, C. Jiménez-Borja, J.L. Valverde, Electrochemical promotion of Pt impregnated catalyst for the treatment of automotive exhaust emissions, J. Appl. Electrochem. 38 (2008) 1151–1157.
[33] A. Toghan, L.M. Rösken, R. Imbihl, The electrochemical promotion of ethylene oxidation at a Pt/YSZ catalyst., Chemphyschem. 11 (2010) 1452–1459.
[34] C.G. Vayenas, Promotion, Electrochemical Promotion and Metal-Support Interactions: Their Common Features, Catal. Letters. 143 (2013) 1085–1097.

Chapter 2 Background and Literature Review

2.1. Promotion in heterogeneous catalysis: history and definitions

The design of commercial catalysts relies heavily on promoters to enhance their efficiency in heterogeneous reactions [1]. While *structural promoters* enhance and stabilize the dispersion of the active phase of the catalyst, *electronic promoters* enhance the catalytic properties of the active phase [2–5]. A classical method of enhancing the electronic structure of a catalyst is through the addition of a chemical species, usually an alkali, on its surface [6]; this usually modifies the chemisorptive bond strength of reactants and intermediates with the surface of a catalyst. Many studies focus on characterizing single crystal surfaces to understand the various species' chemisorption state on the surface of the catalysts [7–10]. While computing reaction rates based on theoretical approaches can be challenging, assumptions towards a realistic atmosphere and operating conditions help understand experimental data. A general model assumption is that the co-adsorbed promoting ions induce a polarization of the substrate metal coupled with an image charge of the opposite sign below the surface [10]. This results in an inhomogeneous electric field at the surface, affecting the adsorption energy of reactants and the rate determining step. While some ions work as promoters, some can be added as poison. An example is the addition of chlorine ions on the surface of copper catalyst that reduces the turnover rate of acetylene cyclization to benzene (Figure 2.1). The presence of Cl ions creates a positive electric field that increases the bond strength of the adsorbed benzene product and the corresponding adsorption energy. Therefore, it becomes harder to desorb benzene and its production rate is lowered.

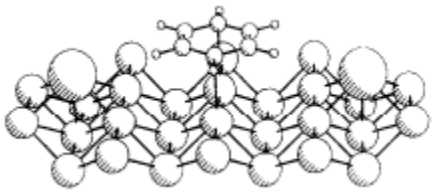

Figure 2.1: $Cu/Cl_2/C_6H_6$ cluster model of co-adsorption of Cl and benzene on copper. With permission from [10]. Copyright 1997 Elsevier.

In general, a positive electric field is induced by electronegative ions; whereas electropositive ions (alkali ions) form a negative field. Depending on the electronegativity of reactants/products, the additive poisons or promotes the reaction. The effect of the

promoter/poison on the bond strength can be measured by a property called work function, Φ [10]. This will be further elaborated in the coming sections.

In classical chemical promotion, when a reactant A reacts with a reactant B to give a product on the surface of a catalyst, at least one bond occurs between reactant A and a metal site M. A-M being the chemisorptive bond has a chemisorption enthalpy ΔH between -1 and -5 eV (-23 and -115 kcal/mol) [2].

Kinetically, the effect of the promoter on the adsorption of reactants can be explained fundamentally by the following equations.

The Langmuir chemisorption surface coverage term, θ_A, is depicted as follows:

$$\theta_A/(1 - \theta_A) = K_A(T)\, p_A \qquad 2\text{-}1$$

where p_A is the partial pressure of A and K_A is the adsorption coefficient of A or equilibrium constant of A on a specific bstrate. K_A is a function of temperature:

$$K_A = exp(\Delta S_A^o/R)\, exp\,(-\Delta H_A^o/RT) \qquad 2\text{-}2$$

where $\Delta S°_A$ is the standard entropy of adsorption of A and $\Delta H°_A$ is the standard chemisorption enthalpy of A that is negative due to the exothermicity of chemisorption, therefore k_A decreases as a function of temperature.

The surface coverage term for A, θ_A can be written as a function of the adsorption coefficients of A and B:

$$\theta_A = K_A\, p_A/(1 + K_A\, p_A + K_B\, p_B) \qquad 2\text{-}3$$

When the limiting step is the surface reaction between co-adsorbed A and B, the Langmuir-Hinshelwood-Hougen-Watson (LHHW) model for the kinetic rate is as follows [11]:

$$r = k_R \theta_A \theta_B \qquad 2\text{-}4$$

where k_R is the reaction constant. Combining eq. 2-4 to eq. 2-3, one gets:

$$r = k_R K_A\, K_B\, p_A\, p_B\, /(1 + K_A p_A + K_B p_B)^2 \qquad 2\text{-}5$$

One more term needs to be added, the surface coverage term for the promoter, θ_p, since it is co-adsorbed on the surface of the catalyst; therefore, eq. 2-6 becomes:

$$r = (1 - \theta_p)\, k_R K_A K_B\, p_A\, p_B\, /(1 + K_A p_A + K_B p_B)^2 \qquad 2\text{-}6$$

The coverage of catalyst surface with the promoter, θ_p, results mathematically in two ends:

$$\left.\frac{\partial r}{\partial \theta_p}\right)_{p_j} > 0 \quad \text{where p is a promoter} \qquad \left.\frac{\partial r}{\partial \theta_p}\right)_{p_j} < 0 \quad \text{where p is a poison} \qquad 2\text{-}7$$

with p_j being constant reactants pressure.

The work function, Φ, mentioned previously, correlates to the electric field of a surface. It is a measurement of the energy required for an electron to escape from its Fermi level to vacuum level such that image charges are negligible, in other words, it is equivalent to the *ionization* energy to lose an electron [2]. A metal surface work function usually varies between 2 eV to 5.5 eV, being the lowest for alkalis and the highest for noble metals such as Pt. Any contamination or crystal plane change results in modification of Φ up to 1 eV. As mentioned earlier, electronegative adsorbates increase Φ of the metal surface, while electropositive adsorbates decrease Φ, due to the formation of a positive field in the first case and a negative field in the latter. The variation in Φ as a function of promoter's coverage is therefore described by Helmholtz equation:

$$\Delta\Phi = \frac{eN_M}{\varepsilon_0}\, P_p \Delta\theta_p \qquad 2\text{-}8$$

where $e=1.6.10^{-19}$ C, $\varepsilon_0=8.85.10^{-12}$ C^2/J.m, N_M is the atomic surface density (atom/m^2) and P_p (C.m) is the dipole moment of the promoter p equal to 3.D or $3.36.10^{-30}$ C.m. Dipole moments being positive for electronegative adsorbates (e.g. $O^{\delta-}$) and negative for electropositive adsorbates (e.g. $Na^{\delta+}$).

From Helmholtz equation, one can relate how adding electropositive promoters such as alkali metals reduces the work function of the surface of the catalyst metal as low as 3 eV; whereas adding electronegative promoters increases the surface work function.

Experiments have shown that the change in work function results in a linear variation of the heat of adsorption, ΔH_{ads} (or energy of adsorption) such that:

$$\Delta|\Delta H_{ads}| = \Delta E_{ads} = \alpha_H \Delta\Phi \qquad 2\text{-}9$$

where α_H is the enthalpic coefficient. The parameter α_H is positive for electropositive adsorbates and negative for electronegative adsorbates; therefore increasing the work function increases the heat of adsorption of electropositive adsorbate and results in a decrease in the heat of adsorption of electronegative adsorbates. The opposite effect is true for the addition of electronegative promoters. A summary of the different effects can be summarized in Table 2-1.

Table 2-1: Relationship between work function and adsorption bond strength.

	Work function change	**Electronegative (electron acceptor) adsorbate**	**Electropositive (electron donor) adsorbate**
Addition of electronegative promoter	$\Delta\Phi>0$ Increase	$\Delta\|\Delta H_{ads}\|<0$ Weaker adsorption bond	$\Delta\|\Delta H_{ads}\|>0$ Stronger adsorption bond
Addition of electropositive promoter	$\Delta\Phi<0$ Decrease	$\Delta\|\Delta H_{ads}\|>0$ Stronger adsorption bond	$\Delta\|\Delta H_{ads}\|<0$ Weaker adsorption bond

2.2. Electrochemical promotion, solid electrolyte and metal catalyst:

Now that the relationship between work function and adsorption strength is clear, it becomes easier to explain the effect of the electric field in modifying the adsorption strength of adsorbates. Electropositive or negative promoters can be pumped electrically to the surface of the catalyst from an ionically conductive electrolyte rather than being added classically during the catalyst's preparation on top. Whether adding positive or negative current/potential will increase or decrease the work function depends on whether the promoters are electronegative or positive. These promoters in electrochemical promotion will be pumped from the solid electrolyte, therefore a review of electrolyte material is necessary. A detailed review can be found in [12]. Solid electrolytes are mainly ionically conducting material. They conduct O^{2-}, H^+, Li^+, Na^+, K^+, Ag^+, Cu^+, F^- and many more ions. Examples of oxygen ion conductors are solid solutions of divalent or trivalent metal oxides (e.g., Y_2O_3, Yb_2O_3, CaO) stabilizing the quadrivalent oxides (e.g., ZrO_2, ThO_2, CeO_2) of fluorite crystal structure [13]. Yttria-stabilized Zirconia (YSZ) (6-10% Y_2O_3 in

ZrO_2) is a widely used ionically conducting material used as an electrolyte as well as in oxygen sensors and fuel cells [14,15]. Na^+ conducting materials include mainly β-alumina material: $Na_{1+x}Al_{11}O_{17+x/2}$ ($0.15 \leq x \leq 0.3$) [16]. Cu^+ conductors include Cu_2Se and $KCuI_5$, and F^- conductors include PbF_2 and CaF_2 material [2]. The conductivity, σ, of these materials, vary as a function of temperature as is shown in Figure 2.2. A low conductivity in the order of 10^{-4} $\Omega^{-1}.cm^{-1}$ is sufficient for electrolyte and sensor applications; whereas a 0.1-1 $\Omega^{-1}.cm^{-1}$ conductivity is usually required for fuel cell applications [17]. For electrochemical promotion studies, YSZ material conducts O^{2-} in a temperature range between 280 and 650 °C [3]. The use of gadolinium doped ceria (GDC) as an O^{2-} ionic conductor has been a focus in Vernoux' lab since it shows ionic conductivity at a temperature as low as 267 °C [12,18].

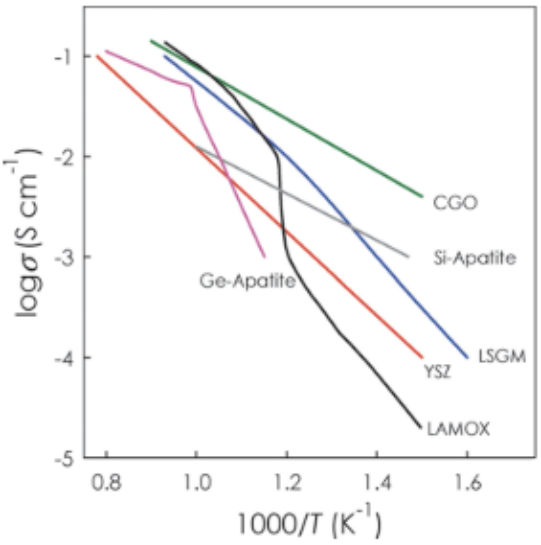

Figure 2.2: Ionic conductivity of various solid electrolytes as a function of temperature. With permission from [12]. Copyright 2013 ACS.

In electrochemical applications, the solid electrolyte is interfaced with conducting metal films, one being the working electrode on one side of the electrolyte, while reference and counter electrodes are found on the other side (Figure 2.3). While the working electrode material is the catalyst film to be tested, the reference and counter electrodes are made of inert material (e.g., gold) to prevent intervention in the catalytic measurements of the working electrode to be tested [19].

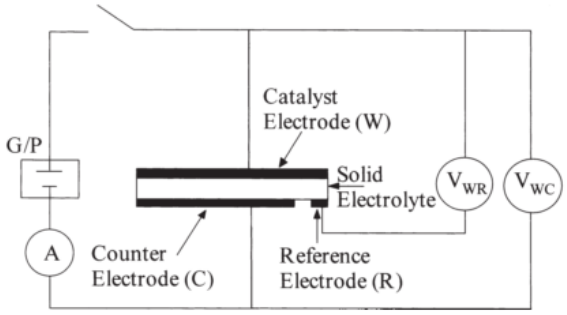

Figure 2.3: Electrode configuration in a NEMCA reactor. With permission from [20]. Copyright 2000 Elsevier.

When using oxygen conducting electrolyte such as YSZ or GDC, applying a potential between the working and reference electrode results in the transfer of oxygen ions. Positive potential results in pumping oxygen ions towards the working electrode (Figure 2.4) while negative potential moves the oxygen ions in the opposite direction [21].

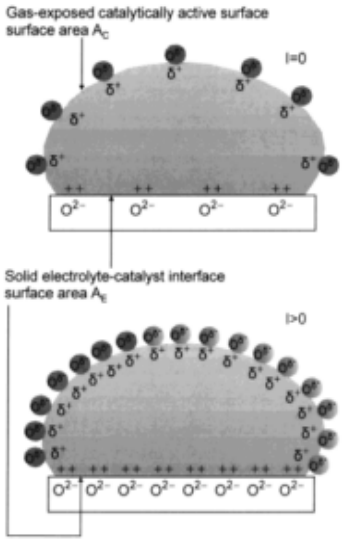

Figure 2.4: Oxygen ions coverage on metal catalyst particle supported on O^{2-} conducting electrolyte (YSZ), under open-circuit (top) and closed-circuit (bottom) conditions. With permission from [22]. Copyright 2001 ACS.

The oxygen charge transfer reaction to the surface of the metal is:

$$O^{2-}\ (YSZ)\ \leftrightarrow O\ (a)\ + 2\ e^{-} \qquad 2\text{-}10$$

The adsorbed ion stays adsorbed on the surface of the metal acting as a promoter that is electronegatively charged and accompanied by its compensating δ^{+} charge:

$$O\ (a)\ =\ O^{\delta-}\ -\ \delta^{+} \qquad 2\text{-}11$$

It can also desorb into oxygen gas O_2:

$$2O\ (a)\ \leftrightarrow\ O_2(g) \qquad 2\text{-}12$$

The coverage of the promoter on the surface of catalyst particle, θ_p can be computed by:

$$\theta_p = \frac{It}{FN_G} \qquad 2\text{-}13$$

here I is current (A), t is time (s), F is Faraday's constant (96 485 $C \cdot mol^{-1}$) and N_G is gas-exposed catalyst surface moles (expressed in moles of oxygen).

In the presence of reactants, adsorbed oxygen has the option of reacting with a gaseous species at the boundary between the electrolyte, the metal and the gas phase called three-phase boundary (tpb) [23].

$$R + O\ (a)\ \leftrightarrow RO\ (g) \qquad 2\text{-}14$$

According to Faraday's law, the application of an electric current allows pumping the ions (e.g., O^{2-}) at a rate of I/nF where I is the current applied, n the charge of the ions (e.g. 2 for O^{2-}) and F the Faraday's constant. Vayenas group were first to report in the 1980s an increase in reaction rate Δr between 10 and 10^5 times greater than the electrochemical rate of supply of (oxygen) ions to the catalyst surface [9,19,24–27]. This non-Faradaic enhancement is denoted by the apparent Faradaic efficiency, Λ, which is greater than 1 (in absolute value):

$$\Lambda = \frac{\Delta r}{I/nF} \qquad 2\text{-}15$$

Therefore, this effect was called *non-Faradaic electrochemical modification of catalytic activity (NEMCA)* or *electrochemical promotion of catalysis (EPOC)* as depicted in Figure 2.5 since not only electrochemical oxidation occurred, instead oxygen ions acted as promoters to enhance adsorption of reactants from the gas.

The enhancement in the reaction rate became:

$$\rho = \frac{r}{r_o} = \frac{r_o + \Delta r}{r_o} \qquad 2\text{-}16$$

where r is the actual closed-circuit catalytic rate and r_o is the open-circuit catalytic rate.

Ethylene, being a common volatile organic compound (VOC) emitted from automobile, has been the reactant of choice for many researchers that used its oxidation reaction as a model

reaction for EPOC studies [27–34]. When the electric circuit is closed, the electrochemical reaction expected to occur with the pumped oxygen ions is:

$$C_2H_4 + 6O^{2-} \rightarrow 2CO_2 + 2H_2O + 12\,e^- \qquad 2\text{-}17$$

which results in an increase in the rate by I/nF. This is showed in Figure 2.5 by the dotted line of the expected increase (noted with 'r_o +I/2F' on top of the line). The actual increase was much bigger (solid line in Figure 2.5) and therefore, this resulted in proving that these oxygen ions pumped on the surface of the catalyst do not only electrochemically react (eq. 2-17), instead they act as promoters and allow an increase in the reaction rate of the ethylene reaction with oxygen from the gas:

$$C_2H_4 + 3O_2\,(g) \rightarrow 2CO_2 + 2H_2O \qquad 2\text{-}18$$

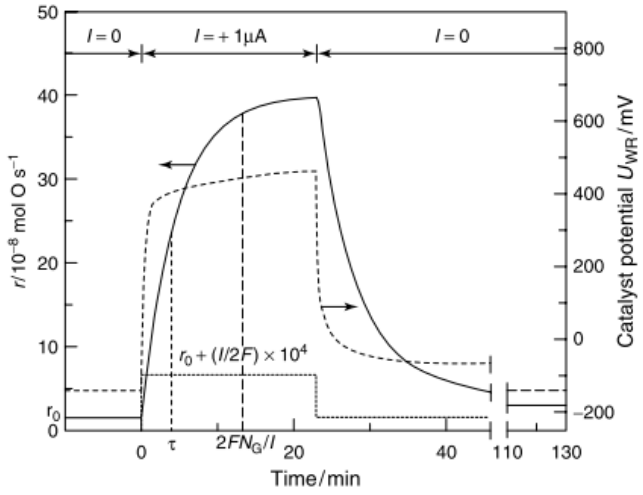

Figure 2.5: Basic EPOC result of increased reaction rate upon current application for C_2H_4 oxidation over Pt catalyst deposited on YSZ; T=370 °C, p_{O_2}= 4.6 kPa, $p_{C_2H_4}$= 0.36 kPa. In dashed line is the catalyst electrode potential U_{WR}. N_G is the Pt/gas interface surface area. τ is the relaxation time. With permission from [2]. Copyright 2001 Springer.

The O_2 from gas adsorbs on the metal into O(a) before reacting with C_2H_4 [24]. The time required to reach 63 % of the maximum reaction rate, r is the relaxation constant denoted by τ and can be also calculated as equal to nFN_G/I where n=2 in case of oxygen [35]; therefore, the active catalyst surface area, N_G can be found from:

$$N_G = \frac{\tau\, I}{2F} \qquad 2\text{-}19$$

And Turn-over frequency (TOF) is equal to the catalytic rate divided by the catalytic surface area:

$$TOF = \frac{r}{N_G} \qquad 2\text{-}20$$

The application of a small current/potential results in modifying the work function of the metal surface as follows [35]:

$$\Delta\Phi\ (eV) = e\Delta U_{WR} \qquad 2\text{-}21$$

where e is the electron charge.

The influence of potential on the work function can now be added to Table 2-1, such a way that an increase in potential increases the work function, Φ, and a decrease in potential decreases Φ; the subsequent effect on adsorption strength follows the same pattern.

The apparent activation energy, E_A has a linear dependence on the catalyst work function [36]:

$$E_A = E_A^0 + \alpha_H\ \Delta\Phi\ = E_A^0 + \alpha_H\ e\Delta U_{WR} \qquad 2\text{-}22$$

where E_A^0 is the activation energy in the unpromoted state and α_H is the NEMCA coefficient, being positive for electrophobic reactions ($\frac{\partial r}{\partial \Phi} > 0$) and negative for electrophilic ($\frac{\partial r}{\partial \Phi} > 0$) reactions.

The enhancement in the reaction rate, ρ (=r/r_o) is consequently changed as follows:

$$ln\left(\frac{r}{r_o}\right) = \frac{\alpha_H\ \Delta\Phi}{k_b \Delta T} \qquad 2\text{-}23$$

where k_b, Boltzmann constant is equal to $1.38.\ 10^{-23}$ J/K and temperature T in K.

In the case where the electron donor adsorbate has the limiting kinetics compared to the electron acceptor adsorbate ($K_Dp_D << K_Ap_A$ and $K_Ap_A >> 1$), increasing Φ results in increasing the electron donor adsorption, allowing an increase in the reaction's rate; the reaction is said to be electrophobic. While, when the electron acceptor adsorbate has the limiting kinetics ($K_Ap_A << K_Dp_D$ and $K_Dp_D >> 1$), decreasing Φ results in increasing the electron acceptor adsorption, allowing an increase in the reaction's rate; the reaction is said to be electrophilic [2]. This is important to understand to know whether potential should be positive or negative to promote the reaction.

The reaction rate can also be related to work function such a way that both increasing or decreasing the work function from the reference metal work function results in decreasing the

catalytic rate; this occurs when kinetics show that both electron donor and acceptor adsorbates are strongly adsorbed on the catalyst surface ($K_Dp_D>>1$ and $K_Ap_A>>1$), meaning that the kinetics exhibits a maximum. This result in volcano-type relation between $\Delta\Phi$ and r where the reaction rate is the highest for $\Delta\Phi$ equal to zero (i.e., Φ is at its intrinsic value) and decreases when decreasing or increasing Φ. On the other hand, when kinetics are positive order in both electron acceptor and donor reactants ($K_Dp_D<<1$ and $K_Ap_A<<1$), an increase in catalytic rate occurs when increasing or decreasing Φ. This is known by inverted volcano-type relation [2]. Multi-scale models for the promotion system can be found in Vayenas *et al.* [4], Brosda *et al.* [5,26] and recently by Fragkopoulos *et al.* [37,38].

2.3. Metal catalyst preparation

The metal catalyst prepared for NEMCA studies used to be a thin film of metal paste deposited by simply brushing it on top of the electrolyte, then dried and calcined at a slow rate [24,39]. This method resulted typically in a catalyst of a thickness in the range of 5-10 μm [25,64] and a metal dispersion less than 0.1% [41]. Various preparation methods have been developed and applied throughout the years to increase the dispersion and reduce the amount of metal used; this includes thermal decomposition, sputtering, wet impregnation, electrostatic spray deposition, and polyol method. Thermal decomposition is based on depositing the precursor salt dissolved in a proper solvent (e.g., water, ethanol) on the corresponding surface material that is heated to evaporate the solvent [29]. Sputtering includes bombarding inert gas ions such as argon on a metal target to deposit a fine layer of the metal onto the surface [42–44]. Wet impregnation is based on dissolving the metal salt precursor in aqueous solution, then depositing, drying and calcining the layers [45–48]. Electrostatic spray deposition (ESD) is based on applying an electric field to atomize a precursor solution towards the heated surface [49–51]. Finally, the polyol method is based on mixing the precursor salt in ethylene glycol and adding sodium hydroxide to control the size of particles, the mixture is refluxed until a colloidal solution is formed; then the solution is deposited, dried and calcined on the solid surface of the electrolyte [28,32,52,53]. When the mixture is being heated and refluxed, ethylene glycol reacts with the metal precursor resulting in oxidizing ethylene glycol to aldehydes then to glycolic and oxalic acid (or glycolate depending on pH). The electron donated from these oxidation results in reducing the metal precursor. The addition of a base, such as sodium hydroxide, results in ionizing glycolic acid to glycolate anion,

which is a stabilizer for the reduced metal in the colloidal form. In Baranova *et al.*, the concentration of NaOH was increased from 0.08 M to 0.13 M; this resulted in a decrease of the particle size of Ru colloid from 3.8 nm to 1.7 nm on average [54]. The importance of these techniques is in the production of small metal nanoparticles that have a higher ratio of surface to bulk atoms and therefore, are able to display different chemical and physical properties from bulk material, playing thus a remarkable role in heterogeneous catalysis [54,55].

2.4. Measurement techniques used

There is a variety of surface science and electrochemical techniques that can be used to test for the origin of electrochemical promotion; this includes work function measurement using ultraviolet photoelectron spectroscopy (UPS) [56] or a Kelvin probe that measures contact potential difference (CPD) [3]. Temperature-programmed desorption (TPD) measures the strength of adsorbents bond [57,58]. AC impedance spectroscopy allows measuring ohmic drop resistance across the electrolyte when analyzing the low-frequency response [34]. X-ray photoelectron spectroscopy (XPS) marks the increase of ionic species coverage on the solid electrolyte to confirm the formation of the ionic double layer on the gas-exposed electrode surface [33,59]. In addition, it detects any shift in the binding energy of the catalyst metal (e.g., Pt4f7/2), usually by $e\Delta U_{WR}$ [60].

To measure the real surface area of a catalyst, surface titration technique can be used [19]. The technique is based on allowing oxygen to flow for a certain time t_{O2}, then purging it with N_2. Then the reactor is purged with CO that reacts with oxygen atoms on the surface of the catalyst and this allows to calculate the surface area per number of atoms. To be able to see particles at the nano-scale and measure them, transmission electron microscopy (TEM) is typically used [61]: a sample is prepared by diluting the catalyst to-be-tested in ethanol and depositing it in a copper grid with a lacy carbon support film [18]. Analysis of the TEM images for particle sizes is performed then using ImageJ software to determine the particles size distribution.

2.5. Summary of EPOC studies performed

Most of the EPOC studies performed used ethylene as the reactant of choice as it is a typical VOC effluent. The reaction rate was found to increase with positive polarization [28,62–65]; however, other behaviors have been observed depending on the reactions' conditions or catalyst used [2,66]. Additional reactions were also tested, such as oxidation of propene [67–69], propane

[44,70–72], CO [73–75] and methane [76–78], reduction of NO in the presence of hydrocarbons [49,79–82], reverse water-gas shift (RWGS) reaction [83] and, recently, SO_2 oxidation to SO_3 that can be used in sulfuric acid plants [36]. Examples of EPOC tests for ethylene, propane, propene, toluene and methane oxidations over YSZ electrolyte are shown in Table 2-2 where preparation method, enhancement ratio and Faradaic efficiency are noted.

In an example of electrochemical promotion for CO oxidation, it was reported that slight promotion for CO oxidation on sputtered Pt nanoparticles (~60 nm) under 2 μA resulted in 30 times rate enhancement [73]. The reason for the common use of Pt catalyst in comparison to other metals is that Pt has the highest ionization potential, therefore, platinum oxide is not stable on its surface compared to Pd or Rh; in other words, Pt is the most stable among noble metals as it demonstrates the highest work function making it attractive to be used [85].

As we mentioned earlier, it is important to have an electrolyte that is ionically conductive. In a test by Nicole *et al.*, TiO_2 was compared to YSZ for its use as a solid electrolyte [60]: the Pt film on YSZ and TiO_2 electrolyte disks have shown that the Faradaic efficiency in the case of TiO_2 is 2.5 % that of the Faradaic efficiency when YSZ was used; this suggested that a fraction equal to 2.5 % in TiO_2 is anionic (O^{2-}) whereas the rest is electronic. In a recent study with a different oxygen-conducting electrolyte, Kambolis *et al.* used GDC material as a solid electrolyte and found an apparent faradaic efficiency of 85 for propane oxidation, when electrochemically promoting dispersed Pt nanoparticles with 200 μA [71]. Propane conversion started at 250 °C when Pt NPs were present, 120 °C lower than the light-off temperature in the absence of Pt. An increase in the oxygen gas consumption from 2.7 up to 4.1 10^{-8} mol O/s was noticed. The Pt nanoparticles were dispersed in LSCF ($La_{0.6}Sr_{0.4}Co_{0.2}Fe_{0.8}O_{3-\delta}$) material. EPOC was tested at a temperature ranging between 267 and 338 °C. Upon polarization at 267 °C, two-step increase was noticed: a fast increase when the current is applied, followed by a second increase after 80 min resulting in an increase in the rate to 19 10^{-8} mol O/s. The step increase in the current can be explained by the fact that the conductivity of the LSCF/GDC electrode is low at this temperature that it requires time to have the electrode reaction delocalizing into the overall layer of the electrode. At negative polarization, the propane conversion decreased for all the temperatures; therefore, propane oxidation on Pt-LSCF/GDC exhibits an electrophobic EPOC behavior.

Table 2-2: Summary of typical EPOC tests for ethylene, propane, propene, toluene and methane oxidation on YSZ support.

Cata-lyst	Catalyst thickness	Loading (mg/cm^2)	Method of application	Potential/ current applied	Temp. (°C)	$P_{reactant}$ (kPa)	P_{O2} (kPa)	Total flow ($mL.min^{-1}$)	Reactant conversion increase (10^{-8} $mol.s^{-1}$)	ρ	Λ	Authors, year & Ref.
Ethylene Oxidation												
Pt	5 µm	N/A	Paste coating	1 µA	370	0.36	4.62	N/A	0.5 to 13.3	27	*74 000*	Bebelis *et al.*, 1989 [24]
Pt	0.2-1.1 µm	0.4-1.9.	Paste coating	2 V	280	0.19	8.2	210	0.063 to 5.93	95	*975*	Koutsodontis *et al.*, 2006 [41]
Pt	30 nm	N/A	Sputtering	270 µA	280	0.19	8.2	420	0.13 to 8.86	67	*188*	Papaioannou *et al.*, 2010 [65]
RuO_2	µm range	0.172	Thermal decomposition	30 V	360	0.1	12	175	4 to 8.3 %	2	N/A	Wodiunig *et al.*, 1999 [62]
RuO_2	µm range	0.097	Thermal decomposition	200 µA	430	2.2	0.9	N/A	0.61 to 6.47	11	170	Constantinou *et al.*, 2005 [29]
IrO_2	µm range	0.126	Thermal decomposition	300 µA	380	0.14	17		0.33 to 4.66	13	41.8	Nicole *et al.*, 1998 [30]
Rh	40 nm	0.041	Sputtering	50 µA	350	2	0.4	200	0.17 to 9.04	52	1024	Baranova *et al.*, 2005 [28]
Propane Oxidation												
Pt	µm range	N/A	Paste coating	3 V	344	0.2	1	112	N/A	2.3	123	Vernoux *et al.*, 2002, [84]
Propene Oxidation												
Pt	86 nm	0.42	Electrostatic spray deposition	-2 V	400	0.2	1	167	2.47 to 5.69	2.3	48	Lintanf *et al.*, 2008 [49]
Toluene Oxidation												
RuO_2	µm range	0.097	Thermal decomposition	100 µA	450	0.2	7.25	35	0.010 to 0.08	8	12	Constantinou *et al.* ., 2005 [29]
Methane Oxidation												
Pd	µm range	N/A	Paste coating	1 V	400	2.6	1.9	N/A	0.295 to 20	68	153	Frantzis *et al.*, 2000 [34]

The obtained rate increase is attributed to the weakening of the Pt-O bond strength, upon backspillover of $O^{\delta-}$ ions from the electrolyte onto the catalyst surface; this results in an increase of the Pt work function [18,71].

In other studies for ionic back-spillover of $O^{\delta-}$, Tsampas *et al.* performed isotopic label studies on Pt catalysts deposited on YSZ in a tubular electrochemical system for propane combustion [86,87]. Using isotopic $^{18}O_2$ gas, the study showed clear proof of the sacrificial promoter model and the contribution of the surface exchange mechanism of oxygen on the catalytic rate. The oxygen ions ^{16}O form the electrolyte spillover onto the catalyst surface and interacts with the normally co-adsorbed oxygen ^{18}O and/or with the co-adsorbed electropositive adsorbates (hydrocarbon adsorption). It was found that in open-circuit the ratio of $C^{16}O^{18}O$ to $C^{18}O_2$ was unity at 350 °C with zero formation of $C^{16}O_2$. This part of the study proved that oxygen vacancies in YSZ favor oxygen exchange reactions between the gaseous oxygen and the electrolyte-provided oxygen, and that the electrolyte oxygen is reacting to produce $C^{16}O^{18}O$. In addition, when an anodic polarization is taking place an enhancement in the catalytic rate is shown; the rate formation of $C^{18}O_2$ increases at a double ratio of the $C^{16}O^{18}O$ showing that the surface oxygen exchange rate is also modified by polarization [87]. The sacrificial ionic species supplied on the catalyst can weaken the Pt-O and increase the propane coverage on the catalyst surface improving the catalytic rate and the oxygen surface exchange rate due to the enhancement in the electromotive force at the three-phase boundary due to the propane presence.

2.6. Scaling-up

Different cell configurations and reactor designs have been applied in these studies, but it was only recently that real efforts to scale-up the design have been shown: Vayenas *et al.* have recently designed a monolithic electrochemical reactor (MECR) to be able to reach commercialization someday, Figure 2.6 [88,89] .Based on Anastasijevic study [90], the fundamental phase of NEMCA was between the years of 1980s and 2000s when basic experiments started. Between 2000 and 2020, the extended fundamental testing, in addition, concept application and scaling-up to pilot scale would be taking place. Between the years of

2020 and 2040, development of reactors and processes would take place and NEMCA would be commercially applied.

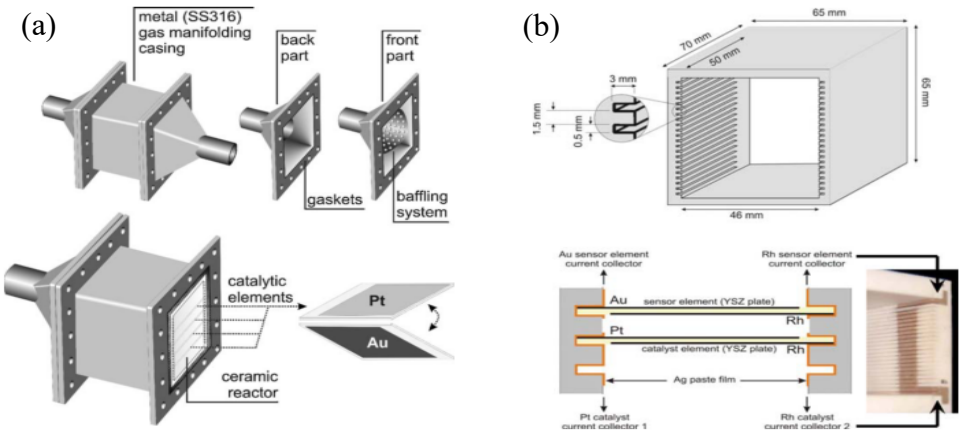

Figure 2.6: Schematic of a monolithic electrochemical promotion reactor. (a) With permission from [88]. Copyright 2009 Elsevier. (b) With permission from [89]. Copyright 2010 Springer.

2.7. Special Study on methane electrochemical promotion

Methane is the most difficult hydrocarbon to oxidize due to its highest ratio of hydrogen to carbon [91]. It is a greenhouse gas with 23 times more effect at warming the atmosphere than CO_2. It is the main component of natural gas (NG) and interest in generating power from NG combustion rather than gasoline or diesel has been increasing with a purpose of meeting emission standards in the metropolitan areas, especially in the United States and Europe [91]. The primary reaction that occurs in NG combustion is presented in eq. 2-24. Risks of forming NO_x from the combination of nitrogen and oxygen occurs only at above 1600 °C, therefore temperatures of the exothermic reaction should be maintained under this value [92]. In addition, oxygen-rich conditions are required to prevent the formation of CO, another greenhouse gas (eq. 2-25).

$$CH_4\,(g) + 2O_2(g) = CO_2\,(g) + 2H_2O\,(l) \quad \Delta H_{298} = -891.2\ kJ/mol \qquad 2\text{-}24$$

$$CH_4\,(g) + 3/2O_2(g) = CO\,(g) + 2H_2O\,(l)\ \Delta H_{298} = -607.3\ kJ/mol \qquad 2\text{-}25$$

Other reactions may occur, this includes steam reforming (eq. 2-26 and 2-27), and water gas shift (eq. 2-28) reactions:

$$CH_4(g) + H_2O(g) = CO(g) + 3H_2(g) \quad \Delta H_{298} = +206.1\ kJ/mol \qquad 2\text{-}26$$

$$2H_2(g) + O_2(g) = 2H_2O(g) \quad \Delta H_{298} = -483.6\ kJ/mol \qquad 2\text{-}27$$

$$CO(g) + H_2O(g) = CO_2(g) + H_2(g) \quad \Delta H_{298} = -41.2\ kJ/mol \qquad 2\text{-}28$$

Steam reforming occurs at temperatures above 550 °C [93]. It is necessary to keep in consideration these additional reactions since temperature and partial pressure conditions, as well as the catalyst in use, can affect the equilibrium of these reactions [94]. In general, a higher temperature favors CO formation, thus the necessity to use catalytic combustion to maintain a low oxidation temperature.

Noble metals and oxides have been used for the oxidation of methane. The three noble metals to show the highest catalytic activity were Pd, Rh, and Pt with Pd showing a much higher conversion (80 % at 500 °C for Pd compared to less than 25 % for Rh and Pt) [85,95]. The support has a great effect in increasing the surface area and stabilizing the catalyst for a longer-term; alumina showed the highest enhancement effect followed by silica then titania [96]. For example, 3.5 % Pd supported on Al_2O_3 resulted in no conversion of methane at 200 °C; at 350 °C, a much higher conversion occurs and at 400 °C, a full conversion is expected [91]. This was in the case were the catalyst was impregnated on the support using the metal precursor that is wetted on the surface of the support then calcined at high temperatures. A note that γ- Al_2O_3 sinters at temperatures above 1000 °C to form α -Al_2O_3 of lower surface area reducing the dispersion of the catalyst.

The reaction mechanism for the chemisorption of alkanes is dissociative through which the alkane dissociate to methyl and hydrogen directly on site. The further steps of dissociation mechanism for methane depends on the crystal phase of PdO as well as on the presence of hydroxyl group which changes the mechanism of the reaction [97]. The dissociative adsorption of methane is the rate determining step and have been demonstrated to be the easiest on Pd (101) surface [98]. Depending on the concentration of oxygen on the surface, the adsorption of CH_4 occurs on a metal site or on an oxygen site depicted as follows:

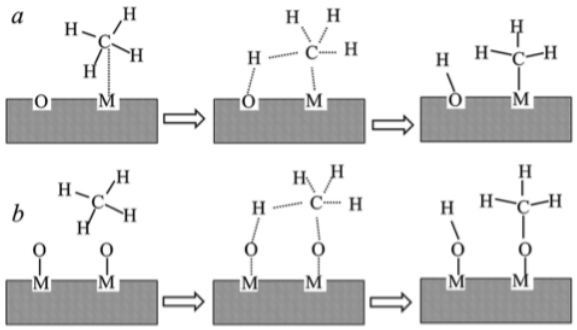

Figure 2.7: Methane dissociative adsorption on (a) a metal site vs (b) oxygen site. With permission from [98]. Copyright 2016 RSC.

Recently, electrochemical promotion of catalysis for the combustion of methane have been finding more attention from researchers. Jimenez-Borja *et al.* performed an anodic polarization on Pd thin film where the application of 20 mA made the reaction rate 2.3 times higher at a temperature of 600 °C [99]. This increase is due to the fact that methane oxidation is electrophobic, resulting in an increase in reaction rate when oxygen coverage on the catalyst increased with the positive polarization. When Pd was supported on CeO_2, a higher voltage was required to reach the same current reached for unsupported Pd; this was due to the lower conductivity of PdO particles and the presence of a semi-conducting film of CeO_2. The enhancement ratio was lower but the overall reaction rate for the supported Pd was 5 times higher when polarized at 10 mA compared to unsupported Pd, polarized at 30 mA. In addition, Jimenez-Borja *et al.* [45] also studied the effect of catalyst preparation technique on the catalyst activity; they compared the activity of Pd prepared by wet impregnation to stand-alone Pd paste or when supported on CeO_2, showing that the highest open-circuit catalytic rate was for impregnated Pd on CeO_2, then wet-impregnated Pd, then Pd paste deposited on CeO_2, and the lowest rate was for Pd paste. Matei *et al.* have also studied electrochemical promotion of methane combustion using palladium catalysts impregnated on porous YSZ and Pd deposited on dense YSZ electrolyte [48,100]. A current of 5 mA was used to enhance the catalytic activity of Pd on porous YSZ by 10 % with a Faradaic efficiency of 10 at 400 °C; on dense YSZ, the catalytic rate was 31 times lower in open- and closed- circuit conditions compared to on porous YSZ, but the enhancement ratio was 2.3. When using platinum as a catalyst, a higher temperature of 700 °C was required to enhance the catalytic rate of methane oxidation [35]. A current of 5 mA resulted in an enhancement rate of 4 and Faradaic efficiency of 1.42. Rhodium,

Rh paste spread in a thin film on YSZ was tested for electrochemical promotion by Nakos *et al.*; using a constant current of 600 μA resulted in a three times increase of the methane oxidation rate and an apparent Faradaic efficiency of 170 at a temperature of 430 °C and a slight excess of O_2 [101].

A note to be mentioned is that methane oxidation to ethane and ethylene does not increase through electrochemical oxidation due to the fact that increasing the number of oxygen on the catalyst does not increase the number of active site for coupling carbon radicals; Eng *et al.* explained that matter by the fact that methane coupling involves a gas-phase reaction step ($2\ CH_3 \rightarrow C_2H_6$) [102].

2.8. Metal-support interaction studies

In the previous sections, we slightly discussed the use of support material such as CeO_2 and YSZ to enhance the catalytic activity. The role of a support in heterogeneous catalysis expanded from only stabilizing a metal dispersion to affecting the behavior of the catalysts and their activity [103–106]. The use of a high surface area support results in increasing the contact between the metal and the support, and often an outstanding increase in the catalytic activity. This is coupled with the use of nanoparticles of precious metals to increase the surface area of contact [107]. The phenomenon is known as metal-support interaction (MSI) that depends on the nature of the support used and the particle size of the catalyst; the smaller the particle size is, the higher the dispersion is, resulting in a stronger active interaction between the metal and support [108] . For instance, Overbury *et al.* showed that gold nanoparticles supported on the higher surface area TiO_2 show better catalytic activity than the lower surface area SiO_2 due to the stronger metal-support interaction [104]. Metcalfe and Sundaresan have shown an increase in the catalytic activity of Pt when supported on TiO_2 than when supported on YSZ or gamma-Al_2O_3 [109]. They also found that Ni supported on TiO_2 and on YSZ showed much higher catalytic activity than TiO_2 or YSZ alone [109]. Mullins *et al.* showed a better support effect of YSZ compared to C or B-alumina on platinum NPs in the case of CO oxidation [110]. In addition, Isaifan *et al.* showed a high conversion of CO and C_2H_4 in an oxygen-free environment when nanocatalyst used is Pt/YSZ, Pt/CeO_2 or Pt/SDC [32].

In this work, we discuss the 'catalytic activity' and its increase when dispersing nanoparticles on variable supports; this catalytic activity is a projection of the metal's effect on the adsorption enthalpy of reactants. The change in the adsorption enthalpy of reactants on the supported catalysts is due to the thermally induced migration of ionic species from the support to the surface of the catalyst. This is referred to as self-induced electrochemical promotion [27,107,109]: the catalyst used is nano-dispersed in the support and therefore, the distance for oxygen ions to migrate from the support to the catalyst is very short (2-5 nm) that thermal force is sufficient to allow the promoting migration of oxygen ions, $O^{\delta-}$ to the catalyst surface. This ionic conductivity behavior of the support occurs under oxidizing conditions (i.e., excess of O_2 gas) [2]. When comparing MSI to EPOC, in the latter, the migration of $O^{\delta-}$ is assisted electrochemically and is controlled in-situ resulting in a prolonged promoter life-time on the catalyst surface compared to supported metal catalysts [27]. Similarly to EPOC, the promotional (MSI) rate enhancement ratio (ρ_{MSI}) is depicted as equal to [60] :

$$\rho_{MSI} = {}^{r}/_{r_u} \qquad 2\text{-}29$$

where r_u is the catalytic rate of the unpromoted (i.e., free-standing) catalyst ($mol \cdot s^{-1}$).

In a study by Acerbi *et al.*, they showed the relationship between the temperature of reduction of CeO_2 support and the work function of different catalyst metals, knowing that the work function correlates with the adsorption strength [111]. The conduction band energy E_c for the support oxide is higher in energy than the Fermi level of the metal; therefore, there is a net transfer of charge from the oxide to the metal lowering the enthalpy of formation of the doubly ionized oxygen vacancy and therefore reducing ceria. The increase in the work function (by changing the metal) decreases the barrier for oxygen-vacancy formation allowing a decrease in the temperature of reduction of CeO_2. This is known by the "junction effect" theory that predicts that the intimate contact between a metal with low work function and a semiconducting oxide with high ionisation energy results easily in establishing an equilibrium of the electrons between the conduction band of the oxides and the energy states surrounding the Fermi level of the metal [112]. The inversely proportional correlation between support reduction temperature and work function was then followed by a volcano-type correlation between support reduction temperature and the d-band location relative to the Fermi level [113]. Other factors such as the degree of filling of the d-bands and coupling matrix element

between the adsorbate states and metal d-states affect the reducibility of the metal oxide but were not studied by the authors [113]. The d-band center, ε_d, defined as the centroid of the d-type density of states in an atomic sphere centered at a surface atom [114], either forms a (d-σ) bonding state with the adsorbate bonding σ orbital or a (d- σ)* anti-bonding state. Metals such as Ru, Rh, Pd and Pt have high-lying d-band centers and therefore, they're able to strongly break the O-O bond; however, this results in a high coverage of oxygenated intermediates [115]. On the other hand, metals such as Ag and Au have low-lying d-band centers and therefore bind less strongly [115]. An optimum is found close to d-band center value of Pt explaining the inverse volcano relationship between reduction temperature and metal d-band center, Figure 2.8. At this value of d-band center, the Pt is able to dissociate H_2 better than Ag or Au and on the other hand, it does not have high affinity to oxygen like Ru, Rh and Pd.

The reduction of a mixed ionic electronic conducting support and the electron transfer from the support to the catalyst metal can result in weakening of the adsorption bond with the reactants depending on their electronegativity [110]. For example, CO adsorption on Pt deposited on CeO_2 is weakened due to the fact that the metal d-band is more filled resulting in weakening of the bond formation with CO 5σ electrons (i.e., overlapping with 5σ orbital) [110]. The decrease in the bond strength between a metal and a substrate due to the support reduction was primarily cited by Tauster *et al.* who showed that precious metals (e.g., Pt, Pd, Rh, Ru. Ir) deposited on titania (TiO_2) lost their ability to chemisorb H_2 [116]. This was also explained by the reduction of TiO_2 to TiO_x and the overlapping of the metal and support d-orbitals. The noble metals were partially covered with an overlayer of TiO_x species leading to the blockage of H_2 chemisorption sites [116,117].

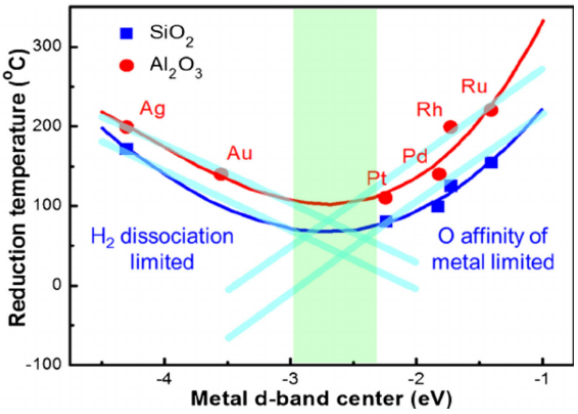

Figure 2.8: Inverse volcano correlation between the temperature of the reduction of ceria and the center d-band energy in CeO_2/Metal supported on Al_2O_3 and SiO_2. With permission from [113]. Copyright 2013 Wiley.

When comparing the catalytic rate of a supported catalyst, to that of an electrochemically promoted catalyst, an analogy can be found in the increase of the catalytic rate using these two methods. A noteworthy study to be mentioned is that of Nicole *et al.* [60] that can be summarized in Figure 2.9. At 50 % dispersion of IrO_2 in TiO_2, the open-circuit catalytic activity is equivalent to the catalytic rate of unsupported IrO_2 that was electrically promoted with a 200 μA current.

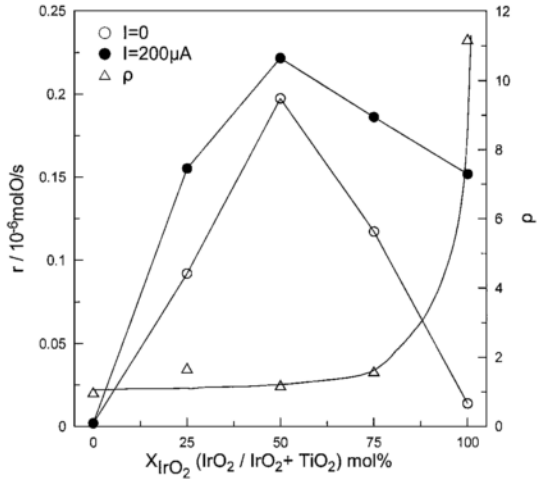

Figure 2.9: Effect of IrO_2 mol fraction on the open-circuit and closed-circuit catalytic (i.e., I= 200 μA) rate at T=380 °C, p_{O2}= 20 kPa, p_{C2H4}= 0.15 kPa. With permission from [60]. Copyright 2001 Elsevier.

2.9. Density functional theory method and modelling

2.9.1. Introduction

When starting work with computational modelling of electrochemical promotion, one has to go back to the basics of quantum mechanics and more specifically, the *Schrödinger equation,* which was developed by Erwin Schrödinger in 1925, and is expressed in an eigenvalue form as follows:

$$\widehat{H}\,\psi_n(\vec{r},\vec{R}) = E_n\,\psi_n(\vec{r},\vec{R}) \qquad 2\text{-}30$$

Where n-particle wave function $\psi_n(\vec{r},\vec{R})$ describes the motion of the electrons and nuclear in the field of the nuclei, $\widehat{H}$ is the time-independent Hamiltonian, and E_n is the energy level of the system, for spatial coordinates of nuclei $\vec{R}$ and electrons $\vec{r}$ [118]. Note that the right-hand side can be written as a function of time as an imaginary component of the derivative of the wave function as a function of t multiplied by the $\hbar$ (reduced Planck's constant).

To simplify the very complex system, variables can be separated based on nuclear and electronic motion following the *Born-Oppenheimer approximation* [119]. This approximation is based on the fact that electrons are much lighter than nuclei; therefore, we can consider that the nuclear and electronic motion are independent. Moreover, electron movement is much more instantaneous than the nuclei and therefore their wave function can be separated and the total wave function can be approximated to be equal to that of electrons. Nevertheless, with a system made out of hundreds or thousands of electrons, the electronic part of the equation is too complicated to solve.

Ab initio ('from scratch') methods to solve the electronic *Schrödinger* equation use first-principle quantum chemistry [120]. Those methods include *wave function* solving methods such as Hartree-Fock (HF), Configuration Interaction (CI) theory, Perturbation theory (PT) and coupled Cluster Methods (CC), and Density Function Theory (DFT) methods, which are more populous [121]. *Wave function* methods can provide high-accuracy results if a high level of Configuration Interactions was offered; however, it is limited to the number of electrons it can be scaled to (10-100 electrons). It is even more restricted (10 electrons) in Transition State calculation, making it an unattractive method. In this thesis, Density Functional Theory was used for calculation as it is less computational-time demanding.

2.9.2. Density functional theory

Due to the electron-electron interaction term in the Hamiltonian, *Schrödinger equation* cannot be solved without large approximations; hence, computational quantum chemical methods have an aim of using approximation solution with an adequate range of applicability.

In the 1920s, Thomas and Fermi [122] made advanced progress towards the resolution of the electronic Hamiltonian, by relating the energy of homogeneous electron gas to its electronic density. Few decades afterward in 1964, Hohenberg and Kohn [123] proved that this relationship can be applied to any kind of electronic system, putting the basis for *Density Functional Theory* (DFT).

The Hamiltonian operator can be described as the sum of three operators: kinetic energy operator $\hat{T}$ arising from the motion of electrons, potential energy operator $\hat{V}$ describing the nuclear-electron attraction and the electron-electron repulsion presented by $\widehat{W}$.

$$\widehat{H} = \hat{T} + \hat{V} + \widehat{W} \qquad 2\text{-}31$$

Hohenberg and Kohn proved that the ground-state molecular energy, its wave function and all related molecular properties can be determined by the specific electron density $\rho(\vec{r})$. DFT is based on Hohenberg-Kohn two main theorems, among them is:

Theorem 1. *The external potential $\hat{V}$ is a unique functional of ρ; since V fixes the Hamiltonian, the particle ground state is a unique functional of ρ. Therefore, there is a direct relationship between the electronic density and the energy (and its individual parts).*

$$E[\rho] = T[\rho] + V[\rho] + W[\rho] \qquad 2\text{-}32$$

The kinetic functional can be split to two contributions, $T_S[\rho]$ and $T_C[\rho]$, the one-particle term and an unsolved term which contains the difference between the real functional and the one particle term. Similarly, the electron-electron repulsion functional includes two terms: the classic interaction between two charges' densities (Coulomb): $W_{CL}[\rho]$ and a non-classical term $W_{NCL}[\rho]$. Therefore, eq. 2-32 can be separated into known terms and an *Exchange-Correlation functional* $E_{XC}[\rho]$ which contains all the unknown terms:

$$\begin{aligned} E[\rho] &= T_S[\rho] + T_C[\rho] + V[\rho] + W_{CL}[\rho] + W_{NCL}[\rho] \\ &= T_S[\rho] + V[\rho] + W_{CL}[\rho] + E_{XC}[\rho] \end{aligned} \qquad 2\text{-}33$$

Finding the analytical expression of the exchange-correlation functional is a major task in DFT; therefore, multiple approximation-functional were proposed.

2.9.3. Exchange-correlation functional

There are two approximations: the *Local Density Approximation* (LDA) and *Generalised Gradient Approximation* (GGA).

LDA assumes that the charge density varies very slowly throughout a molecule such a way that at a local region of the molecule the electron gas can be assumed uniform. Thus, the basis of this model is the uniformity of the electron gas [124].

GGA model adds an additional term to the LDA exchange-correlation energy. It introduces a gradient correction to take into account the variation in the density gradient that affects the exchange-correlation functional [125].

Some of the notable exchange-correlation expressions includes Perdew (P86), Becke (B86, B88), Perdew-Wang (PW91), Laming-Termath-Handy (CAM) and Perdew-Burke-Enzerhof (PBE) for the exchange part and Perdew (P86), Lee-Yang-Parr (LYP), Perdew-Wang (PW91) and Perdew-Burke-Enzerhof (PBE) for the correlation term [126].

A third class of functional in DFT is *hybrid* functional like B3LYP *exchange-correlation* functional which is proven to be a higher accuracy approach; however, it is more time-demanding than *non-hybrid* exchange. It has LDA and GGA factors but also an *exact exchange* energy factor [127].

In this thesis, we used the PBE functional as it is a popular choice with a good description of chemical bonds.

2.9.4. Modelling a periodic system

Metal materials are our object of interest in experiments; when it comes to modeling metal crystals, a difficulty comes up as they have an infinite number of atoms. As a result, when calculating for the wave function, with an infinite number of atoms, the wave function expression will also be infinite. To overcome this difficulty, a *cluster model approach* [128] or a *periodic* or *slab model* [129] can be used. While a *finite cluster model* can be used to describe local properties, they can result in divergence of result on the edge of the cluster unless it was considerably large [130]; hence, periodic models are better suited for adsorption energies

calculation. The *periodic or slab model* is based on the band-structure theory that allows the examination of the quantum mechanical wave functions for an electron in a periodic lattice of atoms. A geometrical repetition of the system in the x or y axes results in a bi-dimensional slab. The periodicity in the z-direction is broken to allow for the creation of a surface (as seen in Figure 2.10). To determine the required vacuum size, different vacuum widths in the z-direction can also be modeled and calculation towards the effect of the vacuum size on the convergence energy is usually performed. Typically, no less than 10 Å of vacuum is required to prevent the interaction with another slab in the z-direction.

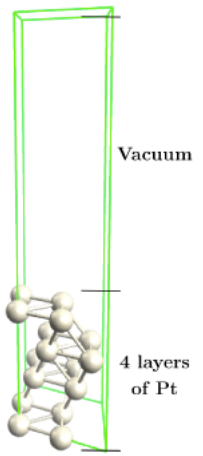

Figure 2.10: Slab model sketch of a fours layer slab repeated in the z-direction with a vacuum of ~8 layers thickness.

While problems related to cluster boundaries are avoided in a *slab model*, a limitation associated to the finite number of atoms and layers has to be controlled; therefore, a need to use a large supercell arises with a concomitant increase in computational cost (i.e., calculation time).

In a perfect metallic crystal, the unit cell is repeated to obtain a system of atoms arranged in a regular way. Based on *Bloch's theorem* [131], the periodicity of the crystal can be used to reduce the infinite number of one-electron wave function and express it as the product of a cell periodic part u and a wave-like part, to find the wave function of the periodic system, $\psi_{n,\vec{k}}$ as:

$$\psi_{n,\vec{k}}(\vec{R}) = e^{i(\vec{K}.r)} u_{n.\vec{k}}(\vec{R}) \qquad 2\text{-}34$$

Where $\vec{R}$ is the position of the crystal, n is the energy level of the periodic systems associated with u a periodic function of the system and $\vec{k}$ is a vector of the reciprocal space of the crystal. The problem with an infinite number of electrons is expressed now as a problem of having the wave function in terms of an infinite number of reciprocal space vectors within the first Brillouin zone (primitive cell in reciprocal space). Therefore, the Brillouin zone is sampled at special sets of k-points. The k-points sample has two methods that can be calculated with: the Chadi-Cohen method [132], or the Monkhorst-Pack method [133], which came as an alternative approach three years after; the latter method is commonly used, and the number of k-points is decided through the DFT calculations, specifically for the modelled cell.

The total wave function at each k-point can be expressed in a 3D-Fourier series as a sum of a finite number of plane waves whose wave vectors $\vec{g}$ are reciprocal lattice vectors of the crystal. As all Fourier series, usually such a set is infinite; however, an energy cut-off can be introduced to reduce the basis set to a finite size as long as it is large enough to converge the set. This energy cut-off $G_{cut\text{-}off}$ depends on the system's total energy; therefore, it needs to be sufficiently high to make the error arbitrarily small. The value of $G_{cut\text{-}off}$ is also tested for, based on the system under investigation.

2.9.5. The VASP code

VASP (Vienna Ab ignition Simulation Package) developed by G. Kresse, J. Furthmüller and J. Hafner [134] is a typical program to apply DFT to periodic systems using pseudopotentials and plane waves for all elements in the periodic system. The pseudopotential methods include the *ultra-soft pseudopotentials* (US-PP) and the *Projector Augmented Wave* (PAW) method. These functions map the complicated wave function onto 'pseudo' wave functions $\tilde{\psi}$. Algorithms in VASP work such that they calculate the electronic ground state for a given geometry, they calculate the forces, then they predict a new geometry based on these forces. These steps are repeated until energy criteria are met (carefully chosen in the INCAR file). A special algorithm is called the *quasi-Newton* (QN), where those energy criteria are ignored and forces are minimized. Transition state structures and energies are also calculated using the VASP code and various technique implemented in VASP such as NEB and Dimer method. Further information about VASP can be found at: http://cms.mpi.univie.ac.at/vasp/vasp/vasp.html.

2.9.6. Transition-state search

A transition state between a given reactant and a desired product is essential to be identified. It gives us information about the activation energy required to reach a certain product if following the minimum energy pathway (MEP). At the transition state, as well as at the reactant and the product, the first derivatives of the energy (forces) are zero. On the other hand, unlike the initial and final state, the transition state is at a maximum point of energy in one direction only (the direction which connects it to the reactant and product) and is at a minimum in all other directions. The second derivative with respect to the reaction coordinate is negative but is positive with respect to all other directions.

Typically, the transition-states are determined using the *Nudged Elastic Band* (NEB) method in combination with the *Dimer* method. As a first step before the NEB or Dimer methods, a first *path* is created as a rough estimation of the trajectory that would be followed from the reactant to the product as shown in Figure 2.11. After a few iterations with NEB, a rough estimation of the minimum energy path (MEP) is found. The two images with the highest energy are chosen to be considered as a rough estimation of where the Transition-state position would be. Those two images are then analyzed using the Dimer method to find the exact transition-state. The Quasi-Newton algorithm is sometimes used as an extra step for finding TS. The calculations are then verified using the vibrational frequency analysis, which should yield a single imaginary frequency that should be consistent with the reaction path under study.

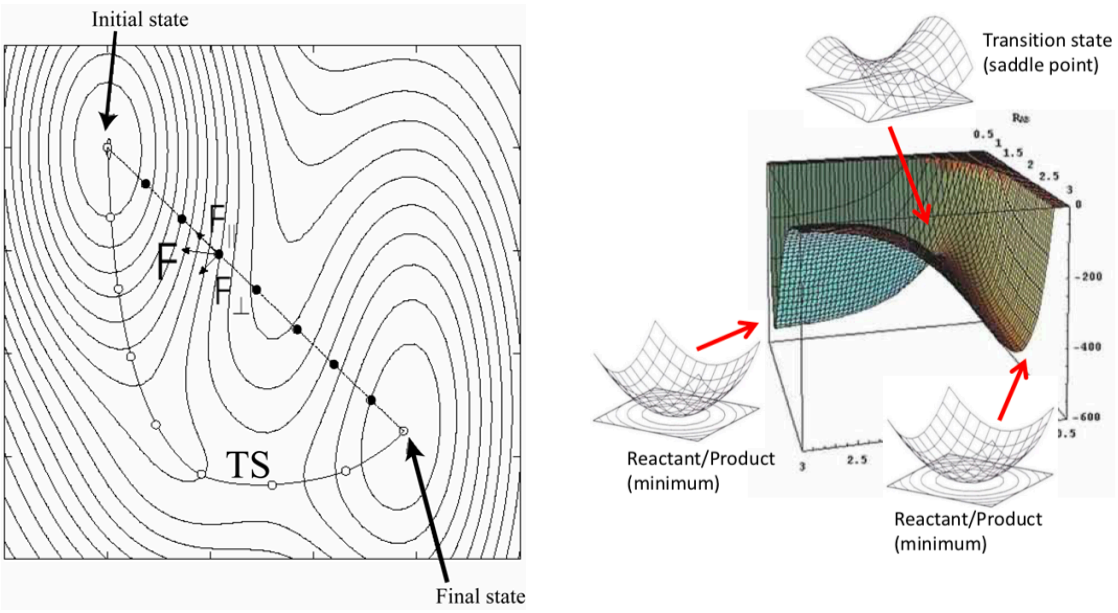

(a) (b)

Figure 2.11: a) Schematic 2D representation of the NEB method: starting with a first guess of energy path (with black dots) to a minimum energy path (with white dots). With permission from [135]. Copyright 2018 C. Michel. *and b) 3D representation of initial, transition and final states.* With permission from [136]. Copyright 2019 Skylaris.

2.9.7. Computational modelling of electrochemical promotion

Theoretical kinetic and to a less extent density functional theory (DFT) modeling of the electrochemical promotion of catalysis were implemented previously to model the oxygen double layer formed upon application of an anodic polarization [137,138]. Brosda *et al.* performed kinetic modeling to demonstrate the electrostatic interaction between the effective double layer and the catalytic adsorbate generated at the catalyst-gas interface [5,26]. A linear correlation between the catalyst's work function and the application of potential was found [138]. Then, Pacchioni *et al.* modeled using point charges the effect of ions presence on the surface of a catalyst using cluster models [9,10]. While in the first work the effect of the charge was linear to the covalent bond strength (of acetylene), the second work showed that there is a second degree effect between the polarization and the migration of the ionic atoms [9,10]. The electrostatic field induced from the adsorption of ions on the surface [139] affects the co-adsorption of another reactant without any direct contact [10]. Similarly, González *et al.* simulated the electric field effect on the adsorption of CO on RhCu bimetallic surface using a

cluster model [140]. And finally, using DFT modeling, Leiva *et al.* investigated the adsorption of oxygen in the presence of sodium on Pt surface [141].

2.9.8. Using the VASPsol solvation model

The addition/removal of electrons from the surface, mimicking the effect of oxygen ion migration, was made possible using the solvation model VASPsol [142,143] which factors in the Poisson-Boltzmann (PB) continuum approximation and incorporate it in the general Kohn-Sham equation. which has been implemented in VASP under the name of VASPsol.

The implicit solvation model places a quantum-mechanical solute in a cavity surrounded by a continuum dielectric description of the solvent. This would allow the mimicking of the effective electrochemical double layer.

The default dielectric constant, simulating aqueous solutions, is usually used; however, changing the solution used (by using another dielectric constant) is important to see the effect of this factor on the calculation. Another important factor that can be manually changed is the cavity size which may have as well an effect on the calculation values if not chosen properly.

This solvation model is relatively new (2015) and has been employed exponentially in electrochemical studies to mimic the presence of an external or internal electric field [144–148].

Norskøv *et al.* showed that the activation energy for CO_2 reduction is effected by an electric field that simulated the presence of sodium ions [148]. Che *et al.* studied the effect of an electric field that mimics the adsorption of K^+ ions or the decrease in the radius of curvature of an electrode tip [144]. In Kuo et al., the VASPsol model was used by Kuo *et al.* to demonstrate the variation in the adsorption energy of oxygen due to pH and protonation [149]. Photoexcitation of metal surfaces was modeled by Xu *et al.,* explaining the effect of photons on the reduction of CO_2 [150]. In solid-oxide fuel cells, a large electric drop may occur due to many factors such as the adsorption species at the interface, the electronic structure of the electrode and the effective potential in the bulk solution [151]. Therefore, VASPsol can be used to model the effect of an electric field on the adsorption of a reactant [152].

References

[1] G. Ertl, H. Knozinger, J. Weitkamp, Handbook of Heterogeneous Catalysis, Wiley-VCH, Weinheim, 1997.

[2] C.G. Vayenas, S. Bebelis, C. Pliangos, S. Brosda, D. Tsiplakides, Electrochemical Activation of Catalysis: Promotion, Electrochemical Promotion, and Metal-Support Interactions, Springer, New York, 2001.

[3] C.G. Vayenas, S. Bebelis, S. Ladas, Dependence of catalytic rates on catalyst work function, Nature. 343 (1990) 625–627.

[4] C.G. Vayenas, S. Brosda, C. Pliangos, Rules and Mathematical Modeling of Electrochemical and Classical Promotion 1. Reaction Classification and Promotional Rules, J. Catal. 203 (2001) 329–350.

[5] S. Brosda, C.G. Vayenas, Rules and Mathematical Modeling of Electrochemical and Classical Promotion 2. Modeling, J. Catal. 208 (2002) 38–53.

[6] M.P. Kiskinova, Poisoning and promotion in catalysis based of surface science: concepts and experiments, 70th ed., Elsevier Science, Amsterdam, 1992.

[7] B. Hammer, J.K. Norskov, Theoretical Surface Science and Catalysis — Calculations and Concepts, Adv. Catal. 45 (2000) 71–129.

[8] D.W. Goodman, Model Studies in Catalysis Using Surface Science Probes, Chem. Rev. 95 (1995) 523–536.

[9] G. Pacchioni, F. Illas, S. Neophytides, C.G. Vayenas, Quantum-Chemical Study of Electrochemical Promotion in Catalysis, J. Phys. Chem. 100 (1996) 16653–16661.

[10] G. Pacchioni, J.R. Lomas, F. Illas, Electric field effects in heterogeneous catalysis, J. Mol. Catal. A Chem. 119 (1997) 263–273.

[11] M. Boudart, G. Djega-Mariadassou, Kinetics of heterogeneous catalytic reactions, Princeton, NJ, 1984.

[12] P. Vernoux, L. Lizarraga, M.N. Tsampas, F.M. Sapountzi, A. De Lucas-Consuegra, J.L. Valverde, S. Souentie, C.G. Vayenas, D. Tsiplakides, S. Balomenou, E.A. Baranova, Ionically conducting ceramics as active catalyst supports, Chem. Rev. 113 (2013) 8192–8260.

[13] W.L. Worrell, Oxide Solid Electrolytes, in: S. Geller (Ed.), Solid Electrolytes, Springer Berlin Heidelberg, Berlin, 1977: pp. 143–168.

[14] W. Gopel, New materials and transducers for chemical sensors, Sensors Actuators B. Chem. 18 (1994) 1–21.

[15] H.S. Subbarao, E C, Maiti, Solid Electrolytes with Oxygen Ion Conduction, Solid State Ionica. 11 (1984) 317–338.

[16] G. Farrington, B. Dunn, J. Thomas, The multivalent Beta-Aluminas, in: T. Takahashi (Ed.), High Conduct. Solid Ion. Conduct., World Scientific, Singapore, 1989: pp. 327–365.

[17] B.C.H. Steele, Dense Ceramic Ion Conducting Membranes, in: H.L. Tuller, J. Schoonman, I. Riess (Eds.), Oxyg. Ion Mix. Conduct. Their Technol. Appl., Erice, 1997.

[18] A. Kambolis, L. Lizarraga, M.N.N. Tsampas, L. Burel, M. Rieu, J.-P. Viricelle, P. Vernoux, Kambolis, L. Lizarraga, Tsampas, Rieu, Viricelle, Vernoux, Electrochemical promotion of propane combustion on highly dispersed Pt nanoparticles, ECS Trans. 45 (2012) 535–541.

[19] I.V. Yentekakis, S. Neophytides, C.G. Vayenas, Solid Electrolyte Aided Study of the Mechanism Polycrystalline Platinum of CO Oxidation on Polycrystalline Platinum, 111 (1988) 152–169.

[20] C.G. Vayenas, Short communication on the work function of the gas- exposed electrode surfaces in solid state electrochemisrtry, J. Electroanal. Chem. 486 (2000) 85–90.

[21] M. Stoukides, C.G. Vayenas, The effect of electrochemical oxygen pumping on the rate and selectivity of ethylene oxidation on polycrystalline silver, J. Catal. 70 (1981) 137–146.

[22] C.G. Vayenas, G.E. Pitselis, Mathematical Modeling of Electrochemical Promotion and of

Metal - Support Interactions, J. Ind. Eng. Chem. Res. (2001) 4209–4215.
[23] D.Y. Wang, A.S. Nowick, Diffusion-controlled polarization of Pt , Ag , and Au electrodes with doped ceria electrolyte, J. Electrochem. Soc. 704 (1981) 55–63.
[24] S. Bebelis, C.G. Vayenas, Non-faradaic electrochemical modification of catalytic activity. 1. The case of ethylene oxidation on Pt, J. Catal. 118 (1989) 125–146.
[25] C.G. Vayenas, A. Katsaounis, S. Brosda, A. Hammad, Electrochemical Modification of Catalytic Activity, in: Handb. Heterog. Catal., Wiley, 1996.
[26] S. Brosda, C.G. Vayenas, J. Wei, Rules of chemical promotion, Appl. Catal. B Environ. 68 (2006) 109–124.
[27] C.G. Vayenas, Promotion, Electrochemical Promotion and Metal-Support Interactions: Their Common Features, Catal. Letters. 143 (2013) 1085–1097.
[28] E.A. Baranova, A. Thursfield, S. Brosda, G. Fóti, C. Comninellis, C.G. Vayenas, Electrochemical promotion of ethylene oxidation over Rh catalyst thin films sputtered on YSZ and TiO2/YSZ supports, J. Electrochem. Soc. 152 (2005) E40–E49.
[29] I. Constantinou, I. Bolzonella, C. Pliangos, C. Comninellis, C.G. Vayenas, Electrochemical promotion of RuO2 catalysts for the combustion of toluene and ethylene, Catal. Letters. 100 (2005) 125–133.
[30] J. Nicole, C.H. Comninellis, Electrochemical promotion of IrO2 catalyst activity for the gas phase combustion of ethylene, J. Appl. Electrochem. 28 (1998) 223–226.
[31] H.A.E. Dole, E.A. Baranova, Ethylene oxidation in an oxygen deficient environment : Why ceria is an active support ?, ChemCatChem. 8 (2016) 1977–1986.
[32] R.J. Isaifan, S. Ntais, M. Couillard, E.A. Baranova, Size-dependent activity of Pt/yttria-stabilized zirconia catalyst for ethylene and carbon monoxide oxidation in oxygen-free gas environment, J. Catal. 324 (2015) 32–40.
[33] S. Ladas, S. Kennou, S. Bebelis, C.G. Vayenas, Origin of non-faradaic electrochemical modification of catalytic activity, J. Phys. Chem. 97 (1993) 8845–8848.
[34] A.D. Frantzis, S. Bebelis, C.G. Vayenas, Electrochemical promotion (NEMCA) of CH4 and C2H4 oxidation on Pd/YSZ and investigation of the origin of NEMCA via AC impedance spectroscopy, Solid State Ionics. 136–137 (2000) 863–872.
[35] P. Tsiakaras, C.G. Vayenas, Non-Faradaic Electrochemical Modification of Catalytic Activity VII. The Case of Methane Oxidation on Platinum, J. Catal. 140 (1993) 53–70.
[36] A. Hammad, S. Souentie, E.I. Papaioannou, S. Balomenou, D. Tsiplakides, J.C. Figueroa, C. Cavalca, C.J. Pereira, Electrochemical promotion of the SO2 oxidation over thin Pt films interfaced with YSZ in a monolithic electropromoted reactor, Appl. Catal. B Environ. 103 (2011) 336–342.
[37] I.S. Fragkopoulos, C. Theodoropoulos, Multi-scale modelling of electrochemically promoted systems, Electrochim. Acta. 150 (2014) 232–244.
[38] I.S. Fragkopoulos, I. Bonis, C. Theodoropoulos, Macroscopic multi-dimensional modelling of electrochemically promoted systems, Chem. Eng. Sci. 104 (2013) 647–661.
[39] C.G.C.G. Vayenas, S. Bebelis, I. V. Yentekakis, H.-G. Lintz, Non-faradaic electrochemical modification of catalytic activity: A status report, Catal. Today. 11 (1992) 303–442.
[40] C.G. Vayenas, S. Bebelis, S. Neophytides, Non-Faradaic Electrochemical Modification of Catalytic Activity, J. Phys. Chem. 92 (1988) 5083–5085.
[41] C. Koutsodontis, A. Katsaounis, J.C. Figueroa, C. Cavalca, C. Pereira, C.G. Vayenas, The effect of catalyst film thickness on the magnitude of the electrochemical promotion of catalytic reactions, Top. Catal. 38 (2006) 157–167.
[42] E.T. Shen, N. Yu, K.T. Park, Low-energy electron diffraction and ultraviolet photoemission spectroscopy study of (1 x 1) TiO2 (110), 2 (2009) 25–27.
[43] P. Vernoux, F. Gaillard, R. Karoum, A. Billard, Reduction of nitrogen oxides over Ir / YSZ electrochemical catalysts, Appl. Catal. B Environ. 73 (2007) 73–83.
[44] L. Lizarraga, M. Guth, A. Billard, P. Vernoux, Electrochemical catalysis for propane

combustion using nanometric sputtered-deposited Pt films, Catal. Today. 157 (2010) 61–65.
[45] C. Jimenez-Borja, F. Matei, F. Dorado, J.L. Valverde, Characterization of Pd catalyst-electrodes deposited on YSZ: Influence of the preparation technique and the presence of a ceria interlayer, Appl. Surf. Sci. 261 (2012) 671–678.
[46] M. Marwood, C.G. Vayenas, Electrochemical promotion of a dispersed platinum catalyst, J. Catal. 178 (1998) 429–440.
[47] A. de Lucas-Consuegra, F. Dorado, C. Jiménez-Borja, J.L. Valverde, Electrochemical promotion of Pt impregnated catalyst for the treatment of automotive exhaust emissions, J. Appl. Electrochem. 38 (2008) 1151–1157.
[48] F. Matei, C. Jimenez-Borja, J. Canales-Vazquez, S. Brosda, F. Dorado, J.L. Valverde, D. Ciuparu, Enhanced electropromotion of methane combustion on palladium catalysts deposited on highly porous supports, Appl. Catal. B Environ. 132–133 (2013) 80–89.
[49] A. Lintanf, E. Djurado, P. Vernoux, Pt/YSZ electrochemical catalysts prepared by electrostatic spray deposition for selective catalytic reduction of NO by C3H6, Solid State Ionics. 178 (2008) 1998–2008.
[50] C. h. Chen, E.M. Kelder, J. Schoonman, Unique porous LiCe02 thin layers prepared by electrostatic spray deposition, J. Mater. Sci. 31 (1996) 5437–5442.
[51] A. Piram, X. Li, F. Gaillard, C. Lopez, A. Billard, P. Vernoux, Electrochemical promotion of environmental catalysis, Ionics (Kiel). 11 (2005) 327–332.
[52] C. Bock, C. Paquet, M. Couillard, G.A. Botton, B.R. MacDougall, Size-selected synthesis of PtRu nano-catalysts: Reaction and size control mechanism, J. Am. Chem. Soc. 126 (2004) 8028–8037.
[53] R.J. Isaifan, H.A.E. Dole, E. Obeid, L. Lizarraga, P. Vernoux, E.A. Baranova, Metal-support interaction of Pt nanoparticles with ionically and non-ionically conductive supports for CO oxidation, Electrochem. Solid-State Lett. 15 (2012) E14.
[54] E.A. Baranova, C. Bock, D. Ilin, D. Wang, B. MacDougall, Infrared spectroscopy on size-controlled synthesized Pt-based nano-catalysts, Surf. Sci. 600 (2006) 3502–3511.
[55] G. Schmid, ed., The Chemistry of Transition Metal Colloids, Weinheim, 1994.
[56] W. Zipprich, H.D. Wiemhofer, U. Vohrer, W. Gopel, In-Situ Photoelectron-Spectroscopy of Oxygen Electrodes on Stabilized Zirconia, Phys. Chem. 99 (1995) 1406–1413.
[57] S.G. Neophytides, C.G. Vayenas, TPD and Cyclic Voltammetric Investigation of the Origin of Electrochemical Promotion in Catalysis, J. Phys. Chem. 99 (1995) 17063–17067.
[58] D. Tsiplakides, C.G. Vayenas, Temperature programmed desorption of oxygen from Ag films interfaced with Y2O3 -doped ZrO 2, J. Catal. 185 (1999) 237–251.
[59] A. Palermo, M.S. Tikhov, N.C. Filkin, R.M. Lambert, I. V Yentekakis, C.G. Vayenas, Electrochemical promotion of NO reduction by CO and by propene, 11th Int. Congr. Catal. - 40th Anniv. Proc. 11th ICC. 101 (1996) 513–522.
[60] J. Nicole, D. Tsiplakides, C. Pliangos, X.E.E. Verykios, C. Comninellis, C.G.G. Vayenas, Electrochemical Promotion and Metal–Support Interactions, J. Catal. 204 (2001) 23–34.
[61] M. Makri, C.G. Vayenas, S. Bebelis, K.H. Besocke, C. Cavalca, Atomic resolution STM imaging of electrochemically controlled reversible promoter dosing of catalysts, Surf. Sci. 369 (1996) 351–359.
[62] S. Wodiunig, F. Bokeloh, J. Nicole, C. Comninellis, Electrochemical Promotion of RuO2 Catalyst Dispersed on an Yttria-Stabilized Zirconia Monolith, Electrochem. Solid-State Lett. 2 (1999) 281–283.
[63] S. Balomenou, G. Pitselis, D. Polydoros, A. Giannikos, A. Vradis, A. Frenzel, C.G. Vayenas, C. Pliangos, H. Putter, Electrochemical promotion of Pd , Fe and distributed Pt, Solid State Ionics. 137 (2000) 857–862.
[64] S. Balomenou, D. Tsiplakides, a. Katsaounis, S. Thiemann-Handler, B. Cramer, G. Foti, C. Comninellis, C.G. Vayenas, Novel monolithic electrochemically promoted catalytic reactor for environmentally important reactions, Appl. Catal. B Environ. 52 (2004) 181–196.

[65] E.I. Papaioannou, S. Souentie, F.M. Sapountzi, A. Hammad, D. Labou, S. Brosda, C.G. Vayenas, The role of TiO2 layers deposited on YSZ on the electrochemical promotion of C2H4 oxidation on Pt, J. Appl. Electrochem. 40 (2010) 1859–1865.
[66] S. Peng-ont, S. Souentie, S. Assabumrungrat, P. Praserthdam, S. Brosda, C.G. Vayenas, Reaction Kinetic-Induced Changes in the Electrochemically Promoted C2H4 Oxidation on Pt/YSZ, Catal. Letters. 143 (2013) 445–453.
[67] R. Karoum, V. Roche, C. Pirovano, R.-N. Vannier, A. Billard, P. Vernoux, CGO-based electrochemical catalysts for low temperature combustion of propene, J. Appl. Electrochem. 40 (2010) 1867–1873.
[68] A. De Lucas-consuegra, A. Princivalle, A. Caravaca, F. Dorado, A. Marouf, Preparation and characterization of a low particle size Pt / C catalyst electrode for the simultaneous electrochemical promotion of CO and C 3 H 6 oxidation, Appl. Catal. A Gen. 365 (2009) 274–280.
[69] F. Dorado, A. de Lucas-Consuegra, P. Vernoux, J.L. Valverde, Electrochemical promotion of platinum impregnated catalyst for the selective catalytic reduction of NO by propene in presence of oxygen, Appl. Catal. B Environ. 73 (2007) 42–50.
[70] S. Souentie, L. Lizarraga, E.I. Papaioannou, C.G. Vayenas, P. Vernoux, Permanent electrochemical promotion of C3H8 oxidation over thin sputtered Pt films, Electrochem. Commun. 12 (2010) 1133–1135.
[71] A. Kambolis, L. Lizarraga, M.N. Tsampas, L. Burel, M. Rieu, J.-P. Viricelle, P. Vernoux, Electrochemical promotion of catalysis with highly dispersed Pt nanoparticles, Electrochem. Commun. 19 (2012) 5–8.
[72] M.N. Tsampas, A. Kambolis, E. Obeid, L. Lizarraga, F.M. Sapountzi, P. Vernoux, Electrochemical promotion of propane oxidation on Pt deposited on a dense β″-Al2O3 ceramic Ag+ conductor, Front. Chem. 1 (2013) 1–6.
[73] C. Xia, M. Hugentobler, Yongdan-Li, C. Comninellis, W. Harbich, Quantifying electrochemical promotion of induced bipolar Pt particles supported on YSZ, Electrochem. Commun. 12 (2010) 1551–1554.
[74] C. Xia, M. Hugentobler, Y. Li, G. Foti, C. Comninellis, W. Harbich, Electrochemical promotion of CO combustion over non-percolated Pt particles supported on YSZ using a novel bipolar configuration, Electrochem. Commun. 13 (2010) 99–101.
[75] L. Lizarraga, S. Souentie, L. Mazri, A. Billard, P. Vernoux, Investigation of the CO oxidation rate oscillations using electrochemical promotion of catalysis over sputtered-Pt films interfaced with YSZ, Electrochem. Commun. 12 (2010) 1310–1313.
[76] V. Roche, R. Revel, P. Vernoux, Electrochemical promotion of YSZ monolith honeycomb for deep oxidation of methane, Catal. Commun. 11 (2010) 1076–1080.
[77] C. Jiménez-Borja, F. Dorado, A. de L.-Consuegra, J.M. G.-Vargas, J.L. Valverde, Electrochemical Promotion of CH4 Combustion over a Pd/CeO2-YSZ Catalyst, Fuel Cells. 11 (2011) 131–139.
[78] C. Jiménez-Borja, B. Delgado, L.F. Díaz-Díaz, J.L. Valverde, F. Dorado, Enhancing the combustion of natural gas by electrochemical promotion of catalysis, Electrochem. Commun. 23 (2012) 9–12.
[79] C. Pliangos, C. Raptis, I. Bolzonella, C. Comninellis, C.G. Vayenas, Electrochemical Promotion of Conventional and Bipolar Reactor Configurations for NO Reduction, Ionics (Kiel). 8 (2002) 372–382.
[80] S. Balomenou, D. Tsiplakides, A. Katsaounis, S. Brosda, A. Hammad, G. Foti, C. Comninellis, S. Thiemannhandler, B. Cramer, C. Vayenas, Monolithic electrochemically promoted reactors: A step for the practical utilization of electrochemical promotion, Solid State Ionics. 177 (2006) 2201–2204.
[81] I. Constantinou, D. Archonta, S. Brosda, M. Lepage, Y. Sakamoto, C. Vayenas, Electrochemical promotion of NO reduction by C3H6 on Rh catalyst-electrode films

supported on YSZ and on dispersed Rh/YSZ catalysts, J. Catal. 251 (2007) 400–409.
[82] C. Koutsodontis, A. Hammad, M. Lepage, Y. Sakamoto, G. Fóti, C.G. Vayenas, Electrochemical promotion of NO reduction by C2H4 in excess O2 using a monolithic electropromoted reactor and Pt-Rh sputtered electrodes, Top. Catal. 50 (2008) 192–199.
[83] D. Theleritis, S. Souentie, A. Siokou, A. Katsaounis, C.G. Vayenas, Hydrogenation of CO2 over Ru/YSZ Electropromoted Catalysts, ACS Catal. 2 (2012) 770–780.
[84] P. Vernoux, F. Gaillard, L. Bultel, E. Siebert, M. Primet, Electrochemical Promotion of Propane and Propene Oxidation on Pt/YSZ, J. Catal. 208 (2002) 412–421.
[85] S.H. Oh, P.J. Mitchell, R.M. Siewert, Methane Oxidation over Noble Metal Catalysts as Related to Controlling Natural Gas Vehicle Exhaust Emissions, in: Catal. Control Air Pollut., 1992: pp. 12–25.
[86] M.A. Fortunato, A. Princivalle, C. Capdeillayre, N. Petigny, C. Tardivat, C. Guizard, M.N. Tsampas, F.M. Sapountzi, P. Vernoux, Role of lattice oxygen in the propane combustion over Pt/yttria-stabilized zirconia : isotopic studies, Top. Catal. 57 (2014) 1277–1286.
[87] M.N. Tsampas, F.M. Sapountzi, A. Boréave, P. Vernoux, Isotopical labeling mechanistic studies of electrochemical promotion of propane combustion on Pt/YSZ, Electrochem. Commun. 26 (2013) 13–16.
[88] D. Tsiplakides, S. Balomenou, Milestones and perspectives in electrochemically promoted catalysis, Catal. Today. 146 (2009) 312–318.
[89] A. Katsaounis, Recent developments and trends in the electrochemical promotion of catalysis (EPOC), J. Appl. Electrochem. 40 (2010) 885–902.
[90] N.A. Anastasijevic, NEMCA-From discovery to technology, Catal. Today. 146 (2009) 308–311.
[91] R.B. Anderson, K.C. Stein, J.J. Feenan, L.J.E. Hofer, Catalytic Oxidation of Methane, Ind. Eng. Chem. 53 (1961) 809–812.
[92] A.F. Sarofim, R.C. Flagan, NOx control for stationary combustion sources, Prog. Energy Combust. Sci. 2 (1976) 1–25.
[93] J.H. Lee, D.L. Trimm, Catalytic combustion of methane, Fuel Process. Technol. 42 (1995) 339–359.
[94] J.R. Rostrup-Nielsen, Catalytic Steam Reforming, in: J.R. Anderson, M. Boudart (Eds.), Catal. Sci. Technol., Springer Berlin Heidelberg, Berlin, Heidelberg, 1984: pp. 1–117.
[95] Y.-F. Yu Yao, Oxidation of Alkanes over Noble Metal Catalysts, Ind. Eng. Chem. Prod. Res Dev. 19 (1980) 293–298.
[96] C.F. Cullis, B.M. Willati, Oxidation of methane over supported precious metal catalysts, J. Catal. 83 (1983) 267–285.
[97] H. Stotz, L. Maier, A. Boubnov, A.T. Gremminger, J.D. Grunwaldt, O. Deutschmann, Surface reaction kinetics of methane oxidation over PdO, J. Catal. 370 (2019) 152–175.
[98] W. Qi, J. Ran, R. Wang, X. Du, J. Shi, J. Niu, P. Zhang, M. Ran, Kinetic consequences of methane combustion on Pd, Pt and Pd-Pt catalysts, RSC Adv. 6 (2016) 109834–109845.
[99] C. Jimenez-Borja, F. Dorado, A. de Lucas-Consuegra, J.M. Garcia-Vargas, J.L. Valverde, Complete oxidation of methane on Pd/YSZ and Pd/CeO2/YSZ by electrochemical promotion, Catal. Today. 146 (2009) 326–329.
[100] F. Matei, D. Ciuparu, C. Jiménez-Borja, F. Dorado, J.L. Valverde, S. Brosda, Electrochemical promotion of methane oxidation on impregnated and sputtered Pd catalyst-electrodes deposited on YSZ, Appl. Catal. B Environ. 127 (2012) 18–27.
[101] A. Nakos, S. Souentie, A. Katsaounis, Electrochemical promotion of methane oxidation on Rh/YSZ, Appl. Catal. B Environ. 101 (2010) 31–37.
[102] D. Eng, M. Stoukides, Catalytic and electrochemical oxidation of methane on platinum, J. Catal. 130 (1991) 306–309.
[103] T. Mitsui, K. Tsutsui, T. Matsui, R. Kikuchi, K. Eguchi, Support effect on complete oxidation of volatile organic compounds over Ru catalysts, Appl. Catal. B Environ. 81 (2008) 56–63.

[104] S.H. Overbury, L. Ortiz-soto, H. Zhu, B. Lee, M.D. Amiridis, S. Dai, Comparison of Au catalysts supported on mesoporous titania and silica : Investigation of Au particle size effects and metal-support interactions, Catal. Letters. 95 (2004) 99–106.
[105] Z. Wang, B. Li, M. Chen, W. Weng, H. Wan, Size and support effects for CO oxidation on supported Pd catalysts, Sci. China Chem. 53 (2010) 2047–2056.
[106] K. Kimura, H. Einaga, Y. Teraoka, Preparation of highly dispersed platinum catalysts on various oxides by using polymer-protected nanoparticles, Catal. Today. 164 (2011) 88–91.
[107] P. Vernoux, M. Guth, X. Li, Ionically Conducting Ceramics as Alternative Catalyst Supports, Electrochem. Solid-State Lett. 12 (2009) 11–13.
[108] S. Ntais, R.J. Isaifan, E.A. Baranova, An X-ray photoelectron spectroscopy study of platinum nanoparticles on yttria-stabilized zirconia ionic support: Insight into metal support interaction, Mater. Chem. Phys. 148 (2014) 673–679.
[109] I.. Metcalfe, S. Sundaresan, Oxygen Tranfer Between Metals and Oxygen-Ion Conducting Supports, AlChE. 34 (1988) 194–208.
[110] D.R. Mullins, K.Z. Zhang, Metal – support interactions between Pt and thin film cerium oxide, Surf. Sci. 513 (2008) 163–173.
[111] N. Acerbi, S.C. Tsang, S. Golunski, P. Collier, A practical demonstration of electronic promotion in the reduction of ceria coated PGM catalysts., Chem. Commun. (2008) 1578–1580.
[112] J.C. Frost, Junction effect interactions in methanol synthesis catalysts, Nature. 334 (1988) 577–580.
[113] N. Acerbi, S.C.E. Tsang, G. Jones, S. Golunski, P. Collier, Rationalization of interactions in precious metal/ceria catalysts using the d-band center model, Angew. Chemie - Int. Ed. 52 (2013) 7737–7741.
[114] A. Ruban, B. Hammer, P. Stoltze, H.L. Skriver, J.K. Norskov, Surface electronic structure and reactivity of transition and noble metals, J. Mol. Catal. A Chem. 115 (1997) 421–429.
[115] F.H.B. Lima, J. Zhang, M.H. Shao, K. Sasaki, M.B. Vukmirovic, E.A. Ticianelli, R.R. Adzic, Catalytic activity - d-band center correlation for the O2 reduction reaction on platinum in alkaline solutions, J. Phys. Chem. C. 111 (2007) 404–410.
[116] S.J. Tauster, Strong metal-support interactions, Acc. Chem. Res. 20 (1987) 389–394.
[117] S.J. Tauster, S.C. Fung, R.L. Garten, Strong Metal-Support Interactions. Group 8 Noble Metals Supported on TiO2, J. Am. Chem. Soc. 100 (1978) 170–175.
[118] J. Sauer, Molecular Models in ab Initio Studies of Solids and Surfaces : From Ionic Crystals and Semiconductors to Catalysts, Chem. Rev. 89 (1989) 199–255.
[119] M. Born, J.R. Oppenheimer, Zur Quantentheorie der Molekeln, Ann. Phys. 84 (1927) 457.
[120] W.J. Hehre, L. Radom, P. v R. Schleyer, J.A. Pople, Ab Initio Molecular Orbital Theory, Wiley, New York, 1986.
[121] J. Almlöf, R. Ahlrichs, Notes on Hartree-Fock Theory and Related Topic, in: B.O. Roos (Ed.), Lect. Notes Quantum Chem. Eur. Summer Sch. Quantum Chem., Springer Berlin Heidelberg, Lund, 1994.
[122] L.H. Thomas, The calculation of atomic fields, Proc. Camb. Phil. Soc. 23 (1927) 542.
[123] P. Hohenberg, W. Kohn, Inhomogeneous Electron Gas, Phys. Rev. B. 136 (1964) 864.
[124] S.H. Vosko, L. Wilk, M. Nusair, Accurate spin-dependent electron liquid correlation energies for local spin density calculations: a critical analysis, Can. J. Phys. 58 (1980) 1200.
[125] J.P. Perdew, K. Burke, M. Ernzerhof, Generalized Gradient Approximation Made Simple, Phys. Rev. Lett. 77 (1996) 3865–3868.
[126] D. Rappoport, N.R.M. Crawford, F. Furche, K. Burke, Which functional should I choose ?, in: E.I. Solomon, R.B. King, R.A. Scott (Eds.), Comput. Inorg. Bioinorg. Chem., Wiley, Chichester, 2008.
[127] A.D. Becke, Density-functional thermochemistry . III . The role of exact exchange, J. Chem. Phys. 98 (1993) 5468.

[128] D. Curulla, A. Clotet, J.M. Ricart, Ab Initio Cluster Model Study of the Chemisorption of CO on Low-Index Platinum Surfaces, J. Phys. Chem. B. 103 (1999) 5246–5255.
[129] N. Ashcroft, I. Mermin, N. David, Solid State Physics, W.B. Saunders Company, New York, 1976.
[130] A. Gil, A. Clotet, J.M. Ricart, G. Kresse, Site preference of CO chemisorbed on Pt (1 1 1) from density functional calculations, Surf. Sci. 530 (2003) 71–86.
[131] N.W. Ashcroft, N.D. Mermin, Solid state physics, Holt, Rinehart and Winston, New York, 1976.
[132] D.J. Chadi, M.L. Cohen, Special Points in the Brillouin Zone, Phys. Rev. B. 8 (1973) 5747.
[133] H.J. Monkhorst, J.D. Pack, Special points for Brillouin-zone integrations, Phys. Rev. B. 13 (1976) 5188–5192.
[134] G. Kresse, J. Hafner, Ab. initio molecular dynamics for liquid metals, Phys. Rev. B. 47 (1993).
[135] C. Michel, Reactivity with VASP, 2018.
[136] C. Skylaris, Density Functional Theory Lecture 10, CHEM6085 -University Southampt. (2019) 1–14.
[137] C.G. Vayenas, S. Brosda, C. Pliangos, Rules and Mathematical Modeling of Electrochemical and Classical Promotion 2. Modeling, J. Catal. 203 (2001) 329–350.
[138] E.P.M. Leiva, C.G. Sánchez, NEMCA effect: Why are the work function changes of the gas exposed catalyst-electrode surface one-to-one related to the changes in the catalyst working electrode potential?, J. Solid State Electrochem. 7 (2003) 588–592.
[139] P. Peljo, J.A. Manzanares, H.H. Girault, Contact Potentials, Fermi Level Equilibration, and Surface Charging, Langmuir. 32 (2016) 5765–5775.
[140] S. González, C. Sousa, F. Illas, Electric field effects in the chemisorption of CO on bimetallic RhCu surface models, Surf. Sci. 548 (2004) 209–219.
[141] E.P.M. Leiva, C. Vázquez, M.I. Rojas, M.M. Mariscal, Computer simulation of the effective double layer occurring on a catalyst surface under electro-chemical promotion conditions, J. Appl. Electrochem. 38 (2008) 1065–1073.
[142] K. Mathew, R.G. Hennig, Implicit self-consistent description of electrolyte in plane-wave density-functional theory, ArXiv. (2016) 1–6.
[143] K. Mathew, R. Sundararaman, K. Letchworth-Weaver, T.A. Arias, R.G. Hennig, Implicit solvation model for density- functional study of nanocrystal surfaces and reaction pathways, J. Chem. Phys. 140 (2015) 084106.
[144] F. Che, J.T. Gray, S. Ha, N. Kruse, S.L. Scott, J.S. McEwen, Elucidating the Roles of Electric Fields in Catalysis: A Perspective, ACS Catal. 8 (2018) 5153–5174.
[145] S.N. Steinmann, C. Michel, R. Schwiedernoch, P. Sautet, Impacts of electrode potentials and solvents onthe electroreduction of CO2: a comparison oftheoretical approaches, Phys. Chem. Chem. Phys. 17 (2015) 13949.
[146] S.N. Steinmann, P. Sautet, Assessing a First-Principles Model of an Electrochemical Interface by Comparison, J. Phys. Chem. C. 120 (2016) 5619–5623.
[147] P. Wang, S.N. Steinmann, G. Fu, C. Michel, P. Sautet, Key Role of Anionic Doping for H2 Production from Formic Acid on Pd(111), ACS Catal. 7 (2017) 1955–1959.
[148] L.D. Chen, M. Urushihara, K. Chan, J.K. Norskov, Electric Field Effects in Electrochemical CO2 Reduction, ACS Catal. 6 (2016) 7133–7139.
[149] D. Kuo, J.K. Kawasaki, J.N. Nelson, J. Kloppenburg, K.M. Shen, D.G. Schlom, J. Suntivich, Influence of Surface Adsorption on the Oxygen Evolution Reaction on IrO2 (110), J. Am. Chem. Soc. 2 (2017).
[150] S. Xu, E.A. Carter, Theoretical Insights into Heterogeneous (Photo) electrochemical CO2 Reduction, Chem. Rev. 119 (2018) 6631–6669.
[151] F. Che, R. Zhang, A.J. Hensley, S. Ha, J.S. Mcewen, Density functional theory studies of methyl dissociation on a Ni(111) surface in the presence of an external electric field, Phys.

Chem. Chem. Phys. 16 (2014) 2399–2410.
[152] F. Che, S. Ha, J.-S. McEwen, Elucidating the Role of the Electric Field at the Ni/YSZ Electrode: A DFT Study, J. Phys. Chem. C. 120 (2016) 14608–14620.

Chapter 3 Investigation of Heterogeneous Catalysis by an Electrochemical Method: Case of Iridium and Nickel Interfaced with Active Oxygen Conductive Supports

Based on:
Y. M. Hajar, H. A. Dole, M. Couillard and E. A. Baranova, ECS Transactions, 2016, 72 (7) pp 161-172.
Y. M. Hajar, M. S.E. Houache, U. Tariq, P.Vernoux, and E. A. Baranova, ECS Transactions, 77 (10) 51-66 (2017).

Recently, metal support interaction (MSI) has been demonstrated to be closely related to electrochemical promotion of catalysis (EPOC) in the functionality of the process through backspillover of ionic species from the conductive support. In the present work, the interaction that iridium oxide (Ir) and nickel (Ni) nanoparticles have with ionic or mixed ionic-electronic conducting (MIEC) materials (i.e., yttria-stabilized zirconia (YSZ), ceria, CeO_2 and titania, TiO_2) was evaluated for the ethylene oxidation. Using Tafel plot calculations from the polarization measurements, the exchange current densities (i_o) was found for each catalyst as well as the self-induced Faradaic efficiency (Λ_{MSI}). The inverse relationship between each catalyst's i_o and catalytic rate r was found in similitude to prior case studies for Pt and Ru. Overall, the catalysts' activity can be predicted using i_o values, reinforcing the functional similarity between MSI and EPOC.

3.1. Introduction

Emission of Volatile Organic Compounds (VOCs) from vehicles and stationary sources is a well-known environmental issue. While CO_2 is considered to be a harmful green-house gas, VOCs emitted to the atmosphere have a higher global warming potential (GWP) making it necessary to fully combust them in a catalytic convertor before the product gas is being emitted to the atmosphere. Ethylene is an anthropogenic compound with a 3.1 times GWP compared to CO_2 typically emitted by thermal engines using gasoline or diesel fuel [1]. Therefore, it is used as a representative VOC for oxidation reactions. Enhancing the efficiency of this type of oxidation reaction is continuously tackled from the catalytic side, and the use of noble metals has long been the solution to enhance the complete oxidation. Pt, Ir, Ru, and Pd are the best catalysts for ethylene and propylene oxidation in that order [2,3], where catalysts have been supported on silica or alumina. Recently, alternative catalysts have been synthesized and modified to enhance their activity for the obvious economic reason. Forming a Ag/Au bimetallic catalyst and supporting it on Al_2O_3, for example, makes the efficiency of the catalyst higher per weight of noble metal for ethylene oxidation [4].

The role of the support is primarily to enhance the dispersion of metallic nanoparticles, the stability, and the catalytic efficiency. SiO_2 and Al_2O_3 are examples of commonly used supports mainly because of their low cost and high specific surface area. However, replacing these supports with ones that show ionic or electronic interaction with the catalyst have been recently increasing [5]. Ceria is a mixed ionic-electronic conductor that has a great capacity to store and/or release oxygen in large amounts giving it a high oxygen-storage capacity (OSC) factor [6]. This is due to its remarkable redox properties and its ability to reduce from Ce^{4+} to Ce^{3+} forming oxygen vacancies [7,8]. Similarly, TiO_2 has been known to strongly influence the performance of the supported metal catalysts due to its reducibility from Ti^{4+} to Ti^{3+} [9]. Another type of emerging novel supports in heterogeneous catalysis is yttria-stabilized zirconia (YSZ), which has predominantly O^{2-} conductivity and possess oxygen storage/transport properties due to the doping effect of yttrium [10–14]. The lower valence of Y^{3+} than the host cation Zr^{4+} results in the formation of oxygen vacancies in the lattice to preserve the latter's neutrality [15]. The presence of oxygen vacancies in the support plays a key role in promoting catalytic reactions [11]. For instance, Vernoux and co-workers showed that oxygen mobility through vacancies from the support to the metal is thermally-driven and varies between different metal/support coupling [16–18]. More recently, the interaction between the metal and the support has been suggested to be at the electronic level and is referred to as electronic metal-support interaction (EMSI) [19]. The d-orbital electrons influence the interaction between the metal and the support and disturb the electronic band structure of the support by re-distributing the electrons without the exchange of any chemical species [20]. This redistribution is due to the ionization of the oxygen vacancies in conductive supports when a high electron affinity oxide is interfaced with a low work function metal. This charge transfer would result in a "bend" of the oxide's electron affinity and the metal's work function so that their vacuum levels align [21,22]. This is in similarity with the interface effect between metals of different work functions such that the low work function (high Fermi level) metal transfers some of its electrons to the high work function (low Fermi level) metal [23,24].

This study investigates complete ethylene oxidation reaction when using iridium nanoparticles (NPs) free-standing and supported on CeO_2, TiO_2, and YSZ, and when using nickel nanoparticles free-standing and when supported on CeO_2 and YSZ. Steady-state polarization measurements were carried to evaluate the exchange current density (i_o). The catalytic reaction

rate was correlated with the electrochemical results to evaluate the extent of the MSI effect and predict it. The results were finally compared to previous related studies of noble metals performances [25,26].

3.2. Materials and methods

3.2.1. Synthesis of free-standing nanoparticles

Iridium nanoparticles were synthesized using a polyol reduction method [27]. To synthesize the iridium colloids, 0.11 g of H_2IrCl_6 (Alfa Aesar, 99.99%) metal basis precursor salt was dissolved in 50 mL of ethylene glycol (anhydrous 99.8% Sigma Aldrich) with NaOH (EM Science, ACS grade) concentration of 0.08 M dissolved in ethylene glycol. The salt solution was stirred at room temperature for 30 minutes then refluxed for 3 hours at 160 °C. The initial solution pH was 10 and after reflux, it dropped to 8. A resulting dark brown colloidal solution containing iridium NPs was formed.

Nickel synthesis method was based on the work of Wu and Ravi [28,29]. Nickel (II) chloride hexahydrate (Sigma Aldrich) was directly dissolved in ethylene glycol [50 mM] (Fisher Scientific) in a three-necked flask. The solution was heated up to 100 °C under stirring condition using a hot plate. After 2 min, 0.1M of hydrazine (N_2H_4 *$1.5H_2O$) (50-60 % purity; degree of hydration, ~1.5, Sigma Aldrich) was added to the mixture. After addition of hydrazine, the color of the solution changed rapidly from green to light blue indicating the formation of Ni-hydrazine complexes $[Ni(N_2H_4)_2]^{+2}$. As soon as 1.5 ml of 0.1 M NaOH was injected, the color of the reaction mixture slowly turned to black indicating the formation of Ni nanoparticles as expressed in the following reaction:

$$2Ni^{2+} + N_2H_4 + 4OH^- \rightarrow 2Ni + N_2 + 4H_2O \qquad 3\text{-}1$$

The solution was maintained at 100 °C under magnetic stirring for 30 min to ensure the completion of the reaction and then cooled down to room temperature. Ni NPs were recovered from the solution using a ferrite ring permanent magnet, then washed with ethanol three times with intermittent centrifugation. The final product is stored in ethanol solution.

3.2.2. Supporting nanoparticles

The nanoparticles were supported by mechanical attachment of the nanoparticles on

the support. A pre-calculated volume of the nanoparticles colloid solution is poured in a deionized water solution while stirring. The amount of metal oxide support powder was then added such that the nanoparticles loading in the final catalyst is 1wt.%. The solution was continuously stirred for 72 h. When stirring is stopped, the solution separates to two phases (clear aqueous top solution and support powder sludge bottom solution), signaling that the colloidal nanoparticles are attached to the support. The solution was then extensively washed with deionized water (18 MΩ·cm) and separated by centrifugation at 6000 rpm. The washing procedure was repeated three times. The supported nanoparticles were afterwards dried using a freeze dryer overnight. The supports used were mixed ionic-electronic conducting support (MIEC) CeO_2 (Alfa Aesar, specific surface area (SSA) 30–50 $m^2\ g^{-1}$), TiO_2 (Acros Organics, Aeroxide® P25, SSA 45-55 $m^2\ g^{-1}$) and an ionically conducting support 8% Y_2O_3-ZrO_2 (Tosoh, SSA 13 $m^2\ g^{-1}$, average size of 0.3 μm).

3.2.3. Catalyst characterization

The iridium NPs and ceria-supported catalysts were characterized by scanning transmission electron microscopy (STEM) while TiO_2-supported catalyst was characterized using a TEM, to determine the average size of the deposited particles. The unsupported iridium NPs are deposited directly on a carbon film (Ted Pella, ultrathin Carbon film on a holey carbon film) whereas the ceria- and titania- supported iridium catalyst powders were dispersed in ethanol then dropped on the carbon film. The STEM equipment used was a FEI Titan3 80 - 300 microscope running at 300 kV and equipped with a CEOS aberration corrector for the probe forming lens, a monochromated field-emission gun, and an EDAX energy dispersive X-ray (EDX) spectrometer. The TEM micrographs were obtained using JEOL JEM 2100F FETEM operating at 200 kV.

The X-ray diffraction (XRD) patterns of Ni NPs were recorded with Rigaku Ultima IV multi-purpose diffractometer with Cu Kα radiation (λ = 1.5418 Å) at 40 kV and 44 mA in the range of 20–80° 2θ with 0.03° 2θ s^{-1} scanning rate. The Ni TEM micrograph was obtained using the same equipment used for Ir/TiO_2.

3.2.4. Electrochemical cell

The solid electrolyte is a 19 mm diameter and 1 mm thickness disk of 8 mol % Y_2O_3-stabilized ZrO_2 (YSZ) (TOSOH®) mechanically pressed and densified to above 95% by heating up

to 1000 °C (10 °C/min) and dwelling for 1 h, followed by heating with similar rate to 1500 °C and dwelling for 6 h [30]. Inert gold counter and reference electrodes were brushed on one side of the YSZ disk using gold paste (C2090428D4, Gwent Group, CAS:98-55-5) followed by annealing at 500 ºC for 1 hour. The free-standing and supported catalysts were deposited as working electrodes on the opposite side of the disks. The geometric surface area of the working electrode was 1 cm^2 which was obtained using a squared-tape mask for the deposition. The supported NPs ink or free-standing colloidal solution were pipetted onto the disk knowing the concentration of the catalyst in the solution to obtain a final loading on the disk of 0.10 mg metal cm^{-2}. The cells were then dried at 60 ºC for 30 minutes.

3.2.5. Catalytic and electrochemical measurements

Catalytic oxidation of ethylene and electrochemical measurements were carried out at atmospheric pressure in a single–chamber capsule reactor (SSCR), as shown in Figure 3.1(a). The reactor is comparable to the one used and described in a previous study [25]. The electrochemical cell, shown in Figure 3.1(b), is enclosed in a tight fit inert ceramic (McMaster-Carr, Mycalex) capsule in which a gold current collector (gold mesh) is mechanically pressed onto the surface of the working electrode (WE) and gold wires are pressed on the other side of the disk onto the reference and counter electrodes (RE and CE). The capsule is slipped vertically into two slits in the quartz inert tube and pressed from the top with a metal clamp (Omega Engineering, Nichrome wire, Ni_{80}/Cr_{20}). The three Au wires connected to the electrodes are enclosed in a ceramic four-bore tube that holds, in its fourth hole, a type-K thermocouple that reaches the vicinity of the cell. The three Au wires are connected to a potentiostat-galvanostat (Arbin Instruments, MSTAT). The ceramic capsule, Nichrome clamp and gold wires are inert under the reaction conditions. The reaction gas mixture consisted of ethylene (Linde, 0.5% C_2H_4 in He), oxygen (Linde, 20.9% O_2 in He), and carrier gas of pure helium (Linde, 99.99% He). The gas composition (i.e., 0.012 kPa C_2H_4, 3 kPa O_2 and He balance) was controlled by mass flow controllers (MKS, 1259C and 1261C Series).

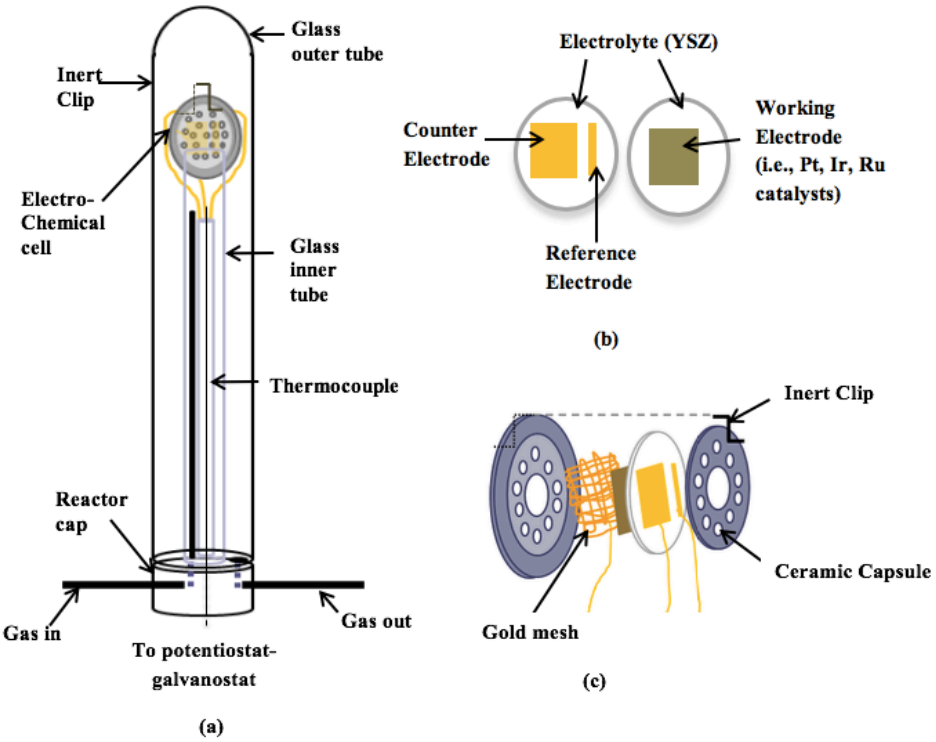

Figure 3.1: Schematic of (a) the SSCR in the reactor system and (b) the two sides of the electrochemical cell configuration and (c) the mechanically pressed cell in a ceramic capsule. The geometric area is 1 cm^2 for the WE – working electrode-catalyst and CE - counter electrode. The RE – reference is a 0.2 cm^2.

The total flow rate was held at 6 L h^{-1}. The CO_2 product gas was analyzed with an on-line CO_2 gas analyzer (Horiba, VA-3000) and the corresponding flow rate was calculated using eq. 3-2. Using stoichiometry of the reaction, the catalytic flow rate was evaluated per moles of oxygen then normalized per gram of catalyst used. The flow rate of the ethylene gas was changed such that its partial pressure was varied between 0.007 and 0.018 kPa. The electrochemical measurements consisted of steady-state polarization experiments in which current passing between the working electrode-catalyst (WE) (geometric area = 1 cm^2) and counter electrode (CE) was measured. The WE potential (U_{WR}) with respect to a pseudo-reference Au electrode ($O^{2-}/0.5O_2$), as well as the cell voltage (U_{cell}) (i.e., between the WE and CE) were also measured. The logarithm of the current density (*i*) was plotted versus U_{WR} to determine the exchange current density (i_0); this is known as the Tafel plot described in detail elsewhere [12,31].

$$r(mol\ CO_2/s) = Total\ Gas\ Flow\ (L/s) \times [\frac{1mol}{22.4\ L} \times \frac{273\ K}{298\ K}] \times \frac{[CO_2]_{out}\ ppm}{10^6\ ppm} \quad 3\text{-}2$$

3.3. Results and discussion

3.3.1. Characterization of catalysts

The STEM images of the free-standing Ir NPs and CeO_2-supported Ir and the TEM of TiO_2-supported Ir catalysts are presented in Figure 3.2. The average particle size was estimated at 1 nm for both free-standing and ceria-supported Ir, while it was 1.2 nm for titania-supported Ir. Furthermore, Ir showed high dispersion over the CeO_2 and TiO_2 supports (Figure 3.2b,c).

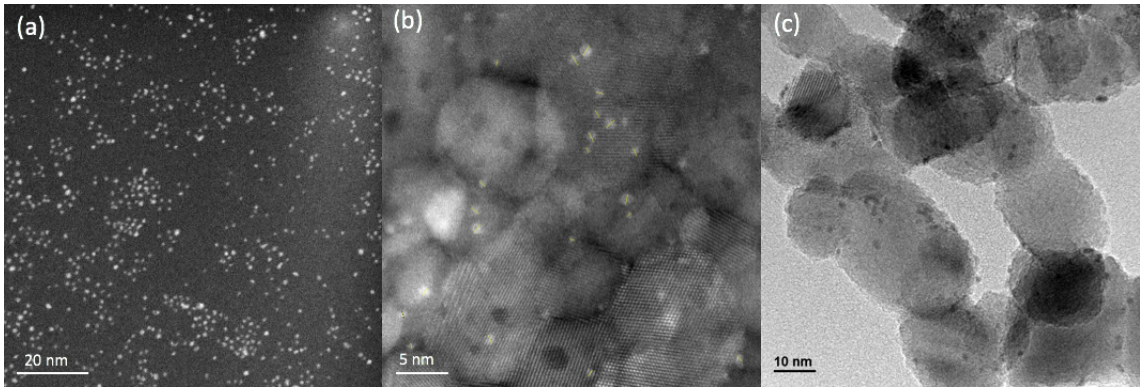

Figure 3.2: STEM images showing (a) free-standing Ir NPs and (b) Ir/CeO_2.catalysts and (c) TEM of Ir/TiO_2 .

While XRD spectrum of the iridium NPs was hard to detect due to their very small particle size, XRD pattern (Figure 3.3a) of the as-prepared nickel nanoparticles illustrates three characteristic peaks at approximately 44, 52 and 77 ° 2θ. The crystallite size of Ni particles based on XRD analysis using Debye-Scherrer equation was found to be 18 nm. However, TEM image of the as-prepared unsupported Ni nanoparticles (Figure 3.3b) shows that Ni nanoparticles have triangular shape and average size of ~70 nm. As-synthesized Ni particles are magnetic and tend to agglomerate into larger aggregates, however the triangular shape remains preserved. A note that no NiO peak was detected in the XRD spectrum.

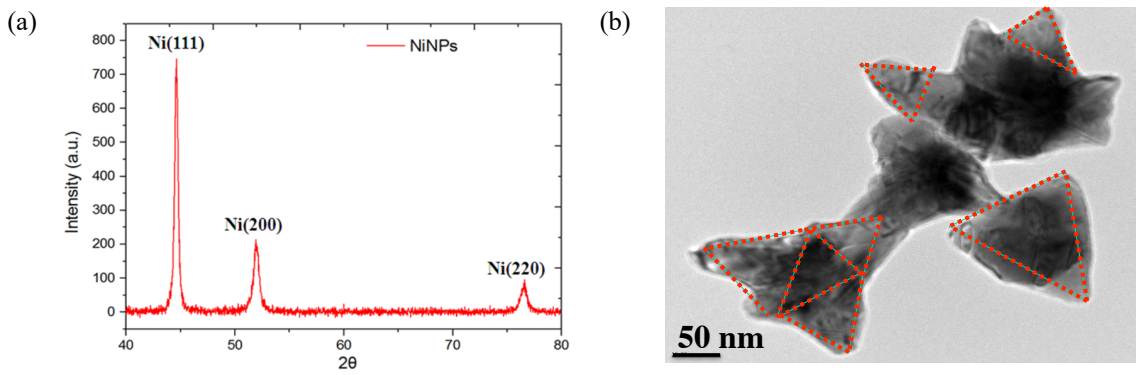

Figure 3.3: (a) XRD patters and (b) TEM of Ni NPs.

3.3.2 Catalytic ethylene oxidation on the supported and free-standing catalysts

Figure 3.4(a-b) shows the reaction rate and corresponding ethylene conversion as a function of temperature for the free-standing and supported nanoparticles, as well as the bare supports alone. In Figure 3.4a, it is shown that Ir/CeO_2 had an earlier on-set temperature compared to Ir/TiO_2 and Ir/YSZ; however, at 350 °C, the ethylene catalytic rate on Ir/YSZ was very similar to that on Ir/CeO_2 even though it had the latest on-set temperature. On the other hand, Ni/CeO_2 and Ni/YSZ resulted in a lower catalytic rate in that order as shown in Figure 3.4b. Both Ir and Ni stand-alone nanoparticles had small activity almost as low as that of the bare supports. These values can be compared to the previous study on Pt, Ru and $Pt_{50}Sn_{50}$ catalytic performance when supported on CeO_2 [31].

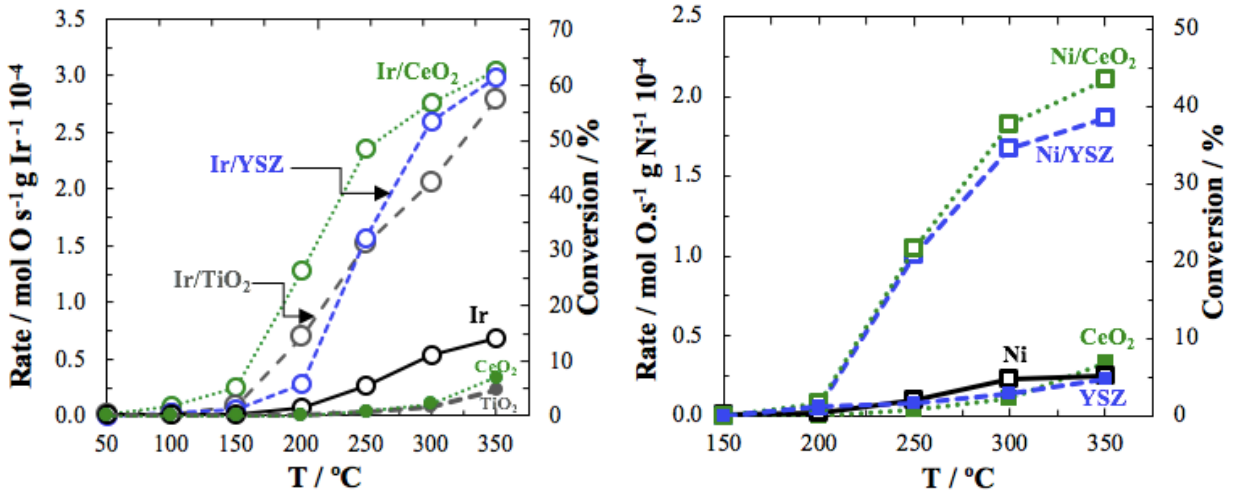

Figure 3.4: Catalytic rates (r) for (a) Ir- and (b) Ni- based catalysts from 50 to 350 °C (0.012 kPa C_2H_4, 3 kPa O_2, balance He; total flow: 6 $L.h^{-1}$). Solid line for forward scan and dashed line for reverse.

Relating MSI to EPOC phenomenon, pioneering work of Nicole *et al.* [32] introduced the metal-support interaction rate enhancement ratio, referred to as the promotional (MSI) rate enhancement ratio (ρ_{MSI}). It is determined as the ratio of the reaction rate on the supported (promoted) catalyst, r over that obtained on the unsupported (un-promoted) catalyst, r_u:

$$\rho_{MSI} = {}^{r}/_{r_u} \qquad 3\text{-}3$$

To estimate the degree of MSI effect we used the self-induced apparent Faradaic efficiency, Λ_{MSI}, proposed earlier [33]. Similarly to the apparent Faradaic efficiency, Λ, in electrochemical promotion of catalysis (EPOC) studies, the self-induced Λ_{MSI} is denoted as:

$$|\Lambda_{MSI}| \approx 2\mathrm{F}r/I_{\mathrm{o}} \qquad 3\text{-}4$$

where F is Faraday's constant, r is the catalytic reaction rate (mol O s^{-1}) and I_o is the exchange current (A).

Figure 3.5 shows the reaction rate as a function of ethylene partial pressure (0.007 and 0.019 kPa) at a constant $p(O_2)$ of 3 kPa. The resulting reaction rate increased with the partial pressure of the limiting reactant. In all cases, the enhancement ratio and conversion had the highest value on Ir/CeO_2 then Ir/YSZ then Ir/TiO_2 followed by Ni/CeO_2 then Ni/YSZ indicating a promotional effect of the supports in that order.

The observed support effect in the catalytic systems is due in part to the increased dispersion of the nanoparticles on the powder support and as a result, a higher active surface area of the nanoparticles. Moreover, the presence of oxygen ion conductivity in the supports plays a key role in the observed enhancement in agreement with the previous studies on hydrocarbon and carbon monoxide oxidation over the noble metal and metal oxide nanoparticles, such as Pt, Ru and $Pt_{50}Sn_{50}$ supported on ionic and MIEC supports [16,17,31,34,35]. According to the proposed mechanism, the spontaneous migration (backspillover) of oxygen ions to the gas exposed active sites takes place spontaneously due to the difference in the work function of the nanoparticle catalyst and the ionization energy of the conductive support [19]. This mechanism is functionally similar to EPOC mechanism, where the migration of $O^{\delta-}$ to the surface of the metal particles is regulated by the applied current or potential. In EPOC, the backspillover of oxygen ions forms an

effective double layer that modifies the adsorption capabilities of the catalyst by attracting electropositive reactant such as C_2H_4.

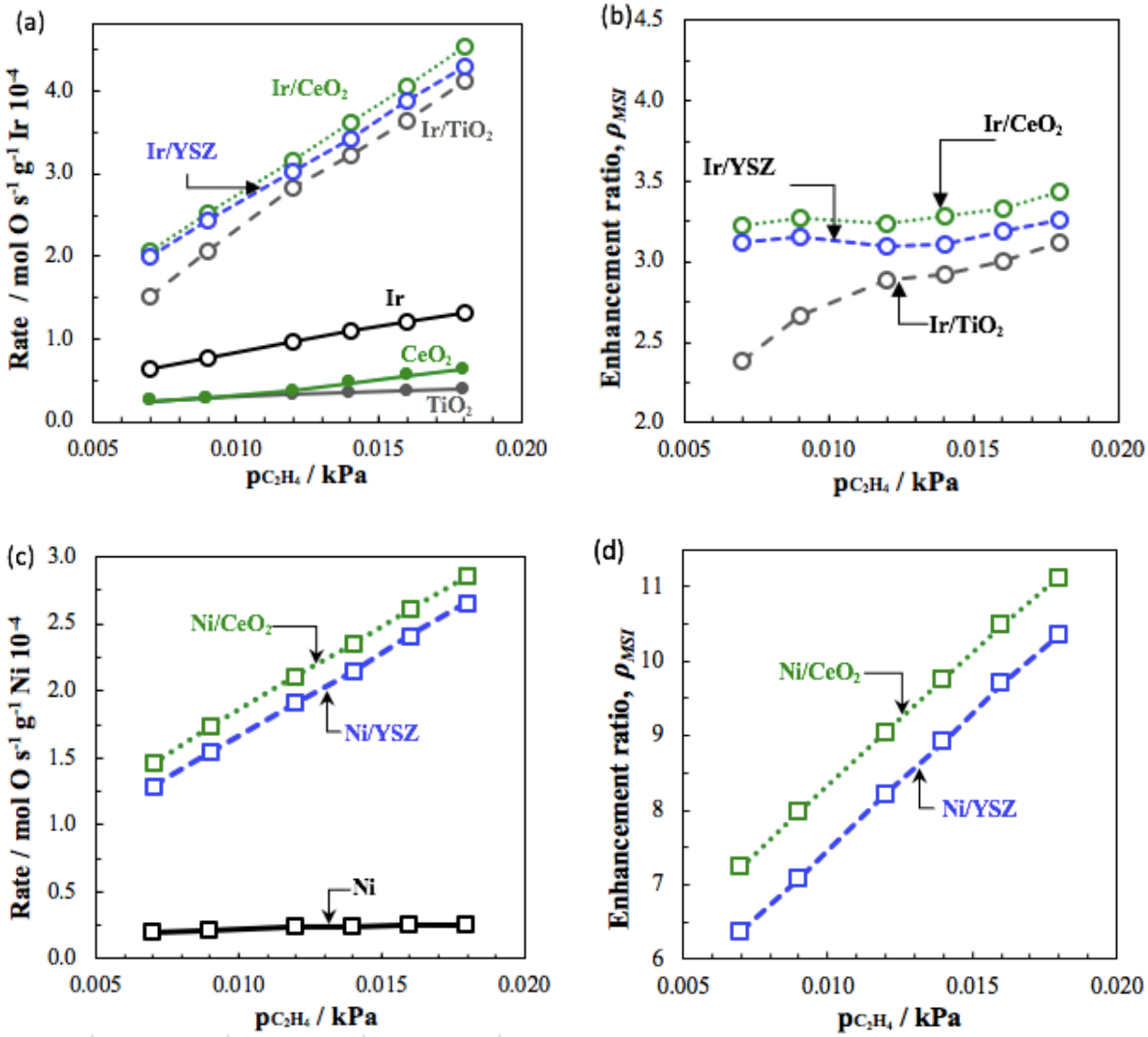

Figure 3.5: (a,c) Catalytic rate for the free-standing and supported catalysts and (b,d) metal-support interaction rate enhancement (ρ_{MSI}) over a range of C_2H_4 partial pressures (3 kPa O_2 and He balance) of supported catalysts at 350 °C (3 kPa O_2, balance He; total flow: 6 $L.h^{-1}$).

3.3.2. Electrochemical characterization of the supported and free-standing

The steady-state polarization measurements for Ir/CeO_2, Ir/TiO_2, Ir/YSZ and stand-alone Ir were determined at three different temperatures (i.e., 350, 375 and 400 °C) and at 325 °C as well for Ir/TiO_2. The results are shown in Figure 3.6(a-d). It was found that the current increases in the positive (anodic) region due to the oxygen evolution reaction (OE), while in the negative (cathodic) region, oxygen reduction to anions takes place at the three phase boundary (tpb), for all four

catalysts. The current density increased as a function of temperature. This demonstrated the increase of the ionic conductivity as a function of temperature.

The polarization curves obtained were used to determine the exchange current density, i_o for each temperature using the Tafel plot method (i.e., log i vs U_{WR} curve where intercept of the tangent to log i at U_{WR}= 0 gives i_o). The exchange current density, i_o is plotted then versus the temperature following an Arrhenius relationship (eq. 3-5):

$$ln(i_0(\mu A\ cm^{-2})) = -E_a/RT + lnA \qquad 3\text{-}5$$

where E_a is the apparent activation energy (J mol^{-1}), R is the gas constant (8.314 J mol^{-1} K^{-1}), T is temperature (K) and A is the pre-exponential factor.

As is seen from Figure 3.6a-d, the current density is higher for the free-standing Ir in comparison with the supported catalysts. Using Tafel plots, exchange current densities were found to be 8.4, 1.8, 1.2 and 1.3 μA.cm^{-2} for Ir, Ir/CeO_2, Ir/TiO_2, and Ir/YSZ, respectively (Table 3-1). The higher exchange current density i_o in the case of the free-standing catalyst can be explained by the fact that there is no support material present in the electrode; therefore, more tpb sites are available for the electrochemical reaction to occur. With the supported catalysts, there are fewer tpb sites available; therefore, the catalytic reaction on the effective two-phase boundary becomes more dominant rather than the electrochemical reaction at the tpb.

Table 3-1: Electrochemical and catalytic properties of free-standing and supported of Ir-based catalysts.

Catalyst	**1 wt.% Ir/CeO_2**	**1 wt.% Ir/TiO_2**	**1 wt.% Ir/YSZ**	**Ir**
Exchange current density, i_o (μA cm^{-2})	1.8	1.2	1.3	8.4
Catalytic rate, r (mol C_2H_4 s^{-1} g Ir) 10^{-6}	51.6	46.6	50.0	11.7
Catalytic rate, r (mol O s^{-1} g Ir) 10^{-4}	3.1	2.8	3.0	0.7
Enhancement ratio, ρ_{MSI}	4.4	4.0	4.3	-
Self-induced Faradaic efficiency, Λ_{MSI}	3319	4496	4453	-

In Figure 3.6 (e), the apparent activation energy for the electrochemical reaction rate is smaller for Ir NPs compared to that of Ir supported on CeO_2, TiO_2 or YSZ, and is slightly smaller for titania than YSZ than ceria, showing that the electrochemical reaction is mostly facilitated on the stand-alone NPs while it is the least occurring on the CeO_2-based catalyst.

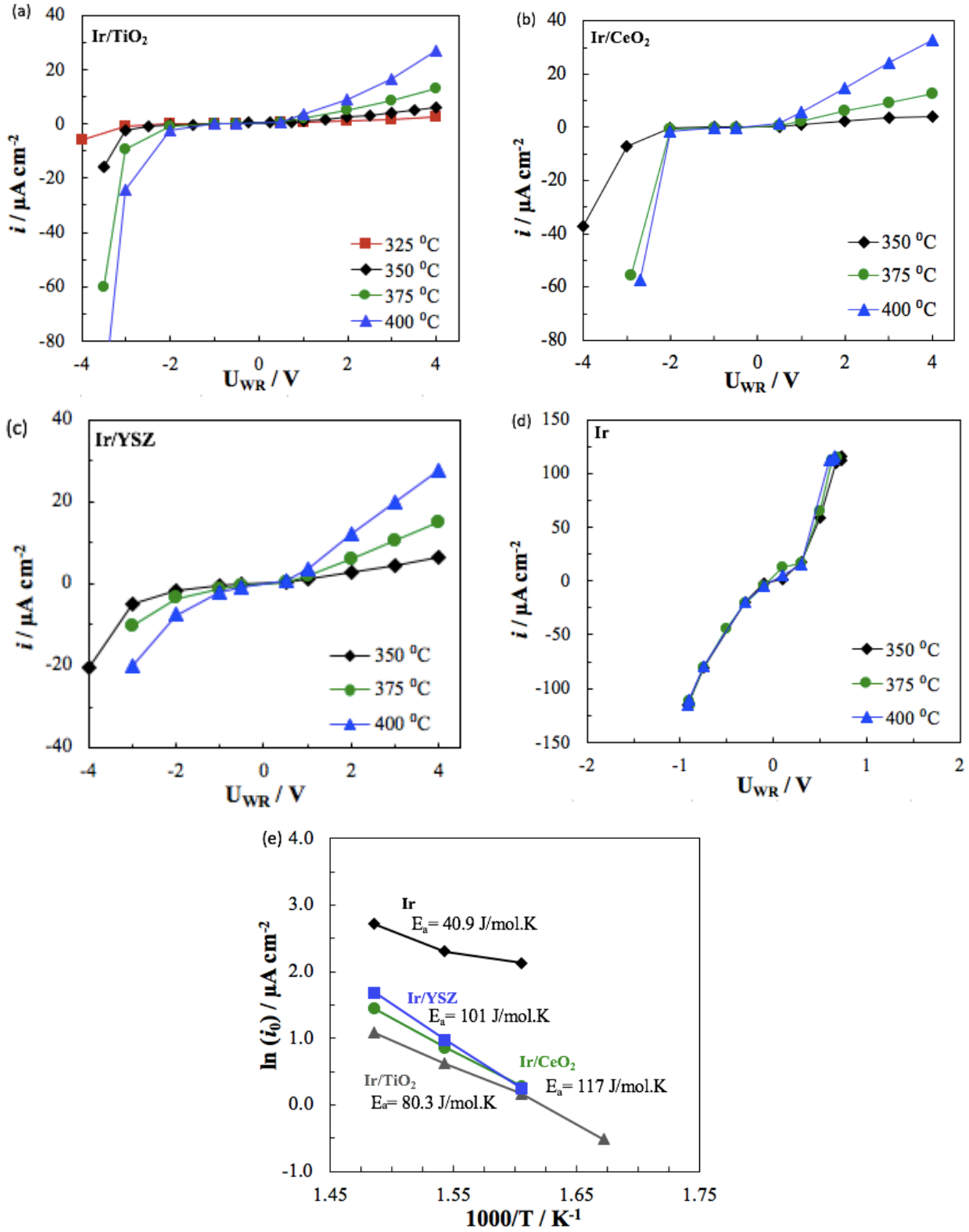

Figure 3.6: Temperature effect shown through steady-state polarization curves for (a) 1 wt.% Ir/TiO_2, (b) 1 wt.% Ir/CeO_2, (c) 1 wt.% Ir/YSZ, (d) stand-alone Ir , and (e) Arrhenius plots for all above (0.012kPa C_2H_4, 3kPa O_2, balance He; total flow: 6 $L.h^{-1}$).

Similarly, polarization measurements of Ni nanoparticles were carried out to find the exchange current density (i_o) of the electrochemical process at the tpb from the corresponding Tafel plots. The electrochemical study was performed on the supported and unsupported Ni using linear sweep voltammetry (LSV) at 2mV s^{-1} starting from the open-circuit potential (ocp) ~ 20-40 mV. First, the catalyst was polarized positively up to +4 V and then from ocp to -4 V. Following the polarization tests (Figure 3.7a), the Tafel plots were produced (Figure 3.7b) from which an exchange current density, i_o was found.

The polarization tests performed in the window of [-4: +4V] showed a decrease in the current response for Ni/CeO_2 and Ni/YSZ (Figure 3.7a). The highest current response was for free-standing Ni NPs followed by Ni/YSZ then Ni/CeO_2. The high i_o of free-standing Ni indicates its good electrocatalytic activity for oxygen evolution reaction (OER) at the tpb. When the catalyst was supported, the current response dropped by at least half, with a higher value for Ni/YSZ than Ni/CeO_2. In the excess of oxygen ($p(O_2)$ = 3 kPa), the total conductivity of CeO_2 is equal to its ionic conductivity (electronic conductivity is negligible below ~600 °C), as it is hard to reduce cerium from Ce^{4+} to Ce^{3+} [8]; therefore, the low i_o value can be attributed to the oxygen mobility alone, which is lower for ceria than YSZ under present conditions.

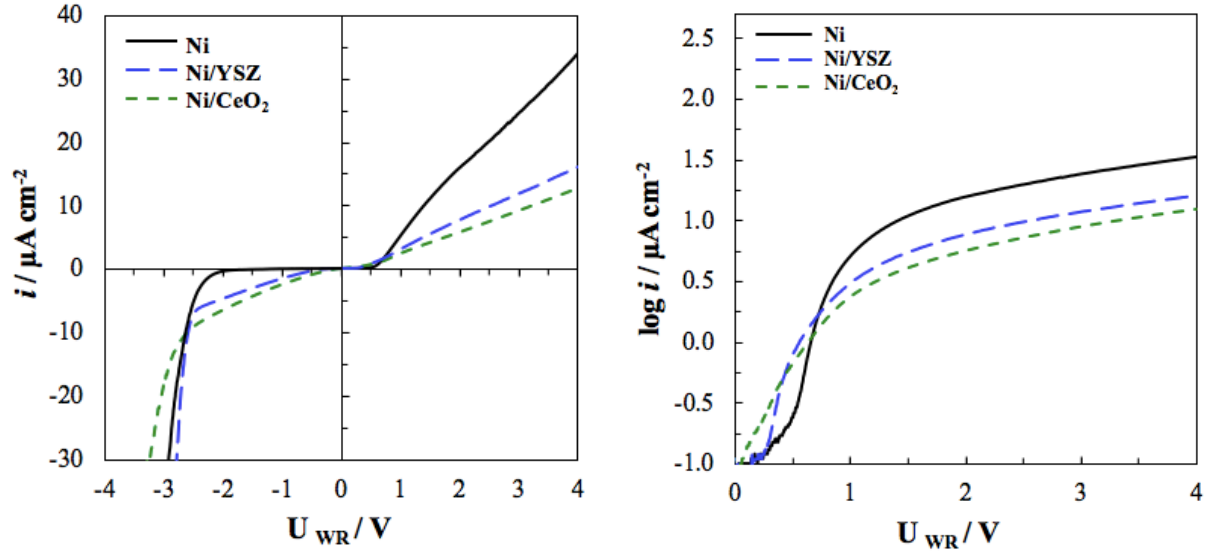

(a) (b)

Figure 3.7: (a) Linear sweep voltammetry for free-standing Ni,supported Ni/YSZ and Ni/CeO_2, (b) corresponding Tafel plot. Scan rate is 2 mV s^{-1}. T= 350 °C (3 kPa O_2, balance He; total flow: 6 L.h^{-1}).

As seen in Table 3-2, Λ_{MSI} is 1269 and 718 for Ni/CeO_2 and Ni/YSZ, respectively. The value is almost the double for Ni/CeO_2 compared to Ni/YSZ catalyst, showing that more oxygen ions in CeO_2 are susceptible to act as promoters for the catalytic reaction. The higher i_o for Ni/YSZ, indicates that a larger amount of oxygen ions is involved in the electrochemical reaction at the tpb.

Table 3-2: Electrochemical and catalytic properties of free-standing and supported Ni NPs at 350 °C.

Catalyst	**1 wt.% Ni/CeO_2**	**1 wt.% Ni/YSZ**	**Ni**
Exchange current density, i_o (μA cm^{-2})	3.2	5.0	7.9
Catalytic rate, r_o (mol C_2H_4 s^{-1} g Ni) 10^{-6}	35.1	31.0	4.1
Catalytic rate, r_o (mol O s^{-1} g Ni) 10^{-4}	2.1	1.9	0.25
Enhancement ratio, ρ_{MSI}	8.6	7.6	-
Self-induced Faradaic efficiency, Λ_{MSI}	1269	718	-

3.3.3. Relationship between electrochemical characterization and catalytic rate

When relating the catalytic rate, r, to i_o for Ir- and Ni-based catalysts, an inverse proportional relationship can be found as showed in Figure 3.8. Those values are directly compared in the figure with previous work on Pt- and Ru-based catalysts [31].

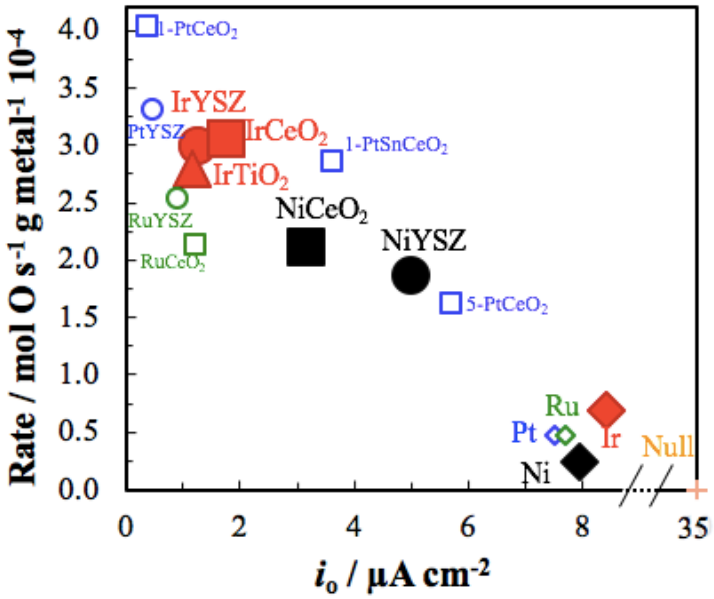

Figure 3.8: Normalized catalytic rate (r) (0.012 kPa C_2H_4, 3 kPa O_2, balance He) as a function of exchange current density (i_o) for colloidal, CeO_2-, TiO_2-, and YSZ-supported catalysts at 350 °C. Symbols code: Diamond for stand-alone catalyst, square for CeO_2-supported, circle for YSZ-supported and triangle for TiO_2-supported catalysts.

The Ir stand-alone NPs showed a lower catalytic rate corresponding to a higher exchange current density whereas the supported Ir exhibited a higher catalytic rate corresponding to their low exchange current density. In addition, Ni/CeO_2 and Ni/YSZ fell on the same inverse-proportional relationship between i_o and r. This is in a good agreement with the Pt- and Ru- based studies [31], proving that the MSI apparent Faradaic efficiency is similar to the one found in EPOC studies under closed-circuit (current or potential application) thus indicating the functional similarity of MSI observed on O^{2-} conductive supports, and EPOC phenomenon.

3.4. Conclusions

Catalytic and electrochemical measurements were used to investigate the catalytic performance of free-standing iridium and nickel nanoparticles and when supported on mixed-ionic electronic supports, i.e., CeO_2 and TiO_2 and ionically conducting YSZ. The effect of the metal-support interaction was shown to be significant when depositing the metals on the support, resulting in an increase in the catalytic rate when compared to the free-standing NPs. Overall, the results showed that the supported Ir resulted in a high catalytic rate of the ethylene oxidation comparable to Pt-based catalyst. Ni/CeO_2 and Ni/YSZ resulted in a lower but still improved catalytic rate. The effect of the catalyst supports is attributed to the interaction between the support and the catalyst and oxygen migration that occurs in between. It is suggested that oxygen ions from the support perform a backspillover to the catalyst surface rather than being consumed at the three-phase boundary (tpb) by the electrochemical reaction, enhancing thus the chemical reaction at the effective double layer. The apparent self-induced Faradaic efficiency was used to quantify the metal-support interaction as it was found to show orders of magnitude increase of the oxygen ions migration involved in the reaction on the surface compared to those consumed in the electrochemical reaction at the tpb. An inverse-proportional relationship was obtained between the catalytic rate and exchange current density, which is in agreement with previous studies of supported Pt- and Ru- based nanoparticles.

References

[1] W.J. Collins, R.G. Derwent, C.E. Johnson, D.S. Stevenson, The oxidation of organic compounds in the troposphere and their global warming potential, Clim. Change. 52 (2002) 453–479.

[2] C.A. Cavalca, G. Larson, C.G. Vayenas, G.L. Haller, Electrochemical Modification of CH3OH Oxidation Selectivity and Activity on a Pt Single-Pellet Catalytic Reactor, J. Phys. Chem. 97 (1993) 6115–6119.

[3] N. Cant, W.K. Hall, Catalytic Oxidation II. Silica supported noble metals for the Oxidation of ethylene and Propylene, J. Catal. 231 (1976) 220–231.

[4] S. Rojluechai, S. Chavadej, J.W. Schwank, V. Meeyoo, Catalytic activity of ethylene oxidation over Au , Ag and Au – Ag catalysts : Support effect, Catal. Commun. 8 (2007) 57–64.

[5] J. Kaspar, P. Fornasiero, N. Hickey, Automotive catalytic converters: current status and some perspectives, Catal Today. 77 (2003) 419–449.

[6] Tana, M. Zhang, J. Li, H. Li, Y. Li, W. Shen, Morphology-dependent redox and catalytic properties of CeO2 nanostructures: Nanowires, nanorods and nanoparticles, Catal. Today. 148 (2010) 179–183.

[7] H. Ay, D. Üner, Dry reforming of methane over CeO2 supported Ni, Co and Ni–Co catalysts, Appl. Catal. B Environ. 179 (2015) 128–138.

[8] I. Kosacki, T. Suzuki, V. Petrovsky, H.U. Anderson, Electrical conductivity of nanocrystalline ceria and zirconia thin films, Solid State Ionics. 136–137 (2000) 1225–1233.

[9] S.J. Tauster, Strong metal-support interactions, Acc. Chem. Res. 20 (1987) 389–394.

[10] W.-P. Dow, T.-J. Huang, Yttria-Stabilized Zirconia Supported Copper Oxide Catalyst, J. Catal. 160 (1996) 171–182.

[11] P. Vernoux, L. Lizarraga, M.N. Tsampas, F.M. Sapountzi, A. De Lucas-Consuegra, J.L. Valverde, S. Souentie, C.G. Vayenas, D. Tsiplakides, S. Balomenou, E.A. Baranova, Ionically conducting ceramics as active catalyst supports, Chem. Rev. 113 (2013) 8192–8260.

[12] C.G. Vayenas, S. Bebelis, C. Pliangos, S. Brosda, D. Tsiplakides, Electrochemical Activation of Catalysis: Promotion, Electrochemical Promotion, and Metal-Support Interactions, Springer, New York, 2001.

[13] H.A.E. Dole, E.A. Baranova, Implementation of Nanostructured Catalysts in the Electrochemical Promotion of Catalysis, in: M. Aliofkhazraei, H.A.S. Makhlouf (Eds.), Handb. Nanoelectrochemistry, Springer International Publishing, Cham, 2015: pp. 1–26.

[14] M.N. Tsampas, F.M. Sapountzi, P. Vernoux, Applications of yttria stabilized zirconia (YSZ) in catalysis, Catal. Sci. Technol. 5 (2015) 4884–4900.

[15] R.G. Silver, C.J. Hou, J.G. Ekerdt, The role of lattice anion vacancies in the activation of CO and as the catalytic site for methanol synthesis over zirconium dioxide and yttria-doped zirconium dioxide, J. Catal. 118 (1989) 400–416.

[16] H.A.E. Dole, R.J. Isaifan, F.M. Sapountzi, L. Lizarraga, D. Aubert, A. Princivalle, P. Vernoux, E.A. Baranova, Low Temperature Toluene Oxidation Over Pt Nanoparticles Supported on Yttria Stabilized-Zirconia, Catal. Letters. 143 (2013) 996–1002.

[17] R.J. Isaifan, H.A.E. Dole, E. Obeid, L. Lizarraga, P. Vernoux, E.A. Baranova, Metal-support interaction of Pt nanoparticles with ionically and non-ionically conductive supports for CO oxidation, Electrochem. Solid-State Lett. 15 (2012) E14.

[18] P. Vernoux, M. Guth, X. Li, Ionically Conducting Ceramics as Alternative Catalyst Supports, Electrochem. Solid-State Lett. 12 (2009) 11–13.

[19] J.C. Frost, Junction effect interactions in methanol synthesis catalysts, Nature. 334 (1988) 577–580.

[20] H.A.E. Dole, E.A. Baranova, Ethylene oxidation in an oxygen deficient environment : Why ceria is an active support ?, ChemCatChem. 8 (2016) 1977–1986.

[21] G. Pacchioni, Electronic interactions and charge transfers of metal atoms and clusters on oxide surfaces, Phys. Chem. Chem. Phys. 15 (2013) 1737–1757.

[22] Q. Fu, T. Wagner, Interaction of nanostructured metal overlayers with oxide surfaces, Surf. Sci. Rep. 62 (2007) 431–498.
[23] S. Bai, C. Wang, M. Deng, M. Gong, Y. Bai, J. Jiang, Y. Xiong, Surface Polarization Matters: Enhancing the Hydrogen-Evolution Reaction by Shrinking Pt Shells in Pt-Pd-Graphene Stack Structures, Angew. Chemie - Int. Ed. 53 (2014) 12120–12124.
[24] P. Peljo, J.A. Manzanares, H.H. Girault, Contact Potentials, Fermi Level Equilibration, and Surface Charging, Langmuir. 32 (2016) 5765–5775.
[25] H.A.E. Dole, L.F. Safady, S. Ntais, M. Couillard, E.A. Baranova, Electrochemically enhanced metal-support interaction of highly dispersed Ru nanoparticles with a CeO2 support, J. Catal. 318 (2014) 85–94.
[26] Y.M. Hajar, H.A. Dole, M. Couillard, E.A. Baranova, Investigation of heterogeneous catalysts by electrochemical method: Ceria and titania supported iridium for ethylene oxidation, ECS Trans. 72 (2016) 161–172.
[27] E.A. Baranova, C. Bock, D. Ilin, D. Wang, B. MacDougall, Infrared spectroscopy on size-controlled synthesized Pt-based nano-catalysts, Surf. Sci. 600 (2006) 3502–3511.
[28] S. Wu, D. Chen, Synthesis and characterization of nickel nanoparticles by hydrazine reduction in ethylene glycol, J. Colloid Interfaces Sci. 259 (2003) 282–286.
[29] B. Paul, R. Eluri, B. Paul, Synthesis of nickel nanoparticles by hydrazine reduction : mechanistic study and continuous flow synthesis Synthesis of nickel nanoparticles by hydrazine reduction : mechanistic study and continuous flow synthesis, J. Nanoparticle Res. 14 (2012).
[30] I.R. Gibson, G.P. Dransfield, J.T.S. Irvine, Sinterability of commercial 8 mol % yttria-stabilized zirconia powders and the effect of sintered density on the ionic conductivity, J. Mater. Sci. 33 (1998) 4297–4305.
[31] H.A.E. Dole, A. Costa, M. Couillard, E.A. Baranova, Quantifying metal support interaction in ceria-supported Pt, PtSn and Ru nanoparticles using electrochemical technique, J. Catal. 333 (2016) 40–50.
[32] J. Nicole, D. Tsiplakides, C. Pliangos, X.E.E. Verykios, C. Comninellis, C.G.G. Vayenas, Electrochemical Promotion and Metal–Support Interactions, J. Catal. 204 (2001) 23–34.
[33] C.G.C.G. Vayenas, S. Bebelis, I. V. Yentekakis, H.-G. Lintz, Non-faradaic electrochemical modification of catalytic activity: A status report, Catal. Today. 11 (1992) 303–442.
[34] R.J. Isaifan, E.A. Baranova, Catalytic electrooxidation of volatile organic compounds by oxygen-ion conducting ceramics in oxygen-free gas environment, Electrochem. Commun. 27 (2013) 164–167.
[35] R.J. Isaifan, E.A. Baranova, Effect of ionically conductive supports on the catalytic activity of platinum and ruthenium nanoparticles for ethylene complete oxidation, Catal. Today. 241 (2015) 107–113.

Chapter 4 Isotopic oxygen exchange study to unravel noble metal oxide/support interactions

Y. Hajar, A. Boreave, A. Caravaca, P. Vernoux and E. Baranova, In preparation for submission.

Nanoparticle metal oxides supported on active ionic and mixed ionic-electronic conductive supports have been continuously receiving great attention due to their high catalytic activity and the interaction that occurs between the nanoparticles and the support. Therefore, the aim of this study is to unravel the mechanism of (noble metal oxide)/(active support) interactions for catalytic purposes. Isotopic oxygen exchange (IOE) tests were performed on Iridium- and Ruthenium-based oxides supported on cerium oxide (CeO_2), titanium oxide (TiO_2), and yttria-stabilized zirconia (YSZ). IOE tests demonstrated the support engagement in the propane oxidation reaction, with YSZ-based catalysts showing the highest exchange rate, while CeO_2 and TiO_2-based catalysts had a limited backspillover of the lattice oxygen in that order. The average particle size and resulting metal oxide dispersion had a significant effect on the exchange ability and the catalytic rate, especially shown in the case of CeO_2 based catalysts.

4.1. Introduction

Metal oxides that are considered as active supports (e.g. CeO_2, TiO_2) due to their lattice oxygen mobility are appealing for their use in heterogeneous catalysis [1,2]. For instance, noble metal or noble metal oxide-based catalysts supported on active supports are commonly used in catalytic oxidation reactions [1,3], low temperature solid oxide fuel cells (SOFC) [4–6] and electrochemical promotion of catalysis [7–9]. The oxygen mobility property is of paramount importance, especially when oxygen from the gas phase is scarce or not stable in concentration [3]. However, to this date it is not completely understood the role of lattice oxygen from the active support in a given catalytic reaction. Therefore, the aim of this work is to use experimental isotopic oxygen exchange (IOE) tests to thoroughly understand the interaction that occurs at the atomistic level between the metal and the active support. This results are of paramount importance to further design efficient heterogeneous catalysts.

IOE has been the method of choice for many researchers [10–18]: Doornkamp et al. used IOE tests to find the rate constants for oxygen exchange mechanisms on various group IV metal oxides [10]. Bouwmeester et al. used pulse IOE to determine the exchange rates of oxygen on YSZ (Y_2O_3-ZrO_2), BSCF ($Ba_{1-y}Sr_yCo_{0.8}Fe_{0.2}O_{3-\delta}$) and $La_2NiO_{4+\delta}$ [11]. Shim et al. used IOE to show

that smaller grain boundary size of YSZ allows the increase of oxygen adsorption from the gas phase [12].

The enhanced effect of an active support is accentuated when having an interface with nanoparticle catalyst as it decreases the rate of their aggregation due to the oxygen vacancies at the interface [13–15]. Dong et al. demonstrated a volcano-shaped relationship with particle size and specific surface area (SSA) [16]. Kai et al. showed that Rh had a higher OSC than Pt and Pd on CZO (CeO_2-ZrO_2) [17]; and Fortunato et al. showed that using an ionically conducting oxide such as YSZ results in the engagement of lattice oxygen from the support in the deep oxidation of propane, as opposed to the case of SiO_2 or ZrO_2 supporting Pt nanoparticles [18].

In this work, the deep oxidation of a light hydrocarbon (propane) was used as a test reaction [19]. While CeO_2-supported Pt and Pd catalysts are the most effective for deep oxidation reactions [20,21], their oxygen storage capacity (OSC) is an order of magnitude smaller than that of Rh, Ir and Ru-based catalysts [22–24]. Furthermore, interest in using other catalysts such as RuO_2/CeO_2 in low temperature SOFC makes this catalyst appealing for further studies [6]. Therefore, Iridium and Ruthenium oxides deposited on pure oxygen ionic (YSZ) and mixed ionic-electronic (CeO_2 and TiO_2) conducting active supports are studied here using IOE measurements.

4.2. Materials and methods

Commercial YSZ (8% Y_2O_3- 92% ZrO_2, Tosoh®, SSA 13 $m^2\ g^{-1}$), CeO_2 (Alfa Aesar®, specific surface area 30-50 $m^2\ g^{-1}$) and TiO_2 (Acros Organics, Aeroxide® P25, SSA 45-55 $m^2\ g^{-1}$) are the supports used in this study. They were used to support pre-synthesized noble metal nanoparticles using a polyol method [25,26]. The synthesis method included two steps: 1) nanoparticles synthesis in colloidal form, and 2) deposition on the support at 1 wt.%. Due to pretreatments and tests under oxygen-based reaction atmospheres, the noble metal nanoparticles are oxidized partially to RuO_2 and IrO_2 form. To synthesize ruthenium and iridium nanoparticles (NPs), 0.11 g of H_2IrCl_6 (Alfa Aesar®, ≥ 99.99%) or 0.21 g of $RuCl_4$ (Sigma–Aldrich®, ≥ 99.99%) was dissolved in 50 mL of ethylene glycol with 0.08 M of NaOH. The solution was refluxed at 160 °C for 3 h, resulting in a pH drop from 10 to 7.5, indicating nanoparticles formation. The NPs colloid solution was mixed with a pre-calculated amount of the supporting metal oxide powder in deionized water for 72 h. The mechanical attachment of the nanoparticles (NPs) to the oxide is signaled by the change of the solution's color to clear when the solid phase sediments upon

cessation of the mixing. The catalyst sludge is centrifuged and dried in a freeze dryer (LabConco®). First, to check on the formation of nanoparticle noble metals, transmission electron microscopy (TEM) (JEOL JEM 2100F FETEM operating at 200 kV) was used for the TiO_2-supported catalysts, and annular dark field Scanning TEM (STEM) (FEI Titan3 80–300 TEM operated at 300 kV) was used for the CeO_2-based material. Image J software allowed the determination of the average particle size of ruthenium and iridium. The specific surface area (SSA) was determined using the Brunauer–Emmett–Teller (BET) method (Quantachrom®, Mod. Nova 2000) with nitrogen adsorption at -195 ºC. The metal loading was checked using X-Ray Fluorescence (XRF) (Olympus®, 40 kV electron beam) and presented in Table 4-1.

The dispersion of the catalyst was estimated from the average particle size determined from the TEM images:

$$\text{Dispersion (\%)} = (600 \cdot Mw_{Metal})/(\rho_{(g/m^3)} \cdot d_{(m)} \cdot a_{metal} \cdot N_a) \qquad 4\text{-}1$$

where M_{Metal} is the molecular weight, a_{Metal} is the atomic surface area, ρ is the metal density, N_a is Avogadro's number, and d is the average particle diameter (m) estimated from TEM or STEM.

The experimental setup used for the isotopic oxygen exchange tests consisted of a U-shape reactor in which 50 mg of the catalyst was introduced. The feed gas consisted of 1% isotopic oxygen (97.37% $^{18}O_2$, 1.1% $^{16}O^{18}O$, 1.53% $^{16}O_2$ from EURISOTOP®) diluted in Helium (Linde®, 99.999%) or 5% $^{16}O_2$ (Linde®, 5% $^{16}O_2$) diluted in Helium, at 30 mL min^{-1} flow rate. Four-port valves were used to switch the feed inlet to the reactor between pre-treatment conditions and reactants feed. Another four-port valve would allow the feed gas to enter the reactor or by-pass it before it continues its flow to the Hiden® quadrupole mass spectrometer where the gas composition is detected by following the masses of 18, 20, 28, 29, 32, 34, 36, 42, 44, 46 m/z.

For the isothermal IOE, the sample was pre-treated with the 5 % $^{16}O_2$ oxygen for two hours at 350 °C. Before starting the experiment, the 1 % $^{18}O_2$ gas feed by-passed the reactor directly to the MS to find the $^{18}O_2$ initial threshold; meanwhile, the reactor was purged with helium to remove $^{16}O_2$ gas from the flow. The two four-port valves were then switched in a way that $^{18}O_2$ gas feed was directed towards the reactor and then to the MS detection. A blank experiment was performed without any catalyst in the reactor to determine the dead volume.

For the catalytic reaction rate tests, 0.4 kPa propane (Linde®, 8000 ppm in He) was fed along with 2 kPa $^{16}O_2$ oxygen (Linde®, 5% in He) for a total flow rate of 40 mL min^{-1} and tested using the aforementioned mass spectrometer at 350 °C. This experiment followed directly the isothermal IOE test with an intermittent purge with He for 5 min

For "ethylene titration reaction", the catalysts were pre-treated under 3 kPa of oxygen from room temperature to 400 °C by a step increase of temperature of 25 °C. The temperature was then dwelled at 400 °C for 2 h before cooling it down to room temperature. The temperature was then increased to 350 °C by step change of 25 °C and 10 min at each temperature under the reaction feed of 0.01 kPa C_2H_4 (Linde, 0.5% C_2H_4 in He) and 3 kPa of $^{16}O_2$ (20 % O_2, Linde®) with a total flow rate of 100 mL min^{-1} (He balance). The reaction mixture was kept for an hour at 350 °C, then the reaction feed was switched to a flow of ethylene alone with balance of He. The CO_2 produced during the titration test was followed using non-dispersive infrared (NDIR) CO_2 gas analyzer (Horiba®, VA-3000).

During the oxygen isotopic exchange, different reactions can occur [27,28]:

- The homomolecular exchange during which oxygen molecules of different labels from the gas phase are scrambled over the catalyst surface (Equation 4-2).

$$^{18}O_{2,g} + {}^{16}O_{2,g} \rightleftharpoons 2{}^{16}O{}^{18}O_g \qquad 4\text{-}2$$

- The heteromolecular exchange during which $^{18}O_2$ is scrambled with lattice oxygen of the oxide solid. A simple heteromolecular exchange involves one atom from the solid (Equation 4-3), whereas multiple heteromolecular exchange reaction involves multiple oxygen atoms from the support (Equation 4-4).

$$^{18}O_{2,g} + {}^{16}O_s \rightleftharpoons {}^{16}O{}^{18}O_s + {}^{18}O_s \qquad 4\text{-}3$$

$$^{16}O{}^{18}O_s + {}^{16}O_s \rightleftharpoons {}^{16}O_{2,g} + {}^{18}O_s \qquad 4\text{-}4$$

Similarly, during propane oxidation, a different source of oxygen can oxidize propane resulting in isotopically labelled CO_2: $C^{16}O_2$, $C^{16}O^{18}O$ or $C^{18}O_2$.

4.3. Results and discussion

Table 4-1 shows a summary of the main physicochemical properties of these materials. Transmission electronic microscopy (TEM) and scanning STEM characterizations (Figure 4.1)

were first performed. The dispersion (Equation 4-1) of Iridium oxide on CeO_2 and TiO_2 averaged to a slightly higher number compared to that of Ruthenium oxide due to their slightly smaller particle size. The Specific Surface Area (SSA) of CeO_2 and TiO_2-based catalysts were higher than that of YSZ-based catalysts. It could be mainly attributed to the intrinsic SSA values of the pure metal oxide supports.

Before testing the catalysts for propane oxidation, isothermal isotopic oxygen exchange test was performed under an $^{18}O_2$ reaction atmosphere. Briefly, during the test, labelled oxygen $^{18}O_2$ bypassed the reactor in the first minute. Then the valve was switched to let the reactive gas flow into the reactor. The isothermal IOE test (Figure 4.2) was performed at 350 ^oC on the different catalysts to detect their oxygen exchange capacity. In addition, the atomic fraction (Equation 4-5) of $^{18}O_2$, $^{18}O^{16}O$ and $^{16}O_2$ in the gas phase as well as the initial rate of exchange (Equation 4-6) were calculated (Table 4-2). Temperature-programmed IOE (TPIOE) was also performed separately (Figure A 2).

During the isothermal IOE test, the multiple heteromolecular exchange (full exchange of $^{18}O_2$ from the gas with two ^{16}O from the support) was the dominant mechanism for YSZ- based catalysts (Figure 4.2) at the beginning of the exchange. This phenomenon was followed by a slow drop in its rate as simple heteroexchange (exchange of $^{18}O_2$ with one ^{16}O from the support to form $^{16}O^{18}O$) was rising. In the case of TiO_2-supported catalysts, comparable simple and multiple heteroexchange reactions occurred with the former being slightly higher and prolonged. As it could be observed in Table 4-2, RuO_2 and IrO_2 supported on YSZ exhibited a similar initial rate of exchange (R_0). However, in the case of the CeO_2 support, the performance of the two catalysts was not similar. IrO_2/CeO_2 shows a significant oxygen exchange capacity compared to that of RuO_2/CeO_2. The total amount of oxygen exchanged can be better analysed when comparing the time required for $^{18}O_2$ to recover its initial value (Figure 4.2). The oxygen exchange rate of the catalysts followed the order: $IrO_2/YSZ > RuO_2/YSZ > IrO_2/CeO_2 > RuO_2/TiO_2 > IrO_2/TiO_2 > RuO_2/CeO_2$. It is worth mentioning that the IOE of the active supports was negligible (Not shown here).

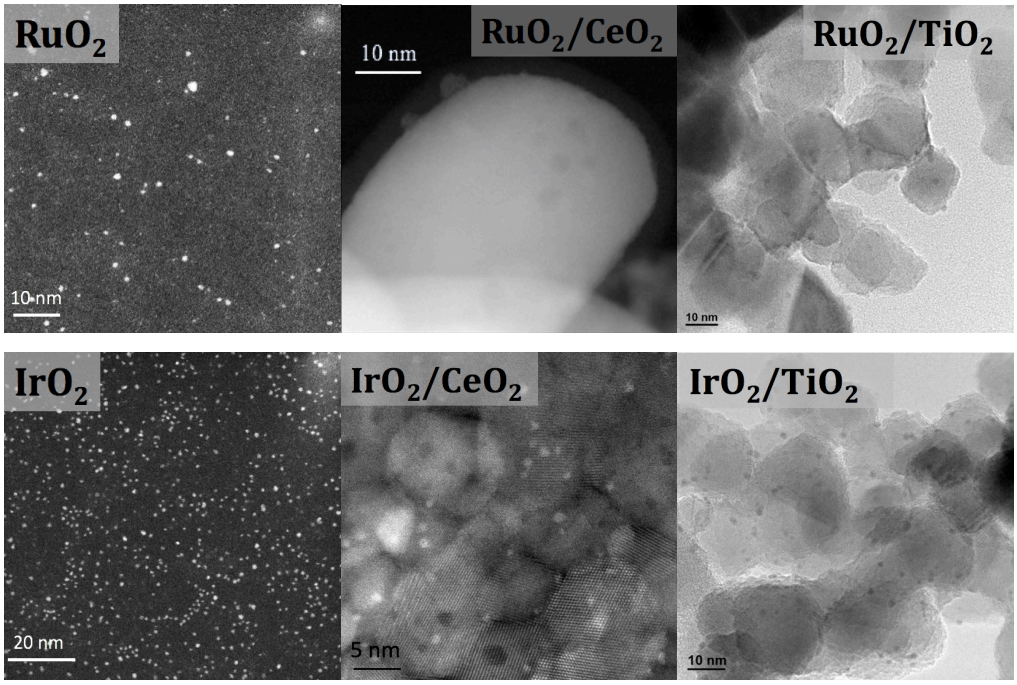

Figure 4.1: STEM of RuO_2 and IrO_2 stand-alone nanoparticles and when supported on CeO_2 (STEM) and on TiO_2 (TEM). Particle size distribution is presented in Figure A 1.

Table 4-1: Characteristics of metal nanoparticles supported on CeO_2, TiO_2 and YSZ metal oxides.

Catalyst	**Average particle size (nm)[a]**	**Dispersion (%)[b]**	**Metal loading (wt.%)[c]**	**Specific Surface Area (m^2/g)[d]**
RuO_2	1.4	-	-	-
RuO_2/CeO_2	1.8	33.0	1.03	48
RuO_2/TiO_2	1.4	42.5	1.07	48
RuO_2/YSZ	n/a	n/a	0.99	12
IrO_2	1.0	-	-	-
IrO_2/CeO_2	1.0	57.7	1.10	40
IrO_2/TiO_2	1.2	48.1	1.04	46
IrO_2/YSZ	n/a	n/a	0.91	14

[a] Determined from TEM, [b] from eq. S1 [c] from XRF measurements, [d] from BET measurements.

$$\alpha_i = \frac{P_i}{P_T} \text{ with i being 32,34,36 and } P_T = P_{32} + P_{34} + P_{36} \qquad 4\text{-}5$$

The initial rate of exchange R_0^e was calculated as follows and is summarized in Table 4-2:

$$R_0^e = 2\frac{\dot{V}}{mRT}(P_{32} + 1/2\ P_{34}) \qquad 4\text{-}6$$

where $\dot{V}$ is the volumetric flow rate, m the catalyst weight, R the gas constant, T standard condition temperature.

Table 4-2: Initial rate of isothermal oxygen exchange and initial catalytic rate of propane oxidation using oxygen from the catalyst for the different catalyst complexes.

	R_0^e (mol ^{18}O s^{-1} g^{-1} 10^{-5})		r of $C^{18}O_2$+1/2 $C^{16}O^{18}O$ (mol ^{18}O s^{-1} g^{-1} 10^{-7})	
NPs	RuO_2	IrO_2	RuO_2	IrO_2
Support				
YSZ	1.21	1.27	1.03	1.13
CeO_2	0.11	1.08	0.27	1.33
TiO_2	0.81	0.56	1.0	0.84

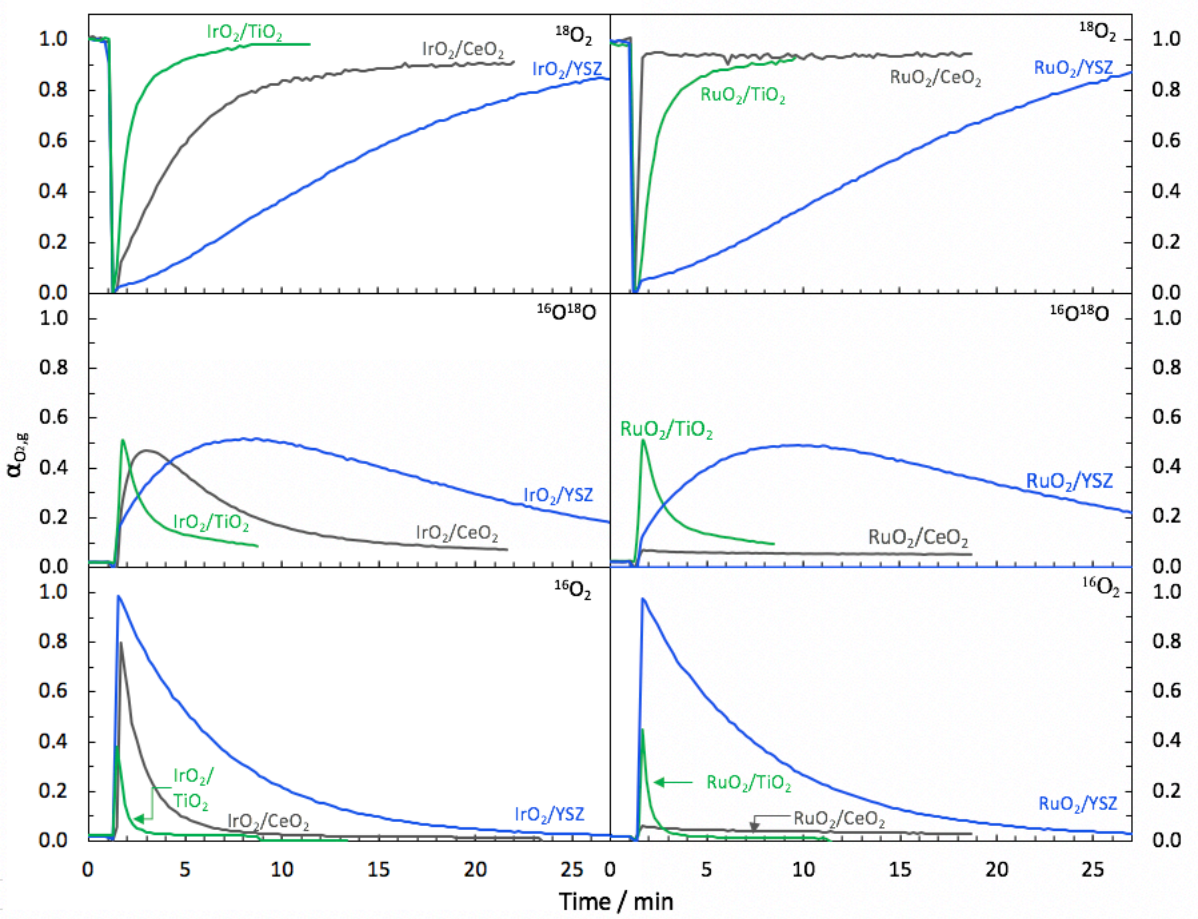

Figure 4.2: Isothermal isotopic oxygen exchange on IrO_2 and RuO_2 supported on CeO_2, TiO_2 and YSZ metal oxides. The four-way valve is switched to the reactor's inlet at t= 1 min. T=350 °C. $P_{^{18}O_2}$= 1 kPa and balance of He. Total flow= 40 mL min^{-1}. The support alone had no oxygen exchange capacity at this temperature.

Furthermore, the catalytic performance of the six catalytic materials was tested for propane oxidation (Figure 4.3). The propane oxidation reaction with $^{16}O_2$ was performed directly after the isothermal oxygen exchange test with a 5 min helium purge in between. Propane oxidation at T=

350 ºC was followed via mass spectrometry, with m/z 44 ($C^{16}O_2$), 46 ($C^{16}O^{18}O$), and 48 ($C^{18}O_2$) being the main products. Therefore, CO_2 gas product containing ^{18}O atoms originates from the catalyst as ^{18}O was stored in the sample during the isothermal IOE experiment described in Figure 4.2. Hence, RuO_2/ and IrO_2/YSZ catalysts exhibited the highest production of $C^{18}O_2$ in good agreement with their highest oxygen exchange rate. While $C^{18}O_2$ production was dominant at first, $C^{16}O^{18}O$ production followed for a few minutes, and then the $C^{16}O_2$ production emerged. This order of CO_2 isotopes production is due to the depletion of the support from the labelled $^{18}O_2$, and its subsequent replacement by ^{16}O from the gas.

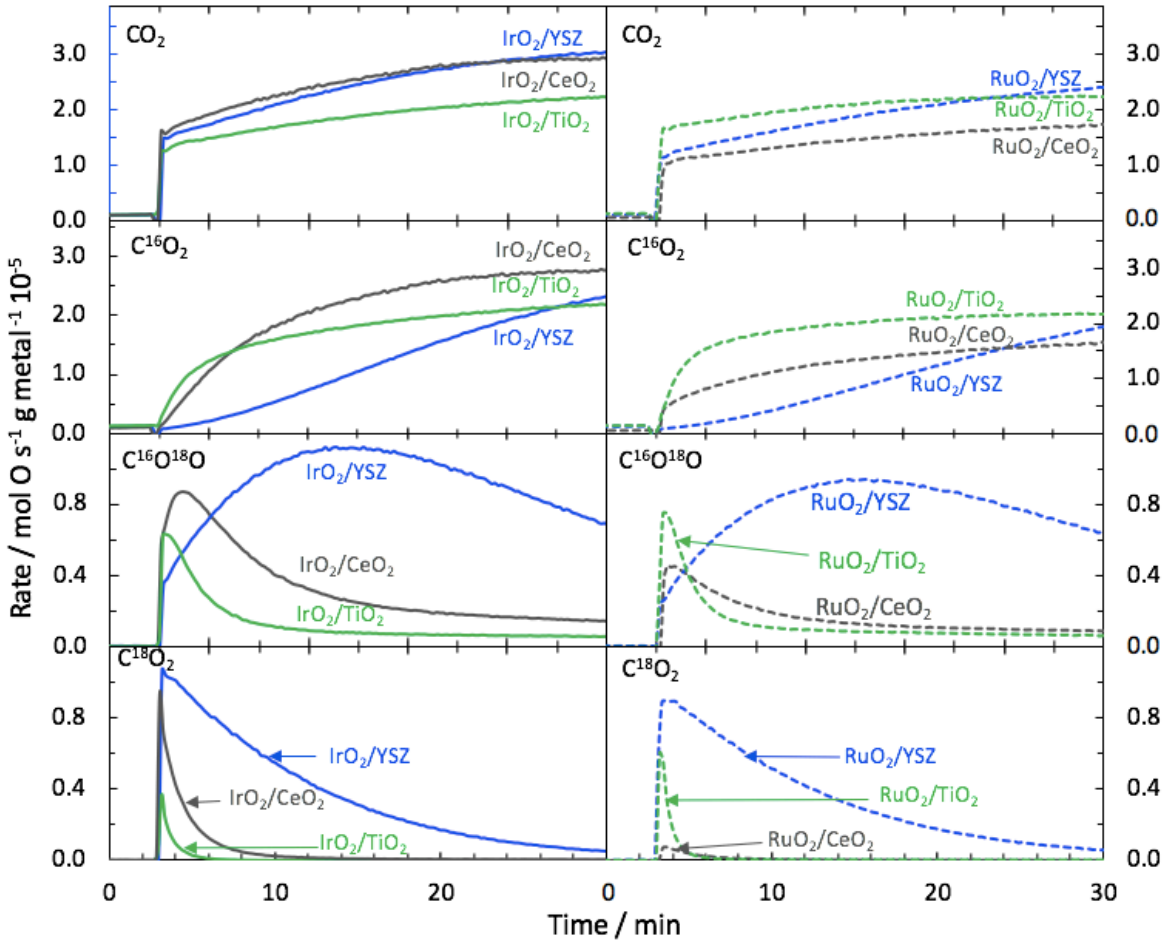

Figure 4.3: Propane oxidation to the different isotopically-labelled CO_2 in the case of IrO_2 supported on CeO_2, TiO_2, and YSZ metal oxides. $P_{C_3H_8}$= 0.4 kPa and $P_{^{16}O_2}$= 2 kPa and balance of He. Total flow rate= 40 mL min^{-1}. The experiment is performed consecutively to the isothermal IOE test. The reactive flow is switched to the reactor at t=3min.

The active nature of YSZ-based catalysts is therefore confirmed by the $C^{18}O_2$ production which was much prolonged compared to the other supports. TiO_2- based catalysts had a little $C^{18}O_2$

production but peaked initially in $C^{16}O^{18}O$ production which is in good agreement with their IOE results of highest $^{16}O^{18}O$ desorption. It could be attributed to the rapid surface oxygen exchange and dominant simple heteroexchange mechanism. Finally, the divergence in the oxygen exchange behavior of the two CeO_2-based catalysts was confirmed by the catalytic tests for propane oxidation (Figure 4.3). Indeed, IrO_2/CeO_2 had a significant $C^{18}O_2$ production whereas it was negligible for RuO_2/CeO_2. In addition, most of the CO_2 produced on RuO_2/CeO_2 was $C^{16}O_2$. It seems to suggest a lower interaction between ceria and RuO_2 . This could be due to the low electronic conductivity of CeO_2 below 600 °C which prevents it from reduction from Ce(IV) to Ce(III) [29].

The involvement of bulk oxygen of the support in a catalytic reaction was also characterized by "ethylene titration tests" under an oxygen deficient atmosphere. In such conditions, any resulting oxidation reaction can only be assisted by lattice oxygen from the support material. In previous works, Isaifan et al. have tested Pt supported on YSZ, Sm-doped CeO_2 and CeO_2 for ethylene oxidation in an oxygen deficient environment [30]. Dole et al. tested ethylene oxidation with and without gaseous oxygen and compared the results between Pt, RuO_2 and IrO_2 supported on CeO_2 [31]. In this work, Figure 4.4 shows the oxygen storage capacity of the catalysts under an oxygen deficient reaction atmosphere at 350 °C. The catalysts were first stabilized under C_2H_4/O_2 condition before the oxygen feed was interrupted at t= 0 h. IrO_2 and RuO_2 supported on YSZ had the highest and most prolonged activity for reacting with gaseous ethylene. It could be attributed to the high bulk oxygen mobility of YSZ mostly due to the high number of oxygen vacancies. TiO_2-based catalysts exhibited a lower reactivity. Regarding the CeO_2-based materials, in the case of IrO_2/CeO_2, a significant ethylene conversion occurred at the beginning of the reducing environment period, followed by an increase of the ethylene conversion before it decreased to zero. This sudden increase in the ethylene conversion could be attributed to the oxygen vacancies associated with the surface reduction of ceria in the proximity of the metal oxide nanoparticles [32]. A similar but shorter trend occurred in the case of RuO_2/CeO_2. This is in good agreement with the lowest oxygen exchange rate that RuO_2/CeO_2 had in the isothermal and temperature-programmed experiments (Figure 4.2 and A 2). Since both IrO_2 and RuO_2 supported on CeO_2 had the same trend in reducing conditions, one can notice that the ability of CeO_2 to be reduced is probably surface limited in the case of both noble metal oxides. The higher catalytic activity of IrO_2/CeO_2 compared to RuO_2/CeO_2 could be attributed to the smaller particle size of

IrO_2 over CeO_2, allowing for a better dispersion and an enhanced oxygen mobility around the metal oxide nanoparticles.

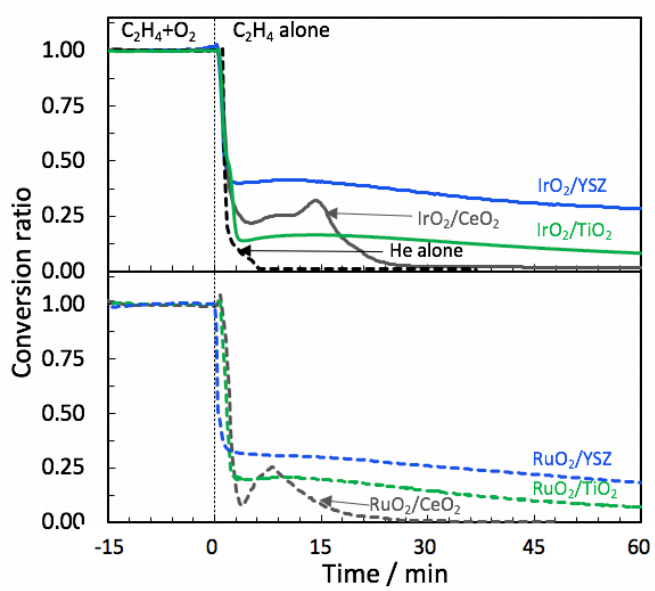

Figure 4.4: Ethylene oxidation in the presence and absence of oxygen in the gaseous feed for the case IrO_2 and RuO_2 supported on CeO_2, TiO_2, and YSZ metal oxides. T=350 °C , $P_{(C_2H_4)}$= 0.01 kPa, $P(o_2)$= 3 kPa (for t<0 h) and Po_2= 0 kPa (for t>0h). Total flow= 100 mL min^{-1}. The "He alone" curve is a reference curve for when no C_2H_4 nor O_2 are flowing in the stream after t=0 h.

4.4. Conclusions

In conclusion, noble-metal oxide/support interactions were studied in this work. To that purpose, nanodispersed IrO_2 and RuO_2 based catalysts supported on YSZ, CeO_2, and TiO_2 were investigated by Isotopic Oxygen Exchange techniques. Metal oxides supported on YSZ exhibited very significant metal oxide/support interactions and the highest oxygen exchange compared to the other supports. It led to a higher catalytic activity for the propane oxidation reaction, and to a higher intrinsic activity of the oxygen species supplied by the support with different hydrocarbons (propane and ethylene). This study clearly demonstrates the high oxidation capacity of Iridium and Ruthenium oxides supported on active supports (mainly YSZ), pointing out the importance of nanoparticles/support interactions.

References

[1] J. Haber, E.M. Serwicka, The role of Oxygen on Catalysis, React. Kinet. Catal. Lett. 35 (1987) 369–379.

[2] C. Mirodatos, Use of isotopic transient kinetics in heterogeneous catalysis, Catal. Today. 9 (1991) 83–95.

[3] L. Liu, A. Corma, Metal Catalysts for Heterogeneous Catalysis: From Single Atoms to Nanoclusters and Nanoparticles, Chem. Rev. 118 (2018) 4981–5079.

[4] S.B. Adler, Factors Governing Oxygen Reduction in Solid Oxide Fuel Cell Cathodes † , Chem. Rev. 104 (2004) 4791–4844.

[5] Y. Takagi, K. Kerman, C. Ko, S. Ramanathan, Operational characteristics of thin film solid oxide fuel cells with ruthenium anode in natural gas, J. Power Sources. 243 (2013) 1–9.

[6] X. Liu, Z. Zhan, X. Meng, W. Huang, S. Wang, T. Wen, Enabling catalysis of Ru-CeO2 for propane oxidation in low temperature solid oxide fuel cells, J. Power Sources. 199 (2012) 138–141.

[7] M.N. Tsampas, F.M. Sapountzi, A. Boréave, P. Vernoux, Isotopical labeling mechanistic studies of electrochemical promotion of propane combustion on Pt/YSZ, Electrochem. Commun. 26 (2013) 13–16.

[8] P. Vernoux, L. Lizarraga, M.N. Tsampas, F.M. Sapountzi, A. De Lucas-Consuegra, J.L. Valverde, S. Souentie, C.G. Vayenas, D. Tsiplakides, S. Balomenou, E.A. Baranova, Ionically conducting ceramics as active catalyst supports, Chem. Rev. 113 (2013) 8192–8260.

[9] C.G. Vayenas, S. Bebelis, C. Pliangos, S. Brosda, D. Tsiplakides, Electrochemical Activation of Catalysis: Promotion, Electrochemical Promotion, and Metal-Support Interactions, Springer, New York, 2001.

[10] C. Doornkamp, M. Clement, V. Ponec, The Isotopic Exchange Reaction of Oxygen on Metal Oxides, J. Catal. 399 (1999) 390–399.

[11] H.J.M. Bouwmeester, C. Song, J. Zhu, J. Yi, M.V.S. Annaland, B.A. Boukamp, A novel pulse isotopic exchange technique for rapid determination of the oxygen surface exchange rate of oxide ion conductors, Phys. Chem. Chem. Phys. 11 (2009) 9640–9643.

[12] J.H. Shim, J.S. Park, T.P. Holme, K. Crabb, W. Lee, Y.B. Kim, X. Tian, T.M. Gu, F.B. Prinz, Enhanced oxygen exchange and incorporation at surface grain boundaries on an oxide ion conductor, Acta Mater. 60 (2012) 1–7.

[13] D. Duprez, Study of surface mobility by isotopic exchange: recent developments and perspectives, in: C. Li, Q. Xin (Eds.), Spillover Migr. Surf. Species Catal., Elsevier Science, 1997: pp. 13–28.

[14] L. Giordano, G. Pacchioni, J. Goniakowski, Properties of MgO(100) ultrathin layers on Pd(100): Influence of the metal support, Phys. Rev. B - Condens. Matter Mater. Phys. 67 (2003) 1–8.

[15] L. Giordano, J. Goniakowski, G. Pacchioni, Characteristics of Pd adsorption on the MgO(100) surface: Role of oxygen vacancies, Phys. Rev. B - Condens. Matter Mater. Phys. 64 (2001) 754171–754179.

[16] F. Dong, T. Tanabe, A. Suda, N. Takahashi, H. Sobukawa, H. Shinjoh, Investigation of the OSC performance of Pt / CeO2-ZrO2-Y2O3 catalysts by CO oxidation and 18O/16O isotopic exchange reaction, Chem. Eng. Sci. 63 (2008) 5020–5027.

[17] L. Kai, W. Xuezhong, Z. Zexing, W. Xiaodong, W. Duan, Oxygen Storage Capacity of Pt- Pd-, Rh/CeO2-BasedOxide Catalyst, J. Rare Earths. 25 (2007) 6–10.

[18] M.A. Fortunato, A. Princivalle, C. Capdeillayre, N. Petigny, C. Tardivat, C. Guizard, M.N. Tsampas, F.M. Sapountzi, P. Vernoux, Role of lattice oxygen in the propane combustion over Pt/yttria-stabilized zirconia : isotopic studies, Top. Catal. 57 (2014) 1277–1286.

[19] L. Li, F. Zhang, N. Guan, M. Richter, R. Fricke, Selective catalytic reduction of NO by propane in excess oxygen over IrCu-ZSM-5 catalyst, Catal. Commun. 8 (2007) 583–588.

[20] T.F. Garetto, E. Rincón, C.R. Apesteguía, Deep oxidation of propane on Pt-supported catalysts: Drastic turnover rate enhancement using zeolite supports, Appl. Catal. B Environ. 48 (2004) 167–

174.
[21] A. Boreave, H. Tan, V. Roche, P. Vernoux, J.P. Deloume, Oxygen mobility in lanthanum nickelate catalysts for deep oxidation of propane, Solid State Ionics. 179 (2008) 1071–1075.
[22] S. Bedrane, C. Descorme, D. Duprez, 16O/18O isotopic exchange: A powerful tool to investigate oxygen activation on M/CexZr1-xO2 catalysts, Appl. Catal. A Gen. 289 (2005) 90–96.
[23] H. Over, Surface Chemistry of Ruthenium Dioxide in Heterogeneous Catalysis and Electrocatalysis: From Fundamental to Applied Research, Chem. Rev. 112 (2012) 3356–3426.
[24] H. Over, M. Muhler, Catalytic CO oxidation over ruthenium - Bridging the pressure gap, Prog. Surf. Sci. 72 (2003) 3–17.
[25] Y.M. Hajar, K.D. Patel, U. Tariq, E.A. Baranova, Functional equivalence of electrochemical promotion and metal support interaction for Pt and RuO2 nanoparticles, J. Catal. 352 (2017) 42–51.
[26] Y.M. Hajar, H.A. Dole, M. Couillard, E.A. Baranova, Investigation of heterogeneous catalysts by electrochemical method: Ceria and titania supported iridium for ethylene oxidation, ECS Trans. 72 (2016) 161–172.
[27] G.K. Boreskov, The Catalysis of Isotopic Exchange in Molecular Oxygen, Adv. Catal. 15 (1965) 285–339.
[28] E.R.S. Winter, Exchange Reactions of Oxides. Part IX, J. Chem. Soc. A. (1968) 2889–2902.
[29] I. Kosacki, T. Suzuki, V. Petrovsky, H.U. Anderson, Electrical conductivity of nanocrystalline ceria and zirconia thin films, Solid State Ionics. 136–137 (2000) 1225–1233.
[30] R.J. Isaifan, E.A. Baranova, Catalytic electrooxidation of volatile organic compounds by oxygen-ion conducting ceramics in oxygen-free gas environment, Electrochem. Commun. 27 (2013) 164–167.
[31] H.A.E. Dole, E.A. Baranova, Ethylene oxidation in an oxygen deficient environment : Why ceria is an active support ?, ChemCatChem. 8 (2016) 1977–1986.
[32] P. Fornasiero, R. Di Monte, G. Ranga Rao, J. Kaspar, S. Meriani, A. Trovarelli, M. Graziani, Rh-Loaded CeO2-ZrO2 Solid Solutions as Highly Efficient Oxygen Exchangers: Dependence of the Reduction Behavior and the Oxygen Storage Cpacity on the Structural Properties, J. Catal. 151 (1995) 168–177.

Chapter 5 Functional Equivalence of Electrochemical Promotion and Metal Support Interaction for Pt and RuO_2 Nanoparticles

Y. M. Hajar, K. D. Patel, U. Tariq and E. A. Baranova, J. of Catalysis, 352 (2017) 42–51.

Electrochemical promotion of catalysis (EPOC) is a general phenomenon of modifying the catalytic activity of a metal or metal oxide in contact with a solid electrolyte by means of current or potential application. In this work, the free-standing (unsupported) platinum and ruthenium oxide nanoparticles (NPs) (2 nm average size) in contact with yttria-stabilized zirconia (YSZ) solid-electrolyte were electrochemically promoted under galvanostatic and potentiostatic conditions for ethylene oxidation reaction. The enhancement ratio of 1.8 and 1.5 was obtained for Pt and RuO_2 NPs, respectively in potentiostatic conditions at 350 °C. The apparent Faradaic efficiency, Λ, was as high as 400 at 250 °C and decreased as the reaction temperature increased. Similar degrees of promotion were achieved under open circuit by dispersing nanoparticles on CeO_2, TiO_2 and YSZ supports (1wt.% metal loading). The results showed the functional equivalence of EPOC and MSI with Pt and RuO_2 NPs. This finding is of considerable value for elucidation of the mechanism of MSI and EPOC, as well as for potential practical implementation of EPOC in industrial catalytic processes that use highly dispersed nanoparticle catalysts.

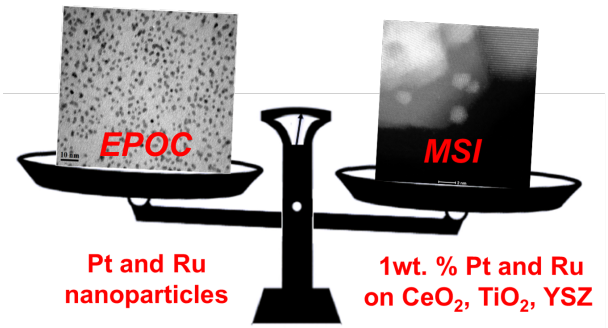

5.1. Introduction

The state of the art heterogeneous catalyst consists of highly dispersed, nano-structured metal or metal oxide deposited on a high surface area support [1–4]. The support is considered to be a structural promoter when stabilizing and increasing the dispersion of a catalyst. The enhancement in the catalytic activity can be also achieved by electronic promoters. These promoters result in changing surface electronic properties of the catalyst and as a result its catalytic properties [5–8]. An electronic type of promotion takes place when covering the catalyst surface, usually during catalyst preparation, with promoters, e.g., sodium, chloride ions, tin, etc. [9–12].

In the last three-decades, a phenomenon of electrochemical promotion of catalysis (EPOC) also called non-Faradaic modification of catalytic activity (NEMCA) has attracted a great deal of interest in catalytic community [5]. By applying a constant electric current or potential between the catalyst-working electrode and a catalytically inert counter electrode, promoting ions from the ionically conducting solid electrolyte move towards or away of the catalyst-working electrode surface and affect in-situ the catalytic rate [13–15]. In the case of oxygen-conducting electrolyte, oxygen backspillover, i.e., migration of ion from the solid electrolyte to the catalyst surface takes place and results in a strongly adsorbed species $O^{\delta-}$ with its image positive charge δ^+ [8]. The non-Faradaic enhancement is observed when the rate of gaseous oxygen (mol O/s) consumption is higher than the electrochemical rate (expressed in mol of ionic O/s provided from the electrolyte) [16–21]. The increase in the catalytic rate, Δr (mol O/s) divided by the electrochemical rate, I/nF (I is current, F is Faraday's constant and n is number of electrons, $n = 2$ for O^{2-}) is denoted by apparent Faradaic efficiency, Λ, and the process is considered non-Faradaic if $|\Lambda|$ is greater than 1. Another parameter used to quantify EPOC is the rate enhancement ratio, ρ_{EPOC}, denoted as the ratio between promoted (closed circuit catalytic rate, r) and unpromoted (open-circuit catalytic rate, r_o) [5].

Parallel to EPOC, the use of a support in heterogeneous catalysis expanded in role from only stabilizing a metal dispersion to affecting the catalyst activity and in some cases its selectivity. The phenomenon is known as metal-support interaction (MSI) and it strongly depends on the nature of the support used and the particle size of the catalyst; the smaller the particles the stronger the interaction is between the metal and the support [22]. For instance, in the case of TiO_2 support, the effect was termed strong metal support interaction (SMSI) [23–25] and was ascribed to migration of partially reduced titania, TiO_x ($x \leq 2$), to the gas exposed surface sites. Active supports, such as ceria (CeO_2), titania (TiO_2), doped-ceria and yttria- stabilized zirconia (YSZ) are able to affect the adsorption bond of the catalyst with the reactants and products [26] due to the presence of mobile oxygen species in the lattice of their crystal structure. These partially charged oxygen species create an inhomogeneous electric field that effects the adsorption bond strength of the metal, resulting in a promotion effect [27]. For nano-sized catalysts, the distance of oxygen species to migrate from the support to the catalyst is short enough (2-5 nm) that thermal forces are sufficient to allow the promoting migration of oxygen species to the catalyst surface [8].

Ceria is a reducible mixed ionic electronic conducting (MIEC) support with high oxygen storage capacity (OSC) and is widely used as a support and/or catalyst for a large number of industrially important reactions. On the other hand, YSZ is a non-reducible ionically conducting ceramic that recently has attracted much attention as an active support material. Vernoux and co-workers confirmed, through isotopical ($^{18}O_2$) labeling studies, that continuous oxygen exchange between YSZ lattice and the gas phase takes place in highly dispersed Pt/YSZ catalyst contrary to Pt dispersed on non-conducting ZrO_2 or SiO_2 supports [28,29]. These oxygen ions from the support act as "sacrificial" promoters and are consumed in the oxidation reaction but at the lower rate than gaseous oxygen. This is in agreement with EPOC mechanism, where the existence of two oxygen adsorption states under EPOC was established by temperature-programmed desorption and temperature programmed oxidation (TPD and TPO) [20] and using isotopic ($^{18}O_2$) TPD/TPO [30,31]. Furthermore, our group has showed high conversion of CO and C_2H_4 in an oxygen-free environment when Pt NPs were supported on YSZ, samarium-doped ceria (SDC) and CeO_2 material [32,33]. The studies proved the mobility of oxygen ions from the surface of conducting ceramics at temperatures as low as 100 ^oC that contributes towards the promotion effect of nanoparticle catalysts [34,35].

In the pioneering work by Nicole *et al.* [8], the functional similarity of MSI and EPOC was demonstrated for a sub-micrometer IrO_2 particles deposited on YSZ electrolyte or mixed with TiO_2 powder for ethylene oxidation. The addition of TiO_2 to IrO_2 particles enhanced the activity of IrO_2 for C_2H_4 oxidation by a factor of 12 and the same maximum rate enhancement was obtained via electrochemical promotion of the IrO_2 catalyst by supplying O^{2-} electrochemically to the IrO_2 catalyst from the YSZ solid electrolyte. The MSI rate enhancement ratio (ρ_{MSI}) was proposed [8] as:

$$\rho_{MSI} = {}^{r}/_{r_o} \qquad 5\text{-}1$$

where r_o is the catalytic rate of the unpromoted, i.e., free-standing catalyst (mol s^{-1}) and r is the rate of promoted, i.e., dispersed catalyst over the support. In the later work, Constantinou *et al.* showed similarity between supporting rhodium film on YSZ and electropromoting it on YSZ electrolyte for NO reduction reaction [36].

Ethylene is a common volatile organic compound (VOC) and is considered as a harmful molecule that contributes to photochemical pollution. The complete ethylene oxidation is of specific interest due to the global need to decrease the hydrocarbon content of stationary and

automotive emissions. Therefore, it has been the reactant of choice for many researchers to test the electrochemical promotion effect on its complete oxidation [15,19,34,37–42].

In the present study, we examined the electrochemical promotion effect of free standing (unsupported) platinum (2.0 nm mean size) and ruthenium oxide (1.8 nm mean size) NPs for ethylene complete oxidation. Furthermore, we compared the reaction rate of free-standing nanoparticles electrically promoted (EPOC effect under a closed circuit) to the reaction rate obtained with the same nanoparticles dispersed in CeO_2, TiO_2 and YSZ commercial supports with 1 wt.% metal loading (MSI). The rate enhancement ratio of both phenomena is compared and functional similarity of EPOC and MSI in ionically and mixed ionic electronic ceramics is discussed.

5.2. Experimental

5.2.1. Synthesis of free-standing nanoparticles

The catalysts used in this study were synthesized using a polyol method described in detail elsewhere [43]. The method consists of mixing the metal precursor with ethylene glycol and sodium hydroxide. The concentration of NaOH, i.e., pH of the synthesis solution, affects the size of the metal particles. At high pH the product of ethylene glycol oxidation is glycolate, which is a stabilizer for the metal colloids [43]. The concentration of NaOH (EM Science, ACS grade) used in this study was 0.08 M (pH = ~10). Precursor $PtCl_4$ (m = 0.26 g) (Sigma-Aldrich, ≥99.99 % metals basis) and $RuCl_4$ (m = 0.21 g) (Sigma-Aldrich, 99.99 % metal basis) were dissolved in 50 mL of ethylene glycol (Fisher-Scientific, certified grade). The solution was stirred at room temperature for 30 min, then refluxed for 3 hours at 160 ºC. The pH of the solution dropped from ~10 to ~7.5 after reflux. Ruthenium is most likely found in its oxidized form (RuO_x $x \leq 2$), therefore it will be referred to as RuO_2 [44].

5.2.2. Supported Pt and RuO_2 nanoparticles

The supported Pt or RuO_2 catalysts were prepared by mixing an appropriate volume of the colloidal solution with the powder support and deionized water (18 MΩ cm) followed by vigorous stirring for 48 hours at room temperature. The volume of the colloidal solution corresponded to a 1 wt.% nominal metal loading. The mixture was then centrifuged three times with a thorough wash with deionized water in between. Afterwards, the solution was dried using a freeze dryer overnight.

The MIEC supports used were CeO_2 (Alfa Aesar, specific surface area (SSA) 30–50 $m^2\ g^{-1}$) and TiO_2 (Acros Organics, Aeroxide^{TM} P25, SSA 50 $m^2\ g^{-1}$), and the ionically conducting support was YSZ (Tosoh, SSA 13 $m^2\ g^{-1}$, average size of 0.3 μm).

5.2.3. Electrochemical cell

YSZ (Tosoh), the same as a support for metals (section 2.2), was used to form solid-electrolyte disk (18 mm diameter and 1 mm thickness) using a procedure described in [45]. To prepare the electrochemical cell, gold paste (C2090428D4, Gwent Group, CAS: 98-55-5) was brushed on one side of the YSZ solid-electrolyte disk to form the counter and reference electrodes 1 and 0.2 cm^2, respectively. This was followed by annealing the gold in air at 500 °C for 1 hour. The catalyst - working electrode was deposited on the other side of the YSZ disk. The geometric area of the working electrode was 1 cm^2.

In the case of free-standing NPs, Pt or RuO_2 colloidal solutions were directly deposited on the YSZ electrolyte disk, inside a square tape mask followed by air-drying at 100 °C. The resulting nanoparticle layer was discontinuous and formed islands of nanoparticles on YSZ surface (Figure B 1 a,b in the appendix) and did not show electrical connectivity.

The supported Pt or RuO_2 nanoparticles were deposited on YSZ by mixing the catalyst powder in isopropanol (1 ml for each 0.01 g catalyst). The mixture was then deposited, 10 μL at a time, inside a square tape mask of 1 cm^2 area, then dried for 5 min at 60 ºC. The representative SEM images (Figure B 1) of 1 wt.% RuO_2/YSZ and RuO_2/TiO_2 deposited on YSZ disc show that both supports have similar structural porosity. The samples were all preconditioned at 350 °C under an O_2 environment (3 kPa in He) for an hour. Equivalent images for Pt supported on YSZ and TiO_2 (not shown) had also the same porous structure. In all cases, the loading of the noble metal catalyst was 0.1 mg metal cm^{-2}.

5.2.4. Experimental setup

The reactants were ethylene (Linde, 0.5 % C_2H_4 in He) and oxygen (Linde, 20.9 % O_2 in He), diluted in helium as a carrier gas (Linde, 99.99 % He). The gas composition of the reactants mixture was controlled using three mass flow controllers (MKS, 1259C and 1261C Series). The total flow rate was held at 100 mL min^{-1} at all times; the partial pressure of C_2H_4 was varied between 0.007 and 0.018 kPa, while the partial pressure of O_2 was held constant at 3 kPa.

The EPOC reactor has been described in detail previously [46]. The electrochemical cell is covered with a gold mesh acting as a current collector on the surface of the catalyst-working electrode while gold wires are connected on the other side of the cell to the reference and counter electrodes. The cell is enclosed in a tight fit inert ceramic (McMaster-Carr, Mycalex®) capsule with aeration holes. The capsule is held in place inside two slits of a quartz tube; its schematics is shown in Figure B 3. The three gold wires connected to the three electrodes are connected to a potentiostat-galvanostat (Arbin Instruments, MSTAT). A thermocouple (OMEGA®) is placed in the vicinity of the catalyst-working electrode and connected to a temperature controller. The three gold wires and thermocouple are fitted in a four-bore inert ceramic tube (OMEGA®).

5.2.5. Electron microscopy characterization

The average size of the catalysts was determined using transmission electron microscopy (TEM) (JEOL JEM 2100F FETEM operating at 200 kV). The scanning transmission electron microscopy (STEM) analysis was carried out on a FEI Titan3 80-300 TEM operated at 300 keV, and equipped with a CEOS aberration corrector for the probe forming lens and an energy dispersive X-ray (EDX) spectrometer (EDAX Analyzer, DPP-II). Annular dark-field (ADF) images, which provide a contrast related to the atomic number (Z) and the thickness of the region analyzed, were acquired with a Fischione detector. The convergence and collection angle were 17 and 60 mrad, respectively. The TEM specimens were prepared by sonicating the as-prepared catalyst powders in ethanol. One drop of the solution was then placed onto a 200 mesh TEM copper grid coated with a lacey carbon support film (Ted Pella) and dried in air. The elemental composition of both the catalyst and the support was also confirmed by spatially-resolved EDX. The use of Image J software allowed for the determination of Pt and RuO_2 particles size distribution.

For scanning electron microscopy (SEM) and Energy Dispersive Spectroscopy (EDS) measurements, the catalytic electrode surface was sputtered with 7 nm of gold before COMPO images were taken at 15 kV using JSM-7500F (JEOL).

5.3. Results and discussion

5.3.1. Catalyst electron microscopy characterization

TEM results for free-standing Pt and RuO_2 as well as 1 wt.% Pt/YSZ, 1 wt.% Pt/CeO_2 and 1 wt.% Ru/CeO_2 have been reported earlier [22,34,35,44]. Figure 5.1 shows representative TEM

(a, b) and ADF-STEM (c-e) images of colloidal (unsupported) and supported nanoparticles. The average particles size is 1.8 nm and 2.0 nm for unsupported RuO_2 and Pt NPs, respectively. Figure 5.1c and d shows ADF-STEM images of Pt/YSZ and Pt/CeO_2. The bright features observed in the ADF-STEM images were identified as the Pt catalyst. The dark features on Figure 5.1e, were confirmed by EDX to be RuO_2. As can be seen, in all cases the NPs are well dispersed on the support and show the same average particle size, 2 nm (Pt) and 1.8 nm (RuO_2) for unsupported and supported catalysts, as reported before [22,34].

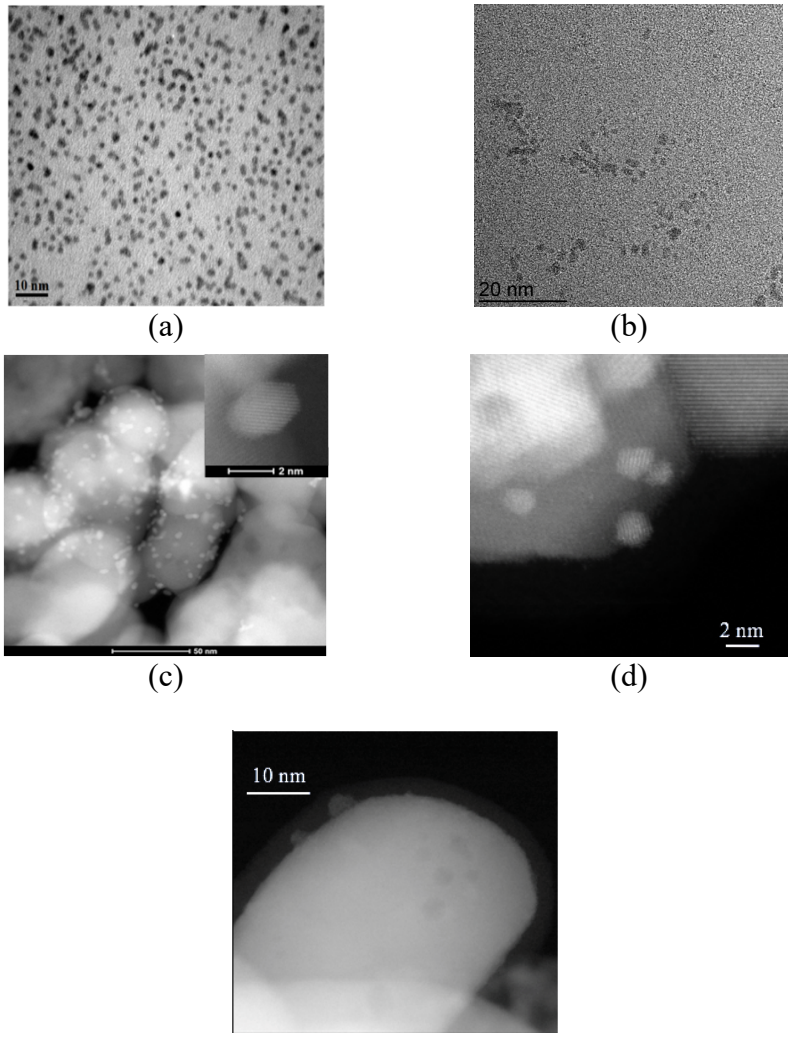

Figure 5.1: Representative TEM and STEM images of unsupported and supported Pt and RuO_2 nanoparticles. TEM of (a) Pt colloids, (b) RuO_2 colloids, and STEM of (c) Pt/YSZ, (d) Pt/CeO_2 and (e) RuO_2/CeO_2.

5.3.2. Electrochemical promotion of free-standing Pt NPs

Figure 5.2 shows the effect of the applied constant potential on the rate of ethylene oxidation on free-standing Pt NPs at 350 °C and its corresponding conversion value. The conversion of ethylene at open-circuit potential (o.c.p.) is already high at ~ 35 % due to relatively good dispersion and high active surface area of Pt NPs. Under closed-circuit conditions, conversion reaches 53 and 60 % at 0.25 V and 0.5 V, respectively; and the values of the current, I, reach 23 and 109 μA (with a ~2 μA fluctuation). In both cases, significant and reversible promotion occurs with the rate enhancement ratio, ρ, reaching values of 1.45 at 0.25 V and 1.80 when potential was doubled. The corresponding Faradaic efficiency, Λ, values are 70 and 23. Thus, in the former case, each O^{2-} ion supplied to the Pt catalyst from the electrolyte causes on average the catalytic reaction of 70 adsorbed O species originating from the gas phase. The electropromotion of Pt at 0.5 V is more pronounced than at 0.25 V but less efficient in the catalytic rate increase per migrated mol of O.

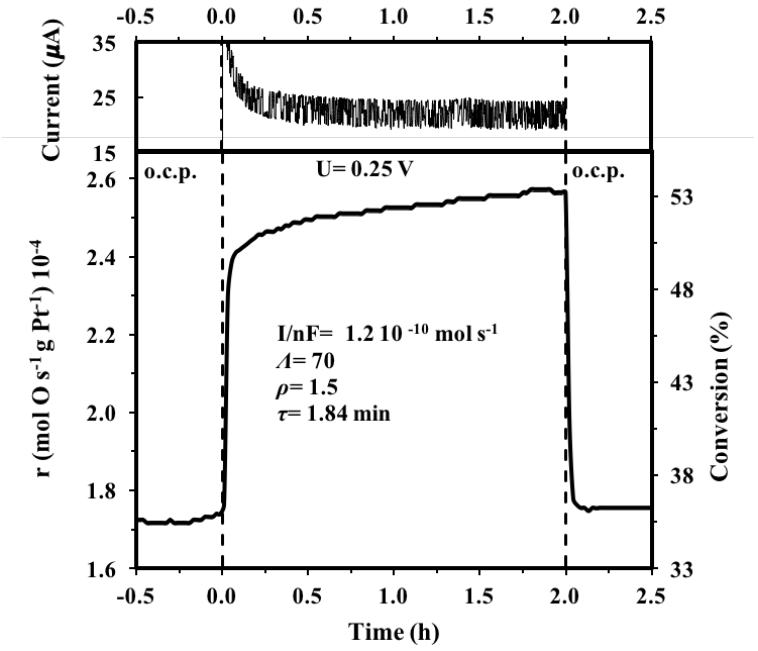

(a)

Figure 5.2 (Continuned ext page)

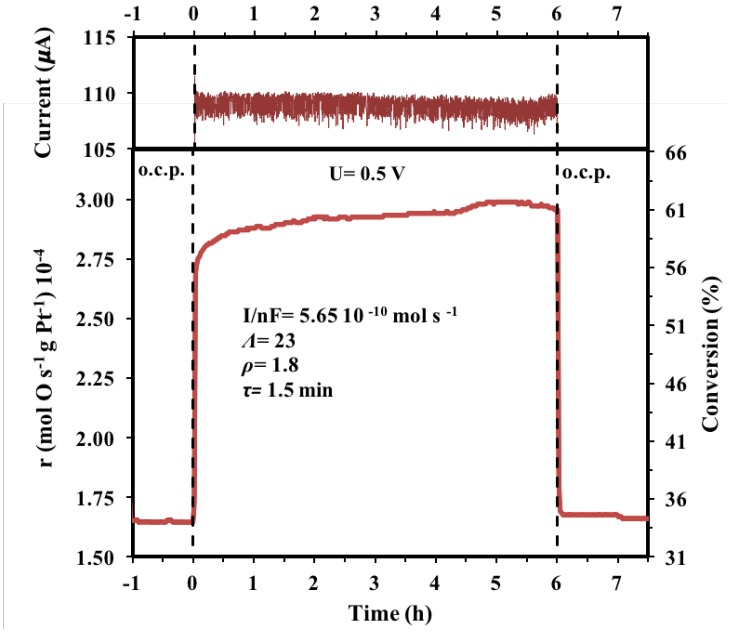

(b)

Figure 5.2: Transient rate response of the free-standing Pt NPs and corresponding current to a step change in applied potential of (a) U = 0.25 V and (b) U = 0.5 V; o.c.p.: open-circuit potential. Conditions: T = 350 °C, 3 KPa of O_2 and 0.012 kPa of C_2H_4, flow rate of 100 mL min^{-1}.

Figure 5.3 presents transient effect of applied constant current on the catalytic rate, as well as the corresponding enhancement ratio, Faradaic efficiency. The results show an increase in the catalytic rate and an increase in the enhancement ratio in function of the current. The apparent Faradaic efficiency was at its highest value at 15 μA, the lowest current at which an increase in the catalytic rate was detected. In addition, upon the positive current application, the time to reach 63 % of the steady-state closed-circuit value, denoted by relaxation time τ [16], was the fastest at 100 μA (1.3 min) and the slowest at 15 μA (6.0 min); τ is considered to be the time required to fill the catalyst surface with a monolayer of promoting oxygen ions ($O^{\delta-}$) [16]; using this time τ, the active catalytic surface area N_G (mol) can be found as follows:

$$N_G = \frac{I\tau}{2F} \qquad 5\text{-}2$$

The average active surface area of Pt was found equal to 3.13 10^{-8} mol of Pt (or mol of O); resulting in a 6.1 % dispersion. The low dispersion value could be due to imperfect electrical contact between the gold mesh and NPs.

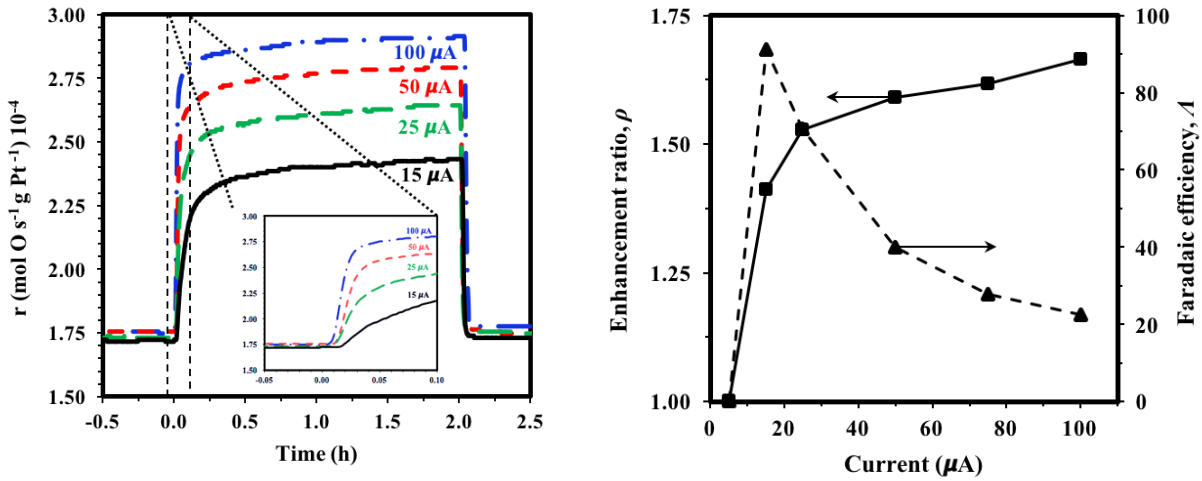

(a) (b)

Figure 5.3: (a) Transient rate response of the free-standing Pt NPs to applied constant current, and (b) the corresponding enhancement ratio, ρ and Faradaic efficiency, Λ as a function of applied constant current. Conditions: idem.

Furthermore, application of negative polarization either in potentiostatic or galvanostatic mode (not shown here) did not lead to noticeable reaction rate changes. This indicates that Pt NPs on YSZ show purely electrophobic behavior, i.e., reaction rate increases with an increase in the work function of the catalyst due to backspillover of $O^{\delta-}$ from YSZ support [7]. This is in agreement with previous studies on Pt catalyst-electrodes deposited on YSZ for ethylene oxidation [16,38,47–49].

Figure 5.4 showed that increasing the partial pressure of ethylene results in an increase of the oxidation rate under open- and closed-circuit (o.c. and c.c.). Both ρ and Λ, increased with increasing p (C_2H_4), indicating improved reaction kinetics at higher p (C_2H_4) / p (O_2) ratios.

When decreasing the temperature from 350 to 225 °C, the potentiostatic polarization at 0.5 V resulted in a decrease in the current flow from 26 to 2 μA. Figure 5.5 shows that despite the very small current at the lower temperatures, an increase in the ethylene oxidation rate was still noticed and the apparent Faradaic efficiency was at its most at 250 °C (i.e., greater than 400) and decreased slightly at 225 °C due to reduction in the thermal migration of oxygen because of the low conductivity at that low of a temperature.

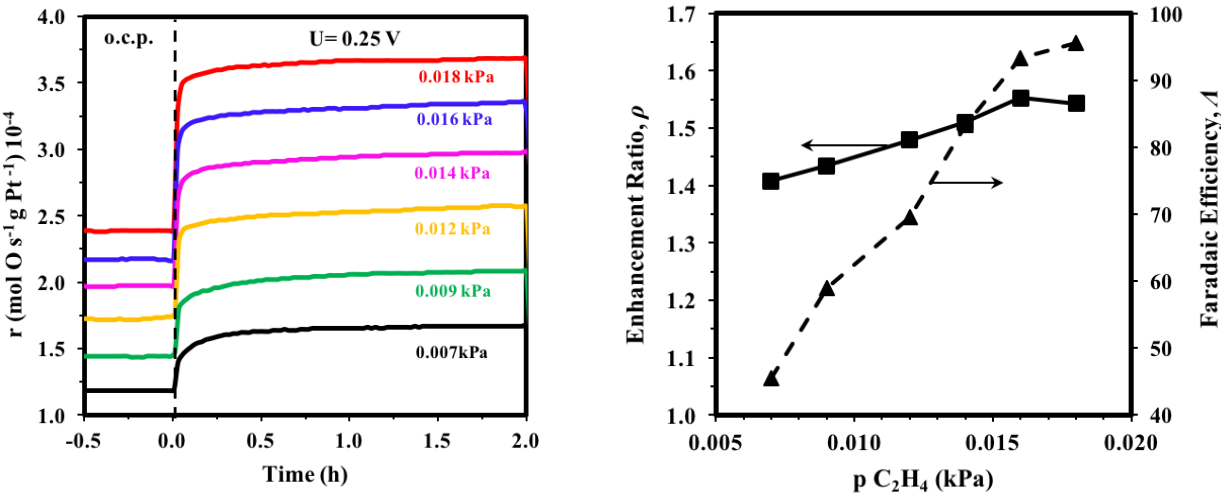

(a) (b)

Figure 5.4: (a) Transient rate response of the free-standing Pt NPs to a step change in applied potential, U= 0.25 V as a function of ethylene partial pressure, and (b) corresponding rate enhancement ratio and Faradaic efficiency. Conditions: T = 350 °C, 3 kPa of O_2 and various partial pressure of C_2H_4 as indicated in the figure, flow rate of 100 mL min^{-1}.

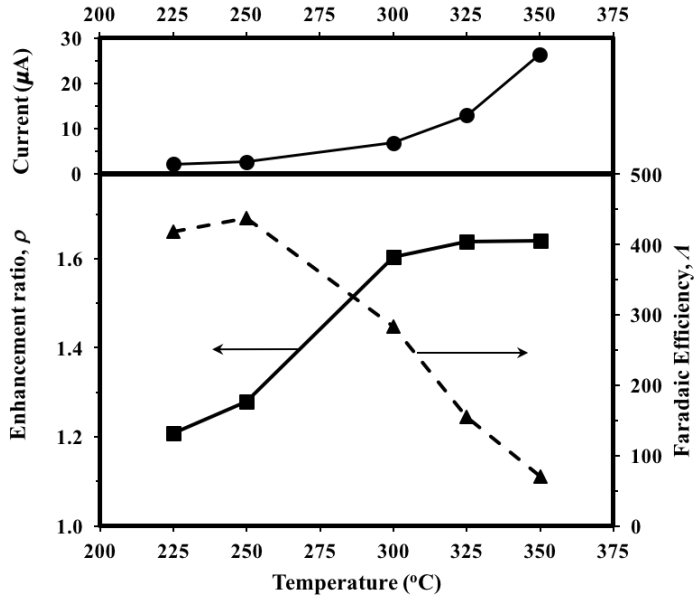

Figure 5.5: Enhancement ratio and Faradaic efficiency (bottom) and corresponding current (top) as a function of temperature for free-standing Pt NPs at U = 0.5 V. Conditions: 3 kPa of O_2 and 0.012 kPa of C_2H_4, flow rate of 100 mL min^{-1}.

5.3.3. Electrochemical promotion of free-standing RuO_2 NPs

Figure 5.6 shows the transient effect of constant potential, 1.5 V, application on the rate of ethylene oxidation, the corresponding conversion and current for RuO_2 NPs at 350 °C. RuO_2 NPs required six-times higher potential than for Pt, i.e., 0.25 V to reach a similar rate of current flow

(i.e., ~25 μA), or in other words, to allow similar flow of oxygen ions from the electrolyte (~1.37. 10^{-10} mol O/s). This oxygen flow allowed a significant and reversible electrochemical promotion with enhancement ratio of 1.45. The corresponding Faradaic efficiency value was 40 compared to 70 for Pt at 0.25 V. The lower Faradaic efficiency is related to the lower intrinsic capability of ruthenium to adsorb ethylene since the ethylene conversion was 25 % in presence of free-standing RuO_2 NPs compared to ~35 % in the presence of Pt NPs, resulting in a lower absolute increase in oxidation rate under polarization.

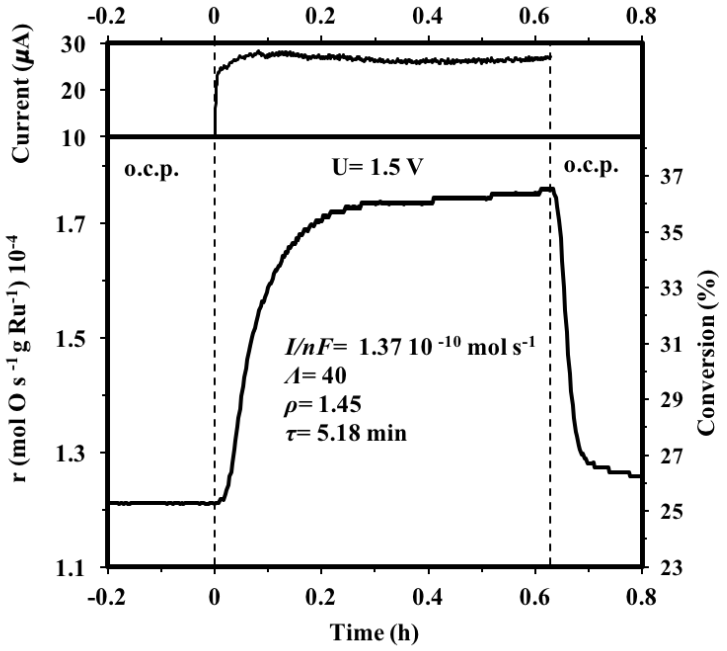

Figure 5.6: Transient rate response of the free-standing RuO_2 NPs to a step change in applied potential, U =1.5V (bottom) and corresponding current (top). Conditions: T = 350 °C, 3 kPa of O_2 and 0.012 kPa of C_2H_4, flow rate of 100 mL min^{-1}.

Figure 5.7 shows the effect of the applied current on the catalytic rate and corresponding ρ and Λ values (Figure 5.7b). Similarly to Figure 5.3, the catalytic rate in Figure 5.7 increased as a function of current, so did the enhancement ratio. The apparent Faradaic efficiency was at its highest value at 25 μA, marking that 45 mol of gaseous oxygen were reacting with ethylene for each mol of ionic oxygen pumped from the electrolyte. The maximum Faradaic efficiency was half of that reached in the case of Pt NPs (at 15 μA). The relaxation time τ decreased significantly between a current of 15 and 30 μA and was almost similar up to a current of 100 μA. Using Equation 5-1, the active catalytic surface area is 5.0 10^{-8} mol Ru and the dispersion of Ru was found to be 5.1 %, explaining the lower catalytic rate than that of Pt NPs.

In addition, the case of cathodic polarization (i.e., -100 μA) is shown in Figure 5.7 to present the insignificant variation in the catalytic rate when a negative polarization is applied. Therefore, RuO_2/YSZ showed purely electrophobic behavior, i.e., reaction rate increase under positive polarization similar to Pt/YSZ and previous studies on ruthenium [16,38,47–49]. Finally, the approach to steady-state upon the positive current application was marked by the time τ and was shown to be slower than that in the case of Pt for all current values, but it was always inversely proportional to current value (decreased from 8.9 to 3.0 min when current increased from 30 to 75 μA).

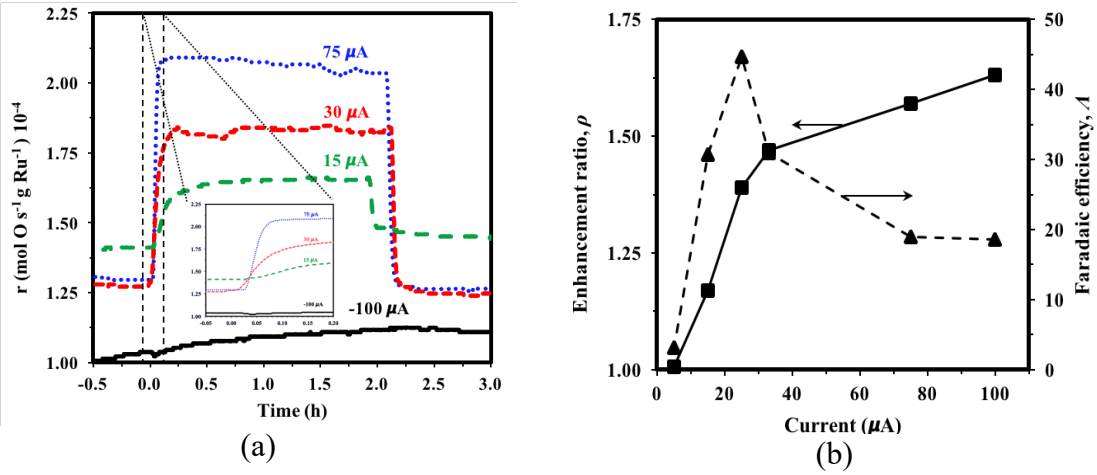

Figure 5.7: (a) Transient rate response of the free-standing RuO_2 NPs to applied constant current and (b) enhancement ratio, ρ and Faradaic efficiency, Λ as a function of applied constant current. Conditions: idem.

Figure 5.8 shows that the conversion increased in function of partial pressure and was more significant in ratio at the lower partial pressure of C_2H_4, unlike what we saw for Pt values. This resulted in a steady-value of Faradaic efficiency in function of partial pressure, except at 0.007 kPa.

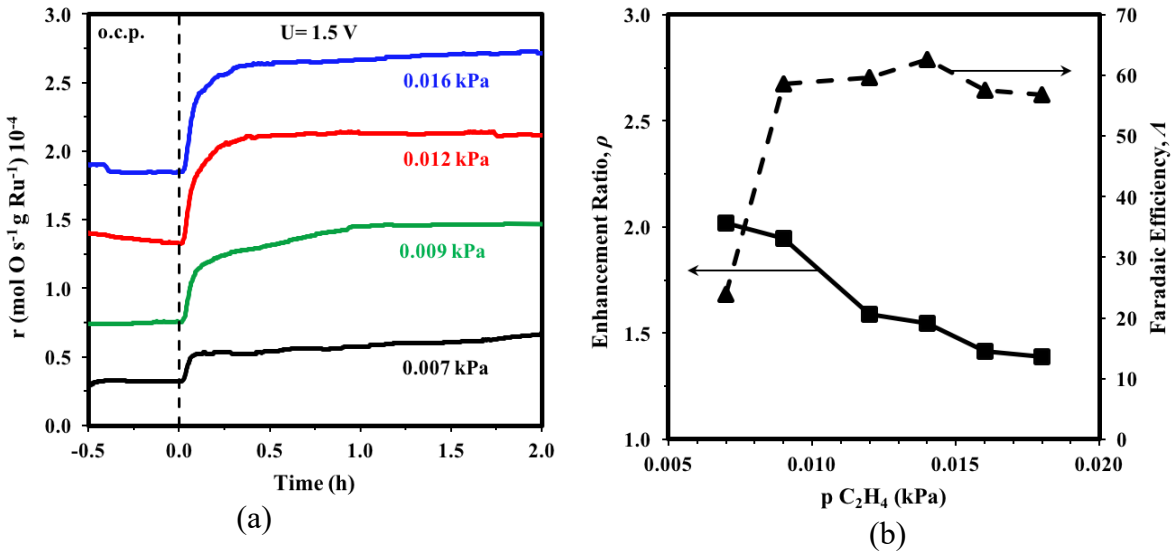

Figure 5.8: (a) Transient rate response of the free-standing RuO_2 NPs to a step change in applied potential, U= 1.5 V as a function of ethylene partial pressure, and (b) corresponding rate enhancement ratio and Faradaic efficiency. Conditions: T = 350 °C, 3 kPa of O_2 and various partial pressure of C_2H_4 as indicated in the figure, flow rate of 100 mL min^{-1}.

5.3.4. Comparison to previous EPOC studies

Table 5-1 compares EPOC of Pt and RuO_2 NPs to previous studies carried out on Pt and RuO_2 catalyst-electrodes for ethylene oxidation using YSZ solid-electrolyte. The table depicts where our results fall in comparison with previous experiments. It can be noted that the metal loading is the lowest in the present work, which is important from the practical point of view; however, the enhancement ratio value is the lowest if compared to other studies carried out with continuous catalyst electrodes. This is due to the high catalytic activity of the free-standing Pt and RuO_2 nanoparticles at open-circuit up to 36 %. The highest enhancement ratio of 95 was reported by Koutsodontis *et al.* for Pt electrode prepared by paste coating (0.2 – 1.1µm thickness) [47]. The open circuit conversion was quite low at 0.1 % while reached 55 % under EPOC. Papaioannou *et al.* studied EPOC effect on Pt electrode prepared by sputtering and showed higher enhancement ratio of 67, however, the actual conversion value was low at 7.5 % compared to our closed-circuit value of 61 % for the same Pt loading [48]. For Ru catalysts, Constantinou *et al.*, reported, for the same metal loading (0.1 mg cm^{-2}), only 3 % conversion at 430 °C compared to 25 % at 350 °C in this work [38]. Moreover, both Pt and RuO_2 showed purely electrophobic behavior in agreement with previous studies [16,38,47–49], where only anodic polarization shows promotional effect on the catalytic rate.

Table 5-1: Summary of electrochemical promotion results of ethylene oxidation over Pt and Ru-based catalysts deposited YSZ solid-electrolyte.

Cata-lyst	Catalyst thickness	Loading/ mg cm^{-2}	Method of application	U/ I applied	T/ ºC	P_{C2H4}/ kPa	P_{O2}/ kPa	Flow rate/ $mLmin^{-1}$	Conversion before / after (%)	ρ	Λ	Ref.
Pt	5 µm	N/A	Paste coating	1 µA	370	0.36	4.62	100	1.06 / 28	27	74000	[16]
Pt	0.2-1.1 µm	0.4-1.9	Paste coating	2 V	280	0.19	8.2	210	0.11 / 55	95	975	[47]
Pt	30 nm	0.125	Sputtering	270 µA	280	0.19	8.2	420	0.2 / 7.5	67	188	[48]
RuO_2	µm range	0.172	Thermal decomposition	30 V	360	0.1	12	175	4 / 8.3	2	N/A	[49]
RuO_2	µm range	0.098	Thermal decomposition	200 µA	430	2.2	0.9	100	3 / 32	11	170	[38]
Pt	nm range	0.10	Polyol method	0.5 V	350	0.012	3.0	100	34 / 61	1.8	23	This work
RuO_2	nm range	0.10	Polyol method	1.5 V	350	0.012	3.0	100	25 / 36	1.5	40	This work

Overall, the obtained results show that Pt and RuO_2 catalyst composed of very small nanoparticles with average size of 2.0 and 1.8 nm, respectively and low metal loading (0.1 mg cm^{-2}), can be efficiently electropromoted using positive polarization, i.e., by supplying $O^{\delta-}$ promoters to the surface-active sites, where catalytic ethylene oxidation takes place. The promotion of NPs interfaced with YSZ follows the mechanism and rules of electrochemical promotion used previously for these metals, solid-electrolyte and type of reaction [5–7].

5.3.5. Functional similarity of EPOC and MSI for Pt and RuO_2 NPs

The catalytic rate under o.c. and c.c. conditions of free-standing Pt and RuO_2 NPs were compared to the o.c. rate of the same NPs deposited on MIEC CeO_2 and TiO_2, and ionically conducting YSZ supports with a 1 wt.% loading. Both free-standing and supported NPs have the same total metal amount of 0.1 mg cm^{-2} and were tested in the same electrochemical cell (Figure B 3). The light-of-curves and reaction rate in function of ethylene partial pressure for all supported catalysts are shown in Figure B 4 and Figure B 5 in Appendix B. The catalytic activity of 1 wt.% Pt/YSZ, Pt/CeO_2 and RuO_2/CeO_2 for ethylene oxidation have been reported earlier [34,35,39]. The supported Pt NPs have high open- circuit catalytic rate (and high conversion > 50 %) at 350 ^oC and therefore electrochemical promotion was not possible for Pt/YSZ and Pt/TiO_2. Dole *et al.* reported the enhancement of the catalytic activity of highly dispersed nanoparticles of RuO_2 supported on CeO_2 as a result of prolonged negative (cathodic) polarization for 6h. The ρ value up to 2.0 was observed and the effect was attributed to the partial reduction of Ce(IV) to Ce(III). The partially reduced CeO_x showed stronger interaction with RuO_2 nanoparticles and beneficial effect on its catalytic activity. At the same time, positive polarization did not lead to any significant reaction rate increase because of RuO_2/CeO_2 catalyst was already in a promoted state via MSI.

Figure 5.9a and b show the reaction rate as a function of ethylene partial pressure for free-standing Pt and RuO_2, as well as for the supported catalysts. The error bar shows the variation in the rate between the repeated experiments (new catalyst layer on YSZ). All supported Pt and RuO_2 nanoparticles exhibit higher reaction rate than free-standing Pt due to better dispersion of NPs on powder support (Figure 5.1) and MSI effect. As can be seen under positive potentiostatic polarization, free-standing NPs approach the rate values for the supported catalysts confirming the similarity of EPOC and MSI effects, which is in particular

striking for RuO_2 NPs. The order of the catalytic rate is Pt (o.c.) << Pt (at U = +0.5V) < Pt/YSZ ≤ Pt/TiO_2 < Pt/CeO_2 and Ru (o.c) << Ru (at U= +1.5V) ≈ Ru/CeO_2 ≈ Ru/TiO_2 ≤ Ru/YSZ. The slightly inferior reaction rate values under EPOC could be related to the difficulty of achieving optimal electrical contact between NPs and the current collector (Au mesh) in the present cell configuration, which could be further optimized for future studies.

From Figure 5.9c and d, one can see the similarity in the enhancement ratio of Pt and RuO_2 NPs using electrochemical promotion (ρ_{EPOC}) and metal-support interaction (ρ_{MSI}). As was shown in [35], the higher loading percentages resulted in lower catalytic rate due to the decrease of NPs dispersion over supports. This means that MSI with 1 wt.% loading is a best-case scenario for comparison with EPOC.

The similar ρ values for EPOC and MSI obtained with the same size NPs under polarization and by dispersing them on active, conductive supports is a confirmation of the functional similarity of the two phenomena in the presence of O^{2-} ionic conductivity in the support. The spontaneous migration of $O^{\delta-}$ in case of MSI could be thermally-induced to achieve an equilibrium in the electrochemical potential of electrons between the metal and the support (quantified by work function, WF (eV) [50]. According to the metal-semiconductor boundary layer theory, at thermodynamic equilibrium, the Fermi energy level of electrons of the two solids in contact is equal [51]. Both Pt and RuO_2 NPs have higher WF than the supports, because of their nanoscopic size and the fact that WF increases as nanoparticle size decreases [52]. For instance, bulk Pt has WF of 5.3 eV and can reach up to 9 eV for a single atom [52]. WF of bulk Ru is 4.71 eV [53] or 4.6 eV for bulk RuO_2 [54]; work function of supports is 4.69 eV for CeO_2 [55], 5.1 eV for YSZ [56] and 4.13 eV for stoichiometric, unreduced TiO_2 [57]. Upon intimate contact between a metal of high work function, with a semi-conducting oxide of lower work function, the formation of oxygen vacancies is promoted and electron equilibrium is established [58]. Electrons are distributed between the conduction band states of the oxides and the states available at the Fermi level of the metal resulting in the reduction of the semi-conductor and weakening of the catalyst-oxygen and strengthening of the catalyst-ethylene bond strength.

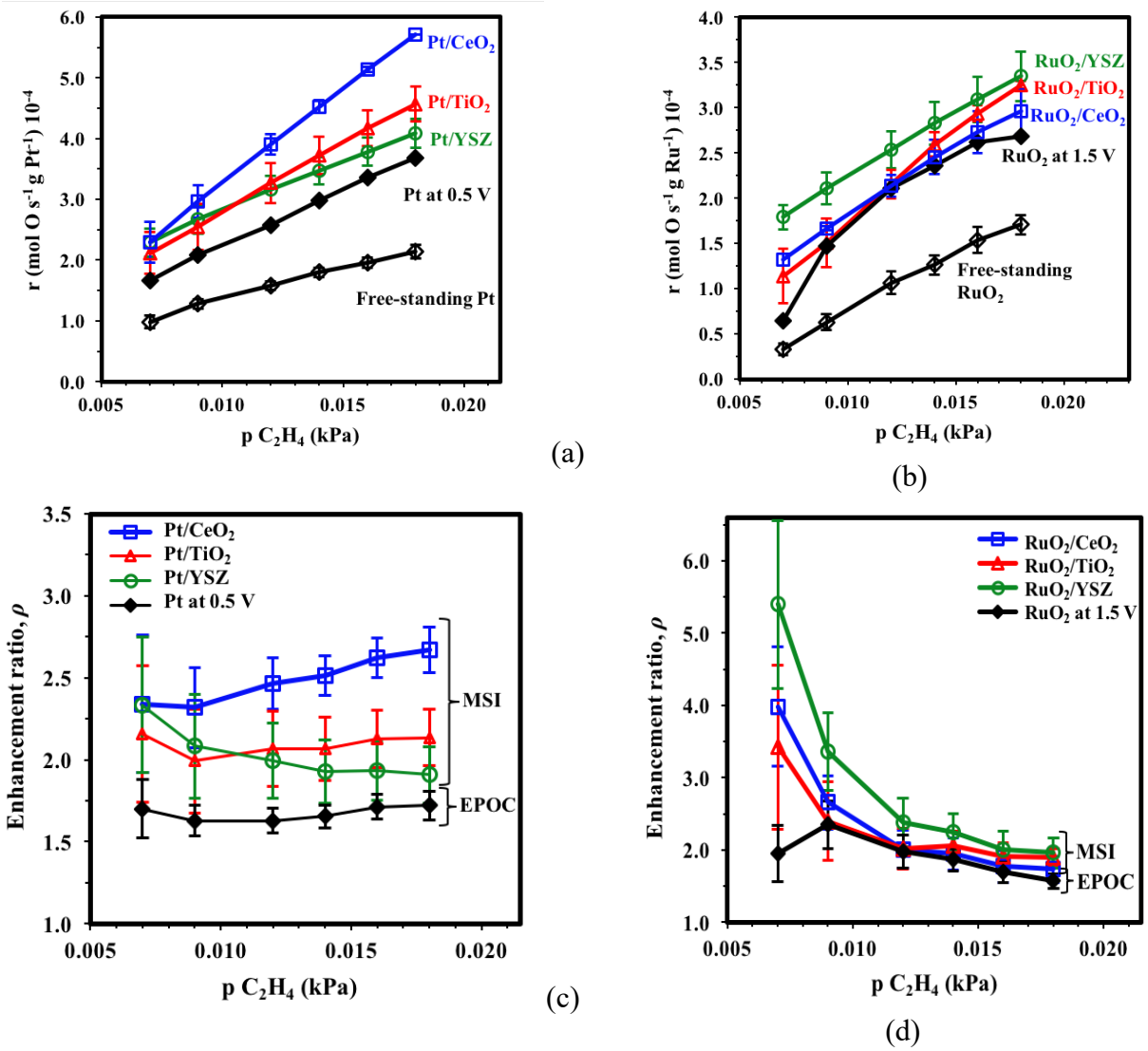

Figure 5.9: Reaction rate as a function of ethylene partial pressure for: (a) free-standing and supported Pt, (b) free-standing and supported RuO_2, and the corresponding enhancement ratio by EPOC and MSI for (c) Pt and (d) RuO_2. Conditions: T = 350 °C, 3 kPa of O_2 and various partial pressure of C_2H_4 as indicated in the figure, flow rate of 100 mL min^{-1}.

Therefore, the increase in the work function due to electrochemically induced migration and adsorption of $O^{\delta-}$ from the support (case of EPOC) or due to doping the Fermi level of the support (case of MSI) shows the mechanistic similarity between the two phenomena [50]. These results are a stepping-stone in further understanding and application of EPOC and MSI phenomena with NPs and could be of significant importance for practical application of EPOC as they show feasibility of electrochemical promotion of nanoparticles with low metal loading that form non-percolated deposit on the surface of YSZ solid-electrolyte.

5.4. Conclusions

Overall, the present work draws a parallel between electrochemical promotion of catalysis (EPOC) and metal-support interaction (MSI) phenomena with well-defined nanoparticles. It shows that Pt and RuO_2 NPs of ~2 nm average size can be efficiently promoted for ethylene complete oxidation by current/potential application or by dispersing NPs with a 1 wt.% loading on conducting supports, i.e., CeO_2, TiO_2 and YSZ. Upon an anodic polarization, the enhancement in the catalytic rate was at a highest of 66 % increase for Pt and 100 % for RuO_2. The Faradaic efficiency reached a maximum of 91 and 45 for Pt and RuO_2 NPs, respectively. The comparison of EPOC enhancement ratios (ρ_{EPOC}) to MSI ratio (ρ_{MSI}), shows very close values, with MSI enhancement being slightly higher than that of EPOC. The comparable enhancement ratio confirms the functional equivalence between the two phenomena. For MSI, one has a spontaneously driven and for EPOC, electrochemically controlled migration of $O^{\delta-}$ from the conducting support to the catalyst surface, thus leading to the remarkable modification of the catalytic properties of NPs.

References

[1] G. Ertl, H. Knozinger, J. Weitkamp, Handbook of Heterogeneous Catalysis, Wiley-VCH, Weinheim, 1997.

[2] G.A. Somorjai, Chemistry in two dimensions : surfaces, Cornell University Press, Ithaca, 1981.

[3] M.P. Kiskinova, Poisoning and promotion in catalysis based of surface science: concepts and experiments, 70th ed., Elsevier Science, Amsterdam, 1992.

[4] L.L. Hegedus, A.T. Bell, N.Y. Chen, W.O. Haag, J. Wei, R. Aris, M. Boudart, B.C. Gates, G.A. Somorjai, Catalyst Design-Progress and Perspectives, Wiley-Interscience, New York, 1988.

[5] C.G. Vayenas, S. Bebelis, C. Pliangos, S. Brosda, D. Tsiplakides, Electrochemical Activation of Catalysis: Promotion, Electrochemical Promotion, and Metal-Support Interactions, Springer, New York, 2001.

[6] C.G. Vayenas, S. Bebelis, S. Ladas, Dependence of catalytic rates on catalyst work function, Nature. 343 (1990) 625–627.

[7] S. Brosda, C.G. Vayenas, Rules and Mathematical Modeling of Electrochemical and Classical Promotion 2. Modeling, J. Catal. 208 (2002) 38–53.

[8] J. Nicole, D. Tsiplakides, C. Pliangos, X.E.E. Verykios, C. Comninellis, C.G.G. Vayenas, Electrochemical Promotion and Metal–Support Interactions, J. Catal. 204 (2001) 23–34.

[9] T. Mitsui, K. Tsutsui, T. Matsui, R. Kikuchi, K. Eguchi, Support effect on complete oxidation of volatile organic compounds over Ru catalysts, Appl. Catal. B Environ. 81 (2008) 56–63.

[10] S.H. Overbury, L. Ortiz-soto, H. Zhu, B. Lee, M.D. Amiridis, S. Dai, Comparison of Au catalysts supported on mesoporous titania and silica : Investigation of Au particle size effects and metal-support interactions, Catal. Letters. 95 (2004) 99–106.

[11] Z. Wang, B. Li, M. Chen, W. Weng, H. Wan, Size and support effects for CO oxidation on supported Pd catalysts, Sci. China Chem. 53 (2010) 2047–2056.

[12] K. Kimura, H. Einaga, Y. Teraoka, Preparation of highly dispersed platinum catalysts on various oxides by using polymer-protected nanoparticles, Catal. Today. 164 (2011) 88–91.

[13] A. Katsaounis, Recent developments and trends in the electrochemical promotion of catalysis (EPOC), J. Appl. Electrochem. 40 (2010) 885–902.

[14] M. Stoukides, C.G. Vayenas, The effect of electrochemical oxygen pumping on the rate and selectivity of ethylene oxidation on polycrystalline silver, J. Catal. 70 (1981) 137–146.

[15] C.G. Vayenas, Promotion, Electrochemical Promotion and Metal-Support Interactions: Their Common Features, Catal. Letters. 143 (2013) 1085–1097.

[16] S. Bebelis, C.G. Vayenas, Non-faradaic electrochemical modification of catalytic activity. 1. The case of ethylene oxidation on Pt, J. Catal. 118 (1989) 125–146.

[17] M. Marwood, C.G. Vayenas, Electrochemical promotion of a dispersed platinum catalyst, J. Catal. 178 (1998) 429–440.

[18] C.G.C.G. Vayenas, S. Bebelis, I. V. Yentekakis, H.-G. Lintz, Non-faradaic electrochemical modification of catalytic activity: A status report, Catal. Today. 11 (1992) 303–442.

[19] J. Nicole, C.H. Comninellis, Electrochemical promotion of IrO2 catalyst activity for the gas phase combustion of ethylene, J. Appl. Electrochem. 28 (1998) 223–226.

[20] X. Li, F. Gaillard, P. Vernoux, Investigations under real operating conditions of the electrochemical promotion by O2 temperature programmed desorption measurements, Top. Catal. 44 (2007) 391–398.

[21] C.G. Vayenas, S. Brosda, C. Pliangos, Rules and Mathematical Modeling of Electrochemical and Classical Promotion 1. Reaction Classification and Promotional Rules, J. Catal. 203 (2001) 329–350.

[22] S. Ntais, R.J. Isaifan, E.A. Baranova, An X-ray photoelectron spectroscopy study of platinum nanoparticles on yttria-stabilized zirconia ionic support: Insight into metal support interaction,

Mater. Chem. Phys. 148 (2014) 673–679.
[23] S.J. Tauster, S.C. Fung, R.L. Garten, Strong Metal-Support Interactions. Group 8 Noble Metals Supported on TiO2, J. Am. Chem. Soc. 100 (1978) 170–175.
[24] S.J. Tauster, Strong metal-support interactions, Acc. Chem. Res. 20 (1987) 389–394.
[25] Y.W. Chung, Y.B. Zhao, Evidence for the migration of MnO upon reduction of Ni-MnOx and its effects on CO chemisorption, in: R.T.K. Baker, S.J. Tauster, J.A. Dumesic (Eds.), Strong-Metal Support Interact., American Chemical Society, 1986.
[26] P. Vernoux, L. Lizarraga, M.N. Tsampas, F.M. Sapountzi, A. De Lucas-Consuegra, J.L. Valverde, S. Souentie, C.G. Vayenas, D. Tsiplakides, S. Balomenou, E.A. Baranova, Ionically conducting ceramics as active catalyst supports, Chem. Rev. 113 (2013) 8192–8260.
[27] G. Pacchioni, J.R. Lomas, F. Illas, Electric field effects in heterogeneous catalysis, J. Mol. Catal. A Chem. 119 (1997) 263–273.
[28] M.A. Fortunato, A. Princivalle, C. Capdeillayre, N. Petigny, C. Tardivat, C. Guizard, M.N. Tsampas, F.M. Sapountzi, P. Vernoux, Role of lattice oxygen in the propane combustion over Pt/yttria-stabilized zirconia : isotopic studies, Top. Catal. 57 (2014) 1277–1286.
[29] M.N. Tsampas, F.M. Sapountzi, A. Boréave, P. Vernoux, Isotopical labeling mechanistic studies of electrochemical promotion of propane combustion on Pt/YSZ, Electrochem. Commun. 26 (2013) 13–16.
[30] A. Katsaounis, Z. Nikopoulou, X.E. Verykios, C.G. Vayenas, Comparative isotope-aided investigation of electrochemical promotion and metal-support interactions: 2. CO oxidation by 18O2 on electropromoted Pt films deposited on YSZ and on nanodispersed Pt/YSZ catalysts, J. Catal. 226 (2004) 197–209.
[31] A. Katsaounis, Z. Nikopoulou, X.E. Verykios, C.G. Vayenas, Comparative isotope-aided investigation of electrochemical promotion and metal–support interactions 1. 18O2 TPD of electropromoted Pt films deposited on YSZ and of dispersed Pt/YSZ catalysts, J. Catal. 222 (2004) 192–206.
[32] R.J. Isaifan, H.A.E. Dole, E. Obeid, L. Lizarraga, P. Vernoux, E.A. Baranova, Metal-support interaction of Pt nanoparticles with ionically and non-ionically conductive supports for CO oxidation, Electrochem. Solid-State Lett. 15 (2012) E14.
[33] R.J. Isaifan, E.A. Baranova, Catalytic electrooxidation of volatile organic compounds by oxygen-ion conducting ceramics in oxygen-free gas environment, Electrochem. Commun. 27 (2013) 164–167.
[34] R.J. Isaifan, S. Ntais, M. Couillard, E.A. Baranova, Size-dependent activity of Pt/yttria-stabilized zirconia catalyst for ethylene and carbon monoxide oxidation in oxygen-free gas environment, J. Catal. 324 (2015) 32–40.
[35] H.A.E. Dole, A. Costa, M. Couillard, E.A. Baranova, Quantifying metal support interaction in ceria-supported Pt, PtSn and Ru nanoparticles using electrochemical technique, J. Catal. 333 (2016) 40–50.
[36] I. Constantinou, D. Archonta, S. Brosda, M. Lepage, Y. Sakamoto, C. Vayenas, Electrochemical promotion of NO reduction by C3H6 on Rh catalyst-electrode films supported on YSZ and on dispersed Rh/YSZ catalysts, J. Catal. 251 (2007) 400–409.
[37] E.A. Baranova, A. Thursfield, S. Brosda, G. Fóti, C. Comninellis, C.G. Vayenas, Electrochemical promotion of ethylene oxidation over Rh catalyst thin films sputtered on YSZ and TiO2/YSZ supports, J. Electrochem. Soc. 152 (2005) E40–E49.
[38] I. Constantinou, I. Bolzonella, C. Pliangos, C. Comninellis, C.G. Vayenas, Electrochemical promotion of RuO2 catalysts for the combustion of toluene and ethylene, Catal. Letters. 100 (2005) 125–133.
[39] H.A.E. Dole, E.A. Baranova, Ethylene oxidation in an oxygen deficient environment : Why ceria is an active support ?, ChemCatChem. 8 (2016) 1977–1986.
[40] D. Tsiplakides, S. Balomenou, Milestones and perspectives in electrochemically promoted catalysis, Catal. Today. 146 (2009) 312–318.

[41] A.D. Frantzis, S. Bebelis, C.G. Vayenas, Electrochemical promotion (NEMCA) of CH4 and C2H4 oxidation on Pd/YSZ and investigation of the origin of NEMCA via AC impedance spectroscopy, Solid State Ionics. 136–137 (2000) 863–872.
[42] H.A.E. Dole, E.A. Baranova, Implementation of Nanostructured Catalysts in the Electrochemical Promotion of Catalysis, in: M. Aliofkhazraei, H.A.S. Makhlouf (Eds.), Handb. Nanoelectrochemistry, Springer International Publishing, Cham, 2015: pp. 1–26.
[43] E.A. Baranova, C. Bock, D. Ilin, D. Wang, B. MacDougall, Infrared spectroscopy on size-controlled synthesized Pt-based nano-catalysts, Surf. Sci. 600 (2006) 3502–3511.
[44] R.J. Isaifan, E.A. Baranova, Effect of ionically conductive supports on the catalytic activity of platinum and ruthenium nanoparticles for ethylene complete oxidation, Catal. Today. 241 (2015) 107–113.
[45] I.R. Gibson, G.P. Dransfield, J.T.S. Irvine, Sinterability of commercial 8 mol % yttria-stabilized zirconia powders and the effect of sintered density on the ionic conductivity, J. Mater. Sci. 33 (1998) 4297–4305.
[46] Y.M. Hajar, H.A. Dole, M. Couillard, E.A. Baranova, Investigation of heterogeneous catalysts by electrochemical method: Ceria and titania supported iridium for ethylene oxidation, ECS Trans. 72 (2016) 161–172.
[47] C. Koutsodontis, A. Katsaounis, J.C. Figueroa, C. Cavalca, C. Pereira, C.G. Vayenas, The effect of catalyst film thickness on the magnitude of the electrochemical promotion of catalytic reactions, Top. Catal. 38 (2006) 157–167.
[48] E.I. Papaioannou, S. Souentie, F.M. Sapountzi, A. Hammad, D. Labou, S. Brosda, C.G. Vayenas, The role of TiO2 layers deposited on YSZ on the electrochemical promotion of C2H4 oxidation on Pt, J. Appl. Electrochem. 40 (2010) 1859–1865.
[49] S. Wodiunig, F. Bokeloh, J. Nicole, C. Comninellis, Electrochemical Promotion of RuO2 Catalyst Dispersed on an Yttria-Stabilized Zirconia Monolith, Electrochem. Solid-State Lett. 2 (1999) 281–283.
[50] C.G. Vayenas, G.E. Pitselis, Mathematical Modeling of Electrochemical Promotion and of Metal - Support Interactions, J. Ind. Eng. Chem. Res. (2001) 4209–4215.
[51] R.T. Tung, Electron transport at metal-semiconductor interfaces: General theory, Phys. Rev. B. 45 (1992) 13509–13523.
[52] E. Roduner, Size matters: why nanomaterials are different, Chem. Soc. Rev. 35 (2006) 583.
[53] W.M. Haynes, ed., CRC Handbook of Chemistry and Physics, CRC/ Taylor & Francis, Boca Raton, 2014.
[54] A.J. Hartmann, M. Neilson, R.N. Lamb, K. Watanabe, J.F. Scott, Ruthenium oxide and strontium ruthenate electrodes for ferroelectric thin-films capacitors, Appl. Phys. A Mater. Sci. Process. 70 (2000) 239–242.
[55] S.S. Warule, N.S. Chaudhari, B.B. Kale, K.R. Patil, P.M. Koinkar, M.A. More, R. Murakami, Organization of cubic CeO2 nanoparticles on the edges of self assembled tapered ZnO nanorods via a template free one-pot synthesis : significant cathodoluminescence and field emission properties, J. Mater. Chem. 22 (2012) 8887–8895.
[56] D. Tsiplakides, C.G. Vayenas, Electrode work function and absolute potential scale in solid-state electrochemistry, J. Electrochem. Soc. 148 (2001) E189–E202.
[57] A. Imanishi, E. Tsuji, Y. Nakato, Dependence of the Work Function of TiO2 (Rutile) on Crystal Faces , Studied by a Scanning Auger Microprobe, J. Phys. Chem. C. 2 (2007) 2128–2132.
[58] N. Acerbi, S.C. Tsang, S. Golunski, P. Collier, A practical demonstration of electronic promotion in the reduction of ceria coated PGM catalysts., Chem. Commun. (2008) 1578–1580.

Chapter 6 Atomic Layer Deposition of Highly Dispersed Pt-nanoparticles on High Surface Area Electrode Backbone for Electrochemical Promotion of Catalysis

Y. Hajar, V. Di Palma, V. Kyriakou, M.A. Verheijen, E.A. Baranova, P. Vernoux, W.M.M. Kessels, M. Creatore, M.C.M. van de Sanden and M. Tsampas, Electrochem. Commun. 84 (2017) 40–44.

A novel catalyst design for electrochemical promotion of catalysis (EPOC) is proposed for overcoming the main bottlenecks that limit EPOC commercialization, i.e., low dispersion and surface area of metal catalysts. We have increased surface area by using a porous composite electrode backbone made of $(La_{0.8}Sr_{0.2})_{0.95}MnO_{3-\delta}/Ce_{0.9}Gd_{0.1}O_{1.95}$ *(LSM/GDC). Highly dispersed Pt nanoparticles with an average diameter of 6.5 nm have been deposited on LSM/GDC by atomic layer deposition (ALD). This novel design offers, for the first time, a controllable and reproducible way for the fabrication of EPOC catalysts. The performance of the bare electrode backbone shows negligible activity for propane oxidation, while in the presence of Pt-nanoparticles a high catalytic activity is obtained above 200 °C. The performance of the Pt loaded LSM/GDC catalyst was significantly improved by application of small currents (I < 500 μA), leading to 27-33% increase as a function of the open circuit catalytic rate, with apparent Faradaic efficiency values from 1000 to 3860 % at 300 °C. Our results point out to EPOC as valid approach to enhance the catalytic activity of nano-structured catalysts.*

6.1. Introduction

The approach of electrochemical promotion of catalysis (EPOC) refers to the pronounced, reversible and controlled changes in catalytic properties (activity and selectivity) upon electrical polarization [1-4]. Since the discovery of the effect [5], more than 100 different catalytic systems have been electrochemically promoted on various metal catalysts supported on different ionic conductors [1-6].

In EPOC studies, an electrochemical cell is employed, in which one of the electrodes is the catalyst for the reaction under study. By controlling the polarization, ions can be pumped to or away from the catalyst, changing its work function and thus its catalytic properties [1-6]. Despite the apparent advantages of this system, such as *in-situ* controlling the coverage of the promoting ions, EPOC has not yet been applied in industry, mainly due to the much lower activity per catalytic mass, than the classic nano-dispersed powders [2,7-12]. Therefore, in the

last few years, EPOC research has been focused on overcoming this issue, which will bring the concept closer to scale-up [2,7-17].

The most promising EPOC catalyst design has been reported by Kambolis *et al.*, in which Pt nanoparticles have been deposited by wet impregnation into the porosity of a LSCF/GDC ($La_{0.6}Sr_{0.4}Co_{0.2}Fe_{0.8}O_{3-\delta}/Ce_{0.9}Gd_{0.1}O_{1.95}$) electrode [10]. This design is inspired by solid oxide electrolyte cells (SOEC) [18] and offers a higher surface area in the porosity of LSCF/GDC than conventional pure metallic films. In addition, LSCF plays mainly the role of electronic conductor and GDC the ionic conductor [19], so their combination provides the two functionalities that are important for electrocatalysis [1-4]. The aforementioned approach has resulted in highly dispersed Pt nanoparticles of 3-20 nm with average size of 8 nm. However, wet impregnation constitutes a poor technique in terms of reproducibility and control of the particle load and its size distribution. Thus, in this study we propose a more reliable deposition method, i.e. atomic layer deposition (ALD) in order to overcome the above limitations.

ALD is a thin film deposition technique based on the chemical reaction of gas phase species on a solid surface. ALD is currently being used commercially by the semiconductor industry and thin-film magnetic head industry. Recently, ALD has raised interest from new application areas, such as photovoltaics and organic electronics. It is performed by the sequential exposure of the substrate to two (or more) different gas species separated in time by purging steps. Each gas species reacts with the substrate up to saturation, through a self-limiting reaction mechanism. Because of its self-limiting nature, the main advantages of ALD are the control of film thickness at atomic scale, high conformity with surface features and high reproducibility [20-26]. On most metal oxides, ALD of a metal generally starts with the growth of small islands (i.e. nanoparticles) and many ALD cycles are required to obtain a film completely closed. Therefore, ALD is ideal for accessing and decorating the entire volume of our porous electrode backbone with Pt-nanoparticles.

Along these lines, the aim of this study is to investigate the electro-promotion of propane oxidation over highly dispersed Pt nanoparticles prepared by ALD. The electrode backbone in which Pt nanoparticles are deposited is a porous $(La_{0.8}Sr_{0.2})_{0.95}MnO_{3-\delta}/Ce_{0.9}Gd_{0.1}O_{1.95}$ (LSM/GDC) composite, which offers mixed ionic-electronic conductivity.

100 Pt ALD cycles were selected based on literature findings of Pt deposition on flat Al_2O_3 substrates where 100 cycles resulted in an average size of 4.5 nm of Pt-nanoparticles [22].

6.2. Experimental

6.2.1. Cell preparation and characterization.

Two commercial partial cells (FuelCellMaterials) with a 50 μm LSM/GDC composite electrode (50%-50%, 17 mm diameter) deposited on a 150 μm Hionic^{TM} electrolyte support (20 mm diameter) were employed in the present study. One was used as a reference cell, while the second was dedicated to the Pt ALD case study.

Two gold films were deposited on the opposite side of the Hionic^{TM} pellet, in order to act as counter and reference electrodes, respectively. Gold was selected due to its negligible catalytic activity in propane oxidation, as verified through blank experiments under experimental conditions. An electrochemical workstation Voltalab PGP 201 (Radiometer) was used in order to apply and measure both potential and current. The catalyst potential ΔU_{WR} was measured between the working electrode Pt-LSM/GDC and the reference electrode (Au).

ALD of Pt on the porous LSM/GDC was performed using a home-made deposition system described in detail elsewhere [24]. The base pressure of the reactor is $<10^{-6}$ mbar. $MeCpPtMe_3$ (98% from Sigma Aldrich) was used as precursor and O_2 gas at 1 mbar as reactant. The precursor was contained in a stainless steel cylinder, heated at 30 ^{0}C, and brought into the reactor using Ar as carrier gas. The lines from the precursor to the reactor are heated at 50 ^{0}C and the reactor wall at 90 ^{0}C. The ALD recipe starts with 4 s of dosing of $MeCpPtMe_3$, then 3 s of Ar to purge the precursor line and 3 s of pumping down. Then O_2 gas is dosed for 10 s and afterwards the reactor is pumped down for 10 s. The deposition was carried out keeping the substrate holder at 300 ^{0}C. The ideal Pt ALD deposition on LSM/GDC procedure is shown in Figure 6.1a.

6.2.2. SEM and TEM microscopy

A cross-sectional sample for Transmission electron microscopy (TEM) analysis was made by means of standard focus ion beam (FIB) lift-out sample preparation and SEM images by an FEI Nova 600 Nanolab SEM/FIB. Prior to FIB milling a stack of protective layers was deposited in the FIB, consisting of SiO_2 and Pt. Subsequent TEM studies were performed using

a JEOL ARM 200 probe corrected TEM, operated at 200 kV, equipped with a 100 mm^2 Centurio SDD EDS detector.

6.2.3. Catalytic activity measurements

The design of the experimental setup has been described in detail elsewhere [6,13]. The reactant gasses were certified mixtures of 0.80, 5.0 and 99.999% for C_3H_8, O_2 and He (Air Liquide), respectively. Reactants and products analysis was carried out by online gas-chromatography (R3000 micro-GC SRA instruments) and IR spectroscopy (Horiba VA3000).

Under closed circuit, the cell-reactor could operate as an electrochemical oxygen "pump". Using an external power source, a current, I, can be imposed through the oxygen-ion (O^{2-}) conducting solid electrolyte, which corresponds to an oxygen-ion flux of I/2F. In order to quantify the EPOC, Vayenas and co-workers [1] have defined two dimensionless parameters apparent Faradaic efficiency, Λ, and rate enhancement ratio, ρ, as:

$$\Lambda=(r-r_o)/(I/nF) \qquad 6\text{-}1$$

$$\rho=r/r_o \qquad 6\text{-}2$$

where r is the close-circuit reaction rate (i.e. under polarization) and r_o is the open-circuit reaction rate (i.e. at I = 0) and I/nF is the imposed flux of O^{2-}, where n is the number of exchanged electrons.

6.3. Results and discussion

Analysis of Pt-nanoparticles deposited on the porous LSM/GDC is not a trivial task. In our previous work [10] we have employed an extractive replica technique for the TEM analysis of the Pt-nanoparticles, which involves electrode crushing and the dissolution of the electrode backbone in a hydrofluoric acid solution. In order to gain further insight on the Pt-distribution on the electrode backbone, we have conducted a TEM analysis on a cross-section of an electrode (after catalysis). Figure 6.1b,c illustrates SEM images of the electrode surface before and during FIB preparation of the TEM lamella. In Figure 6.1d a High Angle Annular Dark Field (HAADF)–Scanning TEM image of the entire TEM lamella is displayed. In this sample 3 areas of interest have been denoted as P1, P2 and P3. TEM images of these areas are shown in Figure 6.1e-g. The presence and distribution of the Pt particles can be clearly discerned. Because of the different inclinations of the grain surfaces with respect to the imaging direction, both vertical as well as lateral dimensions of the Pt particles can be imaged.

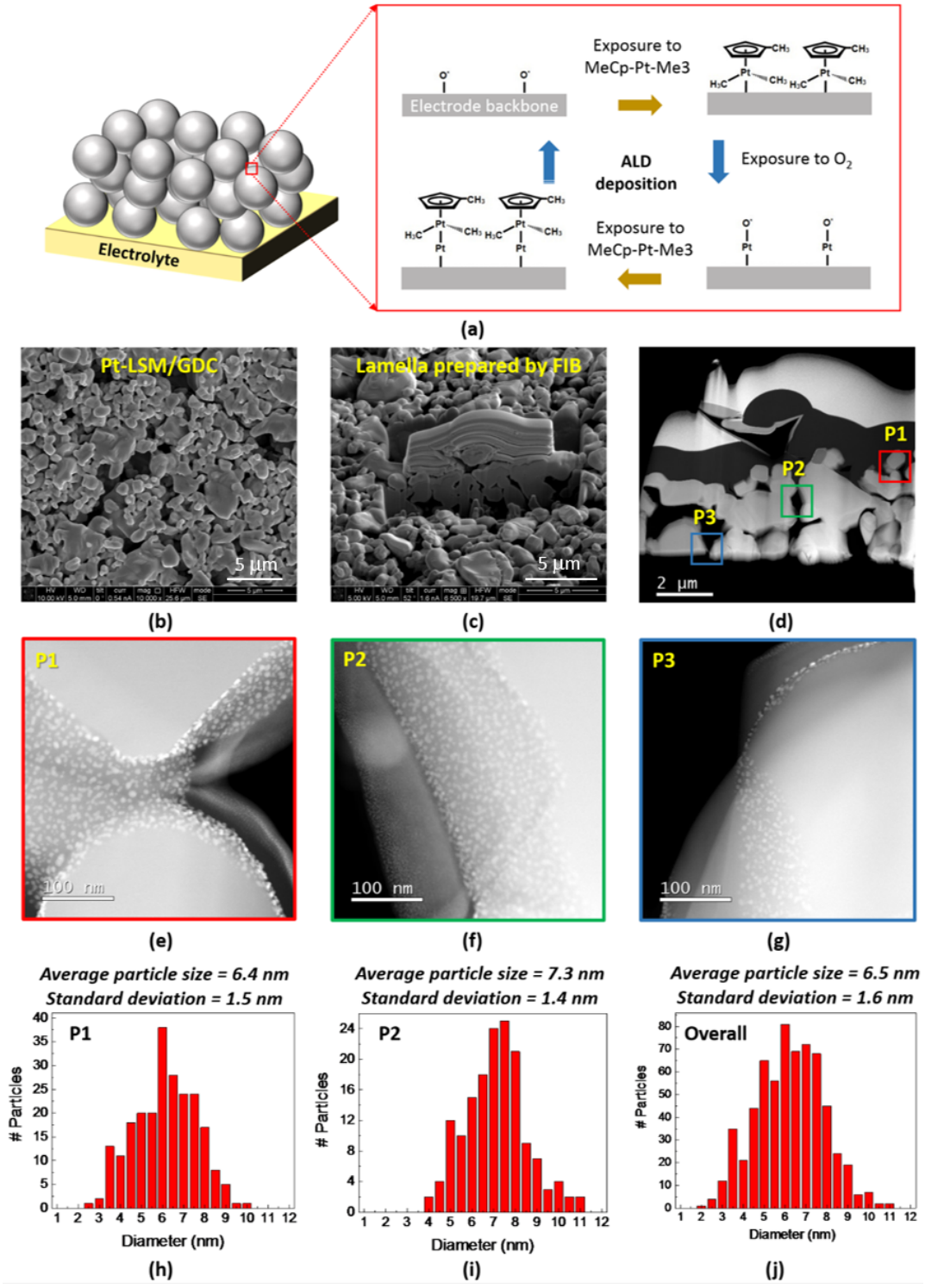

Figure 6.1: (a) Schematic representation of Pt deposition on the porous-LSM/GDC electrode backbone using ALD. (b) and (c) SEM images of the surface of the Pt loaded LSM/GDC, displaying the location of the cross-section. (d) HAADF-STEM image of the TEM lamella. The sample is covered by a stack of protective SiO_2/Pt layers. (e), (f) and (g) HAADF-STEM images of the Pt loaded LSM/GDC at three different points of interest. (h), (i) and (j) the corresponding size distribution at two points and in the overall lamella.

The use of ImageJ software allowed for the determination of Pt particle size distribution, which for P1 and P2 areas are presented in Figure 6.1 h and i and for the entire lamella area in Figure 6.1 j. The Pt-nanoparticles have a uniform distribution with a particle size range of 3-10 nm and 6.5 nm average size. Considering hemi-spherical Pt-nanoparticles, one can estimate a Pt-dispersion of 18.2% [27]. Particle size analysis was performed after catalytic evaluation. It is well known that the particle size might increase after catalysis due to agglomeration [28] Moreover, the nanoparticles growth is influenced by the substrate [22]. Taking into account this, the average Pt particle size of 6.5 nm for 100 ALD cycles is not too far from the reported value of 4.5 nm on Al_2O_3 [22].

In order to evaluate the catalytic performance of Pt-nanoparticles deposited on the LSM/GDC support, light-off experiments were performed on Pt-LSM/GDC (without involving a pre-reduction step for Pt) and bare LSM/GDC samples (Figure 6.1a). The temperature was increased from ambient to 425 ^oC with heating rate of 2 ^oC/min. Figure 6.2a shows the CO_2 production rate and the C_3H_8 conversion as a function of temperature. It can be seen that the LSM/GDC support was totally inactive for propane oxidation, while the addition of the Pt-nanoparticles strongly increased the catalytic activity. For the Pt-loaded sample, the conversion of propane was shown to increase rapidly after 200 ^oC and reach 23% at 425^oC.

The impact of various polarizations between -1.0 V and +1.0 V on the catalytic performance of the Pt-free LSM/GDC sample was investigated at 300°C, in which no modification of the propane conversion was observed. On the other hand, the Pt-loaded LSM/GDC exhibited a non-Faradaic behavior both under positive and negative polarizations. For instance, Figure 6.2b displays the impact of three consecutive steps of small positive currents (I = 300, 500 and 100 μA) on the catalytic rate of CO_2 production at 300 °C. The rate of propane oxidation gradually increases from 2.20 x 10^{-8} mol CO_2 s^{-1} and reaches a steady-state value at 2.88, 2.93 and 2.79 x 10^{-8} mol CO_2 s^{-1}, i.e. a rate enhancement of 131, 133 and 127% (ρ = 1.31, 1.33 and 1.27) respectively. The apparent Faradaic efficiency, Λ, was found to be 14.6, 10.0 and 38.6 for the three different applied currents, respectively. Thus, the enhancement of the catalytic activity is up to 38.6 times higher than that predicted by Faraday's law considering an electro-oxidation of propane with oxygen ions. After current interruption the reaction rate returned slowly to its open-circuit value, thus indicating the reversibility of EPOC.

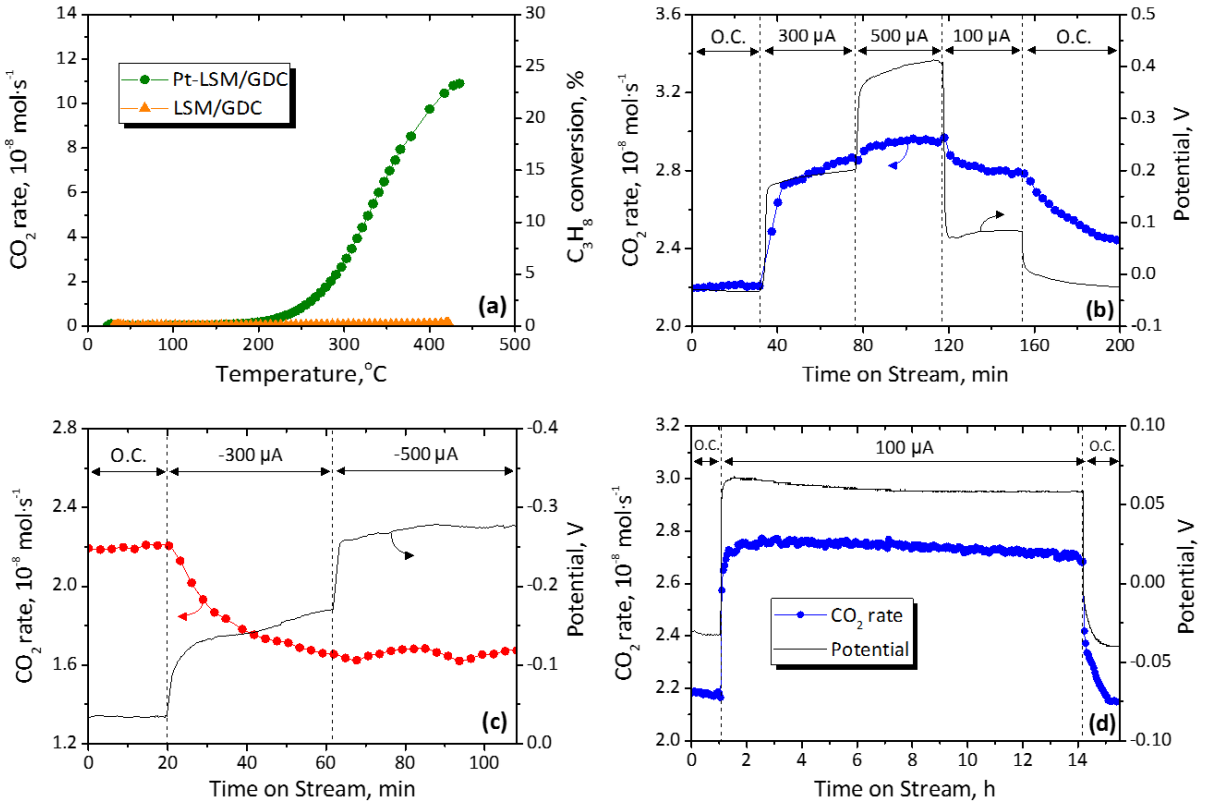

Figure 6.2: (a) Comparison of catalytic (open-circuit) performance for propane combustion for Pt-LSM/GDC, and bare LSM/GDC support. (b) Effect of positive and (c) negative currents on the potential and CO_2 formation. (d) EPOC stability test under positive polarization. P_{C3H8}/P_{O2} = 0.22 kPa/2.2 kPa, T=300 °C, F_t = 100 ml min^{-1} (NTP).

The increase of the reaction rate observed under positive polarization can be explained on the basis of the rules of electrochemical promotion [29]. It has been well-established that the supply of an electronegative ion, such as O^{2-}, to the catalyst-electrode surface, weakens the Pt-O bonds and therefore increases its work function [1-4]. The latter leads to the improved chemisorption of propane, which is known to be linked with the rate-determining step for propane oxidation [30,31]. After current interruption, the $O^{\delta-}$ promoters are consumed and therefore the catalyst returns with time to its initial state [29,30]. The moderate values of the rate enhancement ratio and Faradaic efficiency can be attributed to the pre-activation of the Pt-nanoparticles due to their size via self-driven spillover [1-3]. In addition, only a minor part of the applied current, between the LSM/GDC electrode and the counter electrode, most probably passes across the Pt nanoparticles.

On the other hand, the removal of O^{2-} from the Pt loaded sample (negative current application of -300 and -500 μA) had a poisoning effect on the catalyst, which also resulted in non-faradaic modification on the catalytic rate (Figure 6.2c) in good agreement with literature [10,29]. Interestingly, the poisoning effect was limited to 74% of the initial reaction rate and a Faradaic efficiency of 12.0. Application of even higher negative current (I = -500 μA) does not change the catalytic rate, this demonstrates a saturation effect, which can be attributed to current bypass from the Pt-nanoparticles. In other words, the higher negative current application cannot affect the performance of Pt-nanoparticles, since the extra current (i.e. oxygen pumping) takes place on Pt-free areas of the LSM/GDC surface.

Finally, the stability of the phenomenon was verified by long-term experiment of 100 μA current application (Figure 6.2d). The performance of the catalyst is relatively steady since the CO_2 production rate decrease slightly from 2.78 to 2.73 x 10^{-8} mol $CO_2 \cdot s^{-1}$ after 13 h of polarization. This indicates that possible agglomeration of Pt-nanoparticles during the TPO treatment at higher temperature (i.e. 425 ºC) has resulted in a stable catalyst configuration.

6.4. Conclusions

The combination of ALD with SOEC technological advances led to a Pt decorated composite electrode, which was successfully employed for the electropromotion of propane combustion. In the implemented design, the three functionalities (i.e. catalytic activity, electronic and ionic conductivity) needed for efficient EPOC catalysts are separated by three phases (i.e. Pt, LSM and GDC). The moderate magnitude of electrochemical promotion can be attributed to the pre-activation of the Pt-nanoparticles due to their small size via self-driven spillover or current by-pass. Future plans for enhancing the magnitude of the effect will be directed in the direction of tuning either the Pt loading and/or the electronic conductivity of the electrode backbone.

Utilization of the ALD technique can bring EPOC systems one step closer to commercialization due to minimized catalyst loadings. In view of practical application of EPOC the success of our concept should be verified with reactions of industrial importance, where possible modifications in product selectivity can also occur.

References

[1] C.G. Vayenas, S. Bebelis, C. Pliangos, S. Brosda, D. Tsiplakides, Electrochemical Activation of Catalysis: Promotion, Electrochemical Promotion and Metal-Support Interactions; Kluwer Academic/Plenum, New York, 2001.

[2] P. Vernoux, L. Lizarraga, M.N. Tsampas, F.M. Sapountzi, A. De Lucas-Consuegra, J.L. Valverde, S. Souentie, C. G. Vayenas, D. Tsiplakides, S. Balomenou, E. A. Baranova, Chem. Rev., 113, 10 (2013) 8192-8260.

[3] M.N. Tsampas, F.M. Sapountzi, P. Vernoux, Catal. Sci. Tech., 5 (2015) 4884-4900.

[4] I. Garagounis, V. Kyriakou, C. Anagnostou, V. Bourganis, I. Papachristou, M. Stoukides, Ind. Eng. Chem. Res., 50 (2011) 431-472.

[5] M. Stoukides and C. G. Vayenas, J. Catal., 70 (1981) 137–146.

[6] M.N. Tsampas, A. Kambolis, E. Obeid, L. Lizzaraga, F. Sapountzi, P. Vernoux, Front. Chem., 1 (2013) 13.

[7] S. Balomenou, D. Tsiplakides, A. Katsaounis, S. Thiemann-Handler, B. Cramer, G.Foti, Ch. Comninellis, C.G. Vayenas, Appl. Catal. B, 52 (3) (2004) 181-196.

[8] C. Xia, M. Hugentobler, Y. Li, C. Comninellis, W. Harbich, Electrochem. Commun., 12 (2010) 1551-1554.

[9] D. Poulidi, M.E. Rivas, I.S. Metcalfe, J. Catal., 281 (2011) 188-197.

[10] A. Kambolis, L. Lizarraga, M.N. Tsampas, L. Burel, M. Rieu, J.-P. Viricelle, P. Vernoux, Electrochem. Commun., 19 (2012) 5-8.

[11] J. González-Cobos, D. Horwat, J. Ghanbaja, J.L. Valverde, A. de Lucas-Consuegra, J. Catal., 317 (2014) 293–302

[12] H.A.E. Dole, L.F. Safady, S. Ntais, M. Couillard, E.A. Baranova, J. Catal., 318 (2014) 85–94.

[13] Y.M. Hajar, K. D. Patel, U. Tariq, E.A. Baranova, J. Catal., 352 (2017) 42-51.

[14] E. Ruiz, D. Cillero, P.J. Martínez, A. Morales, G. San Vicente, G. de Diego, J.M. Sánchez, Catal. Today., 236 (2014) 108–120.

[15] A. de Lucas-Consuegra, J. González-Cobos, V. Carcelén, C. Magén, J.L. Endrino, J.L. Valverde, J. Catal., 307 (2013) 18-26.

[16] J. González-Cobos, E. Ruiz-López, J.L. Valverde, A. de Lucas-Consuegra, Int. J. Hydrog. Energy, 41 (2016) 19418-19429.

[17] V. Roche, R. Revel, P. Vernoux, Catal. Commun., 11 (2010) 1076-1080.

[18] J.T.S. Irvine, D. Neagu, M.C. Verbraeken, C. Chatzichristodoulou, C. Graves, M.B. Mogensen, Nature Energy, 1, (2016) 15014.

[19] X. Xi, A. Kondo, T. Kozawa, M. Naito, Adv. Powder Technol., 27 (2016) 646-651.

[20] S. M. George, Atomic layer deposition: an overview, Chem. Rev., 110 (2010) 111–131.

[21] C. Detavernier, J. Dendooven, S. P. Sree, K. F. Ludwig and J. A. Martens, Chem. Soc. Rev., 40 (2011) 5242–5253.

[22] A. J. M. Mackus, M. J. Weber, N. F. W. Thissen, D. Garcia-Alonso, R. H. J. Vervuurt, S. Assali, A. A. Bol, M. A. Verheijen, W. M. M. Kessels, 27 (2016) 034001

[23] J. Lu, J.W. Elam, P.C. Stair, Acc. Chem. Res., 46 (8) (2013) 1806–1815

[24] H.C.M. Knoops, A.J.M. Mackus, M.E. Donder, M.C.M. van de Sanden, P.H.L. Notten, W.M.M. Kessels, Electrochem. Solid-State Lett., 12 (7) (2009) G34-G36.

[25] C. Marichy, M. Bechelany, and N. Pinna, Adv. Mater., 24, (2012) 1017–1032.

[26] B. J. O'Neill, D. H. K. Jackson, J. Lee, C. Canlas, P. C. Stair, C. L. Marshall, J. W. Elam, T. F. Kuech, J. A. Dumesic, and G. W. Huber, ACS Catal., 5, (2015) 1804−1825.

[27] A. Borodzinski, M. Bonarowska,, Langmuir, 13 (1997) 5613-5620.

[28] J. Yang, V. Tschamber, D. Habermacher, F. Garin, P. Gilot, Appl. Catal. B, 83 (3-4) (2008) 229-239.

[29] C.G. Vayenas, S. Brosda,Top. Catal., 57, 14-16 (2014) 1287-1301.

[30] M.N. Tsampas, F.M. Sapountzi, A. Boréave and P. Vernoux, Electrochem. Commun., 26 (2013) 13-16.
[31] L.Lizarraga, M. Guth, A. Billard, P. Vernoux, Catal. Today, 157 (2010) 61-65.

Chapter 7 Electrochemical Promotion of Nanostructured Palladium Catalyst for Complete Methane Oxidation

Y. M. Hajar, B. Venkatesh and E. A. Baranova, Catalysts, 9 (2019) 48-62.

Electrochemical promotion of catalysis (EPOC) was investigated for methane complete oxidation over palladium nano-structured catalysts deposited on yttria-stabilized zirconia (YSZ) solid electrolyte. The catalytic rate was evaluated at different temperatures (400, 425 and 450 °C), reactant ratios and polarization values. The electrophobic behavior of the catalyst, i.e., reaction rate increase upon anodic polarization was observed for all temperatures and gas compositions with an apparent Faradaic efficiency as high as 3000 (a current application as low as 1 μA) and maximum rate enhancement ratio up to 2.7. Temperature increase resulted in higher enhancement ratios under closed-circuit conditions. Electrochemical promotion experiments showed persistent behavior, where the catalyst remained in the promoted state upon current or potential interruption for a long period of time. An increase in the polarization time resulted in a longer-lasting persistent promotion (p-EPOC) and required more time for the reaction rate to reach its initial open-circuit value. This was attributed to continuous promotion by the stored oxygen in palladium oxide, which was formed during the anodic polarization in agreement with p-EPOC mechanism reported earlier.

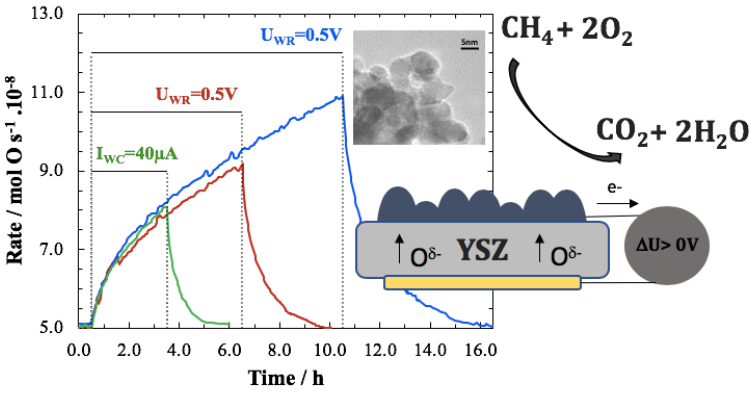

7.1. Introduction

Natural Gas Vehicles (NGVs) have gained considerable attention in the last decade due to much lower greenhouse gas emissions and lower price of methane compared to diesel or gasoline. Not only CH_4 is abundant in natural gas form, but methane can also be produced using anaerobic digestion technologies of bio-derived sources [1–4]. Despite lower emissions of NGVs they often suffer from incomplete methane combustion. Because methane is also 23 times more potent in warming the atmosphere than carbon dioxide its complete conversion to CO_2 is paramount.

Therefore, the development of efficient low temperature catalysts for deep oxidation of methane (CH_4) has recently attracted significant attention [5–10].

Palladium-based catalysts are considered the most efficient for methane activation in excess of oxygen and their activity depends on temperature, methane/oxygen ratio, and catalyst surface oxidation state and composition [5]. The nature of the active surface sites PdO_x vs. Pd was a subject of several studies [6,7]. It was shown that chemisorbed oxygen on Pd metal is poorly active, whereas Pd oxidation with an optimum of 3–4 monolayers forms an active PdO catalyst. Chemisorption of a first layer of oxygen is fast; however, partial bulk oxidation is relatively slow [7].

The innovative field of catalysis that could boost complete methane oxidation reaction over Pd is electrochemical promotion of catalysis (EPOC) or non-Faradaic electrochemical modification of catalytic activity (NEMCA). This general, well-established phenomenon in catalysis aims at controlling in-situ both the activity and the selectivity of a catalyst through application of electric stimuli [8–11]. EPOC is observed with solid electrolyte materials that serve as catalyst support. Ions contained in these electrolytes (O^{2-}, H^+, Na^+ OH^-, etc.) are electrochemically pumped to the catalyst surface, where they act as promoting species leading to modification of catalyst electronic properties and as a result its catalytic activity and selectivity. More precisely, applying an anodic polarization results in the strengthening of electron-donor adsorbates, e.g., chemisorbed methane, and weakening of the binding strength of electron-accepting adsorbates, e.g., dissociatively chemisorbed oxygen [12]. The resulting electrochemical activation magnitude is much higher than that predicted by Faraday's law [13,14]. The increase in the catalytic rate, Δr (mol O/s) divided by the electrochemical rate, I/nF (I is current, F is Faraday's constant and n is number of electrons, 2 for O^{2-}) is denoted as the apparent Faradaic efficiency, Λ, and the process is considered non-Faradaic when $|\Lambda|$ is greater than 1. Another parameter used to quantify EPOC is the rate enhancement ratio, ρ, which is the ratio between the promoted closed-circuit catalytic rate, r and the unpromoted open-circuit catalytic rate, r_o.

The electrochemical promotion of complete methane oxidation was investigated on palladium catalysts prepared using various methods as summarized in Table 7-1 [15–23]. Electrochemical promotion of Pd thick film catalyst electrode prepared using wet impregnation was investigated in the temperature range of 470–600 °C [18]. The rate enhancement of 40% and

an apparent Faradaic efficiency of 1.85 were found in this work. The addition of CeO_2 layer between the YSZ solid-electrolyte and Pd film catalyst increased the open-circuit catalytic rate but decreased the apparent Faradaic efficiency due to the higher electric resistance [18]. Another study on a Pd film catalyst prepared using commercial organometallic paste showed higher enhancement ratio (ρ = 5.6) and Faradaic efficiency (Λ = 579) at 560 °C; however, instability of the catalyst over time and rapid deactivation within 900 min of experiment was also noted [20]. Furthermore, the effect of CeO_2 layer was studied in [24]. It was shown that presence of ceria increased catalytic activity of Pd due to the formation of an active PdO phase, which was stabilized by CeO_2 acting as a continuous source of oxygen, similarly to the oxygen migration from the YSZ electrolyte under EPOC. In another study, an addition of porous YSZ layer between Pd film-catalyst and the dense YSZ solid-electrolyte resulted in a high open-circuit catalytic rate. The authors reported an enhancement ratio of 1.2 and apparent Faradaic efficiency, Λ, of 17 under fuel-rich conditions [23]. EPOC of sputtered Pd catalyst-electrode was compared to impregnated Pd for methane complete oxidation. The sputtered catalysts showed slightly higher Λ of 12 but similar enhancement ratio (ρ = 1.6) [21]. The effect of metal loading and catalyst thickness on EPOC of Pd was studies on Pd catalyst prepared by physical vapor deposition (PVD). It was found that metal loading and catalyst thickness have significant effect on the open-circuit rate and electrochemical promotion, where the thinner films resulted in the highest reaction rates per gram of catalyst at 500 °C [17]. A scaling-up of the system was attempted by electroless deposition of Pd in the channels of a YSZ monolith honeycomb; however, decrease in the conversion of methane occurred under positive and negative polarization [19].

Therefore, from previous EPOC studies on Pd for complete CH_4 oxidation, it is clear that the catalyst preparation method has a strong influence on Pd morphology, structure, oxidation state and as a result, on its catalytic activity, degree of promotion and stability under open and closed circuit conditions. Furthermore, from the practical point of view it is essential to work with low loadings of noble-metal catalysts that exhibit high dispersion and large active surface area In the present work, we report electrochemical promotion of nano-structured, highly dispersed Pd catalyst prepared by polyol reduction method for CH_4 complete oxidation in the temperature range of 400 and 450 °C and various gas compositions.

Table 7-1: Summary of EPOC tests performed for methane oxidation on Pd-YSZ support.

Catalyst Synthesis Method	Loading	I or U Applied	T/°C	P_{CH4}/ kPa	P_{O2}/ kPa	Total Flow/ccm	Rate Change/ mol $O.s^{-1}$ 10^{-8}	ρ	Λ	Authors, Year & Ref.
Paste coating	n/a	+300 µA	400	2.75	1.55	n/a	4.52 to 20.5	4.5	103	[a] Giannikos *et al.* (1998) [15]
Paste coating	n/a	+1 V	400	2.6	1.9	n/a	0.295 to 20	68	153	[a] Frantzis *et al.* (2000) [16]
PVD	24 µg	+100 µA	500	2	10	166	7.3 to 20.4	2.8	258	Roche *et al.* (2008) [17]
Thermal decomposition	1.1 mg/cm^2	+10 mA	600	0.4	1	150	0.47 to 0.68	2.6	<1	[a,b] Jimenez-Borja et al. (2009) [18]
Electroless deposition	5 mg total	+100 µA	400	2	10	166	136.4 to 135.2	0.99	−23	Roche *et al.* (2010) [19]
Paste coating	7 mg/cm^2	+25 µA	560	0.4	1.2	150	1.6 to 9.1	5.6	579	[a] Jimenez-Borja *et al.* (2011) [20]
Sputtered	0.4 mg/cm^2	+1 mA	350	1.3	4.5	200	11.4 to 18.2	1.6	12	Matei *et al.* (2012) [21]
Impregnation	0.4 mg/cm^2	+300 µA	350	1.3	4.5	200	22 to 26	1.18	25	Jimenez-Borja *et al.* (2012) [22]
Impregnation	0.4 mg/cm^2	+5 mA	400	1.4	2.8	200	135 to 158	1.2	17	Matei *et al.* (2013) [23]
Polyol method	0.3 mg/cm^2	+0.5 V	425	2	4	100	6 to 16	2.66	383	[a] This work

[a] Continuous increase in closed-circuit rate post EPOC; [b] Electrolysis effect.

7.2. Experimental

7.2.1. Synthesis of Pd nanoparticles

Mono-metallic Pd NPs were synthesized using 0.133 g of palladium chloride (Fisher Scientific®, Canada) precursor salts dissolved in 25 mL of ethylene glycol and 0.8 M NaOH. The mixture was heated up to 160 °C and kept under stirring conditions for 3 h. The final colloidal solution was cooled down and washed repeatedly with ethanol.

7.2.2. Catalyst characterization

X-ray diffraction (XRD) was performed on the fresh Pd sample using Rigaku Ultima IV multipurpose diffractometer (Rigaku, The Woodlands, TX, USA). The diffractometer was equipped with an X'Celerator detector with monochromatic CuKα radiation (λ = 1.5418 Å) at 40 kV and 44 mA with a divergence slit of 2/3 degree, a scan speed of 0.03 °/s and a scan step of 0.02 degrees between 30 and 80° 2θ.

The transmission electron microscopy (TEM) micrographs were obtained using JEOL JEM 2100F FETEM (JEOL, Peabody, MA, USA) operating with a field emission gun at an acceleration voltage of 200 kV. SEM micrographs were recorded using Phenom™ SEM (Nanoscience Instruments, Virginia, USA). Additional elemental analysis was performed using the energy dispersive X-ray spectroscopy (EDS) attachment.

7.2.3. Electrochemical cell and reactor

The solid electrolyte is a 19 mm diameter and 1 mm thickness disk of 8 mol % Y_2O_3-stabilized ZrO_2 (YSZ) (TOSOH®, Grove city, OH, USA) fabricated following the procedure reported earlier [25]. Inert gold reference and counter electrodes were deposited on one side of the disk by applying thin gold paste coating (Gwent Group, Pontypool, UK) of 0.2 and 1 cm^2 surface areas, respectively. This was followed by annealing in air at 500 °C. The catalyst-working electrode was deposited on the other side of the solid electrolyte disk (1 cm^2 surface area) opposing to the counter electrode. To this end, mono-metallic Pd were dispersed in isopropanol and 10 μL of a suspension were deposited at a time with intermediate drying at room temperature. The resulting total metal loading was 0.5 mg of Pd on YSZ. Catalytic measurements were carried out at atmospheric pressure in the single-chamber capsule reactor reported earlier [26,27]. The working electrode side of the electrolyte was pressed against a gold mesh (1 cm^2) that served as a

current collector, while the counter and reference electrodes were pressed directly against gold wires [28]. Two type K thermocouples (Omega®, Quebec, Canada) were placed in vicinity of the electrochemical cell, one for temperature control and one for data acquisition.

7.2.4. Catalytic and electrochemical measurements

The reaction gases were CH_4 (Linde, 99.99%), O_2 (Linde, 99.99%), and He (Linde, 99.997%) as a carrier gas. The total flow rate was constant at 100 mL min^{-1}. Gas composition was varied using MKS, 1259 C and 1261-C series flow meters and detected using non-dispersive infrared (NDIR) CO_2 gas analyzer (Horiba, VA-3000, Burlington, Canada). Constant electric current or potential were applied using a potentiostat-galvanostat (Arbin Instruments®, MSTAT, College Station, TX, USA) connected to the electrodes of solid-electrolyte electrochemical cell.

7.3. Results and discussion

Transmission electron microscopy (TEM) was used to determine the palladium morphology and particle size (Figure 7.1a,b). The resulting Pd particles are spherical in shape with a diameter of approximately 5 nm, that are coalesced together in larger aggregates of roughly 50 nm in size. Figure 7.1c,d shows SEM images of as-prepared Pd/YSZ catalysts and the same catalyst after catalytic measurements under open circuit and EPOC conditions. It can be seen that as-prepared catalyst-electrode forms a highly dispersed, non-continuous layer on YSZ surface that consists of fine grains and pores. After the reaction, the "spent" catalyst shows much larger catalyst islands indicating a change in the morphology due to the catalyst agglomeration that takes place during the reaction. The resulting energy dispersive X-ray spectroscopy (EDS) spectrum (Figure 7.2a) of as-prepared Pd shows that the only element present is Pd. The x-ray diffraction pattern (XRD) contains several diffraction peaks of Pd (111), (200) and (220) corresponding to face-centered cubic (fcc) structure typical for bulk palladium metal. The crystallite size of Pd found from Pd (111) was 8 nm.

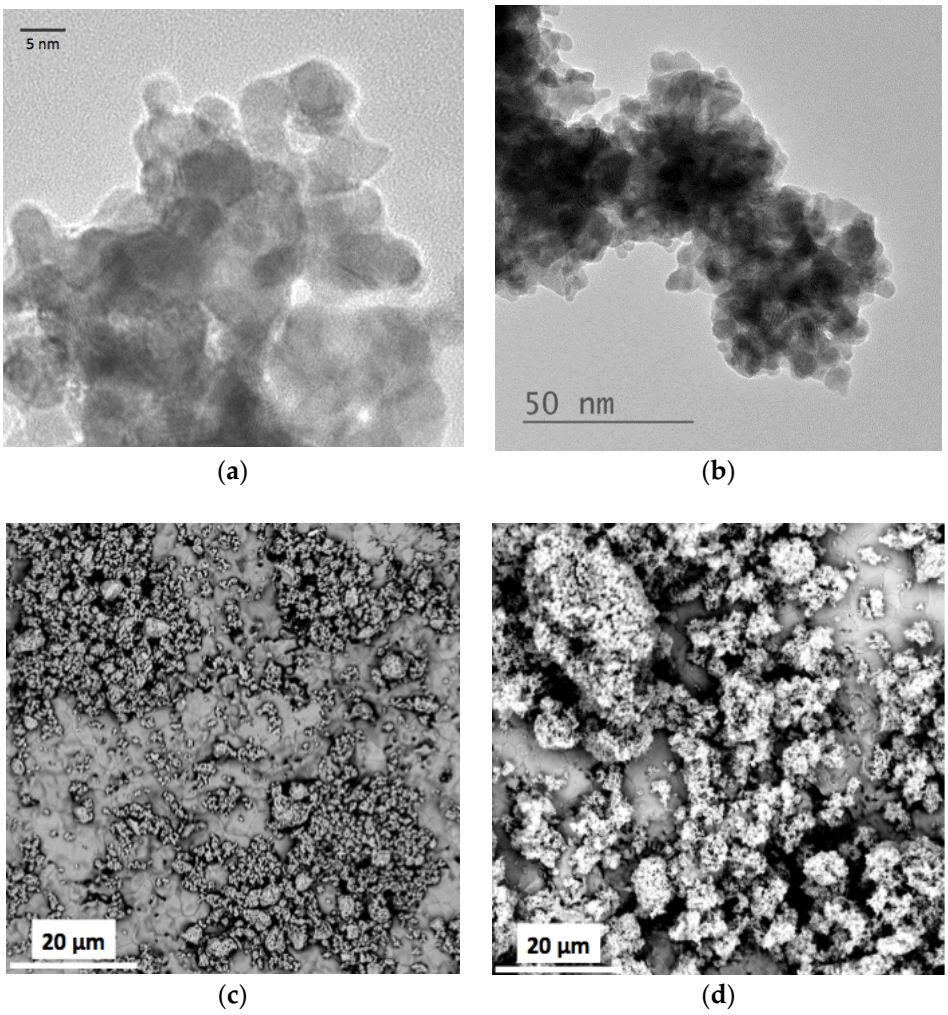

(**a**) (**b**)

(**c**) (**d**)

Figure 7.1: (a,b) TEM images of stand-alone Pd NPs at 5 nm and 50 nm scale; (c,d) SEM images of as-prepared (c) and post-experiment (d) Pd catalyst deposited on YSZ solid electrolyte.

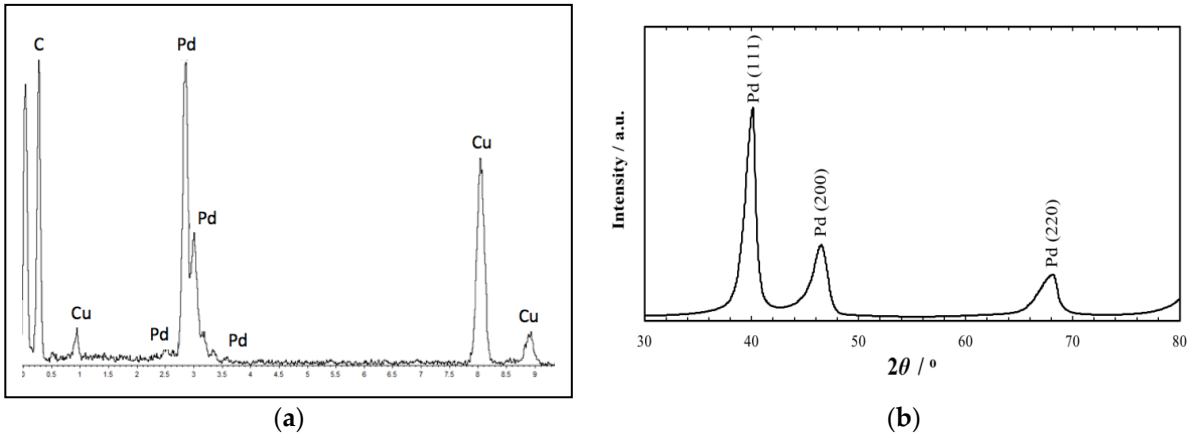

(**a**) (**b**)

Figure 7.2: (a) EDS spectrum and (b) XRD pattern of Pd catalyst.

The open-circuit catalytic rate of methane oxidation was tested at two different temperatures and at various gas compositions (Figure 7.3). It can be seen that for both temperatures the rate increased as a function of oxygen partial pressure. The increase was more significant at 4 kPa of methane where oxygen-to-methane partial pressures ratios were lower. The rate increase in fuel-rich condition is indicative of a Langmuir-Hinshelwood mechanism [15] where methane is able to competitively adsorb on palladium as seen at 450 °C under 4 kPa of CH_4, while the quasi-stable value at higher ratio of oxygen (at 2 kPa of CH_4) can be explained by an Eley-Rideal mechanism as CH_4 reacts on the oxygen covered surface [29].

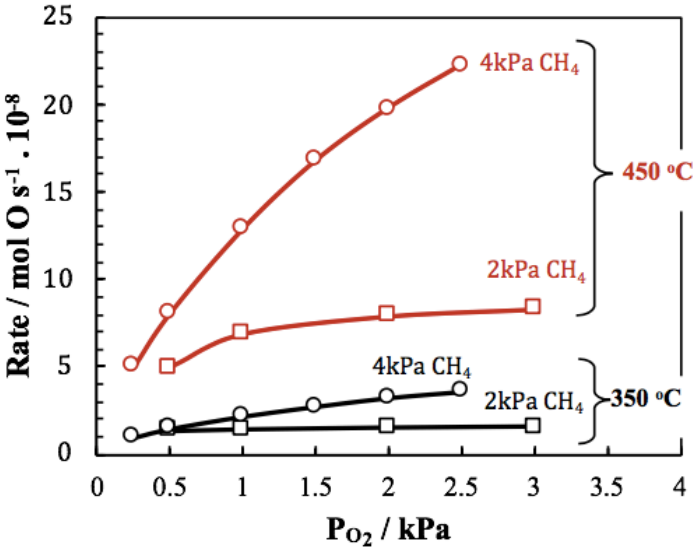

Figure 7.3: Effect of oxygen-to-methane ratio on catalytic rate at 350 and 450 °C.

Figure 7.4 shows the transient rate response to an application of positive current (20 μA) between the Pd working electrode and the counter electrode at 450 °C. Under open-circuit conditions ($t < 0.5$ h), the catalytic rate was at 8.35×10^{-8} mol/s. When a constant current was imposed, the reaction rate gradually increased due to pumping of O^{2-} promoters to the catalyst surface. After 2 h of polarization, the closed-circuit rate increase was 180% higher than its corresponding open-circuit value. In addition, the non-Faradaic behavior resulted in an apparent Faradaic efficiency, Λ, of 610 denoting that the back-spillover of O^{2-} at a I/2F rate gave a 610 times increase in the overall oxidation rate [30]. It should be noted that slight increase in the catalyst-working electrode potential (U_{WR}) was observed upon positive polarization (from 0.39 to 0.42 V). Furthermore, the slow reaction rate increase did not reach a steady-state value even after

2 h of applied polarization and took over 1 h to reach the open circuit value observed before polarization. According to the mechanism of EPOC the reaction rate is due to the supply of oxygen ionic species from YSZ and the formation of an effective double layer at the surface of the catalyst that changes the work function of Pd leading to weakening of the chemisorbed oxygen bond strength thus facilitating the $-O_2C$ desorption from the catalyst surface.

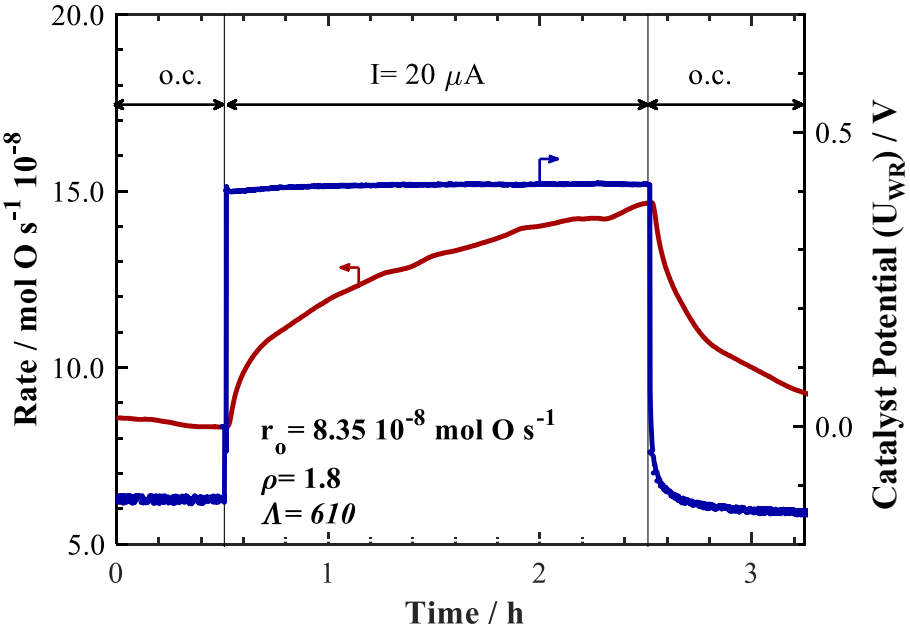

Figure 7.4: Transient rate response of Pd nanoparticles to a current step change. o.c.: open-circuit. Conditions: T = 450 °C, 2 kPa of CH_4 and 4 kPa of O_2. Flow rate: 100 ccm.

A similar behavior was observed under potentiostatic conditions (U_{WR} = 0.25 V) and a stoichiometric flow of reactants at 425 °C (Figure 7.5). The catalytic rate slowly increased in value until it reached 7.0×10^{-8} mol s^{-1} after 2 h. As in the galvanostatic conditions (Figure 7.4) the closed-circuit reaction rate was continuously increasing with time without reaching a steady-state. After 2 h, the rate enhancement ratio of 1.31 and, an apparent Faradaic efficiency of 1107 were obtained. The high Λ value is due to the low current that passed through the cell, which was sufficient to promote Pd catalyst.

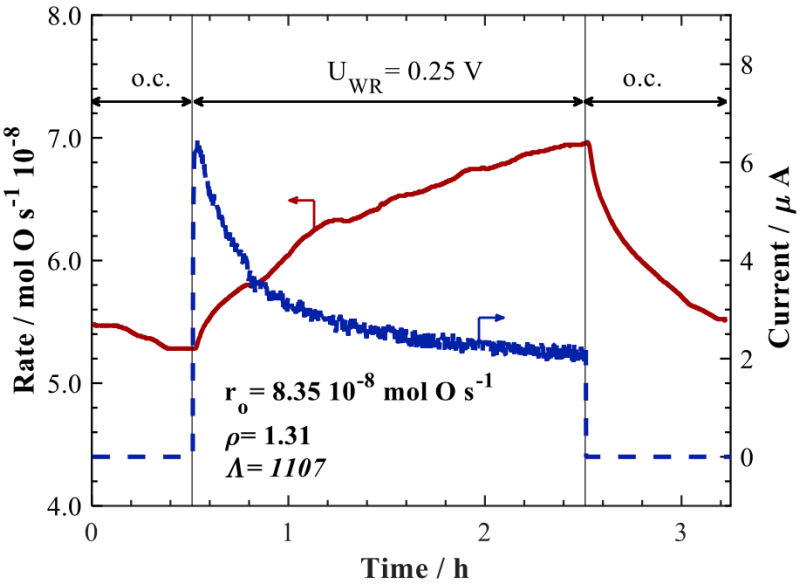

Figure 7.5: Transient rate response of Pd nanoparticles to potential step changes. o.c.: open-circuit. Conditions: T = 425 °C, 2 kPa of CH_4 and 4 kPa of O_2. Flow rate: 100 ccm.

The continuous increase of the catalytic rate in Figure 7.4 and Figure 7.5 can be explained by the continuous oxidation of palladium catalyst to PdO_x, which makes the catalyst more active for methane oxidation. In Figure 7.5, this continuous increase in catalytic rate occurred simultaneously with a decrease in current at a constant applied potential value indicating Pd oxide formation. Upon current or potential interruption the rate slowly returned to its initial state, because oxygen species stored in PdO_x continued acting as sacrificial promoters for methane oxidation reaction.

To confirm PdO_x formation and oxygen storage effect on p-EPOC, the catalyst was polarized for a different duration 3, 6 and 10 h. As seen in Figure 7.6, the closed-circuit catalytic rate was continuously increasing with time under constant current (40 µA for 3 h) and potential (0.5 V for 6 and 10 h) application. It can be seen that even after ten hours of polarization, the closed-circuit rate kept on rising without reaching a steady-state. At the same time, the longer polarization time resulted in longer decrease of the open-circuit rate after polarization was stopped. A proportional relationship (as shown in the inset Figure 7.6) was found between the duration of EPOC and the time to reach the open-circuit rate $r_{o.c}$. The slope of this relationship was 0.5. This persistent electrochemical promotion (p-EPOC) is due to the stored oxygen ions in PdO_x that act as sacrificial promoters when the electrical circuit is open [31].

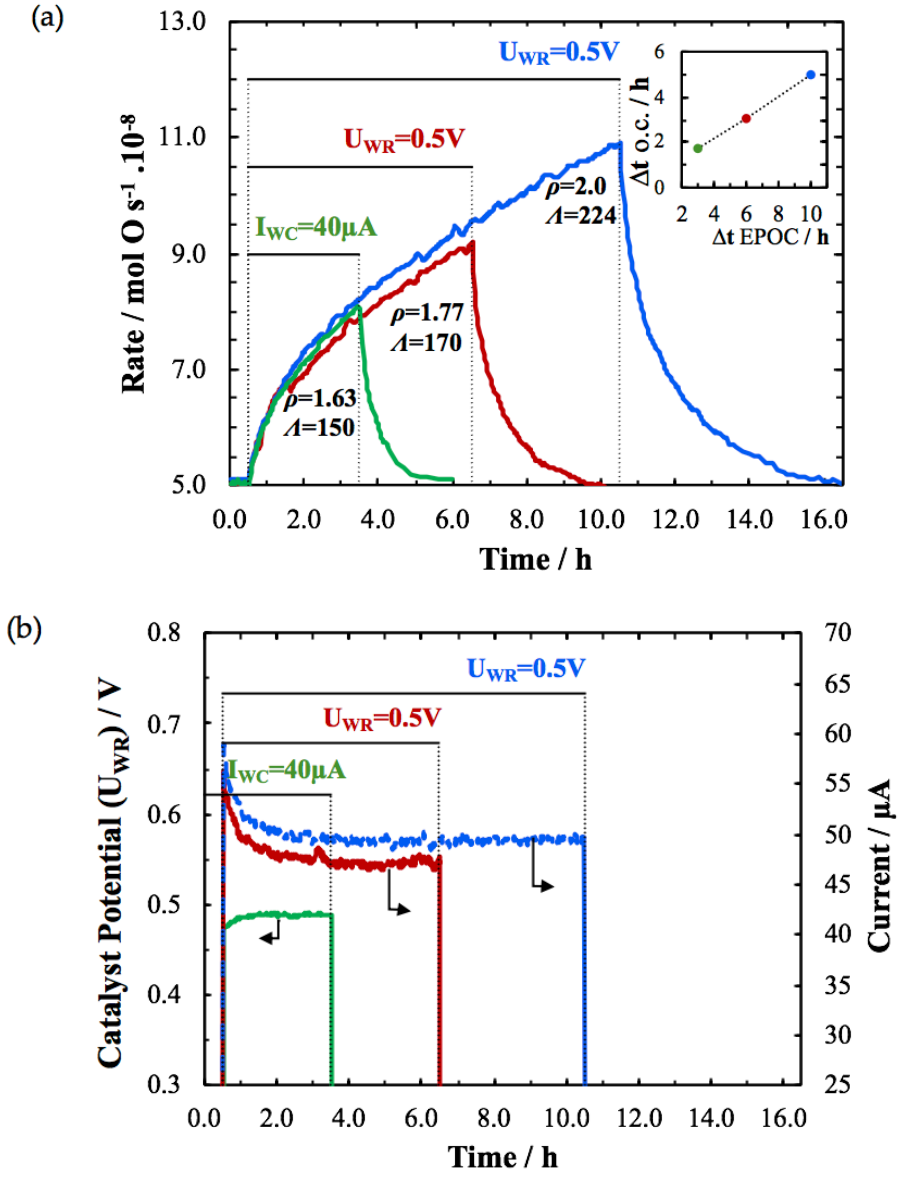

Figure 7.6: Transient rate response of Pd at different duration of EPOC and (b) the potential/current read at potentiostatic or galvanostatic application. Conditions: T = 425 °C, 2 kPa of CH_4 and 4 kPa of O_2. Flow rate: 100 ccm.

This indicates that during the positive polarization two parallel processes take place: i. Migration of $O^{\delta-}$ promoters to the gas exposed catalyst surface and ii. PdO_x formation at the three-phase boundary (tpb) according to the electrochemical reaction:

$$Pd + xO^{2-} \rightarrow PdO_x + xe^- \qquad 7\text{-}1$$

Current decrease and potential increase upon positive potentiostatic (Figure 7.5 and Figure 7.6) and glavanostatic polarization (Figure 7.4), respectively, confirms the formation of PdO_x.

Palladium oxide has lower conductivity than Pd metal, therefore current that flows through the solid-state cell or potential difference of the working catalyst-electrode (U_{WR}) are the clear indication of an electrochemical oxide formation [32].

Figure 7.7 shows a transient rate response at a constant applied potential 0.5 V for 24 h. The reaction rate continuously increased for up to 20 h followed by 2 h of a steady-state rate and then a slight rate decrease. The continuous rate increase indicates constant catalyst activation due to the growth of PdO_x, whereas somewhat rate decrease after 22 h of polarization at 425 °C may be linked with morphology change observed for the "spent" catalysts (Figure 7.1d). The open-circuit rate took more than 6 h to return to its initial value showing a persistent promotional effect.

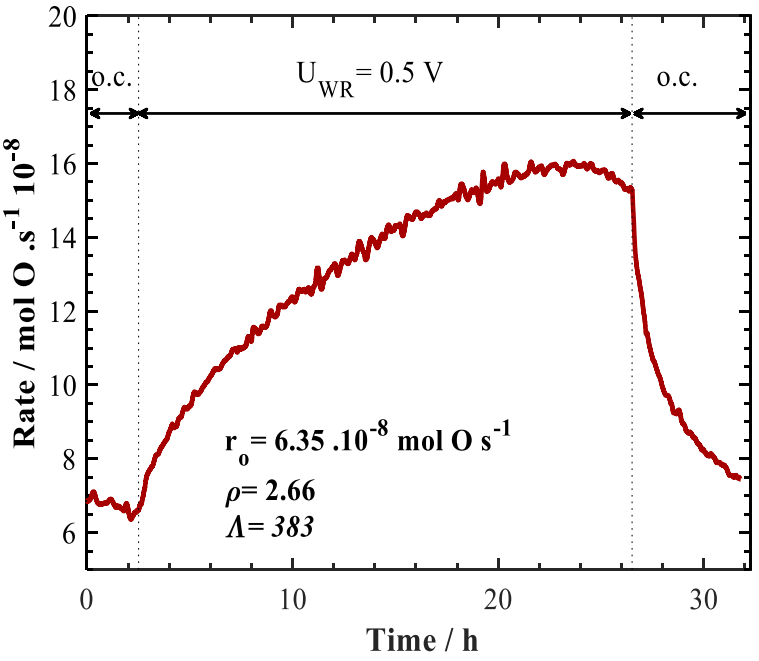

Figure 7.7: Long period transient rate response of Pd to a potentiostatic step change. o.c.: open-circuit. Conditions: T = 425 °C, 2 kPa of CH_4 and 4 kPa of O_2. Flow rate: 100 ccm.

Figure 7.8 shows the catalytic rate and catalyst potential change upon application of constant current as low as 1 μA. This resulted in the continuous catalytic rate increase for 1, 2 and 4 kPa of O_2, accompanied by catalyst potential (U_{WR}) increase, confirming palladium oxide formation. The corresponding Λ values are summarized in Figure 7.9.

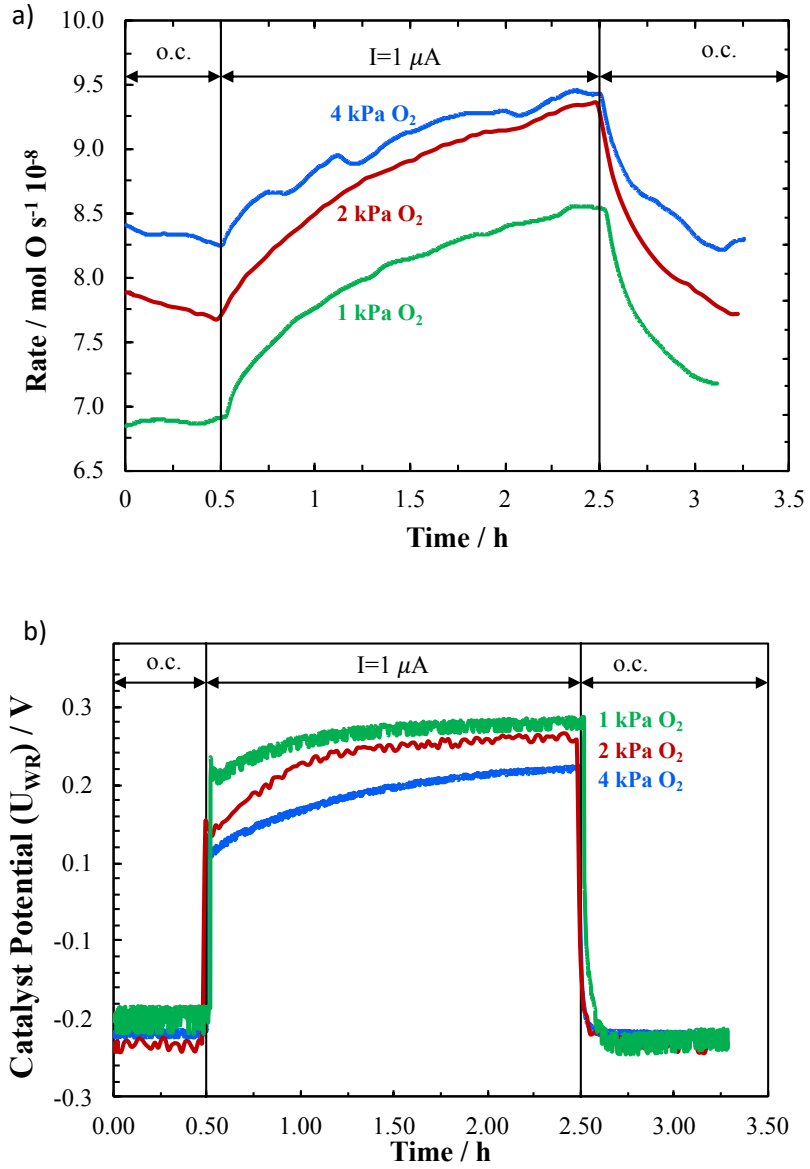

Figure 7.8: (a) Transient rate response of Pd catalyst at different O_2 partial pressure under 1 μA galvanostatic application and (b) the corresponding catalyst potential response. Conditions: T = 450 °C, 2 kPa of CH_4. Flow rate: 100 ccm.

In Figure 7.9, the effect of partial pressure on closed-circuit reaction rate was tested at different galvanostatic conditions. The highest increase in catalytic rate was found at slightly fuel-rich conditions resulting in a ρ value of 1.3; the higher rate can be explained by the advantaged adsorption of gaseous methane over oxygen. At this condition, gaseous methane can be expected to directly adsorb onto Pd, resulting in a competition between oxygen and methane adsorption following a Langmuir-Hinshelwood mechanism. In addition, the desorption of oxygen from the surface becomes facilitated at lower oxygen partial pressure in the atmosphere as the overall

chemical potential of oxygen is reduced [33]. At a partial pressure ratio higher than the stoichiometric ratio, it is perceived that the catalytic rate increase is slightly lower. The slight decrease in the enhancement is due to the competing adsorption of oxygen on the surface of Pd, putting slight mass-transfer limitations on the chemisorption of CH_4.

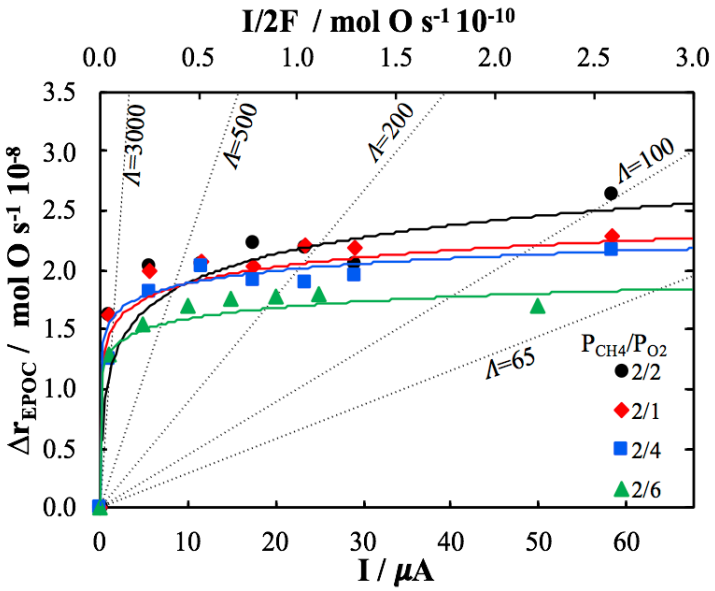

Figure 7.9: Current effect on catalytic rate in function of methane/oxygen ratio. T = 450 °C. Flow rate: 100 ccm.

Similarly, the effect of temperature on closed-circuit reaction rate was tested at different galvanostatic conditions. Figure 7.10 shows that there is an increase in catalytic rate as a function of temperature at all applied positive current values for 400, 425 and 450 °C. It can be noticed that upon application of small current of 1 μA, a significant rate increase was detected, resulting in a logarithmic-shape relationship of rate increase versus applied current. In addition, a highest value of ~2400 was found for the apparent Faradaic efficiency, constructing that a very minimal current was able to result in a change of the Pd surface oxidation state and hence the adsorption strength of methane reactant [15,16,18,20].

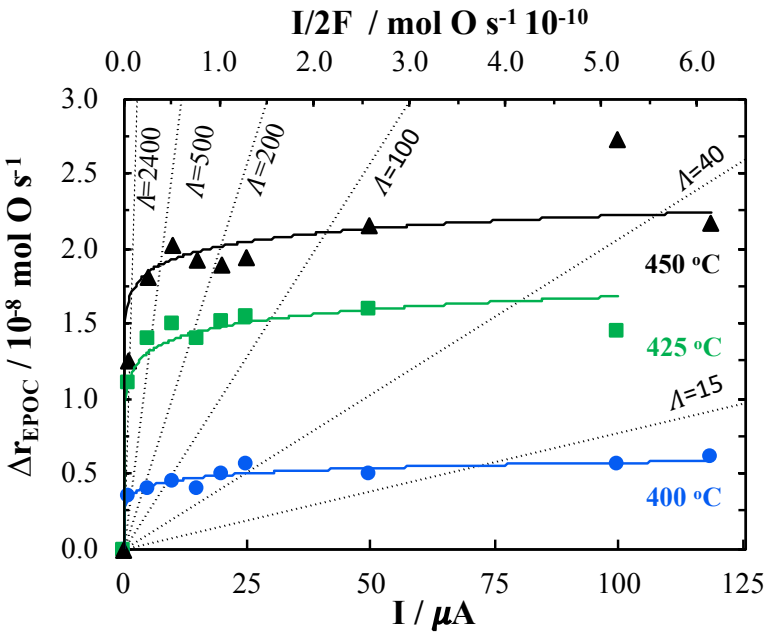

Figure 7.10: Current effect on catalytic rate in function of temperature: 400, 425 and 450 °C. P_{CH4}= 2 kPa and P_{O2} = 4 kPa. Flow rate: 100 ccm.

Table 7-1compares EPOC of methane oxidation on Pd/YSZ found in this work to previous studies carried out on Pd catalyst-electrode deposited on YSZ solid-electrolyte. The table depicts where our results fall in comparison with previous experiments. It should be noted that the metal loading used in this work is the lowest in the temperature range of interest (T ≤ 450 °C), which is important for cold-start emission application. In agreement with previous work, Pd nanostructured catalyst synthesized by polyol method shows electrophobic type of EPOC, where only positive polarization promotes the reaction. Applied polarization led to the supply of $O^{\delta-}$ promoters from YSZ electrolyte to the catalyst surface, resulting in the formation of a more active phase of PdO, on the surface first and in the bulk gradually.

Ionic oxygen migration to the surface altered the adsorption properties of the catalyst surface, resulting in the weakening of gaseous oxygen adsorption and strengthening that of electron-donor methane. The alteration of the catalytic oxidation state was similar under both potentiostatic and galvanostatic application, which have resulted in a continuous increase in catalytic rate and a very slow open circuit rate decrease when the circuit was interrupted. This was explained by the formation of PdO during polarization and oxygen storage in its bulk, which was continuously providing the promoting oxygen species to the surface post-polarization according to p-EPOC mechanism [31].

7.4. Conclusions

Electrochemical promotion of Pd nanostructured catalyst was investigated for the methane oxidation reaction in the 400–450 °C temperature range. The promotion of the catalytic rate of Pd NPs was achieved under anodic polarization. Upon various potentiostatic and galvanostatic tests, non-Faradaic enhancement was achieved, most notably at 450 °C, under the application of 1 μA, where Λ was equal to ~3000, higher than any previous EPOC study on Pd. Continuous increase in the reaction rate was found under EPOC conditions, due to the Pd oxide formation in the vicinity of the tpb. A proportional relationship was found between the duration of polarization and the post-polarization time required to reach the initial open-circuit rate value. Post polarization, a persistent promotion (p-EPOC) was observed due to the promotion of the reaction by the stored oxygen, which was accumulated during positive polarization. Overall, our work revealed interesting behavior of Pd synthesized by polyol method, providing further insight into the application of electrochemical promotion for complete methane oxidation with highly dispersed Pd.

References

[1] A. Demirbaş, Biomass resource facilities and biomass conversion processing for fuels and chemicals, Energy Convers. Manag. 42 (2001) 1357–1378.

[2] H. Cheng, Y. Hu, Municipal solid waste (MSW) as a renewable source of energy: Current and future practices in China, Bioresour. Technol. 101 (2010) 3816–3824.

[3] M. Tripathi, J.N. Sahu, P. Ganesan, Effect of process parameters on production of biochar from biomass waste through pyrolysis: A review, Renew. Sustain. Energy Rev. 55 (2016) 467–481.

[4] Y. Xiao, P. He, W. Cheng, J. Liu, W. Shan, H. Song, Converting solid wastes into liquid fuel using a novel methanolysis process, Waste Manag. 49 (2016) 304–310.

[5] R.J. Farrauto, M.C. Hobson, T. Kennelly, E.M. Waterman, Catalytic chemistry of supported palladium for combustion of methane, Appl. Catal. A Gen. 81 (1992) 227–237.

[6] D. Ciuparu, M.R. Lyubovsky, E. Altman, L.D. Pfefferle, A. Datye, Catalytic combustion of methane over palladium-based catalysts, Catal. Rev. - Sci. Eng. 44 (2002) 593–649.

[7] R. Burch, F.J. Urbano, Investigation of the active state of supported palladium catalysts in the combustion of methane, Appl. Catal. A Gen. 124 (1995) 121–138.

[8] M. Boudart, G. Djega-Mariadassou, Kinetics of heterogeneous catalytic reactions, Princeton, NJ, 1984.

[9] I.M. Campbell, Catalysis at Surfaces, Chapman and Hall, New York, 1988.

[10] C.G. Vayenas, S. Bebelis, S. Neophytides, Non-Faradaic Electrochemical Modification of Catalytic Activity, J. Phys. Chem. 92 (1988) 5083–5085.

[11] S. Ladas, S. Kennou, S. Bebelis, C.G. Vayenas, Origin of non-faradaic electrochemical modification of catalytic activity, J. Phys. Chem. 97 (1993) 8845–8848.

[12] J. Nicole, D. Tsiplakides, C. Pliangos, X.E.E. Verykios, C. Comninellis, C.G.G. Vayenas, Electrochemical Promotion and Metal–Support Interactions, J. Catal. 204 (2001) 23–34.

[13] C.G. Vayenas, S. Bebelis, S. Ladas, Dependence of catalytic rates on catalyst work function, Nature. 343 (1990) 625–627.

[14] C.G. Vayenas, S. Bebelis, C. Pliangos, S. Brosda, D. Tsiplakides, Electrochemical Activation of Catalysis: Promotion, Electrochemical Promotion, and Metal-Support Interactions, Springer, New York, 2001.

[15] A. Giannikos, A.D. Frantzis, C. Pliangos, S. Bebelis, C.G. Vayenas, Electrochemical promotion of CH4 oxidation on Pd, Ionics (Kiel). 4 (1998) 53–60.

[16] A.D. Frantzis, S. Bebelis, C.G. Vayenas, Electrochemical promotion (NEMCA) of CH4 and C2H4 oxidation on Pd/YSZ and investigation of the origin of NEMCA via AC impedance spectroscopy, Solid State Ionics. 136–137 (2000) 863–872.

[17] V. Roche, R. Karoum, A. Billard, R. Revel, P. Vernoux, Electrochemical promotion of deep oxidation of methane on Pd/YSZ, J. Appl. Electrochem. 38 (2008) 1111–1119.

[18] C. Jiménez-Borja, F. Dorado, A. de Lucas-Consuegra, J.M. García-Vargas, J.L.J.L. Valverde, Complete oxidation of methane on Pd/YSZ and Pd/CeO2/YSZ by electrochemical promotion, Catal. Today. 146 (2009) 326–329.

[19] V. Roche, R. Revel, P. Vernoux, Electrochemical promotion of YSZ monolith honeycomb for deep oxidation of methane, Catal. Commun. 11 (2010) 1076–1080.

[20] C. Jiménez-Borja, F. Dorado, A. de L.-Consuegra, J.M. G.-Vargas, J.L. Valverde, Electrochemical Promotion of CH4 Combustion over a Pd/CeO2-YSZ Catalyst, Fuel Cells. 11 (2011) 131–139.

[21] F. Matei, D. Ciuparu, C. Jiménez-Borja, F. Dorado, J.L. Valverde, S. Brosda, Electrochemical promotion of methane oxidation on impregnated and sputtered Pd catalyst-electrodes deposited on YSZ, Appl. Catal. B Environ. 127 (2012) 18–27.

[22] C. Jimenez-Borja, S. Brosda, F. Matei, M. Makri, B. Delgado, F. Sapountzi, D. Ciuparu, F. Dorado, J.L. Valverde, C.G. Vayenas, Electrochemical promotion of methane oxidation on Pd catalyst-electrodes deposited on Y2O3-stabilized-ZrO2, Appl. Catal. B Environ. 128 (2012) 48–54.

[23] F. Matei, C. Jimenez-Borja, J. Canales-Vazquez, S. Brosda, F. Dorado, J.L. Valverde, D. Ciuparu, Enhanced electropromotion of methane combustion on palladium catalysts deposited on highly porous supports, Appl. Catal. B Environ. 132–133 (2013) 80–89.
[24] C. Jimenez-Borja, F. Matei, F. Dorado, J.L. Valverde, Characterization of Pd catalyst-electrodes deposited on YSZ: Influence of the preparation technique and the presence of a ceria interlayer, Appl. Surf. Sci. 261 (2012) 671–678.
[25] I.R. Gibson, G.P. Dransfield, J.T.S. Irvine, Sinterability of commercial 8 mol % yttria-stabilized zirconia powders and the effect of sintered density on the ionic conductivity, J. Mater. Sci. 33 (1998) 4297–4305.
[26] Y.M. Hajar, H.A. Dole, M. Couillard, E.A. Baranova, Investigation of heterogeneous catalysts by electrochemical method: Ceria and titania supported iridium for ethylene oxidation, ECS Trans. 72 (2016) 161–172.
[27] Y.M. Hajar, K.D. Patel, U. Tariq, E.A. Baranova, Functional equivalence of electrochemical promotion and metal support interaction for Pt and RuO2 nanoparticles, J. Catal. 352 (2017) 42–51.
[28] Y.M. Hajar, M.S. Houache, U. Tariq, P. Vernoux, E.A. Baranova, Nanoscopic Ni interfaced with oxygen conductive supports: Link between electrochemical and catalytic studies, Electrochem. Soc. 77 (2017) 51–66.
[29] E. Garbowski, C. Feumi-Jantou, N. Mouaddib, M. Primet, Catalytic combustion of methane over palladium supported on alumina catalysts: Evidence for reconstruction of particles, Appl. Catal. A, Gen. 109 (1994) 277–292.
[30] C.G.C.G. Vayenas, S. Bebelis, I. V. Yentekakis, H.-G. Lintz, Non-faradaic electrochemical modification of catalytic activity: A status report, Catal. Today. 11 (1992) 303–442.
[31] J. Nicole, C.H. Comninellis, Electrochemical promotion of IrO2 catalyst activity for the gas phase combustion of ethylene, J. Appl. Electrochem. 28 (1998) 223–226.
[32] C. Vayenas, S. Brosda, C. Pliangos, The double-layer approach to promotion, electrocatalysis, electrochemical promotion, and metal–support interactions, J. Catal. 216 (2003) 487–504.
[33] K. Reuter, M. Scheffler, Composition, structure, and stability of RuO2 (110) as a function of oxygen pressure, Phys. Rev. B. 65 (2001) 035406.

Chapter 8 Electrochemical Promotion of Bi-metallic Ni_9Pd Core Double-Shell Nanoparticles for Complete Methane Oxidation

Y. M. Hajar, B. Venkatesh, M. S.E. Houache, H. Liu, R. Safari, S. Prabhudev, G. A. Botton and E. A. Baranova, J. of Catalysis, 374 (2019) 127–135.

Electrochemical promotion of Ni_9Pd nanoparticles (NPs) with low Pd content (Ni:Pd = 9:1 atomic ratio) supported on yttria-stabilized zirconia (YSZ) solid-electrolyte was evaluated for the first time for complete methane oxidation. Electron Energy Loss Spectroscopy (EELS) showed a Pd core with a Ni first shell surrounded by 3–4 nm layer of Pd outer shell. This core double-shell structure of Ni_9Pd NPs enhanced the catalytic activity and stability compared to mono-metallic Pd and Ni NPs under open-circuit. The reversible electrochemical promotion of Ni_9Pd was obtained upon positive polarization between 425 and 500 °C. At 425 °C, the reaction rate increase reached 240% corresponding to apparent Faradaic efficiency of 25. On Ni_9Pd NPs the reaction exhibited electrophobic behavior, i.e., the rate increased with anodic polarization, under all experimental conditions of this study. The results demonstrate the advantage of using Ni_9Pd bi-metallic nanoparticles with core double-shell structure for methane complete oxidation due to the synergetic effect between Pd and Ni and very low amount of expensive Pd phase. EPOC with this type of highly dispersed and low noble metal content catalysts may find a way in the real world catalytic converters for gas exhaust treatment.

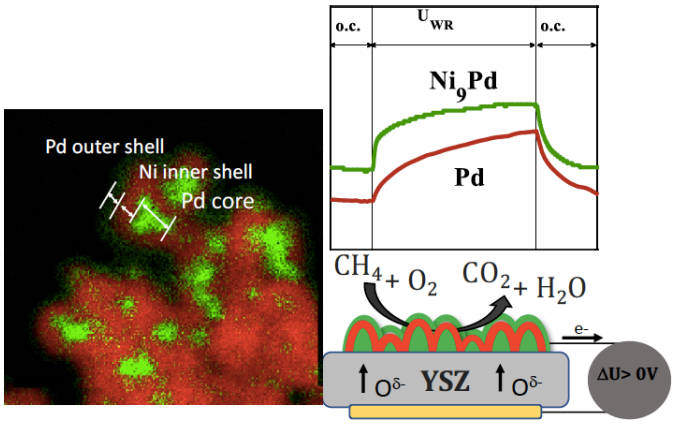

8.1. Introduction

Natural gas (NG) has attracted considerable attention as an alternative fuel due to its high energy density and low environmental impact [1]. NG is already used in natural gas engines in particular natural gas vehicles (NGV) [2]. Depending on its source, NG consists of 90% of methane, which in comparison to gasoline has a low carbon emission per energy produced [3]. Methane is a very stable molecule and the activation of C-H bond represents a challenge, often resulting in release of unburned methane into the atmosphere. Because CH_4 has 23-fold

greenhouse effect compared to CO_2, this makes its full combustion critical to prevent any unburned methane release into the atmosphere [4]. Therefore, to continue to be attractive, NG engines must be associated with post-treatment systems in order to reduce their pollutant emissions by unburned methane. Thus, development of a solution for total elimination of unburned methane residuals has attracted a great attention and would give a real advantage to the NGV industry.

Catalytic combustion of methane at low temperature (< 550 °C) have been the interest of a number of studies as no thermal NO_x would be produced [5]. The competition between complete and partial oxidation of methane takes place above 550 °C (at a ratio exceeding 2-to-1 CH_4/O_2) [6], whereas low to no selectivity towards partial oxidation is found below this threshold [7]. Several catalysts have been investigated for the complete methane oxidation such as palladium [8–11], platinum [12,13], rhodium [14] and perovskites [15]. Amongst these catalytic systems, palladium was found to be the most active catalyst at temperatures below 550 °C [9].

The activity and stability of Pd catalysts can be increased by adding a second metal to form a bi-metallic PdM catalyst [16]. In particular, the addition of Ni to Pd either in the form of bimetallic catalyst or the support lead to the enhanced catalytic activity and stability of Pd [17]. Persson *et al*. studied the influence of adding various metals (Co, Rh, Ir, Ni, Pt) to Pd (synthesized by incipient wetness technique) for the methane oxidation [18]. The authors showed that addition of Ni resulted in superior activity compared to other metals due to the improved thermal stability of PdNi, even though the activity was inferior to that of Pd alone [17,18]. Similar results were found when Pd was supported on nickel-alumina support, which resulted in particle size decrease [19]. In addition, Shen *et al*. studied the effect of different nickel-palladium synthesis methods and showed improvement of the catalytic rate when polyol synthesis was used instead of the conventional impregnation technique [20]. The polyol method resulted in highly active Ni/Pd bi-metallic NPs supported on alumina compared to less active Pd on $NiAl_2O_4$ spinel phase.

Furthermore, the activity and stability of Pd can be improved using electrochemical promotion of catalysis (EPOC) phenomenon. EPOC or Non-Faradaic electrochemical modification of catalytic activity (NEMCA) effect is a general phenomenon in catalysis, where the rate of the catalytic reaction and in some cases reaction selectivity are modified (promoted or inhibited) by current or potential application. In this case, the catalyst also serves as a working electrode in the solid-state electrochemical cell that uses ionic (O^{2-}, Na^+, H^+, OH^-, etc.) conductor

as a solid-electrolyte. As shown using various spectroscopic surface sensitive techniques, this effect is due to electrochemical pumping (removing) of ionic species to (from) the gas-exposed catalyst surface [21–24]. Addition of ionic promoters results in the variation of the catalyst work function (WF) due to an electrochemically controlled migration of ionic species towards (from) the support [25,26]. The change in WF leads to modification of the adsorption strength of reactants and/or intermediates that in turn has a significant effect on the catalytic rate under closed-circuit conditions. The ratio of the closed-circuit rate, r, over the open-circuit rate, r_o, is known as the rate enhancement ratio, ρ:

$$\rho = \frac{r}{r_o} \qquad 8\text{-}1$$

Another parameter used to quantify EPOC effect is the apparent Faradaic efficiency, Λ which shows if the observed rate increase (decrease) is faradaic, i.e., due to electrochemical reactions, $\Lambda \leq 1$ or non-faradaic due to electrochemically induced migration of promoters, $\Lambda > 1$:

$$\Lambda = \frac{r - r_o}{I/nF} \qquad 8\text{-}2$$

where r is the reaction rate under polarization (mol O/s), r_o is the reaction rate under open-circuit condition (mol O/s), I is the current (A), n is number of electrons and F is the Faraday's constant. EPOC of methane complete oxidation have been investigated using several catalysts, such as Pt [27], Rh [28,29], Pd [30,31] and Au and Ag [32]. Similar to conventional catalysis, Pd showed the highest catalytic activity at lower temperatures [30–35]. Roche *et al*. reported NEMCA studies of methane combustion on Pd deposited by physical vapor deposition (PVD) on YSZ. They demonstrated Faradaic efficiency of 2.4 under positive potential (U_{WR} = 1 V) application and a reaction mixture of CH_4/O_2: 2/10% at 500 ºC. The increase in the Faradaic efficiency occurred with the increase of the catalyst thickness, however it resulted in decrease of mass activity. In Matei *et al.*, NEMCA effect was studied for thin Pd film catalysts deposited by impregnation technique on dense and porous YSZ solid-electrolyte disk [33]. The rate enhancement ratio, ρ, of 1.2 and apparent Faradaic efficiency, Λ, of 17 was obtained under galvanostatic polarization (I = 5 mA) at 400 °C. Jiménez-Borja *et al*. investigated NEMCA effect for methane combustion on Pd/YSZ film catalyst with and without CeO_2 interlayer [36]. Addition of ceria interlayer led to significant reaction rate increase compared to Pd/YSZ due to oxygen storage capacity of ceria and stabilization of PdO active phase. The authors showed stable electrochemical promotion with the

rate enhancement ratio up to 2.1 at 470 °C, when CH_4/O_2: 0.4/1% ratio was used [37]. In all previous EPOC studies of methane complete oxidation on Pd, an electrophobic behavior was reported, i.e., reaction rate increase at positive polarization. This corresponds to increase of the catalyst work function that leads to decrease in the adsorption strength of electron acceptor adsorbates, i.e., oxygen, and strengthening of the adsorption bond of electron donor adsorbates, CH_4 [38,39].

Earlier EPOC studies on Pd for methane oxidation and for over 100 other catalytic systems, were carried out using continuous thin-film catalysts [40,41], characterized by high catalyst loading and low dispersion [42]. In the last decade, a strong emphasis has been made on the development and application of EPOC to nano-sized, highly-dispersed catalysts [43–50]. The use of nanostructured catalysts opens up the possibility of practical utilization of EPOC, and allows investigation of other similar phenomena in heterogeneous catalysis, i.e., metal-support interaction (MSI) and chemical promotion [51–56].

In the present work, we synthesized Ni_9Pd (Ni:Pd = 9:1 atomic ratio) nanoparticles using modified polyol method. The prepared Ni_9Pd NPs were deposited on YSZ solid-electrolyte and tested for methane complete oxidation under open-circuit and EPOC conditions, between 425 and 500 °C, and using various gas compositions. To the best of our knowledge, this is the first report on EPOC of bi-metallic nanoparticles with low noble metal content for complete methane oxidation.

8.2. Experimental

8.2.1. Synthesis of Ni_9Pd, Ni and Pd nanoparticles

Ni_9Pd nanoparticles (NPs) with Ni to Pd atomic ratio of 9-to-1 were synthesized using modified polyol synthesis method. To this end, 0.357 g of Nickel (II) chloride hexahydrate (Sigma Aldrich®) and 0.0296 g of palladium chloride (Fisher Scientific®) precursor salts were dissolved in 50 mL of ethylene glycol (Fisher scientific®) in a three-necked flask. The mixture was heated up to 100 °C and after 2 min at 100 °C, 1.7 mL of 0.1 M of hydrazine (50-60% purity - Sigma Aldrich®) was added to the mixture. Addition of hydrazine resulted in the formation of Ni-hydrazine complexes $[Ni\ (N_2H_4)_2]^{2+}$ (detected by the color change to blue) [57]. Then 4.5 mL of 0.1M NaOH was injected to the reaction mixture that reduced $[Ni(N_2H_4)_2]^{2+}$ complexes and Pd^{2+},

and lead to the formation of Ni_9Pd nanoparticles. The mixture was refluxed for additional 30 min to ensure complete reduction of precursor salts and then cooled to room temperature. The final Ni_9Pd nanoparticles were magnetic, which allowed their recovery from the solution using a ferrite ring permanent magnet. The solution was washed with ethanol, then centrifuged repeatedly with additional ethanol washes in between. The product was finally separated and dried in air.

Mono-metallic Ni NPs were synthesized using a procedure reported earlier in details [58], which follows the same aforementioned procedure minus the addition of Pd precursor. Mono-metallic Pd NPs were synthesized using 0.133 g of $PdCl_2$ dissolved in 25 mL of ethylene glycol and 0.8 M NaOH. The mixture was heated up to 160 °C and stirred for 3 h. The final colloidal solution was cooled down and washed several times with ethanol.

8.2.2. Catalyst characterization

The catalysts were examined by X-ray diffraction (XRD) using Rigaku ultima IV multipurpose diffractometer. The diffractometer was equipped with an X'Celerator detector with monochromatic CuKα radiation (λ= 1.5418 A°) at 40 kV and 44 mA. The scan was performed between 20 to 80 °2θ with a step of 0.03 °/s.

The particle crystallite size was estimated using Debye-Scherrer equation:

$$D = \frac{0.94\vartheta_{Cu}}{\beta_{1/2}\cos\theta} \qquad 8\text{-}3$$

where ϑ_{Cu} is the X-ray wavelength, $\beta_{1/2}$ is the line broadening over the full width at half maximum (FWHM) in radians, and θ is the Bragg angle.

Structure and morphology characteristics of the different catalytic layers were found using double aberration-corrected Scanning Transmission Electron Microscopy (STEM) with FEI Titan 80-300 HB in High-Angle Annular Dark-Field (HAADF) mode. To gain insight into the elemental distribution, Energy Electron Loss Spectroscopy (EELS) data at very high spatial resolution was collected with a Gatan K2 direct detection camera. HAADF- Energy Dispersive X-ray Spectroscopy (EDS) mapping was performed using FEI Tecnai Osiris STEM equipped with a field-emission electron source and four silicon drift detectors at 200 keV. Overall, the spatial distribution of nickel-palladium that results in mapping of elements present in a sample is allowed due to correlation between the intensity of energy loss of at a given characteristic energy (for a particular element excited by the primary beam) with the number of atoms probed by the primary

electron beam. Transmission Electron Microscopy (TEM) imaging for the nickel sample was obtained using JEOL 2100F TEM/STEM operating at 200 kV.

8.2.3. Electrochemical cell and reactor

A disk of 8 mol % Y_2O_3-stabilized ZrO_2 (YSZ) (TOSOH®) solid electrolyte with 19 mm diameter and 1 mm thickness was formed following the procedure reported earlier [59]. 1.5 g of YSZ powder was mechanically pressed at 5000 psi and densified to above 95% by heating to 1000 °C (10 °C/min) and dwelling for 1 h, followed by heating with similar rate to 1500 °C and dwelling for 6 hours [59].

Inert gold reference and counter electrodes were deposited on one side of the disk by applying thin gold paste coating (Gwent Group) of 0.2 and 1 cm^2 surface areas, respectively. This was followed by annealing in air at 500 °C. The catalyst-working electrode was deposited on the other side of the solid electrolyte disk (1 cm^2 surface area) opposing to the counter electrode. To this end, Ni_9Pd or mono-metallic Ni and Pd were dispersed in isopropanol and 10 μL of a suspension were deposited at a time with intermediate drying at room temperature. The resulting total metal loading was 0.3 mg of Ni_9Pd on YSZ (0.3 mg in total of which 0.03 mg is Pd). The loading of monometallic Pd and Ni was 0.3 mg.

Catalytic measurements were carried out at atmospheric pressure in the single-chamber capsule reactor reported earlier [53,55]. The working electrode side of the electrolyte was pressed against a catalytically inert gold mesh (1 cm^2) that served as a current collector, while the counter and reference electrodes were pressed directly against inert gold wires [58]. The inertness of gold mesh and electrodes was verified under reaction conditions. Two type K thermocouples (Omega®) were placed in vicinity of the electrochemical cell, one for temperature control and one for data acquisition.

8.2.4. Catalytic and electrochemical measurements

The reaction gases were oxygen (Linde, 99.99% O_2), methane (Linde, 99.99% CH_4), and helium (Linde, 99.997% He) as a carrier gas. The total flow rate was constant at 100 mL min^{-1}, unless otherwise stated. Gas composition was varied using MKS, 1259 C and 1261-C series flow meters. Non-dispersive infrared (NDIR) CO_2 gas analyzer (Horiba, VA-3000) and Mass

Spectrometer (MS) (Ametek®) were used in series to analyze the concentration of CO_2 along with H_2O, CO, CH_4 and O_2. A potentiostat-galvanostat (Arbin Instruments®, MSTAT) was connected to the electrodes to apply constant electric current or potential to the solid-electrolyte electrochemical cell.

8.3. Results and discussion

8.3.1. Physicochemical properties of bi-metallic Ni_9Pd and mono-metallic Ni and Pd nanoparticles

The XRD patterns of the as-prepared Ni_9Pd and mono-metallic Ni and Pd NPs catalysts are shown in Figure 8.1. Both Pd and Ni have face-centered cubic (fcc) structure with characteristic diffraction peaks: (111), (200) and (220). In Ni_9Pd pattern, the (111) reflection peak of Pd appears at 40.5 °2θ while that of Ni (111) at 44.4 °2θ. When compared to mono-metallic diffractograms, the (111) peaks of Pd and Ni are slightly shifted towards each other, i.e., Pd (111) is shifted to higher and Ni (111) is shifted to lower 2θ suggesting formation of bi-phase structure between the two metals. Furthermore, Pd and Ni (200) and (220) crystallite peaks are shifted in the same manner. The summary of the 2θ peak position and full width at half maximum ($\beta_{1/2}$) is shown in Table 8-1. Using the background at 55 °2θ and the FWHM of the corresponding (111) fcc peak, the crystallite size of Pd, in the bi-metallic Ni_9Pd, was found at 4 nm while that of Ni was 5 nm showing equivalent crystallite sizes of the two metals. The crystallite sizes of mono-metallic Pd and Ni were 8 and 30 nm, respectively.

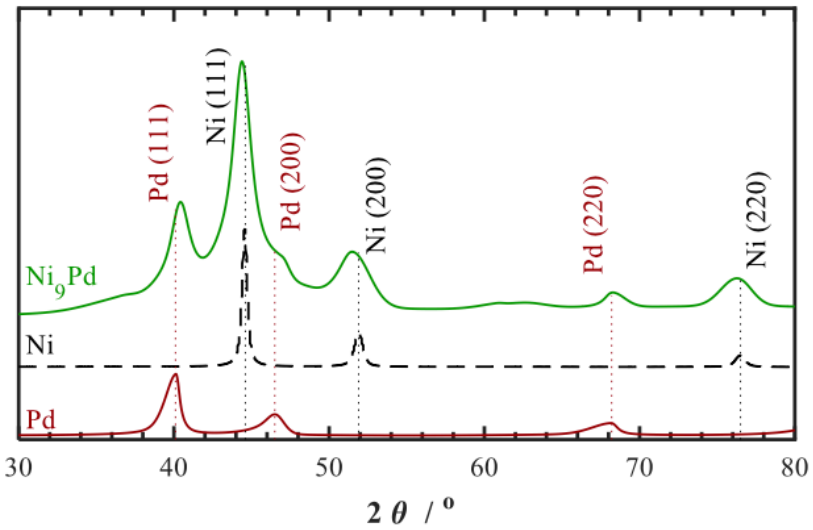

Figure 8.1: XRD patterns of mono-metallic Ni, Pd and bi-metallic Ni_9Pd catalysts.

Table 8-1: The peak position and full width at half maximum ($\beta_{1/2}$) for Ni_9Pd bi-metallic, and Pd and Ni mono-metallic catalysts.

Element	**Pd (111)**	**Ni (111)**	**Pd (200)**	**Ni (200)**	**Pd (220)**	**Ni (220)**
Ni_9Pd bi-metallic						
2θ position (°)	40.5	44.4	N/A	51.5	68.3	76.3
$\beta_{1/2}$ (°)	2.18	1.68	N/A	2.83	1.74	2.48
Ni mono-metallic						
2θ position (°)	-	44.6	-	51.9	-	76.5
$\beta_{1/2}$ (°)		1.5		0.6		0.8
Pd mono-metallic						
2θ position (°)	40.1	-	46.5	-	68.2	-
$\beta_{1/2}$ (°)	1.1		1.76		2.2	

The morphology and particle size were examined using ADF/STEM (Figure 8.2a) for Ni_9Pd and TEM (Figure 8.2b-c) for mono-metallic Ni and Pd. The particles of Ni_9Pd and Pd were spherical in shape with 10 nm average particle size for Ni_9Pd and 5 nm for mono-metallic Pd. Ni mono-metallic showed formation of spikes on its surface, adapting an urchin-like shape and 100-130 nm average particle size.

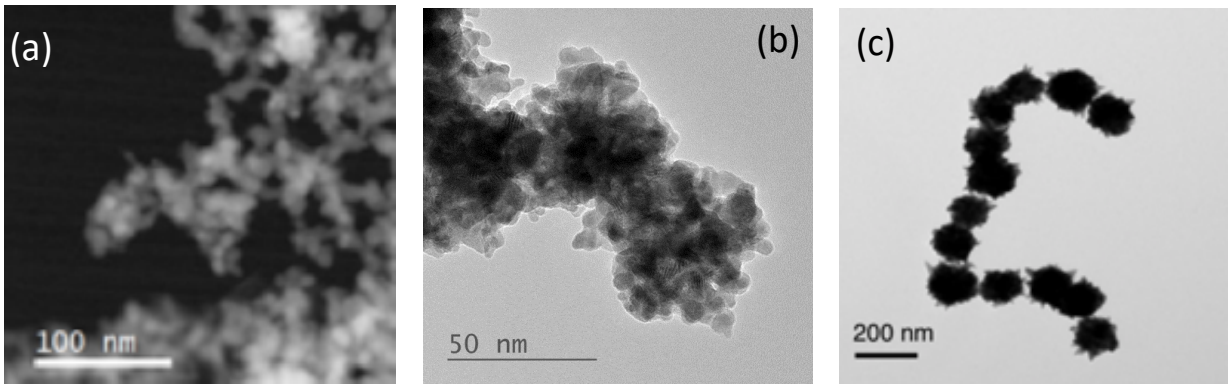

Figure 8.2: (a) HAADF/STEM of Ni9Pd and (b) TEM image of Pd NPs and (c) TEM images of Ni urchin-like NPs.

Further investigation of the structure and composition of Ni_9Pd was carried out using HAADF STEM-EDS and EELS (Figure 8.3 and Figure 8.4, respectively). In Figure 8.3a, HAADF-STEM image shows the morphology of the sample. The overall EDS map of the mixture of Ni and Pd is shown in (b) while their corresponding elemental mapping is shown in (c) and (d). It can be seen in Figure 8.3b the overall homogeneous mixing of both metals Ni and Pd in the catalyst (overlapping yellow color). In addition, more accurate high-resolution EELS mapping at 5 nm scale (Figure 8.4) showed that Ni_9Pd has a core double-shell distribution with palladium-rich core

surrounded with a Ni shell and on top of it a thin 3-4 nm layer of finely dispersed Pd. The Pd-rich core can be explained by the easier reduction of Pd during the NPs synthesis, if compared to Ni. In this case, the initially formed Pd clusters serve as seeds for Ni reduction and growth [60].

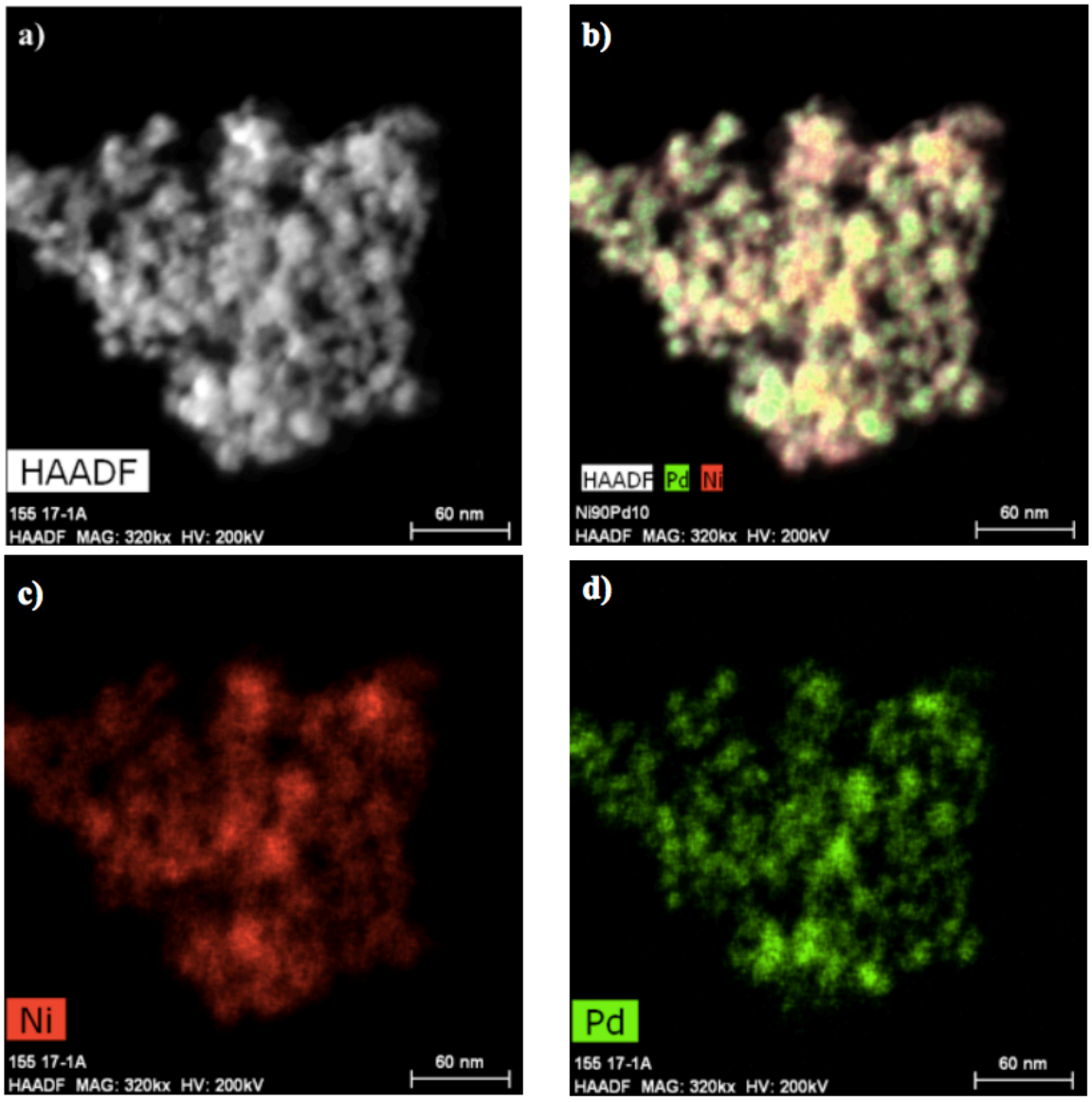

Figure 8.3: HAADF STEM image of Ni_9Pd (a) and resulting EDS mapping of Ni (red) and Pd (green) in (b), (c) and (d). Scale bar is 60 nm.

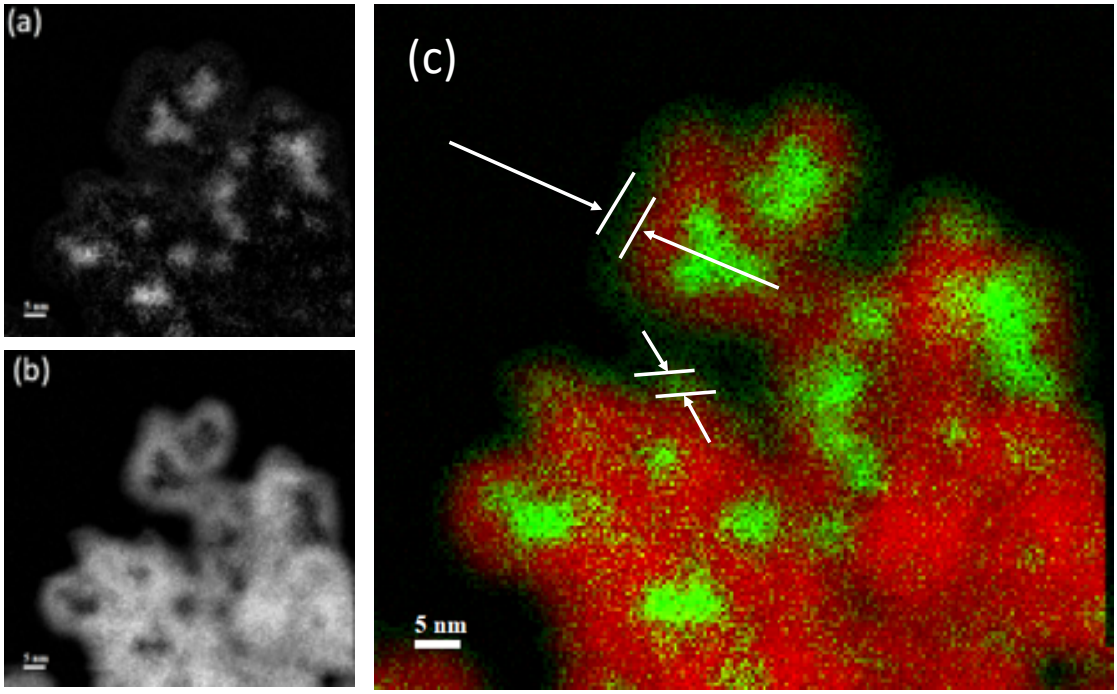

Figure 8.4: HAADF STEM-EELS and element mapping showing (a) Pd at signal range: 364.3-468.0 eV, (b) Ni at signal range: 848.0-885.8 eV and (c) combined color coded map of Pd shown in the core (green areas) and Ni (red) with a further outer Pd shell of 3–4 nm.

8.3.2. Open-circuit methane oxidation

The catalytic activity of Ni_9Pd for complete methane oxidation was investigated under open-circuit and compared to mono-metallic Ni and Pd catalysts. Figure 8.5a shows the higher open-circuit catalytic rate per gram of Pd (left axis) and gram of Ni (right axis) for Ni_9Pd compared to Pd and Ni mono-metallics. The higher mass activity of Ni_9Pd is due to the greater dispersion of small Pd clusters over Ni phase observed in the double shell-core structure (Figure 8.4c). The outer highly dispersed Pd shell is characterized by the higher active surface area and better gas accessibility. Furthermore, an electronic interaction between Ni and Pd clusters cannot be ruled out, as the work function of bulk Pd and Ni is 5.1 eV and 5.3 eV, respectively [61] and could reach much higher values for Pd clusters or single atoms [62]. Monometallic Ni showed very low catalytic activity in this temperature range, which is in agreement with the literature, as much higher temperatures (>550 °C) are required for efficient methane oxidation on Ni [63]. Figure 8.5b presents the variation in reaction rate as a function of reactants partial pressures for Ni_9Pd. For example, at P_{CH_4}=17 kPa and P_{O_2} in the range of 0.5–3.5 kPa, P_{O_2} was the limiting variable and therefore, rate of reaction increased linearly with the increase of P_{O_2}. However, at P_{CH_4}=2 kPa

and where P_{O_2}/P_{CH_4} was close to stoichiometry, insignificant variation of reaction rate occurred as a function of P_{O_2}. This is in agreement with the Eley-Rideal mechanism, where methane weakly bonds on the strongly adsorbed oxygen on Pd sites when partial pressure of oxygen and methane are similar [38]. Whereas, a Langmuir-Hinshelwood mechanism was followed at lower P_{O_2}/P_{CH_4} ratio due to the more available sites for CH_4 adsorption directly on Pd [38].

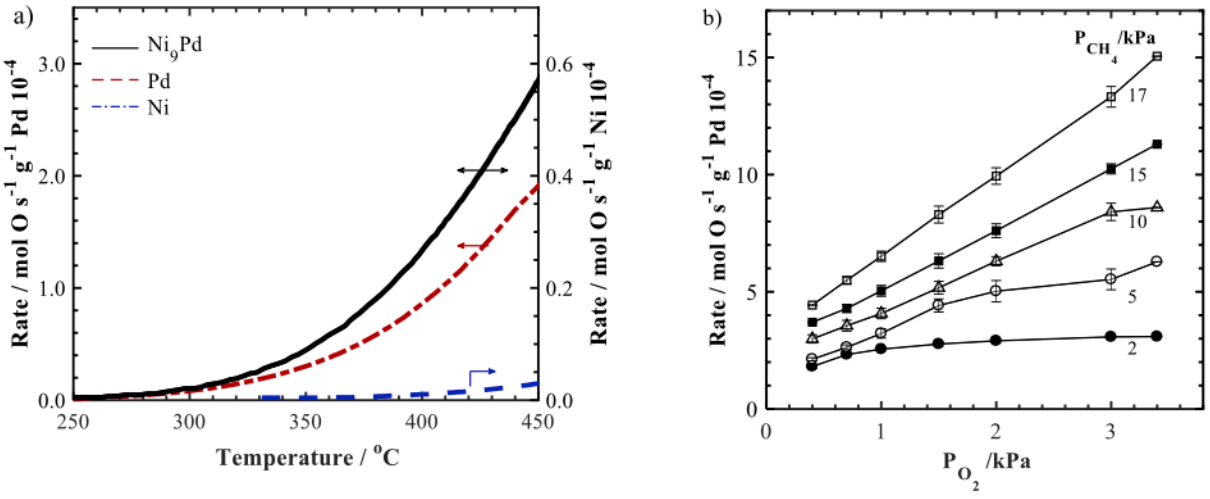

Figure 8.5: (a) Light of curves of catalytic complete methane oxidation (P_{CH_4}=2 kPa and P_{O_2}=4 kPa) over Pd, Ni and Ni_9Pd catalysts (b) Effect of oxygen and methane partial pressure on catalytic rate of Ni_9Pd at 450 °C.

8.3.3. Electrochemical promotion of methane oxidation

Figure 8.6 shows the reaction rate of Ni_9Pd and Pd during a constant positive current application (+80 μA) at stoichiometric ratio of P_{O_2}/P_{CH_4}= 2 at 450 °C. Contrary to Ni_9Pd and Pd NPs, mono-metallic Ni did not show any response to the applied potential or current at any temperature or gas compositions of this study. This could be related to the low open circuit activity of Ni in this temperature range [63]. EPOC of mono-metallic Pd NPs for complete methane oxidation showed lower o.c. catalytic rate in comparison to that of Ni_9Pd and additionally a slower reaction rate increase with positive current application without reaching the steady-state value even after 2h of polarization. This was explained by continuous activation of Pd by forming more active PdO_x surface as demonstrated in [64]. Upon the current interruption, the reaction rate slowly returned to its initial o.c. value for both Ni_9Pd and Pd indicating that the oxygen stored during positive polarization acted as a sacrificial promoters under open circuit. The time to return to the

initial o.c. rate value was 30 min and 1 h for Ni_9Pd and Pd, respectively. The 10 times higher Λ value found for monometallic Pd shows that while the reaction rate per mass of catalyst is in the same range for both catalysts, the rate per mole of oxygen (O s^{-1}) differs noticeably, because Pd loading in the bimetallic catalyst is 10 times less than in monometallic Pd catalysts.

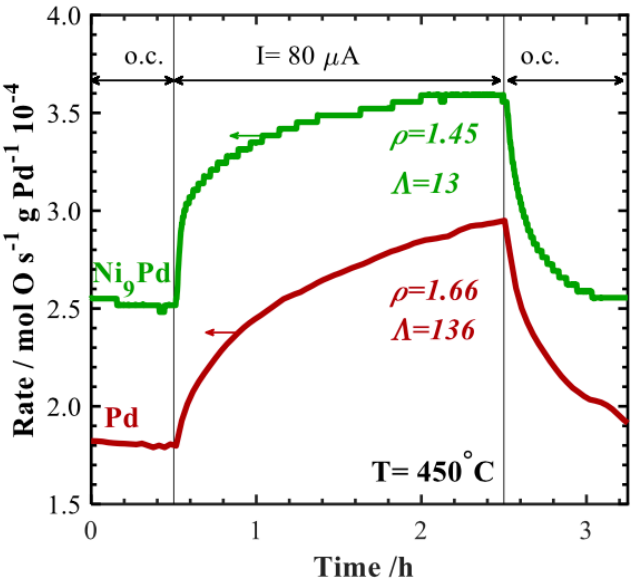

Figure 8.6: Transient rate response of Pd and Ni_9Pd NPs to applied positive current, 80 μA. Reaction conditions: T = 450 °C, P_{CH_4} = 2 kPa and P_{O_2} = 4 kPa, He balance.

Figure 8.7 shows the reaction rate response and corresponding current as a result of a constant positive potential application between the Ni_9Pd catalyst and the counter electrode at 425 °C. At the beginning of the experiment (t < 0.5 h), the open-circuit catalytic rate, r_o, was stable at a value of $1x10^{-8}$ mol O/s. When a constant potential U_{WR}= 0.5 V was applied, it caused an increase in the catalytic rate, reaching a new value of $1.92x10^{-8}$ mol O/s and resulting in a rate enhancement ratio, ρ of 1.92. The reaction rate increase is 21 times larger than the back-spillover supply of $O^{\delta-}$ onto the catalyst surface from the solid electrolyte [32]. According to EPOC mechanism, the presence of $O^{\delta-}$ species at the gas exposed catalyst surface and the resulting effective double-layer formation modifies the work function of the catalyst surface thus affecting the binding strength of covalently bonded adsorbates [25,56,65,66]. In fuel-lean conditions, increasing catalyst potential and its corresponding work function causes a weakening of the binding strength of electron acceptor adsorbates, e.g., chemisorbed oxygen. This results in weakening of Pd-O bond strength and thus facilitating dissociative step of oxygen from the surface of Pd as reported earlier for Pd

catalyst at 500 ºC [30,43]. Once the potential application was interrupted, the catalytic rate slowly (over 0.75 h) decreased to its initial value showing that the observed effect is reversible.

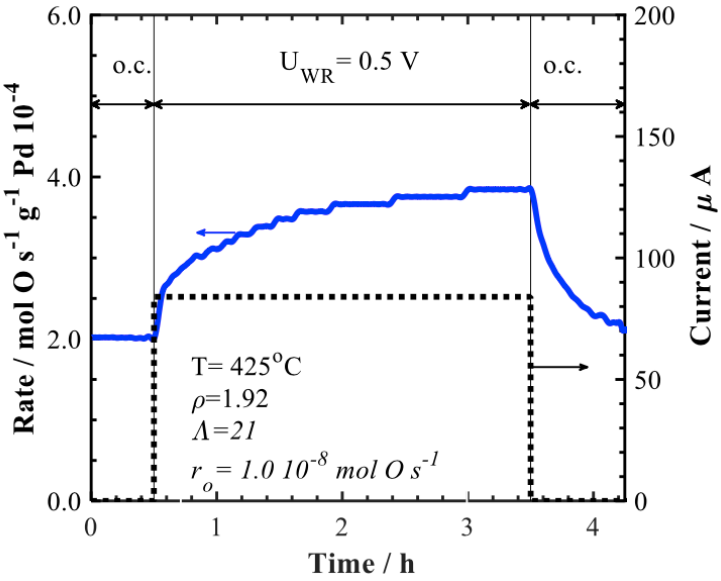

Figure 8.7: Transient rate response of Ni_9Pd NPs and corresponding current to a step change of an applied potential U_{WR} = 0.5 V; o.c.: open-circuit. Reaction conditions: T = 425 °C, P_{CH_4} = 2 kPa and P_{O_2} = 6 kPa, He balance.

Figure 8.8 summarizes the rate enhancement ratio and apparent Faradaic efficiency of EPOC results shown in Figure C 3. Figure 8.8 a demonstrates that the enhancement ratio of the methane oxidation was related to the oxygen coverage on the catalyst surface indicating that less oxygen was adsorbed onto the catalyst sites and hence a partial palladium oxide reduction occurred. In addition, the increase in the surface potential from 0.25 to 0.5 V led to a greater increase in the closed-circuit catalytic rate. The ρ value as a function of partial pressure ratio was higher at 425 °C than at 450 °C as the catalyst is in an already more enhanced state at a higher temperature; therefore, the migration of $O^{\delta-}$ towards the surface has a less significant influence on the rate at 450 than at 425 °C. A similar trend is shown in Figure 8.8 b for the apparent Faradaic efficiency as a function of the partial pressure ratio and temperature. Furthermore, transient rate responses upon constant applied potential at 0.5 V at 475 and 500 °C are shown in Figure C 4 and Figure C 5.

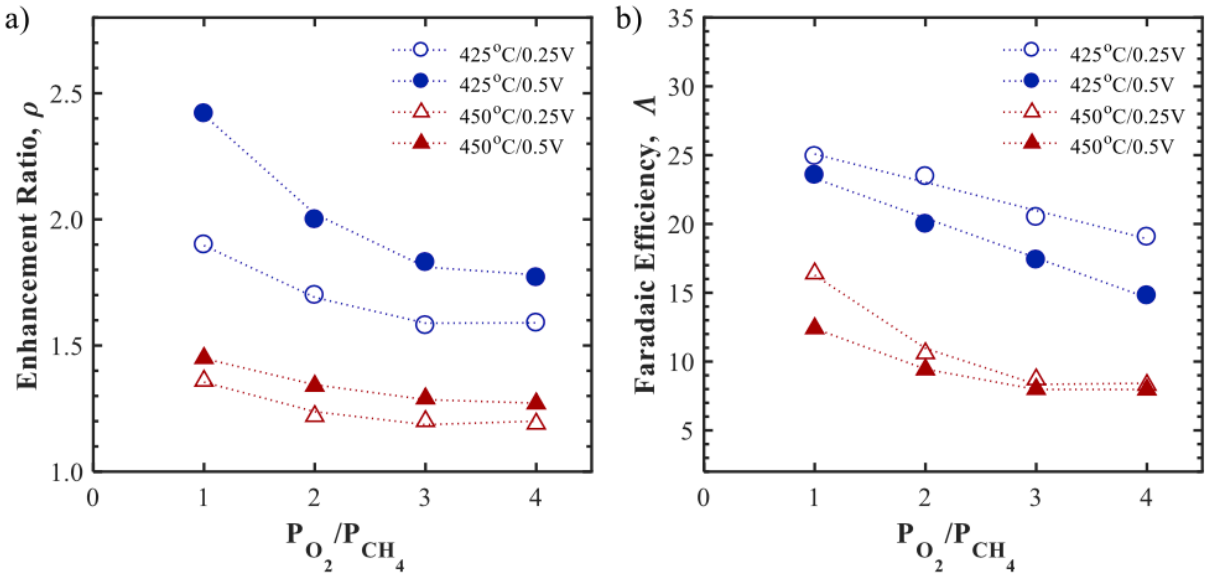

Figure 8.8: Effect of oxygen partial pressure on (a) the enhancement ratio and (b) Faradaic efficiency at 425 and 450 °C; U_{WR}= 0.25 and 0.5V. P_{CH_4}= 2 kPa.

It should be noted that electrochemical promotion of methane oxidation on Ni_9Pd was negligible in very lean fuel-conditions (not shown here). This is also supported by the literature where EPOC experiments were reported in stoichiometric or near stoichiometric conditions, due to the strong bonding of oxygen onto the Pd surface [36,38,43].

To further clarify the effect of oxygen partial pressure on the methane oxidation, we carried out EPOC experiments under fuel-rich conditions. The partial pressure of CH_4 was kept constant at 10 kPa and that of oxygen was varied between 0.4 and 17 kPa. The EPOC transient experiments upon positive polarization are shown in Figure C 6, while the enhancement ratio and apparent Faradaic efficiency are summarized in Figure 8.9 as a function of P_{O_2}/P_{CH_4} ratio. At a very low P_{O_2}/P_{CH_4} ratio, the Faradaic efficiency and enhancement ratio were more significant due to the ease of CH_4 adsorption under a constant positive potential application. This is to show that the electrochemical promotion of the CH_4 adsorption is more significant in reduced conditions where more sights for CH_4 are available on PdO_x surface. These electropromotion results are in good agreement with the open circuit behaviour of Ni_9Pd under various P_{O_2}/P_{CH_4} (Figure 8.5b), where the higher open and closed circuit reaction rates were observed under stoichiometric and fuel-rich conditions. At lower oxygen partial pressure, the partially oxidized PdO_x is more susceptible to positive current or potential application (work function increase), which destabilizes the oxide film forming the active PdO_x surface species. Under excess of oxygen the open circuit rate is low (Figure

8.5b) and no EPOC was observed because Pd is fully oxidized forming a thermodynamically stable oxide film.

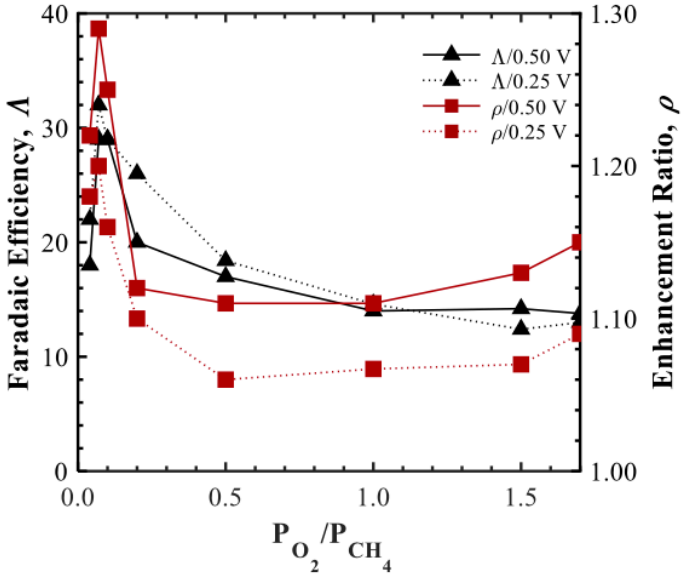

Figure 8.9: Faradaic efficiency and enhancement ratio corresponding to transient rate response of Ni_9Pd to a step change of an applied potential, U_{WR} = 0.25 and 0.5 V. Reaction conditions: T=450 °C. P_{CH_4}= 10 kPa, P_{O_2}/P_{CH_4} is a variable.

Figure 8.10a shows the effect of increasing the positive potential on Ni_9Pd catalyst at a constant P_{O_2}/P_{CH_4} ratio (1/10) and T = 425 °C. The application of higher current or potential corresponds to a great work function increase in agreement with the potential-work function relationship under the action of promoters [21,25].

Figure 8.10b shows the reaction rate increase, Δr, between open-circuit and closed-circuit values as a function of applied potential, represented by $O^{\delta-}$ flux (I/2F). The solid lines depict constant Faradaic efficiency, Λ lines. It can be seen that Faradaic efficiency was higher at lower applied potential, having a maximum value of 25 when 0.25 V was applied (i.e., 2.8 10^{-10} mol $O^{\delta-}$ s^{-1}).

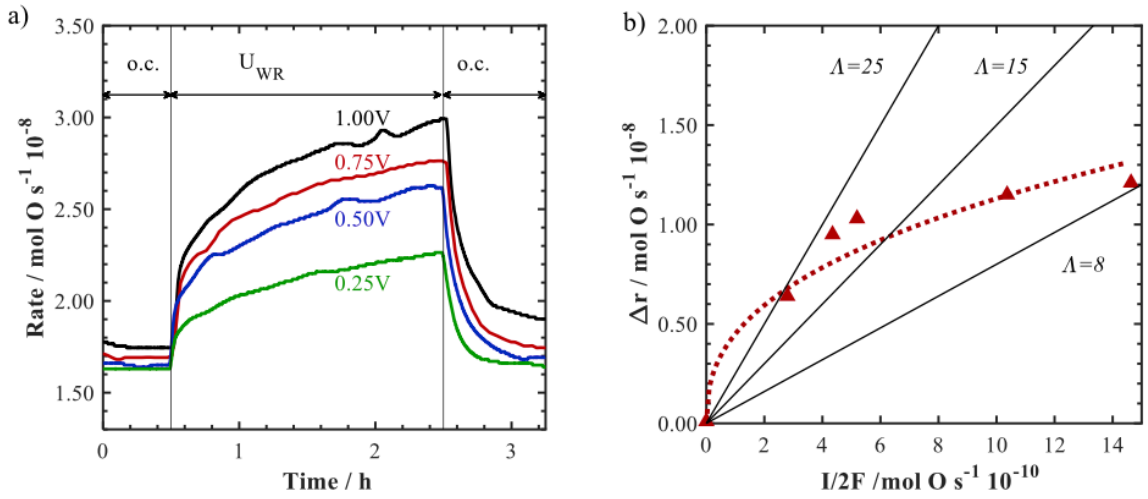

Figure 8.10: (a) Reaction rate response to a constant positive potential application on Ni_9Pd at 425 °C for P_{CH_4}=10 kPa, P_{O_2}= 1 kPa; (b) The reaction rate increase, Δr, as a function of applied potential, represented by $O^{\delta-}$ flux (I/2F).

Our results demonstrated that Ni_9Pd catalyst with core double-shell structure could be efficiently electropromoted using anodic polarization. The Pd core NiPd shell structure with the presence of nm-thick layer of highly dispersed Pd clusters on the Ni shell resulted in an active and stable catalytic performance under open-circuit and EPOC conditions. Furthermore, this configuration allowed a faster and more stable electrochemical promotion of Ni_9Pd compared to mono-metallic Pd (Figure 8.6).

8.4. Conclusions

Electrochemical promotion of Ni_9Pd nanoparticles with Pd core, Ni-Pd double-shell structure was investigated for complete methane oxidation reaction between 425 and 500 °C. The promotion of the catalytic activity of Ni_9Pd supported on YSZ solid electrolyte was achieved at positive polarization and outperformed the activity of mono-metallic Pd nanoparticles under open- and close-circuit conditions. Upon positive potential application between Ni_9Pd catalyst-electrode and the counter electrode, the electrophobic EPOC behavior resulted in a catalytic rate enhancement up to 240% with an apparent Faradaic efficiency of 25 at 425 °C. Variation of reactants composition showed that promotion was the highest under fuel-rich conditions compared to stoichiometric or fuel-lean conditions. The double shell-core structure with highly dispersed Pd clusters on the outer shell is responsible for the high activity of Ni_9Pd catalyst under open- and closed-circuit conditions due to the high active surface area of Pd clusters as well as likely

electronic interaction between Pd and Ni. Our work demonstrates that fabrication of well-defined bi-metallic nanoparticles with low noble metal content, as well as controlled surface structure and composition is of great importance for practical advancement of EPOC. Application of Ni_9Pd nanoparticles for complete methane oxidation has several advantages: the low noble metal content, and fast and stable EPOC. All this makes electrochemically activated Ni_9Pd catalyst potentially attractive for utilization in gas exhaust treatment devices.

References

[1] Z. Ristovski, L. Morawska, G.. Ayoko, G. Johnson, D. Gilbert, C. Greenaway, Emissions from a vehicle fitted to operate on either petrol or compressed natural gas, Sci. Total Environ. 323 (2004) 179–194.

[2] G. Karavalakis, T.D. Durbin, M. Villela, J.W. Miller, Air pollutant emissions of light-duty vehicles operating on various natural gas compositions, J. Nat. Gas Sci. Eng. 4 (2012) 8–16.

[3] J.H. Lee, D.L. Trimm, Catalytic combustion of methane, Fuel Process. Technol. 42 (1995) 339–359.

[4] S.H. Oh, P.J. Mitchell, R.M. Siewert, Methane Oxidation over Noble Metal Catalysts as Related to Controlling Natural Gas Vehicle Exhaust Emissions, in: Catal. Control Air Pollut., 1992: pp. 12–25.

[5] H.M. Cho, B.-Q. He, Spark ignition natural gas engines—A review, Energy Convers. Manag. 48 (2007) 608–618.

[6] B. Christian Enger, R. Lødeng, A. Holmen, A review of catalytic partial oxidation of methane to synthesis gas with emphasis on reaction mechanisms over transition metal catalysts, Appl. Catal. A Gen. 346 (2008) 1–27.

[7] J.B. Branco, A.C. Ferreira, T. Almeida Gasche, G. Pimenta, J.P. Leal, Low Temperature Partial Oxidation of Methane over Bimetallic Nickel-f Block Element Oxide Nanocatalysts, Adv. Synth. Catal. 356 (2014) 3048–3058.

[8] W. Lin, Y.X. Zhu, N.Z. Wu, Y.C. Xie, I. Murwani, E. Kemnitz, Total oxidation of methane at low temperature over Pd/TiO2/Al2O3: effects of the support and residual chlorine ions, Appl. Catal. B Environ. 50 (2004) 59–66.

[9] K. Sekizawa, H. Widjaja, S. Maeda, Y. Ozawa, K. Eguchi, Low temperature oxidation of methane over Pd catalyst supported on metal oxides, Catal. Today. 59 (2000) 69–74.

[10] C. Jimenez-Borja, F. Matei, F. Dorado, J.L. Valverde, Characterization of Pd catalyst-electrodes deposited on YSZ: Influence of the preparation technique and the presence of a ceria interlayer, Appl. Surf. Sci. 261 (2012) 671–678.

[11] M. Cargnello, J.J.D. Jaen, J.C.H. Garrido, K. Bakhmutsky, T. Montini, J.J.C. Gamez, R.J. Gorte, P. Fornasiero, Exceptional Activity for Methane Combustion over Modular Pd@CeO2 Subunits on Functionalized Al2O3, Sci. J. 337 (2012) 713–717.

[12] P. Briot, A. Auroux, Effect of Particle Size on the Reactivity of Oxygen- Adsorbed Platinum Supported on Alumina, Appl. Catal. 59 (1990) 141–152.

[13] M. Primet, E. Tena, L. Urfels, P. Ge, Complete oxidation of methane at low temperature over Pt catalysts supported on high surface area SnO2, Top. Catal. 30 (2004) 1–4.

[14] Y.-F. Yu Yao, Oxidation of Alkanes over Noble Metal Catalysts, Ind. Eng. Chem. Prod. Res Dev. 19 (1980) 293–298.

[15] C. Aliotta, L.F. Liotta, F. Deganello, V. La Parola, A. Martorana, Direct methane oxidation on La 1−x Sr x Cr 1−y Fe y O 3− δ perovskite-type oxides as potential anode for intermediate temperature solid oxide fuel cells, Appl. Catal. B Environ. 180 (2016) 424–433.

[16] A.I. Osman, J.K. Abu-Dahrieh, F. Laffir, T. Curtin, J.M. Thompson, D.W. Rooney, A bimetallic catalyst on a dual component support for low temperature total methane oxidation, Appl. Catal. B Environ. 187 (2016) 408–418.

[17] K. Persson, A. Ersson, S. Colussi, A. Trovarelli, S.G. Järås, Catalytic combustion of methane over bimetallic Pd-Pt catalysts: The influence of support materials, Appl. Catal. B Environ. 66 (2006) 175–185.

[18] K. Persson, A. Ersson, K. Jansson, N. Iverlund, S. Järås, Influence of co-metals on bimetallic palladium catalysts for methane combustion, J. Catal. 231 (2005) 139–150.

[19] H. Widjaja, K. Sekizawa, K. Eguchi, H. Arai, Oxidation of methane over Pd/mixed oxides for catalytic combustion, Catal. Today. 47 (1999) 95–101.

[20] J. Shen, R.E. Hayes, X. Wu, N. Semagina, 100° temperature reduction of wet methane

combustion: Highly active Pd-Ni/Al2O3 Catalyst versus Pd/NiAl2O4, ACS Catal. 5 (2015) 2916–2920.
[21] C.G. Vayenas, S. Bebelis, C. Pliangos, S. Brosda, D. Tsiplakides, Electrochemical Activation of Catalysis: Promotion, Electrochemical Promotion, and Metal-Support Interactions, Springer, New York, 2001.
[22] I. V Yentekakis, A. Palermo, N.C. Filkin, M.S. Tikhov, R.M. Lambert, In situ electrochemical promotion by sodium of the platinum-catalyzed reduction of NO by propene, J. Phys. Chem. B. 101 (1997) 3759–3768.
[23] C. Falgairette, A. Jaccoud, G. Fóti, C. Comninellis, The phenomenon of "permanent" electrochemical promotion of catalysis (P-EPOC), J. Appl. Electrochem. 38 (2008) 1075–1082.
[24] M. Stoukides, C.G. Vayenas, The effect of electrochemical oxygen pumping on the rate and selectivity of ethylene oxidation on polycrystalline silver, J. Catal. 70 (1981) 137–146.
[25] C.G. Vayenas, S. Bebelis, S. Ladas, Dependence of catalytic rates on catalyst work function, Nature. 343 (1990) 625–627.
[26] S. Bebelis, C.G. Vayenas, Non-faradaic electrochemical modification of catalytic activity. 1. The case of ethylene oxidation on Pt, J. Catal. 118 (1989) 125–146.
[27] P. Tsiakaras, C.G. Vayenas, Non-Faradaic Electrochemical Modification of Catalytic Activity VII. The Case of Methane Oxidation on Platinum, J. Catal. 140 (1993) 53–70.
[28] A. Nakos, S. Souentie, A. Katsaounis, Electrochemical promotion of methane oxidation on Rh/YSZ, Appl. Catal. B Environ. 101 (2010) 31–37.
[29] E.A. Baranova, G. Fóti, C. Comninellis, Current-assisted activation of Rh/TiO2/YSZ catalyst, Electrochem. Commun. 6 (2004) 389–394.
[30] V. Roche, R. Revel, P. Vernoux, Electrochemical promotion of YSZ monolith honeycomb for deep oxidation of methane, Catal. Commun. 11 (2010) 1076–1080.
[31] F. Matei, C. Jimenez-Borja, J. Canales-Vazquez, S. Brosda, F. Dorado, J.L. Valverde, D. Ciuparu, Enhanced electropromotion of methane combustion on palladium catalysts deposited on highly porous supports, Appl. Catal. B Environ. 132–133 (2013) 80–89.
[32] C.G.C.G. Vayenas, S. Bebelis, I. V. Yentekakis, H.-G. Lintz, Non-faradaic electrochemical modification of catalytic activity: A status report, Catal. Today. 11 (1992) 303–442.
[33] F. Matei, D. Ciuparu, C. Jiménez-Borja, F. Dorado, J.L. Valverde, S. Brosda, Electrochemical promotion of methane oxidation on impregnated and sputtered Pd catalyst-electrodes deposited on YSZ, Appl. Catal. B Environ. 127 (2012) 18–27.
[34] C. Jimenez-Borja, F. Dorado, A. de Lucas-Consuegra, J.M. Garcia-Vargas, J.L. Valverde, Complete oxidation of methane on Pd/YSZ and Pd/CeO2/YSZ by electrochemical promotion, Catal. Today. 146 (2009) 326–329.
[35] O.A. Mar'ina, V.A. Sobyanin, V.D. Belyaev, V.N. Parmon, The effect of electrochemical oxygen pumping on catalytic properties of Ag and Au electrodes at gas-phase oxidation of CH4, Catal. Today. 13 (1992) 567–570.
[36] C. Jiménez-Borja, F. Dorado, A. de Lucas-Consuegra, J.M. García-Vargas, J.L.J.L. Valverde, Complete oxidation of methane on Pd/YSZ and Pd/CeO2/YSZ by electrochemical promotion, Catal. Today. 146 (2009) 326–329.
[37] C. Jiménez-Borja, F. Dorado, A. de L.-Consuegra, J.M. G.-Vargas, J.L. Valverde, Electrochemical Promotion of CH4 Combustion over a Pd/CeO2-YSZ Catalyst, Fuel Cells. 11 (2011) 131–139.
[38] A. Giannikos, A.D. Frantzis, C. Pliangos, S. Bebelis, C.G. Vayenas, Electrochemical promotion of CH4 oxidation on Pd, Ionics (Kiel). 4 (1998) 53–60.
[39] S. Brosda, C.G. Vayenas, J. Wei, Rules of chemical promotion, Appl. Catal. B Environ. 68 (2006) 109–124.
[40] M. Makri, C.G. Vayenas, S. Bebelis, K.H. Besocke, C. Cavalca, Atomic resolution STM imaging of electrochemically controlled reversible promoter dosing of catalysts, Surf. Sci. 369 (1996) 351–359.
[41] I. Constantinou, I. Bolzonella, C. Pliangos, C. Comninellis, C.G. Vayenas, Electrochemical

promotion of RuO2 catalysts for the combustion of toluene and ethylene, Catal. Letters. 100 (2005) 125–133.
[42] P. Vernoux, L. Lizarraga, M.N. Tsampas, F.M. Sapountzi, A. De Lucas-Consuegra, J.L. Valverde, S. Souentie, C.G. Vayenas, D. Tsiplakides, S. Balomenou, E.A. Baranova, Ionically conducting ceramics as active catalyst supports, Chem. Rev. 113 (2013) 8192–8260.
[43] V. Roche, R. Karoum, A. Billard, R. Revel, P. Vernoux, Electrochemical promotion of deep oxidation of methane on Pd/YSZ, J. Appl. Electrochem. 38 (2008) 1111–1119.
[44] R. Karoum, V. Roche, C. Pirovano, R.-N. Vannier, A. Billard, P. Vernoux, CGO-based electrochemical catalysts for low temperature combustion of propene, J. Appl. Electrochem. 40 (2010) 1867–1873.
[45] A. Kambolis, L. Lizarraga, M.N. Tsampas, L. Burel, M. Rieu, J.-P. Viricelle, P. Vernoux, Electrochemical promotion of catalysis with highly dispersed Pt nanoparticles, Electrochem. Commun. 19 (2012) 5–8.
[46] A. de Lucas-Consuegra, F. Dorado, C. Jiménez-Borja, J.L. Valverde, Electrochemical promotion of Pt impregnated catalyst for the treatment of automotive exhaust emissions, J. Appl. Electrochem. 38 (2008) 1151–1157.
[47] M.N. Tsampas, F.M. Sapountzi, A. Boréave, P. Vernoux, Investigation of the Electrochemical Promotion of Catalysis origins on electrochemical catalysts with oxygen ion conductive supports : Isotopic labeling mechanistic studies, Solid State Ionics. 262 (2014) 257–261.
[48] Y.M. Hajar, V. Di Palma, V. Kyriakou, M.A. Verheijen, E.A. Baranova, P. Vernoux, W.M.M. Kessels, M. Creatore, M.C.M. Van De Sanden, M. Tsampas, Atomic layer deposition of highly dispersed Pt nanoparticles on a high surface area electrode backbone for electrochemical promotion of catalysis, Electrochem. Commun. 84 (2017) 40–44.
[49] C. Xia, M. Hugentobler, Yongdan-Li, C. Comninellis, W. Harbich, Quantifying electrochemical promotion of induced bipolar Pt particles supported on YSZ, Electrochem. Commun. 12 (2010) 1551–1554.
[50] C. Xia, M. Hugentobler, Y. Li, G. Foti, C. Comninellis, W. Harbich, Electrochemical promotion of CO combustion over non-percolated Pt particles supported on YSZ using a novel bipolar configuration, Electrochem. Commun. 13 (2010) 99–101.
[51] H.A.E. Dole, E.A. Baranova, Implementation of Nanostructured Catalysts in the Electrochemical Promotion of Catalysis, in: M. Aliofkhazraei, H.A.S. Makhlouf (Eds.), Handb. Nanoelectrochemistry, Springer International Publishing, Cham, 2015: pp. 1–26.
[52] R.J. Isaifan, E.A. Baranova, Effect of ionically conductive supports on the catalytic activity of platinum and ruthenium nanoparticles for ethylene complete oxidation, Catal. Today. 241 (2015) 107–113.
[53] H.A.E. Dole, A. Costa, M. Couillard, E.A. Baranova, Quantifying metal support interaction in ceria-supported Pt, PtSn and Ru nanoparticles using electrochemical technique, J. Catal. 333 (2016) 40–50.
[54] H.A.E. Dole, E.A. Baranova, Ethylene oxidation in an oxygen deficient environment : Why ceria is an active support ?, ChemCatChem. 8 (2016) 1977–1986.
[55] Y.M. Hajar, H.A. Dole, M. Couillard, E.A. Baranova, Investigation of heterogeneous catalysts by electrochemical method: Ceria and titania supported iridium for ethylene oxidation, ECS Trans. 72 (2016) 161–172.
[56] J. Nicole, D. Tsiplakides, C. Pliangos, X.E.E. Verykios, C. Comninellis, C.G.G. Vayenas, Electrochemical Promotion and Metal–Support Interactions, J. Catal. 204 (2001) 23–34.
[57] G. yong Huang, S. ming Xu, G. Xu, L. yan Li, L. feng Zhang, Preparation of fine nickel powders via reduction of nickel hydrazine complex precursors, Trans. Nonferrous Met. Soc. China (English Ed. 19 (2009) 389–393.
[58] Y.M. Hajar, M.S. Houache, U. Tariq, P. Vernoux, E.A. Baranova, Nanoscopic Ni interfaced with oxygen conductive supports: Link between electrochemical and catalytic studies, Electrochem. Soc. 77 (2017) 51–66.

[59] I.R. Gibson, G.P. Dransfield, J.T.S. Irvine, Sinterability of commercial 8 mol % yttria-stabilized zirconia powders and the effect of sintered density on the ionic conductivity, J. Mater. Sci. 33 (1998) 4297–4305.
[60] Q. Chang, Y. Xu, Z. Duan, F. Xiao, F. Fu, Y. Hong, J. Kim, S. Il Choi, D. Su, M. Shao, Structural Evolution of Sub-10 nm Octahedral Platinum-Nickel Bimetallic Nanocrystals, Nano Lett. 17 (2017) 3926–3931.
[61] H.L. Skriver, N.M. Rosengaard, Surface energy and work function of elemental metals, Phys. Rev. B. 46 (1992) 7157–7168.
[62] E. Roduner, Size matters: why nanomaterials are different, Chem. Soc. Rev. 35 (2006) 583.
[63] M.M. Pakulska, C.M. Grgicak, J.B. Giorgi, The effect of metal and support particle size on NiO/CeO2 and NiO/ZrO2 catalyst activity in complete methane oxidation, Appl. Catal. A Gen. 332 (2007) 124–129.
[64] Y.M. Hajar, B. Venkatesh, E.A. Baranova, Electrochemical Promotion of Nanostructured Palladium for Complete Methane Oxidation, Catalysts. 9 (2018) 48.
[65] A.D. Frantzis, S. Bebelis, C.G. Vayenas, Electrochemical promotion (NEMCA) of CH4 and C2H4 oxidation on Pd/YSZ and investigation of the origin of NEMCA via AC impedance spectroscopy, Solid State Ionics. 136–137 (2000) 863–872.
[66] C.G. Vayenas, C.G. Koutsodontis, Non-Faradaic electrochemical activation of catalysis, J. Chem. Phys. 128 (2008).

Chapter 9 Theoretical Insight into Origin of Electrochemical Promotion of Ethylene oxidation on Ruthenium Oxide

Y. M. Hajar, L. Treps, C. Michel, E. A. Baranova and S. N. Steinman, Accpeted in Catal. Sci & Tech.
doi: 10.1039/c9cy01421g.

In electrochemical promotion of catalysis (EPOC), the adsorption energies of reactants and products, and subsequently the overall reaction catalytic rate are modified by applying an electrochemical potential to the catalyst. In this paper, the oxidation of ethylene on ruthenium oxide was studied by experiments and theoretical modeling in order to elucidate the atomistic origin of EPOC. The experimental results have shown an increase in the reaction rate under negative and positive polarization. Density functional theory (DFT) based surface free energies demonstrated that there is an increase in oxygen coverage on the ruthenium surface as a function of the potential, conforming with the backspillover model of EPOC. Furthermore, DFT results demonstrated that the positive polarization and the associated electric field, which increases the work function, results in enhanced adsorption and facilitated cleavage of the C-C bond of ethylene. Under negative polarization, on the other hand, it is the oxygen activation that is facilitated. Together, these two pieces of the puzzle explain the experimental increase of the ethylene oxidation rate as a function of positive and negative potential, proving the effect of an electric field on the adsorption rate and activation energy of ethylene oxidation.

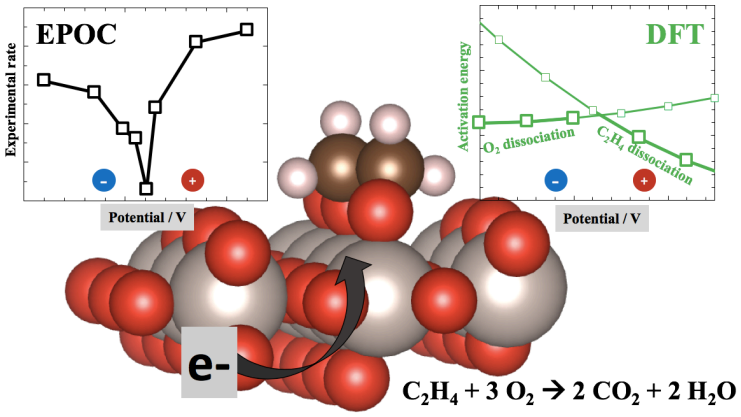

9.1. Introduction

Metal-support interaction (MSI) and alkali metal doping are two methods that tune a catalyst performance through the modification of the surface's electronic structure, and concomitantly, the binding energy of the chemisorbed species [1,2]. Alternatively, based on the work of Wagner [3], Vayenas and co-workers progressed in working on the effect of an electrochemical supply or removal of ions to or from a catalyst deposited on solid ionically-conducting electrolytes, e.g., Y_2O_3-doped ZrO_2 (YSZ, O^{2-} conductor), $BaZr_{0.8}Y_{0.2}O_{3-\delta}$ (BZY , H^+ conductor), β"-Al_2O_3 (K^+ conductor), etc. [4–7]. They demonstrated a reversible alteration of

catalytic activity and in some cases selectivity when an electric current or potential is applied [8–10]. This phenomenon, called Electrochemical Promotion of Catalysis (EPOC), or Non-Faradaic Electrochemical Modification of Catalysis (NEMCA), has been shown to be functionally equivalent to MSI effect between a dispersed catalyst phase and conducting supports (TiO_2, CeO_2, ZrO_2, etc.) but is operationally more controlled, as it allows an *in-operando* modification of the electronic properties of catalysts [8]. Our recent paper has demonstrated the functional equivalency between EPOC and MSI as we have compared the promotive effect of supporting nanoparticles on metal oxides to electrochemically promoting the nanoparticles. The rates increase due to EPOC and supporting the catalysts on active metal oxides were similar in the case of platinum and ruthenium catalysts [11]. Furthermore, many highly dispersed electrochemically promoted systems have been established, rendering the practical application of EPOC more attractive [11,12,21–24,13–20]. Experimentally, the origin of EPOC is mostly explained by the electrochemically induced promoters (see Figure 9.1), which have been substantiated by many in-situ and ex-situ techniques: x-ray photoelectron spectroscopy (XPS) [25,26], in-situ XPS [27], temperature-programmed desorption (TPD) [28,29], scanning tunneling microscopy (STM), photoemission spectroscopy (PES) [30], in-situ AC impedance spectroscopy [31,32], and isotopic exchange [33]. When applying an electrochemical potential across a solid electrolyte on which a metallic catalyst is adsorbed, ions originating from the solid electrolyte, $O^{\delta-}$ in case of YSZ, are (partially) discharged at the three-phase boundary and migrate to the gas exposed catalyst surface to formally form a double layer $O^{\delta-}$ - δ^+ (δ^+ is the mirror charge in the conductor for preserving the neutrality). Figure 9.1 demonstrates the oxygen migration in the case of a continuous catalyst film similar to what has been used in previous papers [34–36]. It has been determined that in the presence of oxygen ions there is a one-to-one correlation between the applied potential (U_{WR}) and the change in work function ($\Delta\Phi$) at the metal-gas interface in a wide range of temperatures [6,37] (Equation 9-1):

$$e\Delta U_{WR} = \Delta\Phi \qquad 9\text{-}1$$

Therefore, the density of this double layer and subsequently the work function of the catalyst are *in-operando* controlled by an electrochemical potential application. The change of work function leads to catalytic rate and selectivity alternation due to the change in the adsorption properties of reactants and/or intermediates. Since the coverage effect is experimentally detectable, most of EPOC is rationalized in terms of an increased/decreased availability of the promoter on

the surface, suggesting a direct implication of the promoter. However, these experiments do not directly observe the reactive surface species and the promoter might just generate an electrostatic field, which itself impacts the kinetics of the reaction [38,39]. Therefore, computational mechanistic studies are complementary to the experimental characterizations.

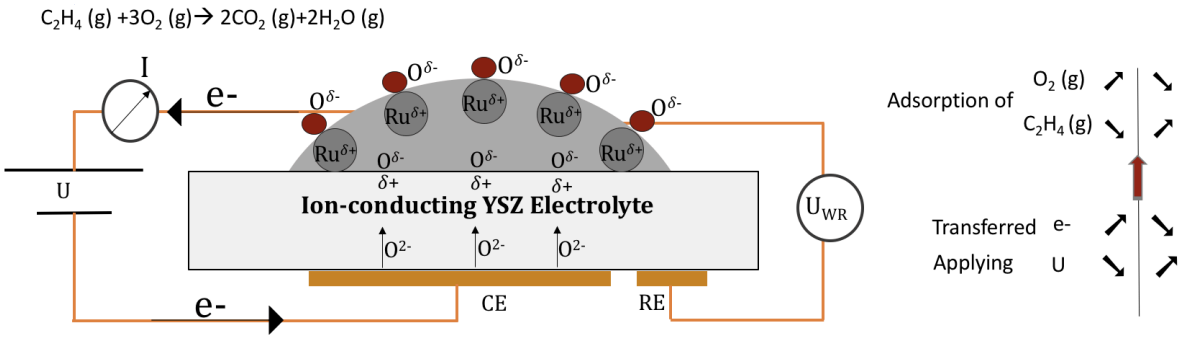

Figure 9.1: A schematic representation of ruthenium electrode deposited on O^{2-} conducting YSZ solid electrolyte, showing the locations of the metal/electrolyte double layer [$O^{\delta-}$ $\delta+$] and the effective double layer created at the metal/gas interface. The potential-controlled ion migration (backspillover) and charge transfer affect the adsorption strength of electropositive ethylene and electronegative oxygen gas species (shown on the right).

Early theoretical modeling of EPOC was performed using clusters of metallic atoms to model the Cl adsorption on Cu and O adsorption on Pt surface [40,41]. In the case of co-adsorption of Cl and benzene on the surface of Cu, Pacchioni *et al.* showed that Cl induces an increase in the Cu work function and therefore an increase in the adsorption energy of the benzene product resulting in an inhibition of the acetylene trimerization reaction [40]. In the case of O adsorption on Pt, the authors drew a correlation between the increase in the catalyst-electrode potential and corresponding work function and the decrease in the experimental peak temperature of adsorbed oxygen [41]. However, they showed subsequently that the oxygen desorption temperature is not directly correlated to the oxygen desorption energy, concluding that the effect of the change in work function on the bonding of adsorbed molecules (reactants and products) depends on the nature of the surface's chemical bond [40]. Later, Leiva *et al.*, have investigated the effect of the positive charge of Na on the work function of the Pt surface and compared it to when oxygen was jointly present [42].

In more recent theoretical modeling studies, the effect of external and internal electric field on the activity of catalysts was investigated with correspondence to solid oxide fuel and electrolysis cells [38,39,42–46]. A cluster model and hybrid density functional theory (DFT) calculations were used by González *et al.* to simulate the electric field effect on the adsorption of

CO on Cu, Rh and their bimetallics [44]. They concluded that the CO bond increases in strength with a positive electric field. Chen *et al.* used a dipole layer to model the electric field effect on the Ni/YSZ interface [43]. They found that a positive potential increases the activation energy of oxygen vacancy formation, therefore reducing the deactivation mechanism of the catalyst-electrode at the three-phase boundary. In another work, the activation energy of C-H dissociation in methane was found to increase as a function of the field strength resulting in a decrease of the methane steam reforming reaction [38].

Herein, we rely on the model reaction of ethylene oxidation [31,32,34–36,47–50] to demonstrate, using ab-initio computations, the effect of electrochemical potential on the surface reactivity. We elucidate on the one hand the impact of the electrochemical potential on the surface state compared to thermal catalysis and on the other hand, the impact of the potential generated electric field on the reactivity of ethylene and oxygen activation. To be more precise, the most stable surface oxygen termination is determined as a function of the electrochemical potential. For a given surface state, the adsorption and dissociation energies of gaseous ethylene and oxygen are dependent on the potential-generated electric field, which is modeled through modification of the total surface charge.

9.2. Theory and computational method

9.2.1. Slab model and computational details

Plane wave DFT calculations were performed using projector augmented wave pseudopotentials provided in VASP (Vienna Ab-initio Simulation Package) [51,52]. The energy evaluation exploited the generalized gradient approximation (GGA) with a Perdew-Burke-Ernzerhof (PBE) exchange-correlation functional together with the density-dependent dispersion correction dDsC [53,54]. Additional computations at the Heyd-Scuseria-Ernzerhof (HSE) level of theory of the work function of the three main surfaces of RuO_2 show that the PBE work function is in excellent agreement with experimental values (5.8 to 6.6 V) [55], while the HSE results are 0.5 V higher compared to PBE and reach 7.1 V for the most oxygenated surface (Figure S17). Nevertheless, even the 0.5 V difference between HSE and PBE is small enough to ensure that the qualitative mechanistic insight gained in this study does not significantly depend on the level of theory.

In the bulk rutile structure of RuO_2, the Ru atoms are six-fold coordinated to oxygen atoms, while O atoms are coordinated to three Ru atoms in a planar sp^2 hybridization [56]. The surface energies of the bulk-truncated, bridging-oxygen- terminated RuO_2 (110), RuO_2 (100), and RuO_2 (101) surfaces were determined by previous DFT calculations and the (110) facet shown to be the most stable one and thus prevailing for polycrystalline RuO_2 [57]. On the RuO_2 (110) surface, a weakly bound oxygen species can be found to adsorb on-top (O^{ot}) of the otherwise five-fold coordinatively unsaturated Ru (5*f*-cus-Ru), while stronger bridging oxygen (O^{br}) atoms are found on the otherwise four-fold coordinated Ru sites (6*f*-cus-Ru) [58].

The slab used to model RuO_2 (110) rutile [59] film is made out of three layers of Ru with intermediate O resulting in a ~10 Å thick slab. The intermediate layer is fixed, but all other atoms are allowed to relax during the computation until the forces are less than 0.03 eV/Å. A vacuum spacing of 15 Å was included to reduce the periodic interaction in the surface normal direction. The effect of vacuum spacing is shown in Figure D 9. In terms of unit size, a 6.2058 x 6.2897 x 25.1387 $Å^3$ cell with a corresponding 6 x 6 x 1 Monkhorst-Pack k-point mesh is used. The highest frequency of the plane wave basis set corresponds to a cut-off energy of 550 eV (Figure D10) and the electronic energy is converged to reach a threshold of 10^{-6} eV. Isolated molecules are optimized using the same parameters at the gamma point using a cubic box of $(8000\ Å)^3$.

The electrochemical promotion effect on the catalyst slab was modeled by the surface charging method [60], also known as grand-canonical DFT [61–64]. In this method, the number of electrons is changed, which modifies the surface charge and thus the work function of the slab considered. Since the system is periodic, a counter charge has to be introduced. The use of an implicit solvent model through the linearized Poisson-Boltzmann equation, [65,66] as implemented in the VASPsol module, [67] has been validated for the adsorption of pyridine on Au (111) by Steinmann *et al.* [68]. The use of symmetric slabs together with the linearized Poisson-Boltzmann equation allows to unambiguously reference the Fermi-level to the potential far away from the surface, assumed to correspond to vacuum. The effect of the addition of charges on the electrochemical potential (i.e., work function) for different systems is shown in Figure D11. Such a surface polarization by modifying the surface charge also introduces an electric field as analyzed by us in our previous work [69]. Moreover, the implicit solvation model places a quantum-mechanical solute in a cavity surrounded by a continuum dielectric description of the solvent and counter-charge distribution, allowing to mimic the effective electrochemical double layer [70,71].

In EPOC there is no solvent present, just an effective double layer generated, in our case, by the varying amount of oxygen species. The diffuse counter-charge added through the linearized Poisson-Boltzmann equation to neutralize the system is a proxy to model the effect of smoothly varying oxygen coverages, in analogy to our previous work on the indirect effects of bases in heterogeneous catalysis [69,72]. We have carefully assessed the influence of the relative permittivity of the "solvent" and the cavity size (Figure D12 and D13). Both have been found to have a negligible effect on the surface free energies of the three main surface terminations ($2O^{br}/2O^{ot}$, $2O^{br}/2Ru$, and 2Ru/2Ru). We conclude, therefore, that the obtained results do not significantly depend on the choice of technical parameters that have no clear meaning in EPOC and that the surface charging in combination with the linearized Poisson-Boltzmann equation is a convenient and efficient computational model to investigate EPOC.

To find the minimum energy pathway between adsorption of ethylene and its consecutive dissociation, transition state computations were performed using the *Nudged Elastic Band* (NEB) method in combination with *Dimer* method and *Quasi-Newton* (QN) optimization. In practice, the NEB computations were used to generate good guesses for the TS for the neutral surface, i.e., the NEB is not converged. This guess is then converged to the TS by the Dimer method and the obtained structure was verified to yield a single imaginary frequency consistent with the reaction path under study using vibrational frequency analysis. Finally, the potential dependence of the TS is obtained by optimizing the TS using the QN algorithm as a function of the surface charge.

9.2.2. Ab initio atomistic thermodynamics including the electrochemical potential

Thermodynamic stability of a surface can be derived by comparing a multitude of surface structures and their corresponding surface free energy (SFE) $\gamma\left(T, P_{O_2}\right)$ (Equation 9-2). The surface with the lowest SFE is the most stable structure. Following the work of Reuter *et al.*[73], the two variables that are required for the calculation of RuO_2 (110) surface free energy are temperature (*T)* and oxygen partial pressure (P_{O_2}).

$$\gamma\left(T, P_{O_2}, N_{Ru}, N_O\right) = \frac{1}{2S}\left\{E^{slab}_{RuO_2}(N_{Ru}, N_O) - N_{Ru}\, E^{bulk}_{RuO_2} + (2\,N_{Ru} - N_O)\,\frac{1}{2}\left[\mu^o_{O_2}(T) + RTln\frac{P_{O_2}}{P^o_{O_2}}\right]\right\} \qquad 9\text{-}2$$

Where 2S serves to normalize γ by the two surfaces S of the symmetrical unit cell. The Gibb's energy of the bulk is taken equal to the electronic energy computed for the primitive cell of the bulk $E_{RuO_2}^{bulk}$, while the free energy of the surface is approximated by the electronic energy $E_{RuO_2}^{slab}$. N_{Ru} and N_O are numbers of Ru and O atoms in the supercell, while $P_{O_2}^o$ is the standard pressure. The determination of the standard chemical potential of oxygen $\mu_{O_2}^o$ and the detailed derivations are given in section 4 of the ESI.

In equation 2, the oxygen supply is gaseous, whereas, in EPOC conditions, the oxygen is supplied in its ionic form from the oxygen-conducting electrolyte material as follows:

$$O^{2-}(YSZ) + RuO_2 \rightarrow O@RuO_2 + 2e^- \qquad 9\text{-}3$$

It has been established that the equilibrium potential of SOE with respect to vacuum is 5.14 V [74], whereas that of SHE is 4.44 V [75]. Therefore, the equilibrium potential of SHE with respect to SOE is equal to -0.7 V.

As shown in the ESI, the chemical potential of oxygen anions $\mu_{O^{2-}}$ is linked with the chemical potential of oxygen from the gas phase and the applied potential, so that the surface free energy becomes:

$$\gamma\left(T, P_{O_2}, N_{Ru}, N_O, U_{anode/SHE}\right) = \frac{1}{2S}\left\{\begin{array}{c} E_{RuO_2(N_{Ru}, N_O, U_{anode/SHE})}^{slab} - N_{Ru}\, E_{RuO_2}^{bulk} \\ +(2\,N_{Ru} - N_O)\left(\frac{1}{2}\left[\mu_{O_2}^o(T) + RTln\frac{P_{O_2}}{P^o}\right] + 2e\left(U_{anode/SHE} - 0.7\,V\right)\right) \end{array}\right\} \qquad 9\text{-}4$$

9.2.3. Adsorption energy calculation including electrochemical potential

The adsorption energy on a symmetrical RuO_2 surface adsorbing one C_2H_4 from each side is expressed by:

$$E_{ads} = \frac{1}{2}\left[E_{2C_2H_4/surf} - \left(2 \times E_{C_2H_4} + E_{surf}\right)\right] \qquad 9\text{-}5$$

Where $E_{2C_2H_4/surf}$ is the energy of the state containing two symmetrically adsorbed C_2H_4, E_{surf} is the energy of the bare surface, and $E_{C_2H_4}$ is the energy of an isolated C_2H_4 molecule in the gas phase. From the equation above, a more negative value for the adsorption energy indicates a more stable adsorbed C_2H_4 on the RuO_2 (110) surface. The adsorption is performed symmetrically

on both surfaces to avoid spurious dipole interactions. The C_2H_4 coverage corresponded to 25 % of the Ru density on the surface.

The presence of an electrochemical potential is likely to affect the electronic energy of the surface and of the ethylene adsorbed on the surface, resulting in a change of the adsorption energy of molecule as follows:

$$E_{ads}\left(U_{\frac{anode}{SHE}}\right) = \frac{1}{2}\left[E_{2C_2H_4/surf}(U_{anode/SHE}) - \left(2 \times E_{C_2H_4} + E_{surf}(U_{anode/SHE})\right)\right] \quad 9\text{-}6$$

As explained in section 2.1, the VASPsol module allows the modification of the surface charge (and thus the work function, i.e., the electrochemical potential) of the slab and thus mimicking the effect of the effective double layer. Performing geometry optimisations at various charges, we can fit the relation between the electronic energy and the electrochemical potential for the bare slab, E_{surf}, and for the one containing two symmetrically adsorbed C_2H_4, $E_{2C_2H_4/surf}$. Then, the dependence of the adsorption energy upon the electrochemical potential is trivially derived. The procedure is illustrated in Figure S15 and is analogously applied for all adsorbed species, including transition states, as illustrated in Figure S16.

9.3. Experimental details

9.3.1. Synthesis of RuO_2 nanoparticles

Ruthenium oxide (RuO_x) nanoparticles were synthesized using the polyol synthesis method [76]. In short: 0.105 g of Ruthenium (III) chloride (Sigma Aldrich®) precursor salt was dissolved in 15 mL of ethylene glycol (Fisher Scientific®) containing 0.25 M tetra-methyl ammonia hydroxide (TMAH) (Sigma Aldrich®). The solution was pre-mixed for an hour in a round-bottom flask then heated up to 160°C under reflux and cooled down directly after the temperature was reached. The initial pH of the synthesis solution was 12 and dropped to 7 after the reflux indicating nanoparticles formation [76].

9.3.2. Physiochemical characterization

The Scanning Transmission Electron Microscopy (STEM) micrographs of ruthenium oxide nanoparticles were performed using FEI Titan3 80 - 300 microscope operated at 300 kV and equipped with an energy dispersive X-ray (EDX) spectrometer. Annular Dark Field (ADF) images

were taken using a Fishione detector to provide a contrast between the nanoparticles and the support at convergence and collection angles of 17 and 60 mrad, respectively. The RuO_2 colloidal solution was diluted and sonicated in ethanol and then deposited dropwise on a 200 mesh copper grid coated with a lacy carbon support film (Ted Pella). The ImageJ® software was used to find the distribution of the ruthenium oxides RuO_x nanoparticles size. Figure 9.2a shows a representative STEM of the free-standing nanoparticles of ruthenium oxide. The ADF image represents the nanoparticles as bright spots on the darker background. The particle size distribution is shown in the histogram in Figure 9.2b and the average particle size was calculated to be 0.9 nm.

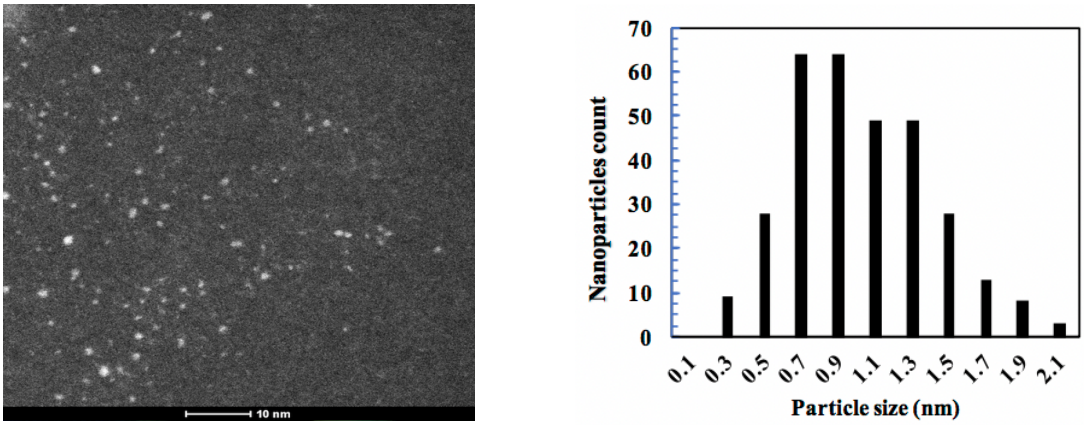

(a) (b)

Figure 9.2: STEM of ruthenium colloid and corresponding particle size distribution. Scale bar is 10 nm.

9.3.3. Electrochemical cell and reactor

Colloidal solution of ruthenium oxide nanoparticles was deposited 10 μL at a time on the yttria-stabilized zirconia (YSZ) solid electrolyte (1.9 cm^2), with intermittent drying at 100 °C. The final metal loading was 0.1 mg of RuO_x covering 1 cm^2 surface area of the YSZ electrolyte. On the other side of the electrolyte, the catalytically inert gold counter electrode (CE) and reference electrode (RE) were deposited using commercial gold paste (Gwent group) prior to the deposition of RuO_x catalyst. The surface area of CE and RE was 1 and 0.2 cm^2, respectively. Catalytic measurements were carried out at atmospheric pressure in the single-chamber capsule described in our previous work [77,78]. The working electrode side of the electrolyte was pressed against a gold mesh (1 cm^2) that served as a current collector, while the counter and reference electrodes were pressed directly against gold wires [79]. Two type K thermocouples (Omega®) were placed in the vicinity of the electrochemical cell, one for temperature control and one for data acquisition. A schematic of the system is shown in Figure D 1.

The reaction gases were ethylene (Linde, 0.5% C_2H_4 in He), oxygen (Linde, 20% O_2 in He), and helium (Linde, 99.999% He) as a carrier gas. The total flow rate was constant at 100 mL min^{-1}. Gas composition was varied using MKS, 1259-C and 1261-C series flow meters and detected using a non-dispersive infrared (NDIR) CO_2 gas analyzer (Horiba, VA-3000). A potentiostat-galvanostat (Arbin Instruments®, MSTAT) was connected to the electrodes to apply constant electric current or potential on the electrochemical cell (Figure D 2).

9.4. Results and discussion

9.4.1. Electrochemical promotion of RuO_x for complete ethylene oxidation reaction

Figure 9.3a shows the evolution of the reaction rate of the RuO_2 catalyst during a potentiostatic step of 0.5 V. At t=0.5 h, the constant potential was applied and resulted in a 30% increase in the reaction rate, reaching a new constant value over a duration of two hours. At potential interruption (t=2.5h), the reaction rate decreased to its initial steady-state value within an hour. The ratio of the closed-circuit rate r over the open-circuit rate r_o is denoted as the rate enhancement ratio, ρ (9-7).

$$\rho = \frac{r}{r_o} \qquad 9\text{-}7$$

Another determining parameter of the EPOC effect is the apparent Faradaic efficiency Λ:

$$\Lambda = \frac{\Delta r}{I/nF} \qquad 9\text{-}8$$

Where Δr is the difference between the closed and open circuit reaction rate ($\Delta r = r - r_o$), I is the applied current, n is the number of electrons transferred (2 for O^{2-}), F is the Faraday constant. The ρ and Λ values in Figure 9.3a are 1.23 and 6, respectively.

Figure 9.3b shows the reaction rate change under a negative galvanostatic step of -100 μA. The reaction rate of ethylene oxidation showed an enhancement in its value under the cathodic polarization as well reaching a 30% increase in the catalytic rate with Λ of -6. This increase in the rate under negative polarization was not detected previously except under fuel-rich conditions [34]. Therefore, this could be related to the contamination of previous catalysts with Na which inhibited any promotional effect at the cathodic counterpart [11] or due to the morphology obtained in the current sodium-free catalyst which has an average particle size below 1 nm.

Finally, multiple step-change galvanostatic tests were carried under cathodic and anodic polarization and are summarized in Figure 9.3c showing the effect of the applied current on the

catalytic rate increase and the corresponding measured catalyst-electrode potential. The increase in the rate under cathodic and anodic polarization shows that the change in the work function in both directions result in an enhancement of the catalytic rate. However, anodic polarization had a stronger effect on the rate than cathodic polarization. A maximum Λ factor of 92 at an applied current of 0.5 μA was reached and the highest increase of the catalytic rate by 41% was found at +50 μA.

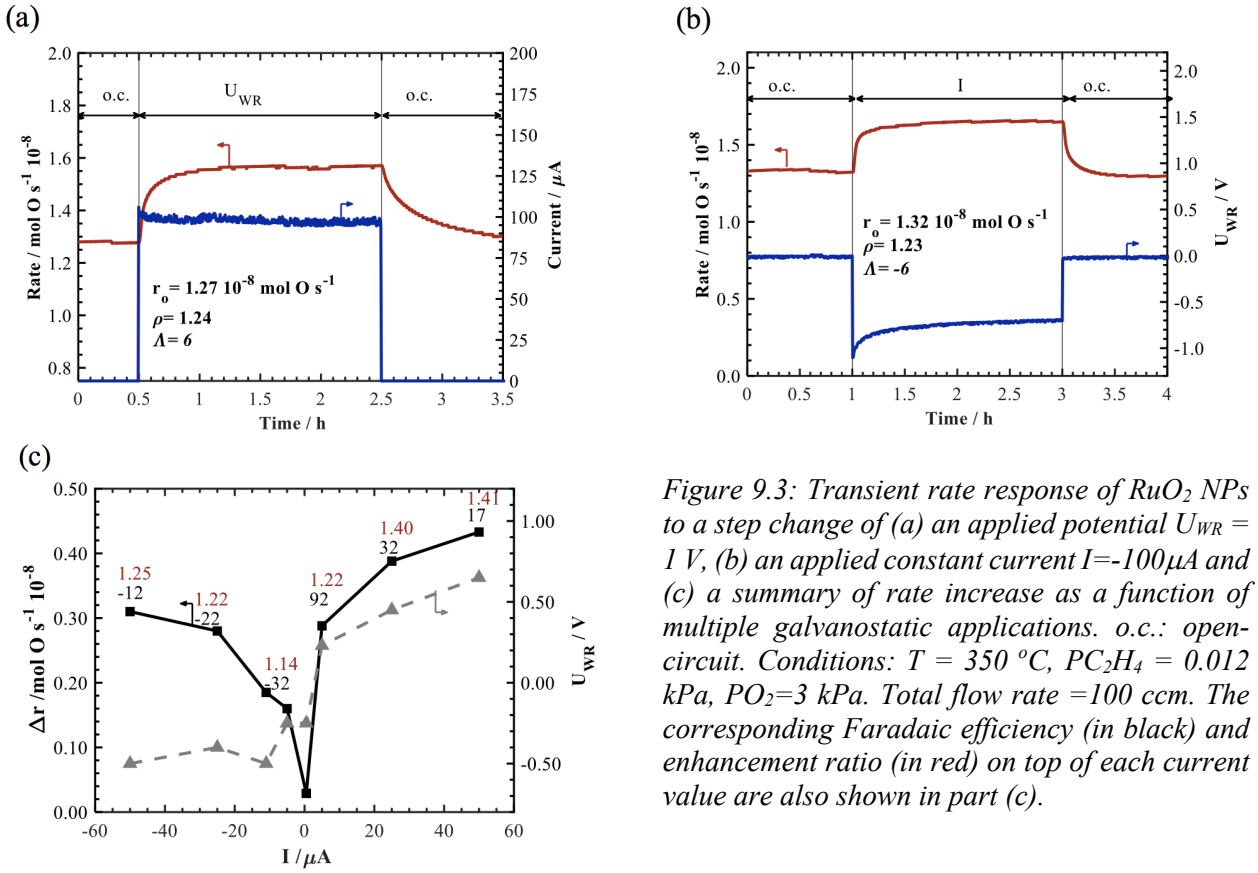

Figure 9.3: Transient rate response of RuO_2 NPs to a step change of (a) an applied potential U_{WR} = 1 V, (b) an applied constant current I=-100μA and (c) a summary of rate increase as a function of multiple galvanostatic applications. o.c.: open-circuit. Conditions: T = 350 °C, PC_2H_4 = 0.012 kPa, PO_2=3 kPa. Total flow rate =100 ccm. The corresponding Faradaic efficiency (in black) and enhancement ratio (in red) on top of each current value are also shown in part (c).

9.4.2. DFT modeling of RuO_2 (110) rutile structure and ethylene adsorption

9.4.2.1. RuO_2 (110) rutile structure

In the RuO_2 rutile bulk [73,80] every metal atom is coordinated with six oxygens and every oxygen links to three metal neighbors. The oxygen bonds to Ru are not all equivalent and can be distinguished into four in-plane ones of 1.97 Å length and two orthogonal ones of 1.92 Å length. The nomenclature for the oxygen on the surface will be O^{ot} for oxygen directly on top of Ru and O^{br} for oxygen bridging between two ruthenium atoms. Ru[4,5,6f] nomenclature will be used to refer

to the number of coordination such that sixfold, 6*f* coordination is for Ru saturated with six bonds of oxygen, 5*f* is for Ru missing O^{ot} coordination and 4*f* is for Ru missing two O^{br} coordination. This nomenclature is similar to Reuter *et al.* [73] and differs from Over *et al.* [58] where 1*f* and 2*f* nomenclature was used for Ru coordinated with O^{ot} and O^{br}, respectively. As to the surface calculations, the representative unit cell used was chosen to be a nearly square p(2x2) super-cell with three layers of Ru in the z-direction. The middle layer was fixed depicting the bulk whereas the remaining ones were free to move. The coordination of Ru atoms at top and bottom open surfaces changed coordination accordingly to the three surfaces being tested.

The three common surface terminations are presented in Figure 9.4 (side and top views) such that (a) and (d) show a termination where all Ru have their saturated six-fold coordination due to the O^{br} and O^{ot} atoms, called $2O^{br}/2O^{ot}$; (b) and (e) present the stoichiometric RuO_2 (110) terminated with $2O^{br}$/2Ru, and (c) and (f) show a termination that lacks oxygen and therefore its surface ends with 2Ru/2Ru which are fourfold- and fivefold- coordinatively unsaturated.

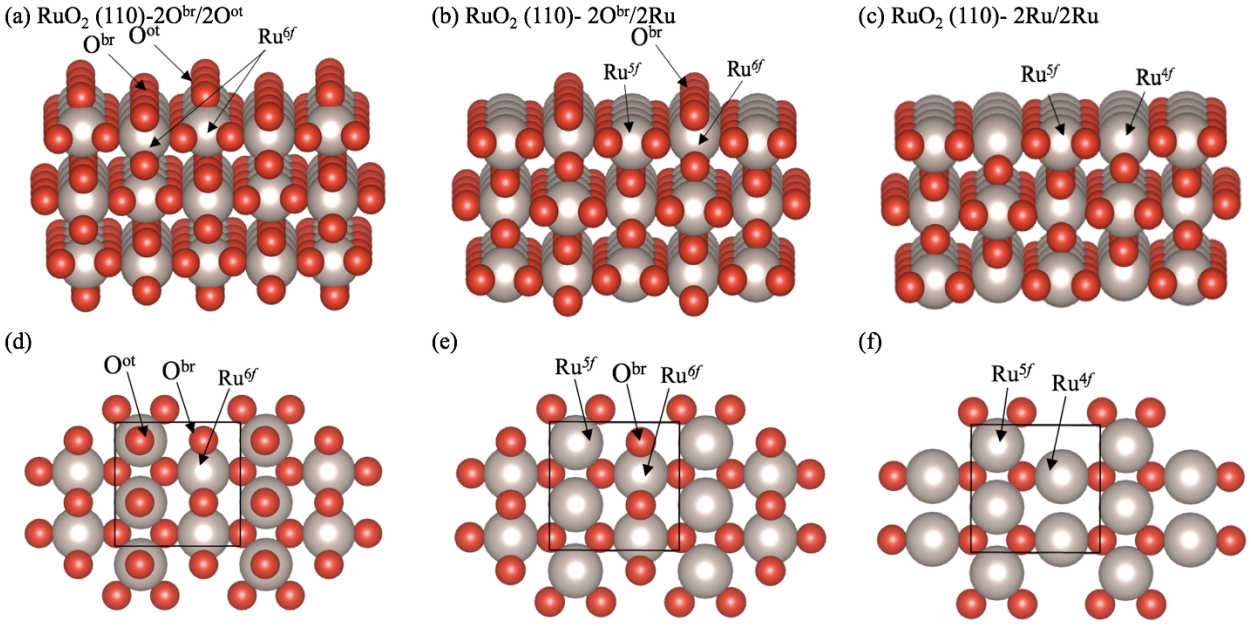

Figure 9.4: Possible three terminating planes of RuO_2 (110) surface; side (perspective) view of surface with a) $2O^{br}/2O^{ot}$, b) $2O^{br}$/2Ru and c) 2Ru/2Ru termination; (d–f) are top view of the three surfaces. (Ru: large light spheres, O: red small spheres). Solid lines representing the cell boundary.

9.4.2.2. Prediction of RuO_2 (110) termination

Under open-circuit conditions, the most stable surface termination was identified using the minimal surface free energy (SFE) approach. The oxygen chemical potential μ_{O_2} effect on the SFE

of RuO_2 slab truncated at different oxygen positions was compared to that found in Reuter *et al.* as shown in Figure D 4 and the most stable surface is presented as a function of temperature and oxygen partial pressure. It was found that the surface termination with $2O^{br}/2O^{ot}$ was the most stable at the considered temperatures and oxygen partial pressures. Only at $P(O_2)$ as small as 10^{-10} kPa, the $2O^{br}$/2Ru surface becomes the most stable above a temperature of 500 °C. The energy of a reduced surface (with 2Ru/2Ru termination) was unstable in comparison, which rules it out as a stable surface under open-circuit potential conditions. SFE calculation for RuO_2 (110) that has a $2Ru/2O^{ot}$ termination without O^{br} atoms was compared as an alternative form of a stoichiometric surface. However, it was found to be less stable than the other surfaces under all conditions.

9.4.2.3. Effect of potential on surface free energy

The previous section showed that RuO_2 (110) with $2O^{br}/2O^{ot}$ termination is the most stable structure under open-circuit conditions. In this section, we introduce the effect of potential on the stability of the RuO_2 surface termination using 9-4. At a partial pressure of oxygen equal to 1 kPa (used as a lower limit for experimental conditions), the effect of temperature and electrode potential on the most stable surface structure is depicted in Figure 9.5.

At the experimental temperature of 350 °C, it can be seen that structure B ($2O^{br}/2O^{ot}$) is the most stable surface termination in the electrode potential range of -0.5 to +0.15 V vs SOE. At the cathodic side, as the temperature increases, the oxygen chemical potential decreases, which results in stabilizing the surface with less oxygen. At 350 °C, the stable surface termination transitions from structure C ($2O^{br}/1O^{ot}$Ru) to structure D ($2O^{br}$/2Ru) as the potential decreases. At the extreme cathodic polarization (under -1.2 V vs SOE), which is outside the experimental range of +/- 0. 8 V vs SOE (-0.1 – 1.5 V vs SHE) (see Figure 9.3), the 2Ru/2Ru surface termination becomes the most stable. At the positive side of the potential range, SFE calculations demonstrated that an additional structure with an extra oxygen on the O^{ot} atom is more stable than $2O^{br}/2O^{ot}$. At 350 °C, above a potential of 0.15 V vs SOE (0.85 V vs SHE), structure A ($2O^{br}/4O^{ot}$) became the most stable. Calculation for an intermediate structure $2O^{br}/3O^{ot}$ showed that it was not more stable compared to $2O^{br}/4O^{ot}$ in the given potential range. These findings prove that as the potential value increases, the surface which is covered with a higher number of oxygen atoms becomes more stable, as shown in the surface phase diagram (Figure 9.5). This increase of oxygen concentration on the surface

with increased potential conforms with the oxygen backspillover process that was discussed extensively in previous experimental and theoretical papers.

Compared to the temperature and O_2 pressure dependence discussed above, the surface state is more strongly dependent on the applied electrochemical potential. In general, this explains part of the EPOC effect, since tuning the electrochemical potential provides an efficient means to control the catalyst surface state, which in turn modifies the reactivity of the catalyst.

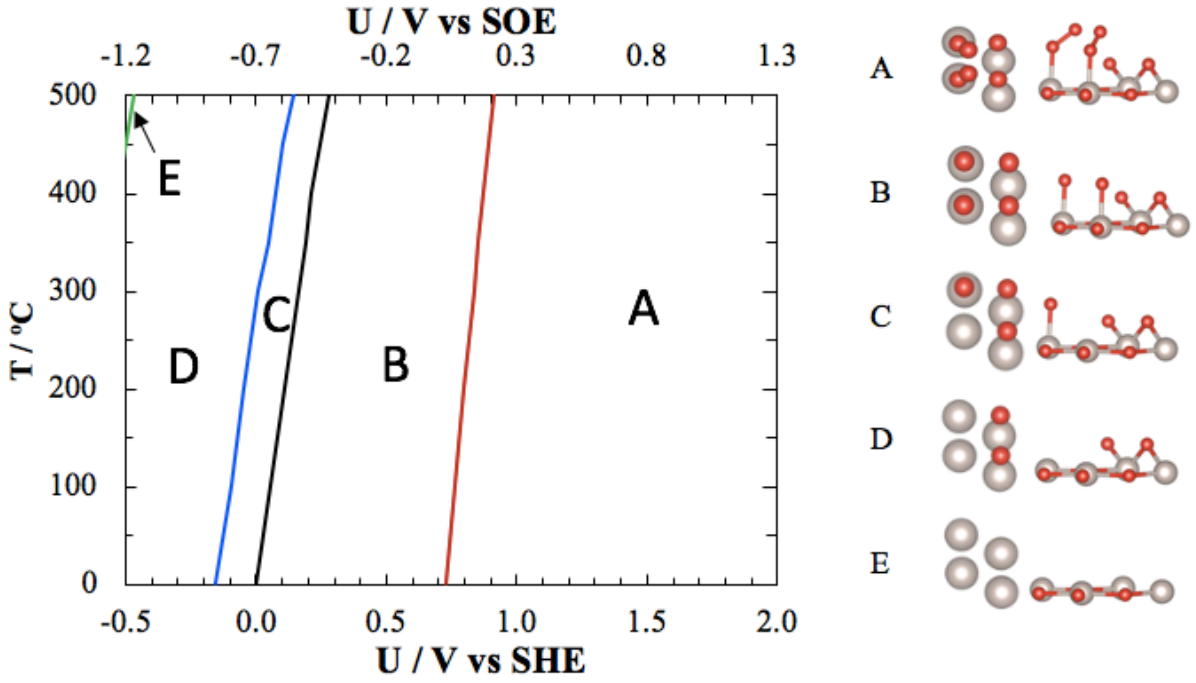

Figure 9.5: Surface phase diagram of stable structure of RuO_2 as a function of potential and temperature. $P(O_2)$=1 kPa. Structures A to E are illustrated on the right with top and side view.

9.4.2.4. Adsorption of ethylene on the surface

Non-EPOC related DFT modeling of ethylene oxidation on ruthenium has been studied previously: In Lopez *et al.*, adsorption of π-C_2H_4 directly on a free Ru atom was studied and its migration to form oxametallacycle (OMME) intermediate was shown. However, when the RuO_2 surface has full coverage of oxygen, ethylene adsorption transitions from epoxide to the more stable O-C_2H_4-O form [81]. Only the C-H bond dissociation was studied in Liang *et al.,* showing the facilitation of the C-H cleavage on a fully oxidized surface compared to a stoichiometric one [82].

Here, ethylene adsorption is studied on RuO_2 (110) with the most stable $2O^{ot}/2O^{br}$ surface termination prior to polarization. σ-C_2H_4 molecule adsorption energy was calculated for three positions: on the $2O^{ot}$, $2O^{br}$, and $O^{ot}O^{br}$. The adsorption energy under open-circuit potential (ocp) condition was the lowest when ethylene adsorbed on $2O^{ot}$ in σ form (-2.9 eV), and the highest when adsorbed in π-form on O^{ot} (-1.6 eV). σ-bond on $2O^{br}$ and diagonally on $O^{ot}O^{br}$ yields intermediate adsorption energies of -2.0 and -2.8 eV, respectively (shown in Figure D 13).

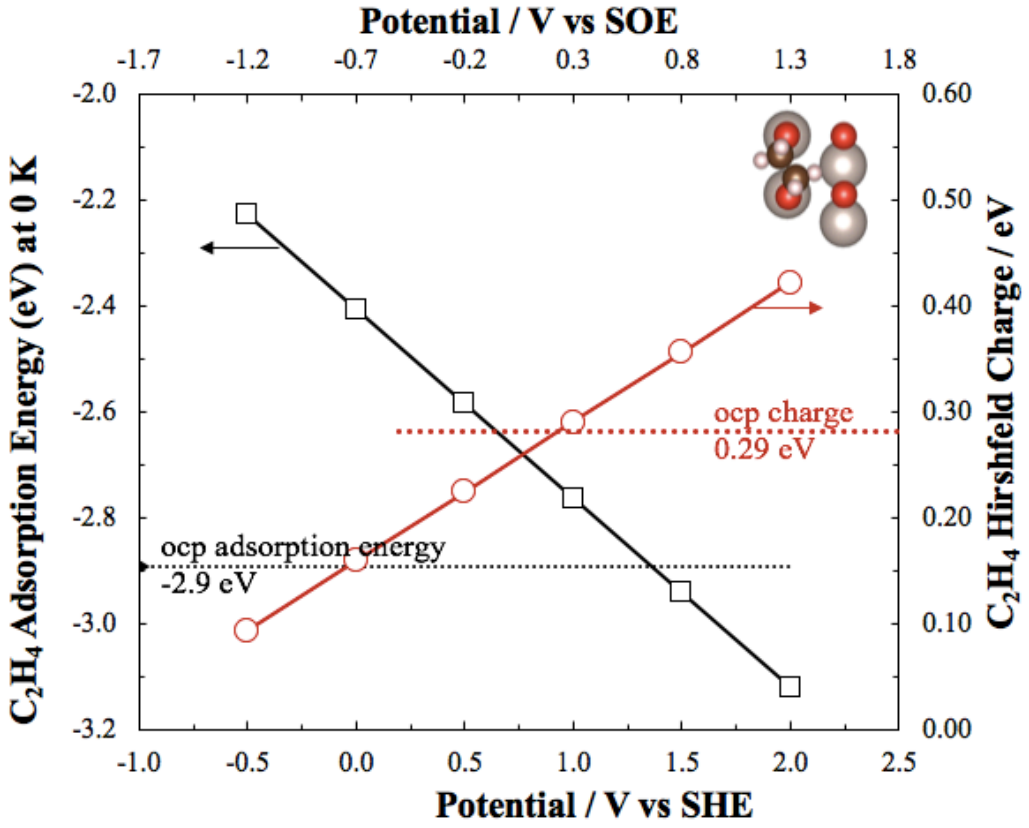

Figure 9.6: C_2H_4 adsorption energy and its total charge as a function of potential on RuO_2 (110) surface with $2O^{br}/2O^{ot}$ termination. Dotted line corresponds to ocp values.

Figure 9.6 shows the effect of the electrode potential on the stability of σ-C_2H_4 adsorption energy. It can be seen that the increase in the electrode potential (proportional to the surface work function) results in increasing (in absolute value) the heat of adsorption of σ-C_2H_4 rendering ethylene adsorption more stable than at ocp beyond a potential of 1.3 V vs SHE. This trend is paralleled by the increasing positive partial charge of the molecule (determined from Hirshfeld charge) as a function of potential (right axis of Figure 9.6). Thus, this figure confirms the EPOC mechanism [8] that the increase in the work function results in an increase in the heat of adsorption (produced thus negative) of ethylene and its *electropositive* behavior.

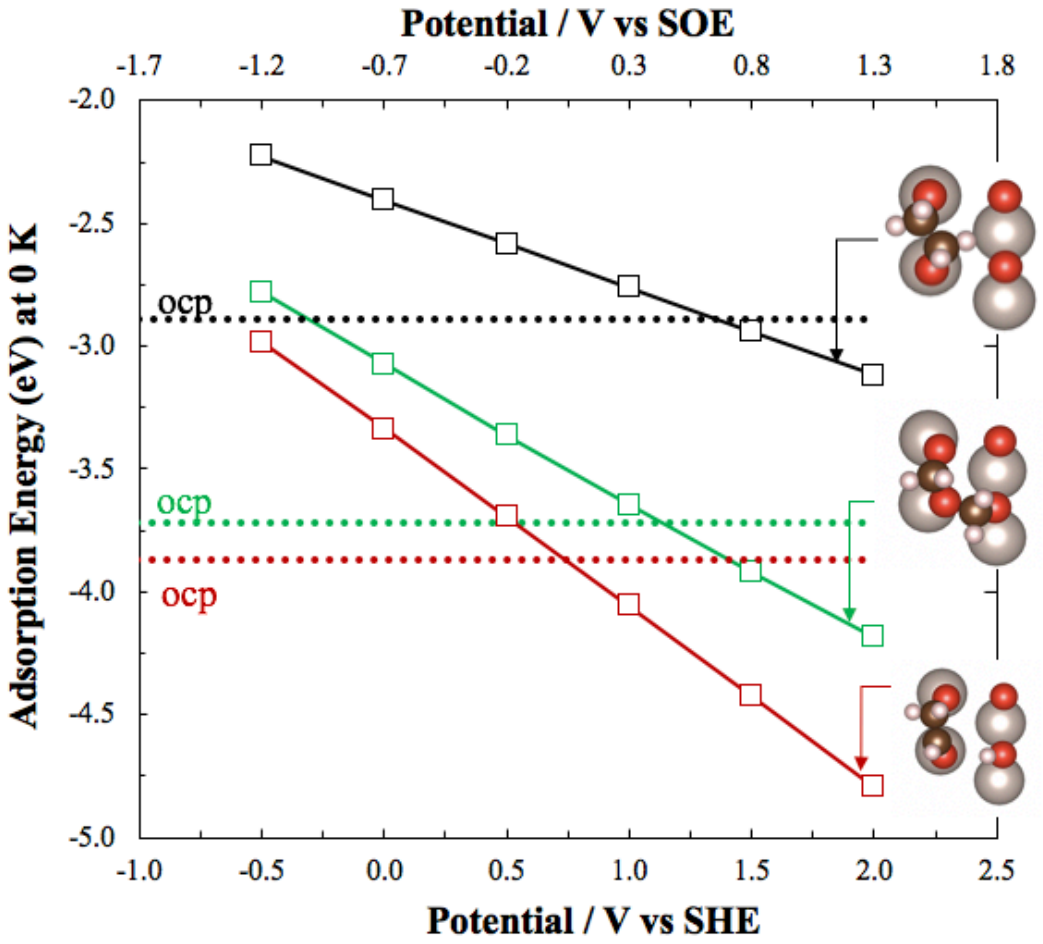

Figure 9.7: C_2H_4 and consecutive intermediates' adsorption energy as a function of potential on RuO_2 (110) surface with $2O^{br}/2O^{ot}$ termination. Dotted line corresponds to ocp adsorption value, while the solid line corresponds to adsorption energy variation as a function of potential value.

The effect of the potential was similar on the dissociation intermediates (dissociated C-H and dissociated C-C) (Figure 9.7), i.e., the adsorption energy of these intermediates is strengthened as a function of increasing potential.

9.4.2.5. DFT prediction of ethylene dissociation on 2Obr/2Oot surface termination

Figure 9.8 shows the energy diagram computed using DFT for the C-C bond dissociation on the $2O^{br}/2O^{ot}$ RuO_2 (110) surface termination. Our results (Figure 9.8b) demonstrate that the energy barrier for C-C bond dissociation decreases as a function of increasing applied potential and becomes smaller than under ocp conditions beyond a potential of 0.3 V vs SHE or -0.4 V vs SOE. The activation energy continues to decrease beyond this potential value which demonstrates the advantageous effect of potential on the facilitation of the C-C bond dissociation step. Similarly,

the reaction energy decreased as a function of the electrode potential rendering the reaction more exothermic as a function of increasing potential.

The corresponding transition state is shown more clearly in Figure 9.9 where the stretching of the C-C bonds occurs at the intermediate step. The distance between the two carbons stretched from an initial length of 1.5 Å to a final value of 2.6 Å, passing by 2.1 Å at the transition state.

At ocp, the C-H bond dissociation has an activation energy barrier of 0.58 eV (Figure D 14) compared to the C-C bond dissociation, which is at 0.53 eV. The C-H bond dissociation activation energy also decreased as a function of potential, accelerating it for potentials beyond 0.6 V vs SHE compared to ocp conditions. When comparing the potential effect on C-H vs C-C bond rupture, it can be seen that the potential effect on the C-C bond dissociation is more pronounced than on the C-H bond, which makes the prior the preferred dissociation step.

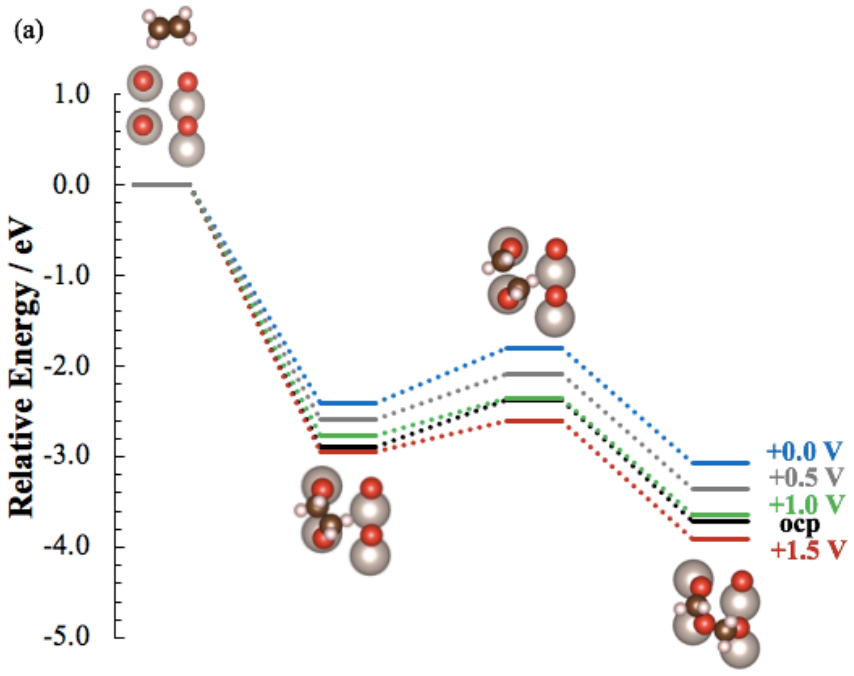

Figure 9.8 (continued next page)

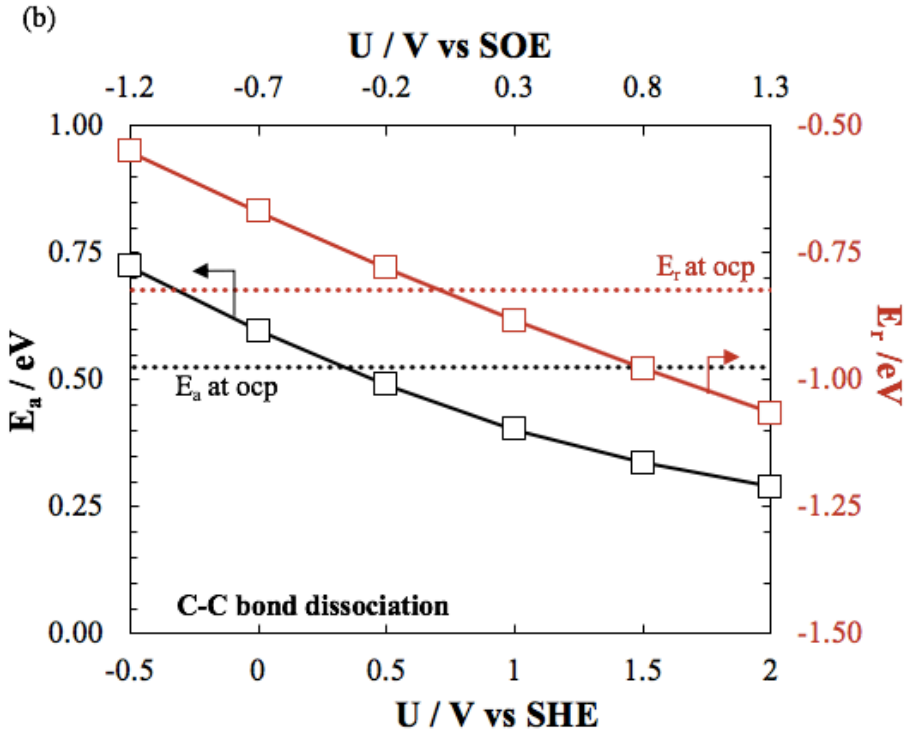

Figure 9.8: (a) Energy diagram and (b) corresponding activation and reaction energies as a function of potential for C-C bond dissociation over $2O^{br}/2O^{ot}$ surface termination of RuO_2 (110).

The increase in the adsorption energy of ethylene as a function of potential as well as the decrease of the activation energy for C-C (and C-H) bond dissociation explains the enhancement in the experimental catalytic rate observed under the application of an anodic potential. In summary, the removal of electron charges off the surface results in an increase of the electrode potential and a subsequent increase in the heat of adsorption of σ-C_2H_4 and a decrease in the activation energy of C-C bond dissociation.

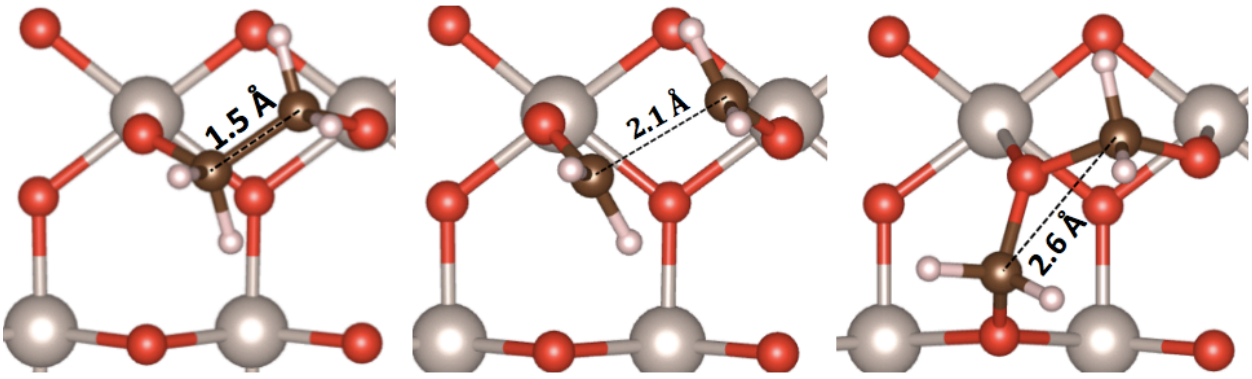

Figure 9.9: Structure of the initial, transition and final state of (C-C) bond dissociation on $2O^{br}/2O^{ot}$ RuO_2 (110) surface.

9.4.3. DFT prediction of oxygen adsorption and dissociation on the $2O^{br}$/2Ru surface termination

The enhancement in the reaction rate of ethylene oxidation was also found to experimentally occur under negative potential as demonstrated in Figure 9.3. Since the surface state strongly depends on the electrochemical potential (Figure 9.5), we have hypothesized that under negative polarization it is the activation of O_2 that is accelerated. Therefore, further computation was performed to investigate the effect of potential on the filling of the $2O^{ot}$ vacancies by adsorbing gaseous O_2. Note, that there are two sources of oxygen: The electrochemical one that determines the surface state and is source for the electron charges, and the gas-phase oxygen, which is the one for which we have computed the activation and adsorption energy. Since the electrochemical potential and the O_2 gas-flow are fixed independently, the chemical potentials of these two oxygen sources are not equalized, i.e., the system is not in equilibrium. The oxygen required for the non-Faradaic C_2H_4 oxidation is taken from the gas phase. Therefore, it is a key point that EPOC has a non-equilibrium nature such that the reactivity of oxygen stemming from YSZ (Faradaic reaction) is different than the one from gas-phase (non-Faradaic reaction).

It can be seen in Figure 9.10 that the adsorption of a bonded oxygen molecule at ocp (dotted red line) is -1.43 eV and decreases to -2.1 eV when the O-O bond breaks (dotted green line). The adsorption energy of intact and dissociated dioxygen decreases with negative potential (decreasing work function) which forms an opposite trend compared to the adsorption energy of the electropositive ethylene. This is in agreement with empirical EPOC rules which state that a decrease in the work function results in an increase in the chemisorptive bond of electron acceptors, e.g., O_2 and CO_2 [8]. The effect of potential on the adsorption of oxygen and ethylene is directly compared in Figure 9.1 to highlight the difference between an electron donor and an electron acceptor. The addition of electrons results in a decrease of the electrode potential (and proportionally a decrease of the work function). With this trend, the adsorption of oxygen can be seen to increase (in absolute value) compared to under ocp condition, becoming more stable below a potential value of 0.5 V vs SHE for “intact” O_2 and 0.7 V vs SHE for dissociated O_2 (Figure 9.10).

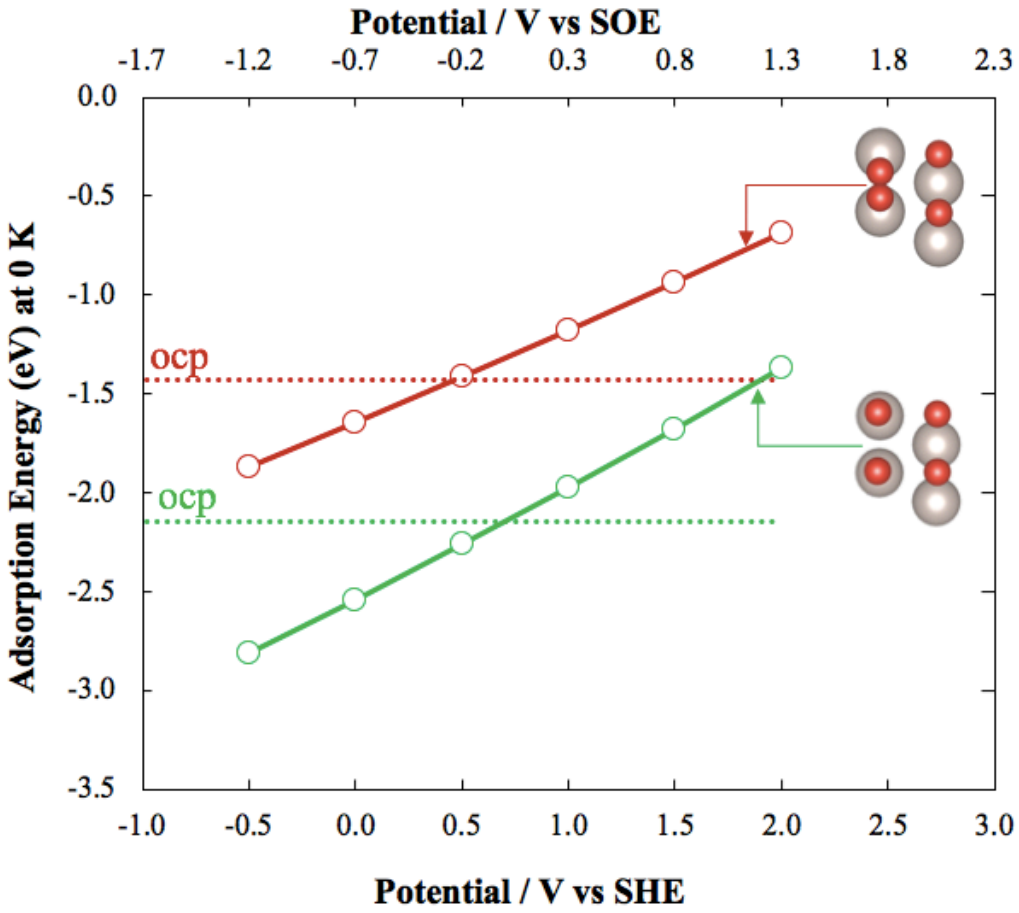

Figure 9.10: Adsoprtion energy of bonded and dissociated oxygen as a function of potential on RuO_2 (110) surface with $2O^{br}/2Ru^{t}$ termination. Dotted line corresponds to ocp adsorption value, while the solid line corresponds to adsorption energy variation as a function of potential value.

Figure 9.11 shows the effect of applied potential on the binding energy of oxygen. Not only the adsorption energy but also the activation and reaction energies for oxygen dissociation decrease as a function of decreasing electrochemical potential. Thus, the dissociation of an oxygen molecule is facilitated when applying a negative potential. This decrease in the activation energy is in good agreement with the experimental cathodic reaction rate that showed a higher rate compared to under ocp condition.

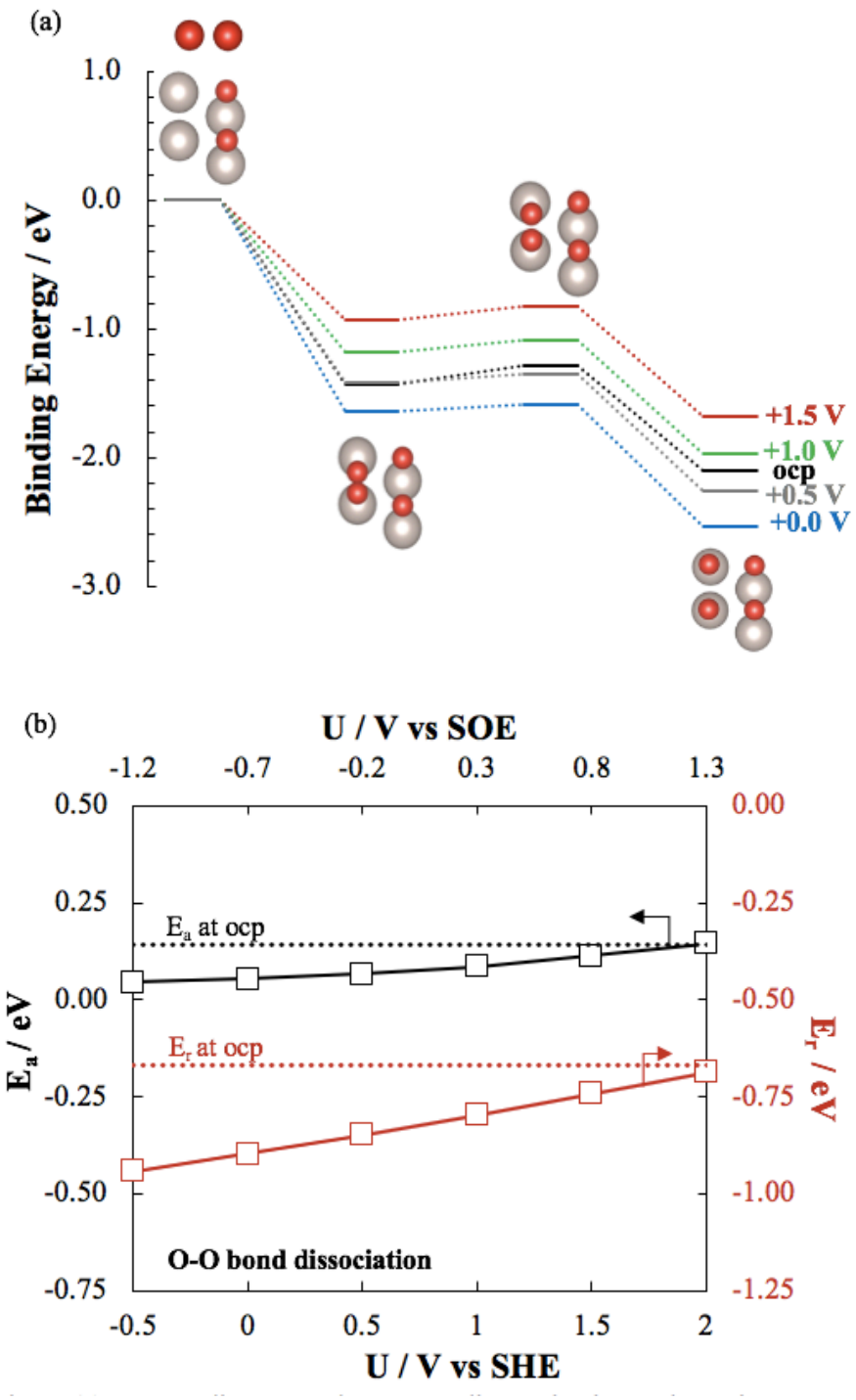

Figure 9.11: Energy diagram and corresponding activation and reaction energy as a function of potential for O-O bond dissociation over $2O^{br}$/2Ru surface termination of RuO_2 (110).

The geometries for oxygen dissociation are given in Figure D 17, which shows the oxygen bond dissociation and its transition state. The distance between the two oxygens increased from an initial length of 1.4 Å to a final value of 3.1 Å, passing by 1.7 Å at the transition state.

9.4.4. Experimental and DFT results comparison

In conclusion, the increase in the experimental catalytic rate as a function of positive potential can be explained by the facilitation of the C-C bond dissociation, whereas the increase in the catalytic rate as a function of negative polarization is due to the ease in the oxygen bond rupture. Those two potential effects can be correlated to the experimental data of Figure 9.3c, Furthermore, it should be noticed that the slope of the decreasing activation energy of C-C bond dissociation as a function of increasing potential is higher than that of the O-O bond dissociation as a function of decreasing potential value. This higher change in the activation energy at the positive potential is in agreement with the higher experimental increase in the catalytic rate under anodic potential application compared to the cathodic one. Interestingly enough, if overlaying Figure 9.7 and Figure 9.10, it can be seen that the adsorption energy of dissociated ethylene as a function of potential becomes smaller than that at ocp, above 0.7 V vs SHE while the adsorption energy of dissociated oxygen is smaller than that at ocp at potentials below 0.7 vs SHE. In summary, the atomistic origin of the EPOC effect on the ethylene oxidation rate on the surface of ruthenium oxide has therefore been identified to be due to the potential-dependent electric field at the catalyst surface, paralleling results of the effect of the addition of a base for formic acid decomposition [69]. This electric field complements the tuning of the surface state due to the backspillover.

9.5. Conclusions

For the first time, experimental results for the electrochemical promotion of ethylene oxidation on the surface of RuO_2 (110) have been rationalized using Density Functional Theory (DFT) modeling, explicitly taking into account the effect of the applied electrochemical potential. Experimentally, we obtained an increase in the catalytic rate under anodic and cathodic potential for the ethylene oxidation over RuO_2 nanoparticles. In order to elucidate the experimental findings, we have studied the adsorption and dissociation of σ-C_2H_4 on the $2O^{br}/2O^{ot}$ surface termination of RuO_2 (110) surface. We found that C_2H_4 preferably adsorbs on the two O^{ot} atoms via a σ-bonded structure and that the heat of adsorption produced increases with increasing potential. Concomitantly, the activation energy of the C-C bond dissociation was found to decrease as a function of potential. Under negative potential, the adsorption of oxygen is facilitated and the activation energy of the O-O dissociation decreased. The facilitation of the C-C bond dissociation under positive potential and of the O-O bond dissociation under negative potential, explain the

experimentally observed catalytic rate increase under both anodic and cathodic polarization, respectively. Furthermore, these findings are supported by the fact that surface free energy calculation showed that the surface with higher coverage of oxygen became more stable as a function of increasing potential. This is in excellent agreement with the mechanism of oxygen ion back-spillover and the rules of electrochemical promotion of catalysis.

References

[1] M. Boudart, G. Djega-Mariadassou, Kinetics of heterogeneous catalytic reactions, Princeton, NJ, 1984.

[2] I.M. Campbell, Catalysis at Surfaces, Chapman and Hall, New York, 1988.

[3] C. Wagner, Adsorbed Atomic Species as Intermediates in Heterogeneous Catalysis, Adv. Catal. 21 (1970) 323–381.

[4] M. Stoukides, C.G. Vayenas, The effect of electrochemical oxygen pumping on the rate and selectivity of ethylene oxidation on polycrystalline silver, J. Catal. 70 (1981) 137–146.

[5] C.G. Vayenas, S. Bebelis, S. Neophytides, Non-Faradaic Electrochemical Modification of Catalytic Activity, J. Phys. Chem. 92 (1988) 5083–5085.

[6] C.G. Vayenas, S. Bebelis, S. Ladas, Dependence of catalytic rates on catalyst work function, Nature. 343 (1990) 625–627.

[7] A. Wieckowski, E.R. Savinova, C.G. Vayenas, Catalysis and Electrocatalysis at Nanoparticle Surfaces, CRC/ Taylor & Francis, New York, 2003.

[8] C.G. Vayenas, S. Bebelis, C. Pliangos, S. Brosda, D. Tsiplakides, Electrochemical Activation of Catalysis: Promotion, Electrochemical Promotion, and Metal-Support Interactions, Springer, New York, 2001. http://link.springer.com/10.1007/b115566.

[9] C.G. Vayenas, Promotion, Electrochemical Promotion and Metal-Support Interactions: Their Common Features, Catal. Letters. 143 (2013) 1085–1097.

[10] P. Vernoux, L. Lizarraga, M.N. Tsampas, F.M. Sapountzi, A. De Lucas-Consuegra, J.L. Valverde, S. Souentie, C.G. Vayenas, D. Tsiplakides, S. Balomenou, E.A. Baranova, Ionically conducting ceramics as active catalyst supports, Chem. Rev. 113 (2013) 8192–8260.

[11] Y.M. Hajar, K.D. Patel, U. Tariq, E.A. Baranova, Functional equivalence of electrochemical promotion and metal support interaction for Pt and RuO2 nanoparticles, J. Catal. 352 (2017) 42–51. http://dx.doi.org/10.1016/j.jcat.2017.05.001.

[12] Y.M. Hajar, V. Di Palma, V. Kyriakou, M.A. Verheijen, E.A. Baranova, P. Vernoux, W.M.M. Kessels, M. Creatore, M.C.M. Van De Sanden, M. Tsampas, Atomic layer deposition of highly dispersed Pt nanoparticles on a high surface area electrode backbone for electrochemical promotion of catalysis, Electrochem. Commun. 84 (2017) 40–44.

[13] Y.M. Hajar, B. Venkatesh, E.A. Baranova, Electrochemical Promotion of Nanostructured Palladium for Complete Methane Oxidation, Catalysts. 9 (2018) 48.

[14] F. Matei, C. Jimenez-Borja, J. Canales-Vazquez, S. Brosda, F. Dorado, J.L. Valverde, D. Ciuparu, Enhanced electropromotion of methane combustion on palladium catalysts deposited on highly porous supports, Appl. Catal. B Environ. 132–133 (2013) 80–89. http://dx.doi.org/10.1016/j.apcatb.2012.11.011.

[15] F. Matei, D. Ciuparu, C. Jiménez-Borja, F. Dorado, J.L. Valverde, S. Brosda, Electrochemical promotion of methane oxidation on impregnated and sputtered Pd catalyst-electrodes deposited on YSZ, Appl. Catal. B Environ. 127 (2012) 18–27.

[16] E.A. Baranova, A. Thursfield, S. Brosda, G. Fóti, C. Comninellis, C.G. Vayenas, Electrochemical promotion of ethylene oxidation over Rh catalyst thin films sputtered on YSZ and TiO2/YSZ supports, J. Electrochem. Soc. 152 (2005) E40–E49.

[17] I. Kalaitzidou, T. Cavoué, A. Boreave, L. Burel, F. Gaillard, L. Retailleau-mevel, E.A. Baranova, M. Rieu, J.P. Viricelle, D. Horwat, P. Vernoux, Electrochemical promotion of propylene combustion on Ag catalytic coatings, Catal. Commun. 104 (2018) 28–31. http://linkinghub.elsevier.com/retrieve/pii/S1566736717304168.

[18] I. Kalaitzidou, A. Katsaounis, T. Norby, C.G. Vayenas, Electrochemical promotion of the hydrogenation of CO2 on Ru deposited on a BZY proton conductor, J. Catal. 331 (2015) 98–109. http://dx.doi.org/10.1016/j.jcat.2015.08.023.

[19] D. Theleritis, S. Souentie, A. Siokou, A. Katsaounis, C.G. Vayenas, Hydrogenation of CO2 over Ru/YSZ Electropromoted Catalysts, ACS Catal. 2 (2012) 770–780.

[20] H.A.E. Dole, E.A. Baranova, Implementation of Nanostructured Catalysts in the Electrochemical Promotion of Catalysis, in: M. Aliofkhazraei, H.A.S. Makhlouf (Eds.), Handb. Nanoelectrochemistry, Springer International Publishing, Cham, 2015: pp. 1–26. http://dx.doi.org/10.1007/978-3-319-15207-3_29-1.
[21] A. Katsaounis, Recent developments and trends in the electrochemical promotion of catalysis (EPOC), J. Appl. Electrochem. 40 (2010) 885–902.
[22] I. V. Yentekakis, P. Vernoux, G. Goula, A. Caravaca, Electropositive Promotion by Alkalis or Alkaline Earths of Pt-Group Metals in Emissions Control Catalysis: A Status Report, Catalysts. 9 (2019) 157.
[23] P. Vernoux, Recent advances in electrochemical promotion of catalysis, 2017.
[24] J. González-Cobos, A. de Lucas-Consuegra, A Review of Surface Analysis Techniques for the Investigation of the Phenomenon of Electrochemical Promotion of Catalysis with Alkaline Ionic Conductors, Catalysts. 6 (2016) 15. http://www.mdpi.com/2073-4344/6/1/15.
[25] S. Ladas, S. Kennou, S. Bebelis, C.G. Vayenas, Origin of non-faradaic electrochemical modification of catalytic activity, J. Phys. Chem. 97 (1993) 8845–8848. http://apps.webofknowledge.com/full_record.do?product=UA&search_mode=GeneralSearch&qid=1&SID=Y2i1RO3h4qfWMOLT4HA&page=1&doc=2&excludeEventConfig=ExcludeIfReload.
[26] B. Luerßen, S. Günther, H. Marbach, M. Kiskinova, J. Janek, R. Imbihl, Photoelectron spectromicroscopy of electrochemically induced oxygen spillover at the Pt/YSZ interface, Chem. Phys. Lett. 316 (2000) 331–335. https://www.sciencedirect.com/science/article/pii/S0009261499013020 (accessed February 28, 2019).
[27] A. Katsaounis, D. Teschner, S. Zafeiratos, The Effect of Polarization and Reaction Mixture on the Rh/YSZ Oxidation State During Ethylene Oxidation Studied by Near Ambient Pressure XPS, Top. Catal. 61 (2018) 2142–2151.
[28] S.G. Neophytides, C.G. Vayenas, TPD and Cyclic Voltammetric Investigation of the Origin of Electrochemical Promotion in Catalysis, J. Phys. Chem. 99 (1995) 17063–17067.
[29] M.N. Tsampas, F.M. Sapountzi, A. Boréave, P. Vernoux, Investigation of the Electrochemical Promotion of Catalysis origins on electrochemical catalysts with oxygen ion conductive supports : Isotopic labeling mechanistic studies, Solid State Ionics. 262 (2014) 257–261.
[30] J. Poppe, A. Schaak, J. Janek, R. Imbihl, Electrochemically induced surface changes on microstructured Pt films on a Solid YSZ electrolyte, Berichte Der Bunsengesellschaft. 102 (1998) 1019.
[31] S. Brosda, T. Badas, C.G. Vayenas, Study of the Mechanism of the Electrochemical Promotion of Rh/YSZ Catalysts for C2H4 Oxidation Via AC Impedance Spectroscopy, Top. Catal. 54 (2011) 708–717.
[32] A.D. Frantzis, S. Bebelis, C.G. Vayenas, Electrochemical promotion (NEMCA) of CH4 and C2H4 oxidation on Pd/YSZ and investigation of the origin of NEMCA via AC impedance spectroscopy, Solid State Ionics. 136–137 (2000) 863–872.
[33] M.N. Tsampas, F.M. Sapountzi, A. Boréave, P. Vernoux, Isotopical labeling mechanistic studies of electrochemical promotion of propane combustion on Pt/YSZ, Electrochem. Commun. 26 (2013) 13–16.
[34] I. Constantinou, I. Bolzonella, C. Pliangos, C. Comninellis, C.G. Vayenas, Electrochemical promotion of RuO2 catalysts for the combustion of toluene and ethylene, Catal. Letters. 100 (2005) 125–133.
[35] S. Wodiunig, F. Bokeloh, J. Nicole, C. Comninellis, Electrochemical Promotion of RuO2 Catalyst Dispersed on an Yttria-Stabilized Zirconia Monolith, Electrochem. Solid-State Lett. 2 (1999) 281–283.
[36] S. Wodiunig, V. Patsis, C. Comninellis, Electrochemical promotion of RuO2 -catalysts for the gas phase combustion of C2H4, Solid State Ionics. 137 (2000) 813–817.
[37] S. Brosda, C.G. Vayenas, J. Wei, Rules of chemical promotion, Appl. Catal. B Environ. 68 (2006)

109–124.
[38] F. Che, J.T. Gray, S. Ha, J.S. McEwen, Improving Ni Catalysts Using Electric Fields: A DFT and Experimental Study of the Methane Steam Reforming Reaction, ACS Catal. 7 (2017) 551–562.
[39] F. Che, J.T. Gray, S. Ha, N. Kruse, S.L. Scott, J.S. McEwen, Elucidating the Roles of Electric Fields in Catalysis: A Perspective, ACS Catal. 8 (2018) 5153–5174.
[40] G. Pacchioni, J.R. Lomas, F. Illas, Electric field effects in heterogeneous catalysis, J. Mol. Catal. A Chem. 119 (1997) 263–273.
[41] G. Pacchioni, F. Illas, S. Neophytides, C.G. Vayenas, Quantum-Chemical Study of Electrochemical Promotion in Catalysis, J. Phys. Chem. 100 (1996) 16653–16661.
[42] E.P.M. Leiva, C. Vázquez, M.I. Rojas, M.M. Mariscal, Computer simulation of the effective double layer occurring on a catalyst surface under electro-chemical promotion conditions, J. Appl. Electrochem. 38 (2008) 1065–1073.
[43] F. Che, S. Ha, J.-S. McEwen, Elucidating the Role of the Electric Field at the Ni/YSZ Electrode: A DFT Study, J. Phys. Chem. C. 120 (2016) 14608–14620. https://doi.org/10.1021/acs.jpcc.6b01292.
[44] S. González, C. Sousa, F. Illas, Electric field effects in the chemisorption of CO on bimetallic RhCu surface models, Surf. Sci. 548 (2004) 209–219.
[45] J.K. Nørskov, J. Rossmeisl, A. Logadottir, L. Lindqvist, J.R. Kitchin, T. Bligaard, H. Jónsson, Origin of the overpotential for oxygen reduction at a fuel-cell cathode, J. Phys. Chem. B. 108 (2004) 17886–17892.
[46] E.P.M. Leiva, C.G. Sánchez, NEMCA effect: Why are the work function changes of the gas exposed catalyst-electrode surface one-to-one related to the changes in the catalyst working electrode potential?, J. Solid State Electrochem. 7 (2003) 588–592.
[47] P. Beatrice, C. Pliangos, W. Worrell, C. Vayenas, Electrochemical promotion of ethylene and propylene oxidation on Pt deposited on yttria–titania–zirconia, Solid State Ionics. 136–137 (2000) 833–837. https://www.sciencedirect.com/science/article/pii/S016727380000518X (accessed March 1, 2019).
[48] E.I. Papaioannou, S. Souentie, F.M. Sapountzi, A. Hammad, D. Labou, S. Brosda, C.G. Vayenas, The role of TiO2 layers deposited on YSZ on the electrochemical promotion of C2H4 oxidation on Pt, J. Appl. Electrochem. 40 (2010) 1859–1865.
[49] C. Koutsodontis, A. Hammad, M. Lepage, Y. Sakamoto, G. Fóti, C.G. Vayenas, Electrochemical promotion of NO reduction by C2H4 in excess O2 using a monolithic electropromoted reactor and Pt-Rh sputtered electrodes, Top. Catal. 50 (2008) 192–199.
[50] J. Nicole, C.H. Comninellis, Electrochemical promotion of IrO2 catalyst activity for the gas phase combustion of ethylene, J. Appl. Electrochem. 28 (1998) 223–226.
[51] M. Setvin, C. Franchini, X. Hao, M. Schmid, M. Kaltak, C.G. Van De Walle, G. Kresse, U. Diebold, A direct view at excess electrons in TiO2 rutile and anatase, Phys. Rev. Lett. 113 (2014) 086402.
[52] G. Kresse, J. Furthmiiller, Efficiency of ab-initio total energy calculations for metals and semiconductors using a plane-wave basis set, Comput. Mater. Sci. 6 (1996) 15–50.
[53] S.N. Steinmann, C. Corminboeuf, Comprehensive Benchmarking of a Density-Dependent Dispersion Correction, J. Chem. Theory Comput. 7 (2011) 3567–3577.
[54] S. Gautier, S.N. Steinmann, C. Michel, P. Fleurat-lessard, P. Sautet, Molecular adsorption at Pt(111). How accurate are DFT functionals?, Phys. Chem. Chem. Phys. 17 (2015) 28921–28930.
[55] A. Böttcher, H. Niehus, Oxygen adsorbed on oxidized ru(0001), Phys. Rev. B - Condens. Matter Mater. Phys. 60 (1999) 14396–14404.
[56] S. Wendt, A.P. Seitsonen, K.Y. D, M. Knapp, H. Driss, H. Over, Complex redox chemistry on the RuO2(110) surface: experiment and theory, Surf. Sci. 505 (2002) 137–152.
[57] Y.D. Kim, S. Schwegmann, A.P. Seitsonen, H. Over, Epitaxial Growth of RuO2 (100) on Ru(10$\bar{1}$0): Surface Structure and Other Properties, J. Phys. Chem. B. 105 (2001) 2205–2211. http://dx.doi.org/10.1021/jp003650y.

[58] H. Over, M. Muhler, Catalytic CO oxidation over ruthenium - Bridging the pressure gap, Prog. Surf. Sci. 72 (2003) 3–17.
[59] P.I. Sorantin, K. Schwarz, Chemical Bonding in Rutile-Type Compounds, Inorg. Chem. 31 (1992) 567–576.
[60] S.N. Steinmann, P. Sautet, C. Michel, Solvation free energies for periodic surfaces: comparison of implicit and explicit solvation models, Phys. Chem. Chem. Phys. 18 (2016) 31850–31861.
[61] N.G. Hörmann, O. Andreussi, N. Marzari, Grand canonical simulations of electrochemical interfaces in implicit solvation models, J. Chem. Phys. 150 (2019) 041730. http://dx.doi.org/10.1063/1.5054580.
[62] M.M. Melander, M.J. Kuisma, T.E.K. Christensen, K. Honkala, Grand-canonical approach to density functional theory of electrocatalytic systems: Thermodynamics of solid-liquid interfaces at constant ion and electrode potentials, J. Chem. Phys. 150 (2019) 041706. http://dx.doi.org/10.1063/1.5047829.
[63] H. Zhang, W.A. Goddard, Q. Lu, M.J. Cheng, The importance of grand-canonical quantum mechanical methods to describe the effect of electrode potential on the stability of intermediates involved in both electrochemical CO2 reduction and hydrogen evolution†, Phys. Chem. Chem. Phys. 20 (2018) 2549.
[64] R. Sundararaman, W.A. Goddard, T.A. Arias, Grand canonical electronic density-functional theory: Algorithms and applications to electrochemistry, J. Chem. Phys. 146 (2017) 114104.
[65] C.W. Outhwaite, L.B. Bhuiyan, An improved modified Poisson-Boltzmann equation in electric-double-layer theory, J. Chem. Soc. Faraday Trans. 2 Mol. Chem. Phys. 79 (1983) 707–718.
[66] L.B. Bhuiyan, C.W. Outhwaite, D. Henderson, A modified Poisson-Boltzmann analysis of the capacitance behavior of the electric double layer at low temperatures, J. Chem. Phys. 123 (2005) 034704.
[67] VASPsol, (n.d.). https://github.com/henniggroup/VASPsol/blob/master/docs/USAGE.md.
[68] S.N. Steinmann, P. Sautet, Assessing a First-Principles Model of an Electrochemical Interface by Comparison, J. Phys. Chem. C. 120 (2016) 5619–5623.
[69] P. Wang, S.N. Steinmann, G. Fu, C. Michel, P. Sautet, Key Role of Anionic Doping for H2 Production from Formic Acid on Pd(111), ACS Catal. 7 (2017) 1955–1959.
[70] K. Mathew, R. Sundararaman, K. Letchworth-Weaver, T.A. Arias, R.G. Hennig, Implicit solvation model for density- functional study of nanocrystal surfaces and reaction pathways, J. Chem. Phys. 140 (2015) 084106.
[71] K. Mathew, R.G. Hennig, Implicit self-consistent description of electrolyte in plane-wave density-functional theory, ArXiv. (2016) 1–6.
[72] Q. Gu, P. Sautet, C. Michel, Unraveling the Role of Base and Catalyst Polarization in Alcohol Oxidation on Au and Pt in Water, ACS Catal. 8 (2018) 11716–11721.
[73] K. Reuter, M. Scheffler, Composition, structure, and stability of RuO2 (110) as a function of oxygen pressure, Phys. Rev. B. 65 (2001) 035406. http://link.aps.org/doi/10.1103/PhysRevB.65.035406.
[74] D. Tsiplakides, C.G. Vayenas, Electrode work function and absolute potential scale in solid-state electrochemistry, J. Electrochem. Soc. 148 (2001) E189–E202.
[75] S. Trasatti, The Absolute Electrode Potential: an Explanatory Note, Pure Appl. Chem. 58 (1986) 955–966.
[76] E.A. Baranova, C. Bock, D. Ilin, D. Wang, B. MacDougall, Infrared spectroscopy on size-controlled synthesized Pt-based nano-catalysts, Surf. Sci. 600 (2006) 3502–3511.
[77] Y.M. Hajar, H.A. Dole, M. Couillard, E.A. Baranova, Investigation of heterogeneous catalysts by electrochemical method: Ceria and titania supported iridium for ethylene oxidation, ECS Trans. 72 (2016) 161–172.
[78] H.A.E. Dole, A. Costa, M. Couillard, E.A. Baranova, Quantifying metal support interaction in ceria-supported Pt, PtSn and Ru nanoparticles using electrochemical technique, J. Catal. 333 (2016) 40–50.

[79] Y.M. Hajar, M.S. Houache, U. Tariq, P. Vernoux, E.A. Baranova, Nanoscopic Ni interfaced with oxygen conductive supports: Link between electrochemical and catalytic studies, Electrochem. Soc. 77 (2017) 51–66.
[80] K. Reuter, M. Scheffler, Composition and structure of the RuO2(110) surface in an O2 and CO environment: implications for the catalytic formation of CO2, Phys. Rev. B. 68 (2003) 1–11. http://arxiv.org/abs/cond-mat/0301602%0Ahttp://dx.doi.org/10.1103/PhysRevB.68.045407.
[81] N. Lopez, G. Novell-Leruth, Rules for selectivity in oxidation processes on RuO2(110), Phys. Chem. Chem. Phys. 12 (2010) 12217–12222.
[82] Z. Liang, M. Kim, T. Li, R. Rai, A. Asthagiri, J.F. Weaver, Adsorption and Oxidation of Ethylene on the Stoichiometric and O-Rich RuO2 (110) Surfaces, J. Phys. Chem. C. 121 (2017) 20375–20386. http://pubs.acs.org/doi/abs/10.1021/acs.jpcc.7b06865.

Chapter 10 Conclusions, Contributions and Recommendations

10.1. Conclusions

Air pollution and emission of greenhouse gases to the atmosphere are a remaining drawback in the 21st century due to the continuous growth of the energy sector from fossil fuel and natural gas, while a shift to renewable sources of energy remains unhurried (Figure 10.1). News like the shale gas revolution [1–3] and need for Trans-Canada pipeline expansion are projections of the reality of the world's energy sector and the economic return they bring, despite its climate change drawbacks. In this thesis, we focused on developing catalysts tailored for the full oxidation of volatile organic compounds (VOCs) and methane to CO_2, a less of all evils, having the lowest global warming potential. Our focus was on enhancing the efficiency of the catalysts used in the oxidation reactions, tackling, on different levels, two phenomenon: electrochemical promotion of catalysis (EPOC) and metal-support interaction (MSI).

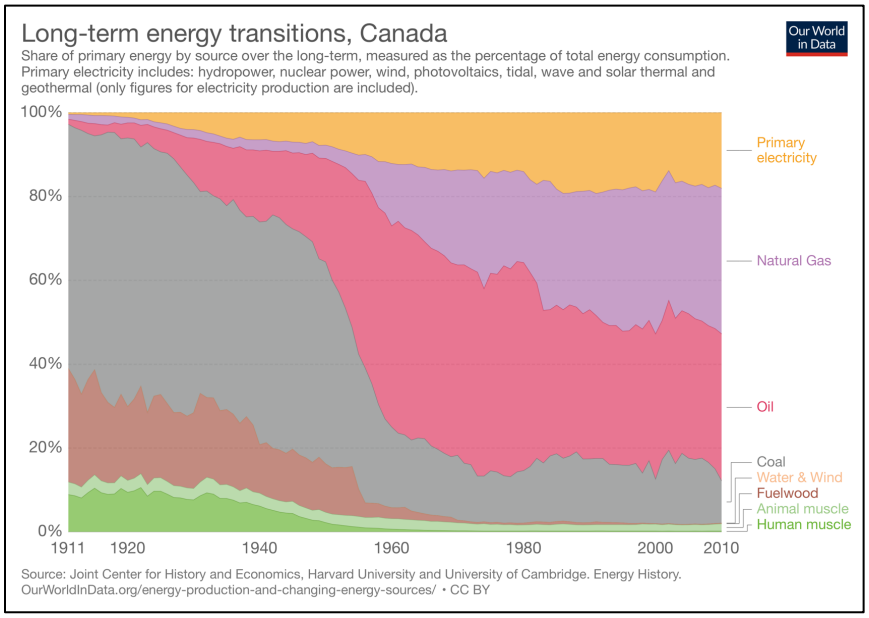

Figure 10.1: Long term energy transition in Canada.
Adapted from: http://www.fas.harvard.edu/~histecon/energyhistory/energydata_beta.html

In heterogeneous catalysis, there is a continuous work on enhancing the properties of the catalysts used using various methods. Of those methods, the two phenomena, MSI and EPOC are prominent in the promotional effect they result in. Overall, to achieve our goals, we (i) developed novel catalytic nanoparticles: Pt, RuO_2, IrO_2, Pd, (ii) used specially-designed bimetallic catalyst, Ni_9Pd and monometallic Ni, (iii) enhanced the design of the testing reactor and system, (iv) elaborated on the electrochemical characteristics of these catalysts, (v) performed catalytic characterization, (vi) demonstrated experimentally the promotional effect of polarization of the catalysts under different temperature, partial pressure, potential conditions, (vii) showed through isotopic measurement tests the involvement of lattice oxygen in the oxidation reaction when using active metal oxide supports, (viii) theoretically modeled the EPOC phenomenon and showed the potential effect on the adsorption, activation and reaction energy of ethylene oxidation.

10.2. Contributions

The ultimate goal of this thesis was to increase the efficiency of the catalysts per mass used. Furthermore, the functional similarity in increasing the catalytic efficiency by electrochemical promotion and metal support interaction was proven through the comparison of the catalytic rate values from electrochemically promoted catalysts and from supported catalysts, along with isotopic oxygen exchange characterization and theoretical modeling of the EPOC phenomenon.

Through each chapter, we contributed to the heterogeneous catalysis and electrochemical field as follows:

- In Chapter 3, a well-defined and size controlled iridium- and nickel-based catalysts were developed using a well-explained synthesis and deposition methods. Their resulting catalytic rate for the ethylene oxidation was found and compared. Using electrochemical measurements (chronoamperometry and linear sweep voltammetry), the exchange current densities of each catalyst were calculated from Tafel plots. The fundamental relationship between the catalytic rate and the exchange current density was confirmed in this chapter for the case of iridium- and nickel- based catalysts, similarly to previous work on platinum and ruthenium proving the universal identity of the MSI apparent Faradaic efficiency relationship.

- In Chapter 4, lattice oxygen engagement from active supports, i.e., YSZ, CeO_2 and TiO_2 was elaborated using isotopic oxygen exchange measurements (IOE). Temperature-programmed and isothermal IOE allowed a better understanding of the mechanism of the propane oxidation reaction on iridium and ruthenium based catalysts. We found that YSZ-based catalysts had the highest engagement of oxygen from the support due to its oxygen vacancies formed due to yttrium doping. At the low temperature of 350 °C, electronic conductivity of CeO_2 and TiO_2 is relatively low, which hinders their reducibility; therefore any oxygen spillover occurring in those two supports is mostly due to their ionic conductivity. The oxygen exchange capacity correlated fairly well with the ethylene titration experiment where YSZ-based catalysts showed the highest and most prolonged production of CO_2 using lattice oxygen. Particle size effect was clear in the case of RuO_2/CeO_2 as its higher particle size resulted in a major impedance of the oxygen engagement from the support
- In Chapter 5, we compared the catalytic rate of ethylene oxidation on Pt and RuO_2 that were promoted under electrochemical promotion of catalysis (EPOC) with when dispersed on active supports. We have demonstrated the similarity in the increase of the catalytic rate by applying a potential to when the nanoparticles were supported. This chapter resulted in better explaining the effect of EPOC in operationally changing the catalytic rate of the reaction and the similarity in that effect to when supporting the noble metal nanoparticles on active support.
- In Chapter 6, we promoted for the first time Pt nanoparticles deposited by atomic layer deposition on an industrial LSCF/GDC material used as a dispersive intermediate layer between the catalyst and an oxygen-conductive solid electrolyte (Hionic^{TM}). The dispersion of Pt in the intermediate layer resulted in an average particle size of 4.5 nm and had a good stabilizing effect that can be further investigated as a method of dispersion and stabilization.
- In Chapter 7, we synthesized Pd nanoparticle using the polyol method and used them to successfully promote methane oxidation using electrochemical promotion of catalysis (EPOC). The polarization tests showed that Pd bulk changes to oxide phase when continuous polarization is applied. This resulted in a continuous increase in the catalytic rate and a semi-permanent promotion such that a proportional relationship was found between the polarization time and the time required to revert to the open-circuit catalytic rate.
- In Chapter 8, core double-shell Ni_9Pd nanoparticles were synthesized with highly dispersed Pd atoms on the Ni shell. This configuration resulted in increasing the catalytic rate of the methane oxidation under open circuit conditions. In addition, under EPOC conditions, the methane oxidation was promoted to a higher level with an overall stability longer than any other catalyst.

- In Chapter 9, we contributed to the theoretical explanation of EPOC through density functional theory (DFT) modeling. We found a variation of the adsorption energy of the electronegative ($O_{2,gas}$) and electropositive ($C_2H_{4,gas}$) reactants as a function of applied potential, which affected as well the activation and reaction energies required for their corresponding bond dissociation on the surface of RuO_2 (110).

10.3. Recommendations

The most important recommendations are as follows:

- First and foremost, the transition to synthesizing and analyzing bimetallic noble/non-noble catalysts must be continued. A synergetic effect in combining noble/non-noble metals was found to be better than using non-noble metals alone. Therefore, expanding to the use of iron, copper and cobalt as a first step should be progressed for the methane complete oxidation. In a further step, varying the ratio of the bimetallic is very important as well; while 9:1 ratio was ideal for NiPd, another ratio might be better for a combination of other two metals. In addition, nickel alone for example did not show high catalytic activity for the methane oxidation, nevertheless, other non-noble metals might, especially when synthesized at the nano-scale. Therefore, prior testing of non-noble metals alone should be performed in heterogeneous catalysis tests.
- Once new bimetallics with distinguished properties are developed, performing electrochemical promotion tests on the non-noble metals and their bimetallics is a must. Ni_9Pd results showed that nickel was able to better disperse Pd; therefore, this advantageous property is key for long term polarization and EPOC tests without a supporting material.
- As for metal-support interaction experiments, possibly other type of supports such as zirconia-ceria, Ce_x-$Zr_{1-x}O_2$ or ceria-yttria-zirconia, $Ce_xY_yZr_{1-x-y}$ could be tested for their catalytic rate enhancement effect and their oxygen storage capacity when supporting non-noble metals as in the case of Ni/YSZ and Ni/CeO_2 and possibly their bimetallics. Therefore, any other metal oxide support can be used for Ni as well as for Fe, Co, Cu and for the synthesized bimetallics. This could result in an enhanced performance that can be very similar to that of supported noble metals.

- On the subject of isotopic studies for MSI performance, similar studies to what was performed in this thesis could be performed on the other metals such as palladium which showed, in the electrochemical promotion tests, interesting oxidation/reduction cycles when a potential was applied. In addition, desorption tests at higher temperature might be more interesting, but care should be taken with regards to sintering and loss of catalyst properties, which means more expensive experiments and higher amount of catalyst used. While 50 mg of catalyst was used in this thesis for the isotopic study, some metal oxide supports have showed limitation to their oxygen storage and therefore, limitation to the desorption was found as a function of temperature (i.e., TiO_2-based catalysts). If one was to measure the oxygen storage capacity as a function of temperature for a longer period of time, 200 mg of the catalyst would be at least required.
- Atomic layer deposition as a method for catalyst deposition is used in a multitude of industries. If one can measure the metal loading from ALD deposition (using ICP-MS or another method), an interesting work would result in comparing the deposition methods effect on the catalytic activity of the same metal, taking into account the average particle size effect that might change due to the different deposition method. A note that one can learn that percolation of the catalyst islands is very important to result in a current flow in the surface of the catalyst as for example 50 cycles of Pt ALD was not enough to have a current flow, unlike in the case of 100 cycles. Therefore, care and characterization of the catalyst morphology (before and after test) for catalysts of different cycle number can explain the different results found.
- On the scaling-up point of view, and based on Anastasijevic study mentioned in Chapter 2, 2020 marks the transition year for a higher scale of EPOC studies. Therefore, focus on scaling-up of the process should be performed with a bigger budget to take the process into an industrial step. This could be paired up with initial testing of electrochemical promotion on a mix of volatile organic compounds or on a typical gaseous mixture from a car exhaust or a smoke stack.
- When it comes to modeling theoretically the process of electrochemical promotion, it will be interesting to study the case of methane oxidation on palladium and the effect of potential on the oxidation state of Pd. This could back up the experimental findings of the persistent increase of the catalytic rate of methane oxidation when a constant potential was applied.

References

[1] D.J. Hughes, A reality check on the shale revolution, Nature. 494 (2012) 307–308.
[2] E.L. Morse, Why shale is the next shale, Foreign Aff. 93 (2014) 3–8.
[3] R.D. Blackwill, M.L.O. Sullivan, The geoploticial consequences of the shale revolution, Foreign Aff. 93 (2014) 102–114.

APPENDICES

The appendices are

- Appendix A: Supplementary information for Chapter 4
- Appendix B: Supplementary information for Chapter 5
- Appendix C: Supplementary information for Chapter 8
- Appendix D: Supplementary information for Chapter 9
- Appendix E: Scholarly contributions

Appendix A: Supplementary Information to Chapter 4

1. Histogram of the particle size distribution

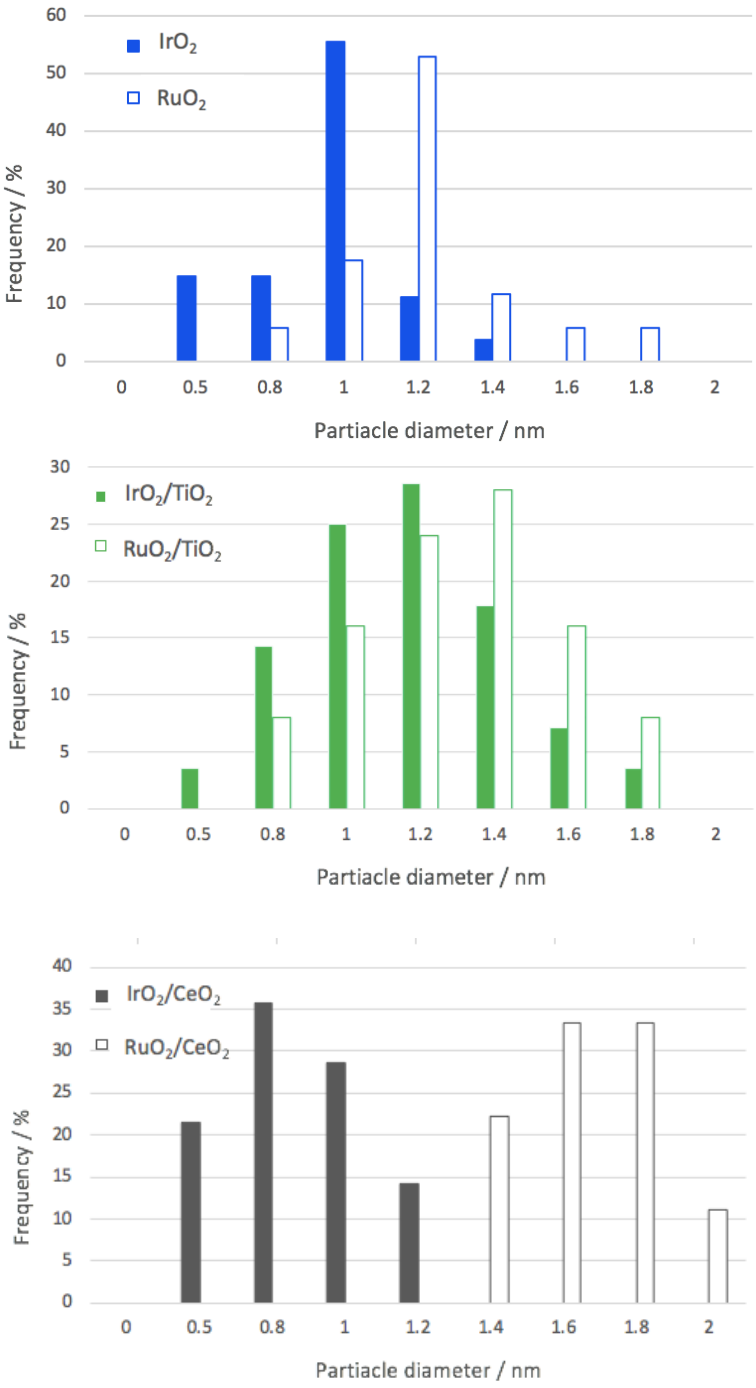

Figure A 1: Histogram of the particle size of RuO_2 and IrO_2 when (a) stand-alone and when supported on (b) TiO_2 and (c) CeO_2

2. Temperature-programmed isotopic oxygen exchange

A temperature-programmed isotopic oxygen exchange (TPIOE) was performed (Figure A 2) on the six catalysts to see the temperature effect on the catalysts' oxygen exchange capacity detected through the variation in the atomic fraction of $^{18}O_2$, $^{18}O^{16}O$, $^{16}O_2$ in the gas phase. 30 mL min^{-1} of $^{16}O_2$ (Linde®, 5% in He) was used to pre-treat the sample for two hours at 350 °C. The sample was cooled down, then a feed of 1 % of $^{18}O_2$ was introduced to the reactor with a balance of He, at a flow of 30 mL min^{-1}. The temperature was increased to 350 °C with a heating rate of 10 °C min^{-1}.

YSZ had the highest oxygen exchange capacity, shown by its greatest ability to consume $^{18}O_2$ from the gas. This was in parallel with the increase of the atomic fraction of $^{16}O_2$ and $^{16}O^{18}O$ in the gas as dioxygen was desorbing from surface by combining two atoms originating from the lattice of the support ($^{16}O_2$), or one from the support and one from the gas ($^{16}O^{18}O$). The desorption of $^{16}O_2$ was more significant than $^{16}O^{18}O$ in the case of YSZ, suggesting that the multiple heteroexchange mechanism was more dominant than the simple heteroexchange reaction when supporting both iridium and ruthenium.

While the same pattern of oxygen exchange was found in the case of Iridium and Ruthenium supported on YSZ, the oxygen exchange was not similar for the two metal oxides on CeO_2 and TiO_2. This difference shows well the importance of the metal oxide/support interactions. In the case of CeO_2, Iridium exhibits higher oxygen exchange capacity compared to Ruthenium. It could be attributed to the relatively higher particle size of Ruthenium (1.8 nm) on CeO_2. Unlike in the case of YSZ, the simple heteroexchange was the dominant mechanism for the oxygen exchange on CeO_2 and TiO_2 based catalysts, showing that either the rate of desorption of $^{16}O^{18}O_s$ was faster than the full spillover of $^{18}O_2$, or that there is not enough active lattice oxygen in the oxides. Therefore, the oxygen exchange rate of the catalysts respected the following order: $IrO_2/YSZ > IrO_2/CeO_2 > RuO_2/YSZ > RuO_2/TiO_2 > IrO_2/TiO_2 > RuO_2/CeO_2$.

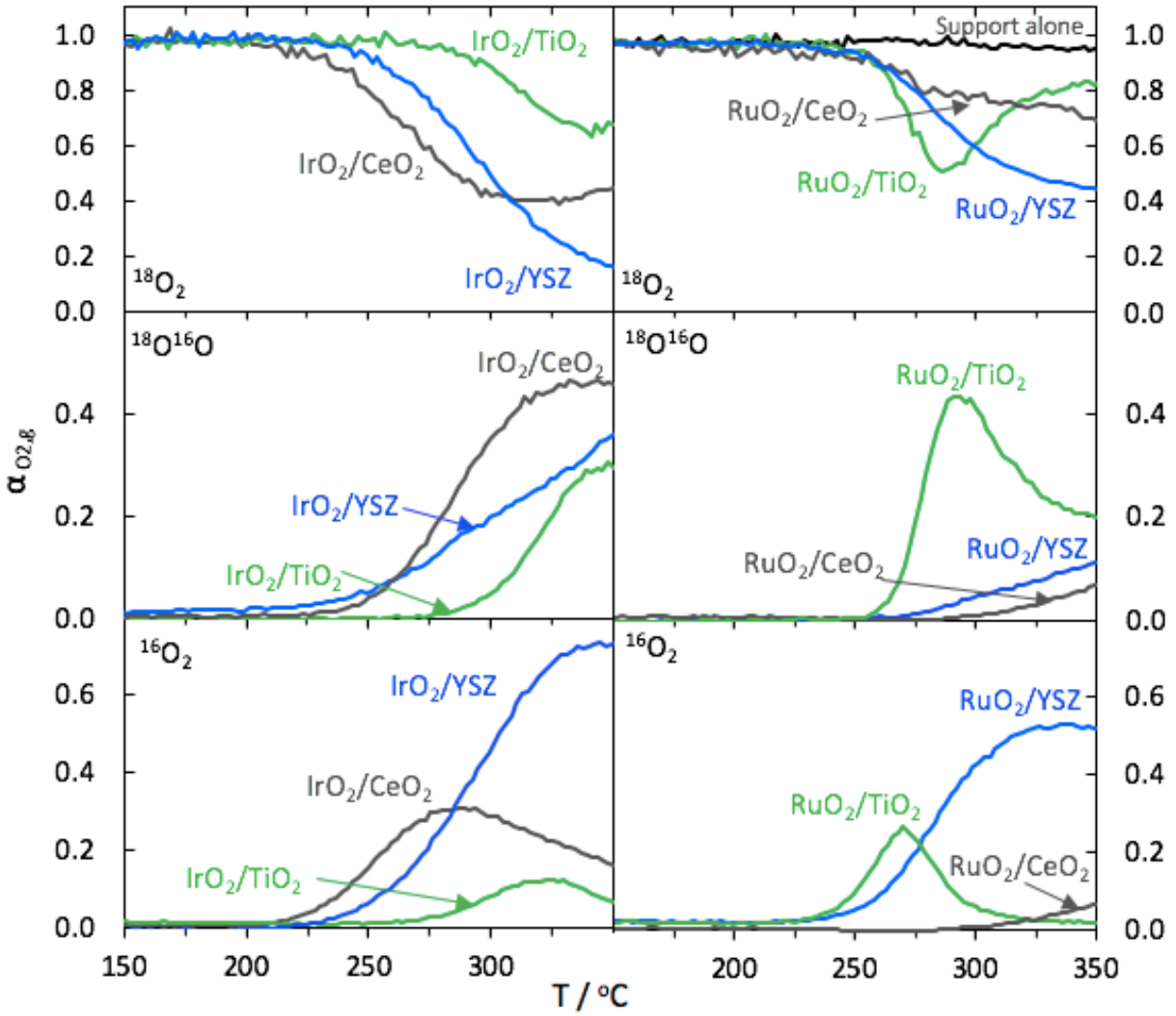

Figure A 2: Temperature-programmed isotopic oxygen exchange on IrO_2 and RuO_2 nanoparticles supported on CeO_2, TiO_2, and YSZ metal oxides. $P^{18}O_2$= 1 kPa and balance of He. Total flow of 30 mL min^{-1}. The support alone (CeO_2, TiO_2 or YSZ) alone had no oxygen exchange capacity.

Appendix B: Supplementary Information to Chapter 5

Functional Equivalence of Electrochemical Promotion and Metal Support Interaction for Pt and RuO_2 Nanoparticles

The representative SEM images type COMPO are shown for Pt colloid deposited on YSZ electrolyte when freshly made and used (Figure B 1). The white features are Pt as confirmed by EDS analysis. As can be seen the nanoparticles agglomerate in small islands of sub micrometer size and do not form a continuous film on YSZ surface. Figure B 2 shows RuO_2 supported on TiO_2 and YSZ powder supports after applying it on YSZ disk. The supported RuO_2/TiO_2 and RuO_2/YSZ form highly porous and continuous layers on YSZ disk. From this figure, it is not possible to distinguish RuO_2 NPs due to the low resolution achieved by SEM and only the two supports TiO_2 and YSZ are seen.

Figure B 3 shows the electrochemical cell and the electrode arrangement used for catalytic measurements under open and closed circuit [44]. Only free-standing Pt and RuO_2 NPs were polarized; whereas the supported catalysts were studied under open circuit but place in the same cell configuration to have the same mass and heat transfer conditions.

Figure B 4 and Figure B 5 are representation of the catalytic rate of platinum and ruthenium, respectively as a function of variating temperature and partial pressure of ethylene, showing the difference between when the NPs are free-standing and supported.

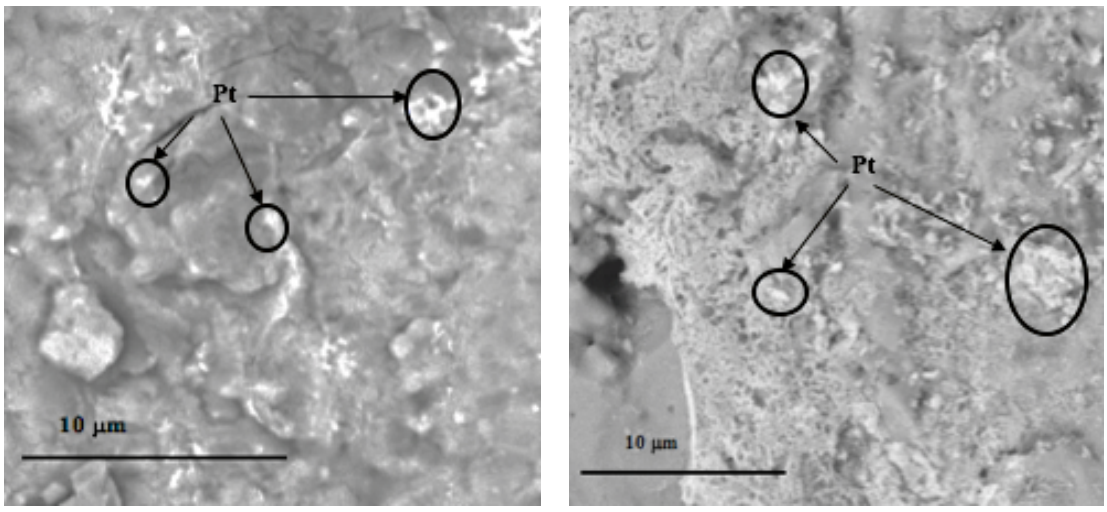

(a) (b)

Figure B 1: SEM images (COMPO) of fresh (a) and used (b) free-standing Pt nanoparticles at 15kV.

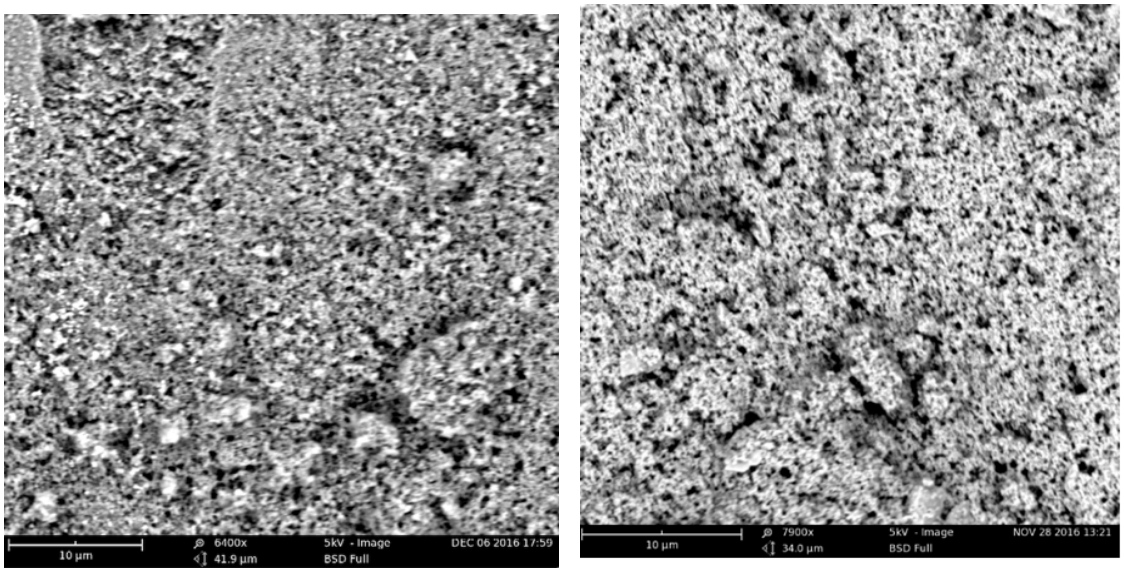

(a) (b)

Figure B 2: SEM images of (a) RuO_2/TiO_2 and (b) RuO_2/YSZ catalyst layer deposited on YSZ disk, at 5 kV.

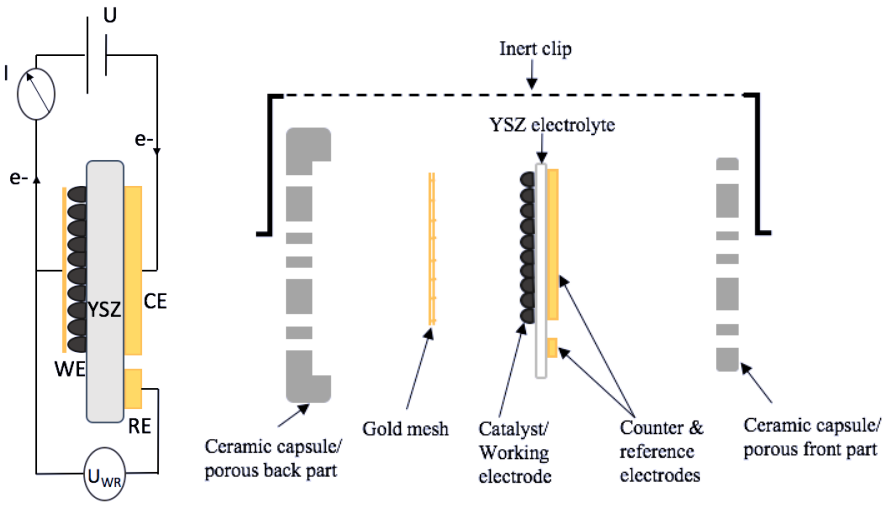

Figure B 3: Schematic of the cross-view of the electrochemical cell showing its electrical connection and the ceramic capsule in which it is enclosed.

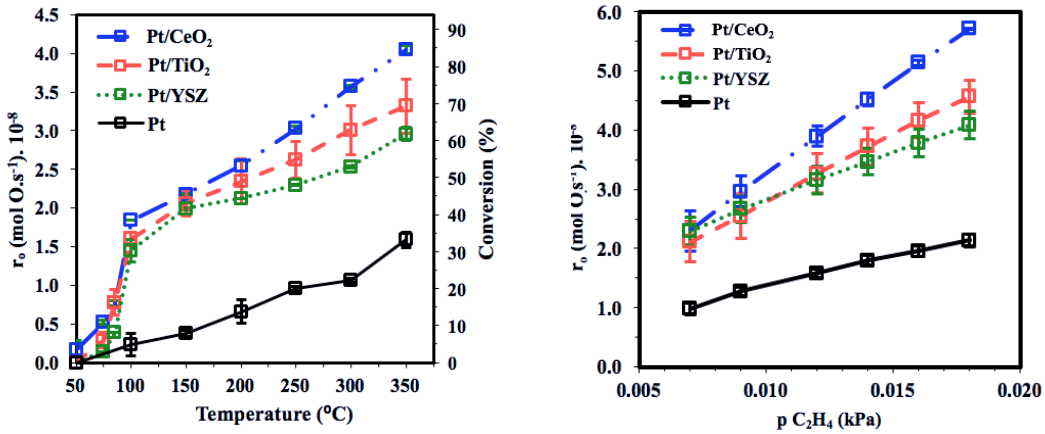

(a) (b)

Figure B 4: (a) Open-circuit catalytic rate for free-standing Pt NPs, Pt/YSZ and Pt/TiO_2 in function of temperature between 50 to 350 °C at 0.012 kPa of C_2H_4 and 3 kPa of O_2 and (b) in function of partial pressure of C_2H_4 (0.007 to 0.018 kPa).

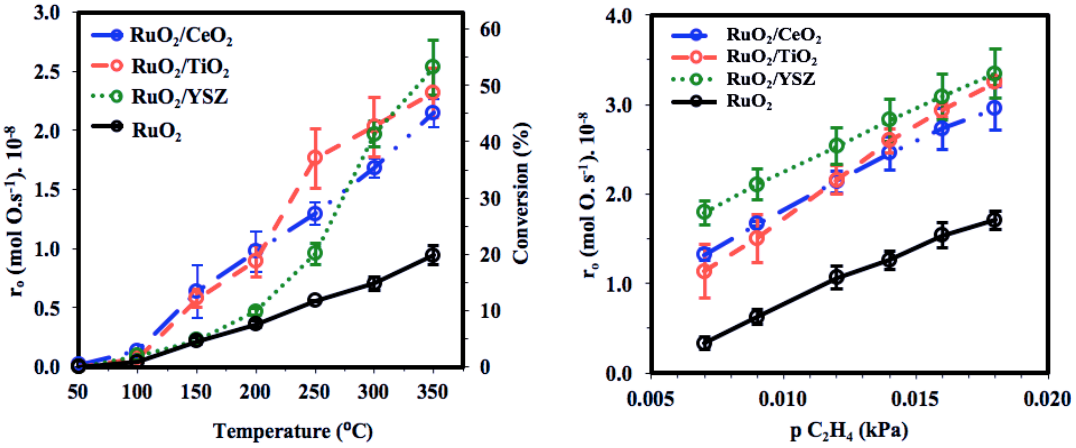

(a) (b)

Figure B 5: (a) Open-circuit catalytic rate for free-standing RuO_2 NPs, RuO_2/YSZ and Ru/TiO_2 in function of temperature between 50 to 350 °C; 0.012 kPa of C_2H_4 and 3 kPa of O_2 and (b) in function of partial pressure of C_2H_4 (0.007 to 0.018 kPa).

Appendix C: Supplementary Information to Chapter 8

Electrochemical Promotion of Bi-metallic Ni_9Pd Core Double-Shell Nanoparticles for Complete Methane Oxidation

Figure C 1 shows additional EDS images of Ni_9Pd catalyst on the micro-scale level and elemental mapping of Ni (red) and Pd (green) in the same location.

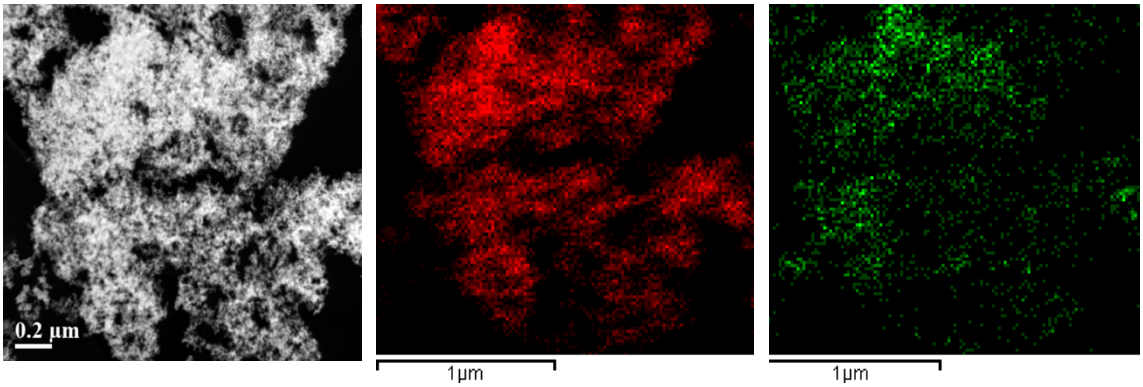

Figure C 1: EDS image mapping of Ni_9Pd showing microscale dispersion of Ni in red and Pd in green.

Figure C 2 is a representation of the specific peaks related to energy loss of Pd and Ni. The peak at ~ 850 eV corresponds to Ni L_{edge} while palladium peak is situated at around 400 eV. Additionally, oxygen peak was found because of oxidation of sample over time.

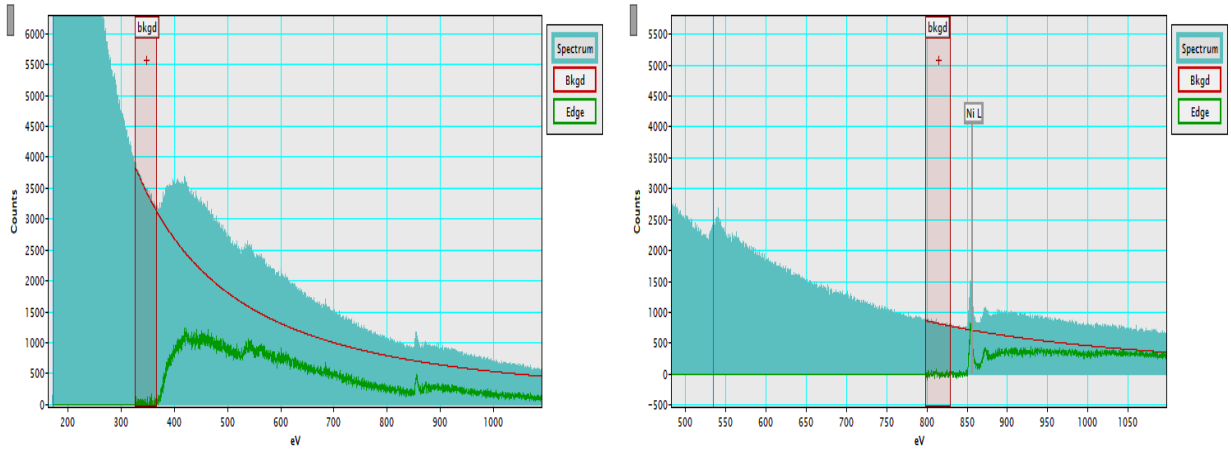

Figure C 2: Selection of Pd peak from spectrum for mapping between 370.5-475.0 eV (left) and Ni peak from spectrum for mapping between 848.0-885.8eV (right).

Figure C 3 shows the transient rate response to application of positive potential (U_{WR} = 0.25 and 0.5V) in function of time at different P_{O_2}/P_{CH_4}, for which the enhancement ratio and Faradaic efficiency are shown in Figure 9.8 in the article.

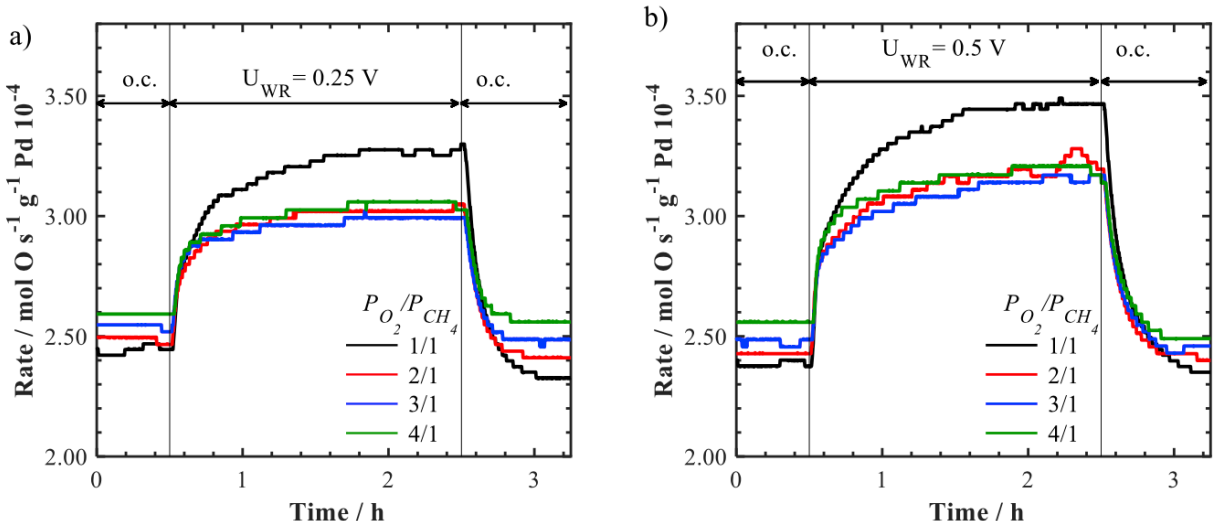

Figure C 3: Transient rate response of Ni_9Pd at different oxygen partial pressure to a step change of potential: (a) U_{WR} = 0.25 V and (b) U_{WR} = 0.5 V; o.c.: open-circuit. Reaction conditions: T = 450 °C, P_{CH_4} = 2 kPa, flow rate of 100 mL min^{-1}.

Electrochemical promotion of Ni_9Pd at 500 °C at P_{CH_4} = 2 kPa and P_{O_2} =1 kPa is illustrated in Figure C 4. When a positive potential of 0.5 V was applied to the catalyst-electrode this resulted in concurrent increase in current to 220 μA and rate to 6.10^{-4} mol/s per gram of Pd. Upon potential interruption the reaction rate returned to its initial open circuit value.

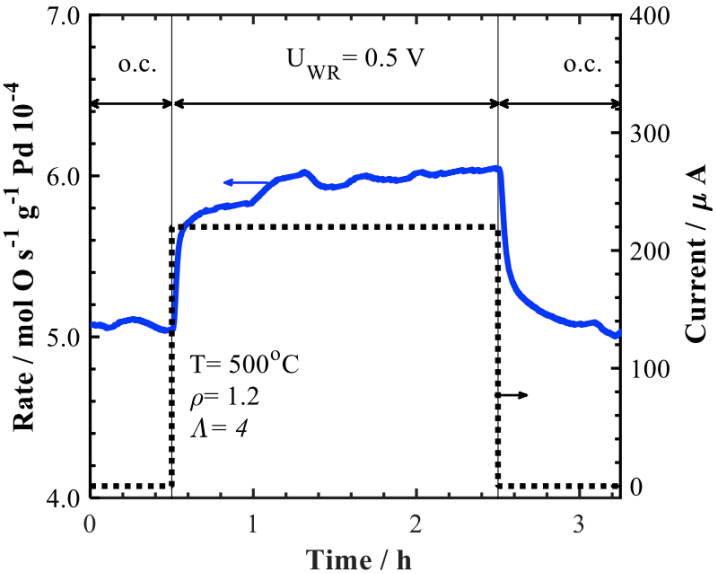

Figure C 4: Transient rate response of Ni_9Pd at 500 °C to an applied potential of 0.5V. P_{CH_4} = 2 kPa and P_{O_2} = 1 kPa; He in balance.

Figure C 5 shows electrochemical promotion of Ni_9Pd at 475 °C at P_{CH_4}= 2 kPa and P_{O_2} =0.4 kPa. Upon positive potential application (U_{WR} = 0.5 V) the reaction rate of methane complete oxidation increased resulting in the rate enhancement ratio of 1.2 and apparent faradaic efficiency of 10. Upon potential interruption the reaction rate returned to its initial open circuit value.

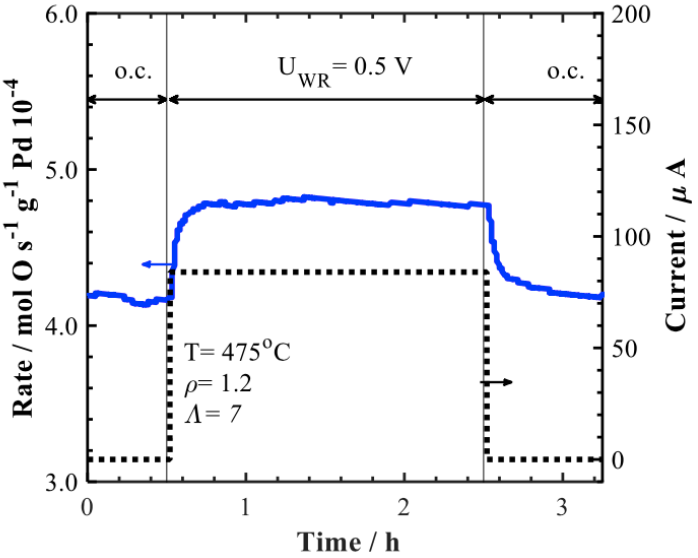

Figure C 5: Transient rate response of Ni_9Pd at 475 °C to an applied potential of 0.5V. P_{CH_4} = 2 kPa and P_{O_2} = 0.4 kPa; He in balance.

Figure C 6 represents the transient rate response that occurs on the surface of Ni_9Pd in fuel-rich conditions at 450 °C. Those transients and others are summarized in Figure 9.8 of the article to represent the effect of partial pressure ratios of O_2 to CH_4 on the Faradaic efficiency and enhancement ratio.

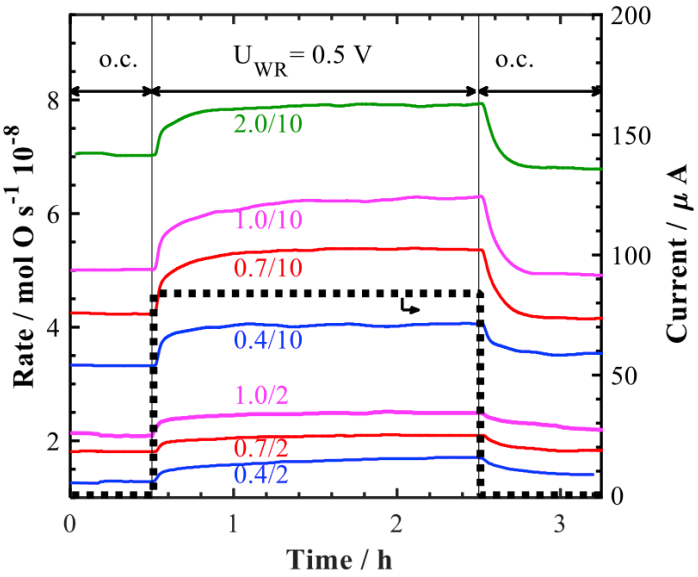

Figure C 6: Transient rate response of Ni_9Pd to a step change of an applied potential, U_{WR} = 0.5 V at different P_{O_2}/P_{CH_4} partial pressures ratios, corresponding to fuel-rich conditions. T=450 °C.

Appendix D: Supplementary Information to Chapter 9

Theoretical Insight into Origin of Electrochemical Promotion of Ethylene oxidation on Ruthenium Oxide

D 1. Reactor design

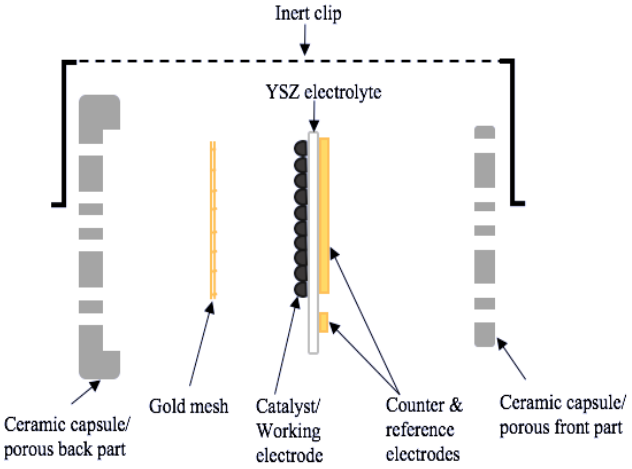

Figure D 1: Schematic of the electrochemical cell showing the electrolyte, the working electrode WE, counter electrode CE and reference electrode RE sandwiched in a ceramic capsule.

(a) *(b)*

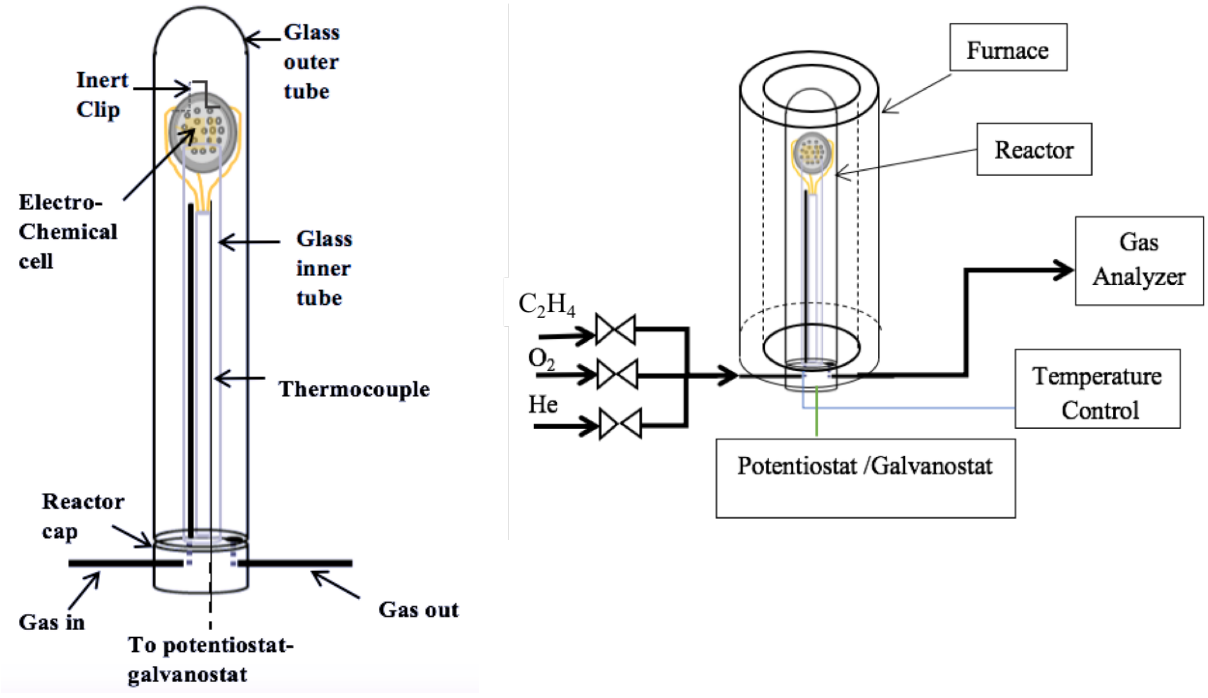

Figure D 2: (a) Schematics of the quartz reactor showing the suspended the electrochemical cell and (b) Schematic of the overall experimental apparatus for EPOC experiments.

D 2. Typical result from electrochemical promotion of catalysis experiment

Figure D 3 shows a typical electrochemical promotion of catalysis result when applying a constant current. In here for example a current of 100 μA is applied, following Faraday's law the value of r_{elec} would be the expected new value based on the electrochemical reaction occurring; however, an increase in the rate to a new value r occurs, defying the Faraday's law and hence the promotion is called non-Faradaic. As explained in the manuscript, the increase in the rate to higher values is due to change in adsorption strength and decrease of activation energy, upon potential application.

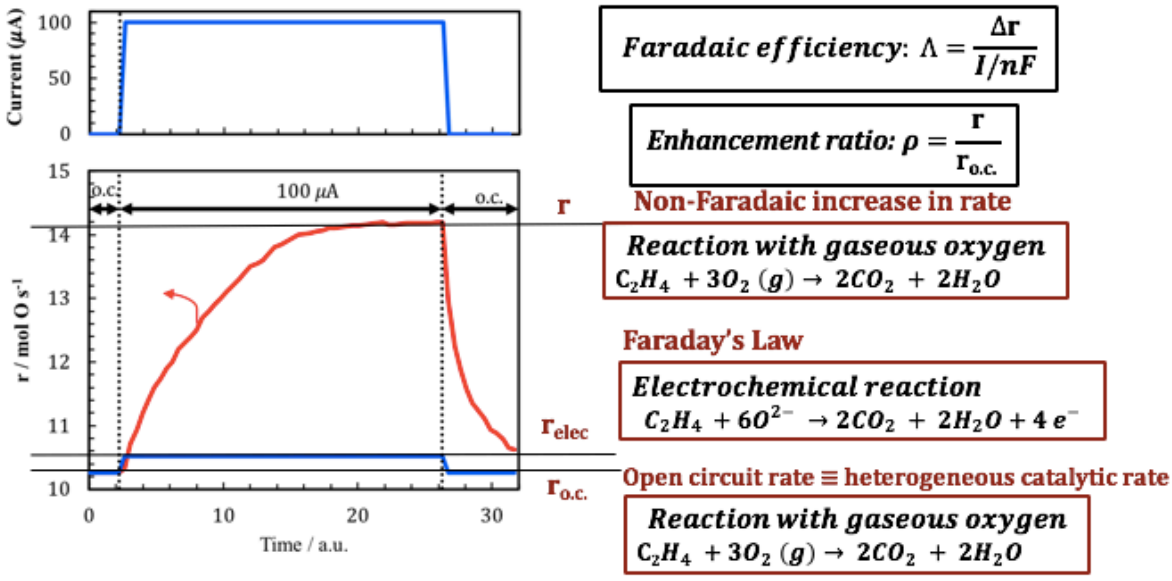

Figure D 3: Typical change in the rate of reaction (r_{oc} to r) upon application of a constant current vs the expected increase due to the electrochemical reaction (r_{elec}).

D 3. Cyclic voltammetry effect on catalytic rate

An additional cyclic voltammetry test was performed to show the on-line enhancement in the catalytic rate as a function of the potential applied. The current response as well as the catalytic rate are shown in Figure D 4. A potential window range between -0.8 and 0.8 V was set and the scan rate used was 2 mV/s. Upon the increase in potential in the [+0 V – +0.8 V] range, the catalytic rate can be seen gradually increasing concomitantly with the current increase up to 107 μA; this was followed by a short stabilization of the catalytic rate before it started dropping back to its

initial catalytic open circuit (o.c.) rate. Upon the start of the cathodic range of the CV, an increase in the catalytic rate resurfaced, proving the inverted-volcanic EPOC effect on RuO_2.

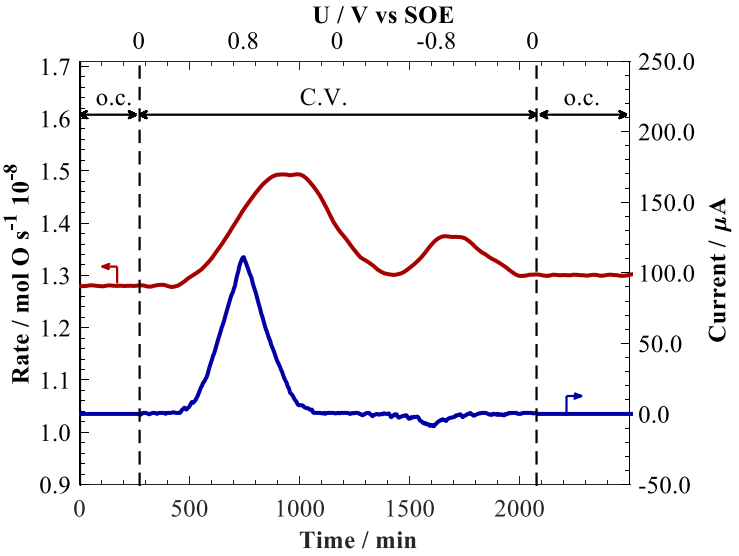

Figure D 4: Transient rate response of RuO_2 NPs to cyclic voltammetry in the [-0.8V – 0.8V]. open-circuit. Conditions: T = 350 °C, $P_{C_2H_4}$ = 0.012 kPa, P_{O_2}=3 kPa. Total flow rate = 100 ccm.

D 4. Ab Initio atomistic thermodynamics

Thermodynamic stability of a surface can be derived by comparing a multitude of surface structures and their corresponding surface free energy (SFE) $\gamma\left(T, P_{O_2}\right)$. The surface with the lowest SFE is the most stable structure. Two main variables that are required for the calculation of RuO_2 (110) surface free energy are temperature (T) and oxygen partial pressure (P_{O_2}). The environment in which RuO_2 surface is tested has constant T and p regardless of the exchange that occurs between surface and the environment (acting as a reservoir). The system's Gibbs free energy G is essential to such calculations as it represents the thermodynamic potential of the system with a dependency on the number of atoms of Ru and O (N_{Ru} and N_O), P_{O_2} and T. The free surface energy calculated to find the most stable surface composition and geometry is defined as follows based on the work of Reuter *et al.* [1] (eq. D 1):

$$\gamma\left(T, P_{O_2}, N_{Ru}, N_O\right) = \frac{1}{2S}\left\{G^{slab}_{RuO_2(T,P_{O_2},N_{Ru},N_O)} - N_{Ru}\,\mu_{Ru(T,P_{O_2})} - N_O\mu_{O(T,P_{O_2})}\right\} \qquad D\ 1$$

Where the chemical potentials of Ru and O are μ_{Ru} and μ_O, and N_{Ru} and N_O are the number of Ru and O atoms in the three-dimensional supercell. SFE is normalized by dividing by the total surface area 2S of the two symmetrical sides in the unit cell plane direction.

The bulk material available in the slab acts as a thermodynamic reservoir and relates the chemical potentials of Ru and O; therefore, allowing the substitution of the chemical potential of Ru by its relation to the Gibbs free energy of bulk oxide, $g_{RuO_2}^{bulk}$. Since in experimental settings it is the partial pressure of O_2 molecule that is controlled, SFE becomes a function of μ_{O_2}. In addition, the influence of temperature and pressure are negligible on solids; therefore, the Gibb's energy of the bulk will be considered equal to the electric energy computed for the primitive cell of the bulk $e_{RuO_2}^{bulk}$. Similarly, the free energy of the surface $G_{RuO_2}^{slab}$ is considered equivalent to its electric energy $E_{RuO_2}^{slab}$. This results in SFE being equal to eq. D 2:

$$\gamma\left(T, P_{O_2},\, N_{Ru},\, N_O\right) \qquad D\ 2$$

$$= \frac{1}{2S}\left\{E_{RuO_2(\,N_{Ru},\,N_O)}^{slab} - N_{Ru}\, e_{RuO_2}^{bulk} + (2\,N_{Ru} - N_O)\,\frac{1}{2}\,\mu_{O_2(T,P_{O_2})}\right\}$$

The chemical potential of oxygen μ_{O_2} is then described as a function of the standard chemical potential $\mu_{O_2}^o$, T and p as follows (eq. D 3):

$$\mu_{O_2(T,P)} = \mu_{O_2(T,P^o)}^o + RTln\frac{P_{O_2}}{P_{O_2}^o} \qquad D\ 3$$

The standard chemical potential of an oxygen molecule within the ideal gas approximation is equal to its Gibbs free energy ($g_{O_2(T,P^o)}^{gas}$). Directly expressing the oxygen Gibbs free energy in terms of an electronic internal energy does not result in accurate values when using GGA functionals [2]. Therefore, the oxygen Gibbs free energy is derived from the water formation reaction. The Gibbs free energy of oxygen is related to the Gibbs free energy of water formation and the Gibbs free energies of hydrogen and water at standard conditions (eq. D 4).

$$\mu_{O_2(T,P^o)}^o \approx g_{O_2\left(T,P_{O_2}^o\right)}^{gas} = -2\,\Delta G_{H_2O}^f + 2\,g_{H_2O\left(T,P_{H_2O}^o\right)}^{gas} + 2\,g_{H_2\left(T,P_{H_2}^o\right)}^{gas} \qquad D\ 4$$

D 4.1 Surface potential effect on the ab initio atomistic thermodynamics

The electrochemical promotion effect on the catalyst slab electric energy was modeled by adding the Poisson-Boltzmann equation [3,4] to the general Kohn-Sham equation using the

VASPsol module [5]. The solution to the new equation is added to the electronic ground state resulting in a modification of the total free energy and forces. This method has been validated for the adsorption of pyridine on Au (111) by Steinmann *et al.* [6]. The implicit solvation model places a quantum-mechanical solute in a cavity surrounded by a continuum dielectric description of the solvent [7,8]. The relative permittivity of the solvent used tested in Figure D 13, while the cavity size effect is demonstrated in Figure D 12. Both have been shown to have a negligible effect on the SFE value for the three possible surface termination ($2O^{br}/2O^{ot}$, $2O^{br}/2Ru$ and $2Ru/2Ru$).

In the previous SFE equation, the oxygen supply is gaseous, whereas in EPOC conditions, the oxygen is supplied in its ionic form from the oxygen-conducting electrolyte material as follows (eq. D 5):

$$O^{2-}(YSZ) + RuO_2 \rightarrow O@RuO_2 + 2e^- \qquad D\ 5$$

The chemical potentials of gaseous oxygen μ_O is replaced by that of oxygen anion $\mu_{O^{2-}}$ and the corresponding SFE equation is described as follows (eq. D 6).

$$\gamma\left(T, P, N_{Ru}, N_O, U_{anode/SHE}\right) \qquad D\ 6$$

$$= \frac{1}{2S}\Big\{E^{slab}_{RuO_2(N_{Ru}, N_O, U)} - N_{Ru}\, e^{bulk}_{RuO_2} + (2N_{Ru} - N_O)\,\mu_{O^{2-}(T,P,U)}\Big\}$$

The chemical potential of oxygen anions $\mu_{O^{2-}}$ is linked through eq. *D 7* with the chemical potential of oxygen from the gas phase and the potential applied versus a Standard Oxygen Electrode (SOE).

$$\begin{aligned}\mu_{O^{2-}} &= \frac{1}{2}\mu_{O_2} + 2eU_{anode/SOE}\\ &= \frac{1}{2}\mu_{O_2} + 2e(U_{anode/vac} + U_{vac/SOE})\\ &= \frac{1}{2}\mu_{O_2} + 2e(U_{anode/SHE} + U_{SHE/vac} + U_{vac/SOE})\\ &= \frac{1}{2}\mu_{O_2} + 2e(U_{anode/SHE} + U_{SHE/SOE})\end{aligned} \qquad D\ 7$$

It has been established that the equilibrium potential of SOE with respect to vacuum is 5.14 V [9], whereas that of SHE is 4.44 V [10]; therefore the equilibrium potential of SHE with respect to SOE is equal to -0.7 V and the SFE equation as a function of potential vs SHE is as follows (eq. *D 8*).

$$\gamma\left(T, P,\ N_{Ru},\ N_O, U_{anode/SHE}\right) = \frac{1}{2S}\left\{E^{slab}_{RuO_2(N_{Ru}, N_O, U_{anode/SHE})} - N_{Ru}\, e^{bulk}_{RuO_2} + (2\,N_{Ru} - N_O)\left(\frac{1}{2}\mu_{O_2(T,P)} + 2e\left(U_{anode/SHE} - 0.7\right)\right)\right\} \quad D\ 8$$

D 5. Additional Figures and Sensitivity analysis on numerical setting

D 5.1 Effect of chemical potential, temperature and oxygen partial pressure

Before investigation of the potential effect on the nature of the surface termination, calculation for the effect of oxygen chemical potential on the surface free energy was performed to show that under open-circuit potential, the surface with $2O^{br}/2O^{ot}$ is the most stable surface termination (Figure D 5). The results we obtained are in agreement with the findings of Reuter et al. [1]. Furthermore, Figure D 6 shows the change of the surface termination at ocp as a function of temperature and oxygen partial pressure. This proves the stability of the $2O^{br}/2O^{ot}$ for the experimental pressure and temperature range.

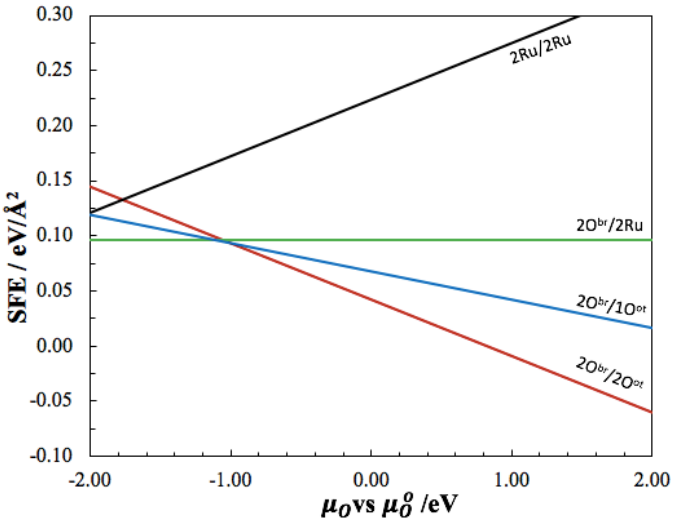

Figure D 5: Surface free energy of RuO_2 (110) as a function of chemical potential at 350 °C vs standard chemical potential, under open-circuit potential conditions.

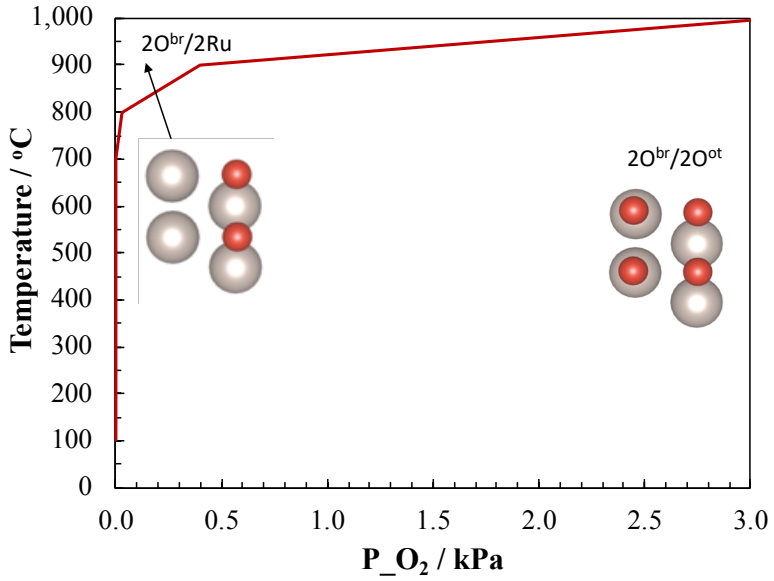

Figure D 6: RuO_2 (110) phase diagram as a function of temperature and oxygen partial pressure, under open-circuit potential conditions.

To clarify better the minimal effect of oxygen partial pressure, Figure D 7a&b compares the SFE values as a function of electric potential applied under 1 kPa of oxygen partial pressure in (a) and under10^{-10} kPa in (b). The point at which the transition occurs from one state to another shifts slightly between the two figures proving the limited effect of partial pressure of O_2 on the phase diagram.

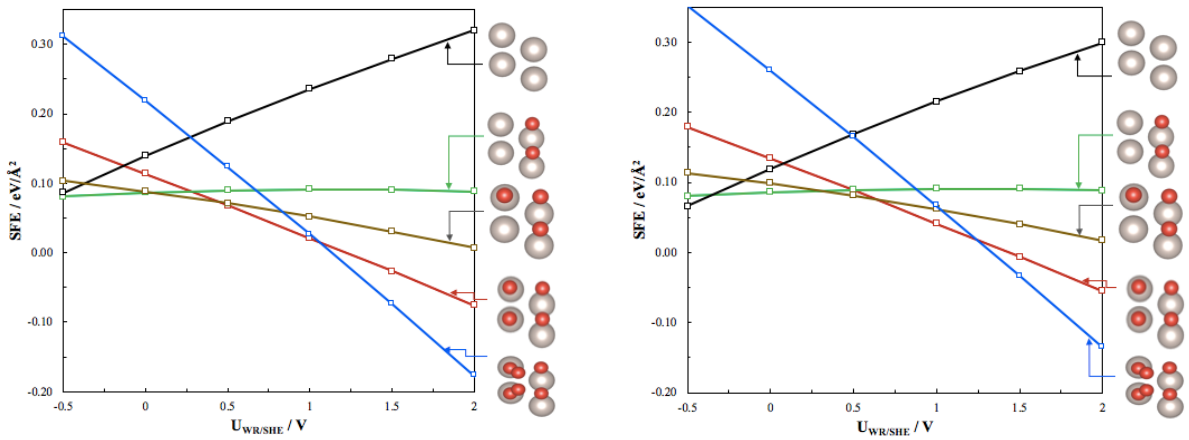

(a) *(b)*

Figure D 7: Surface free energy of RuO_2 (110) as a function of electrical potential applied at 350 ° C at a partial pressure of oxygen of (a) 1 kPa (experimental and (b) 10^{-10} kPa (ultra-high vacuum chamber conditions).

D 5.2 Effect of Number of Ru layers

The number of Ru atoms layers was varied between 2 and 6 layers and the surface free energy was calculated for a unit cell (Figure D 8a). It can be seen that the surface energy was stable as a function of the number of Ru layers confirming that the size of the unit cell used does not wrongly effect our calculations. Similarly, adsorption energy of ethylene and oxygen on the most stable surface position was calculated as a function of the number of Ru layers; this confirmed as well the choice of 3 layers of Ru (Figure D 8b).

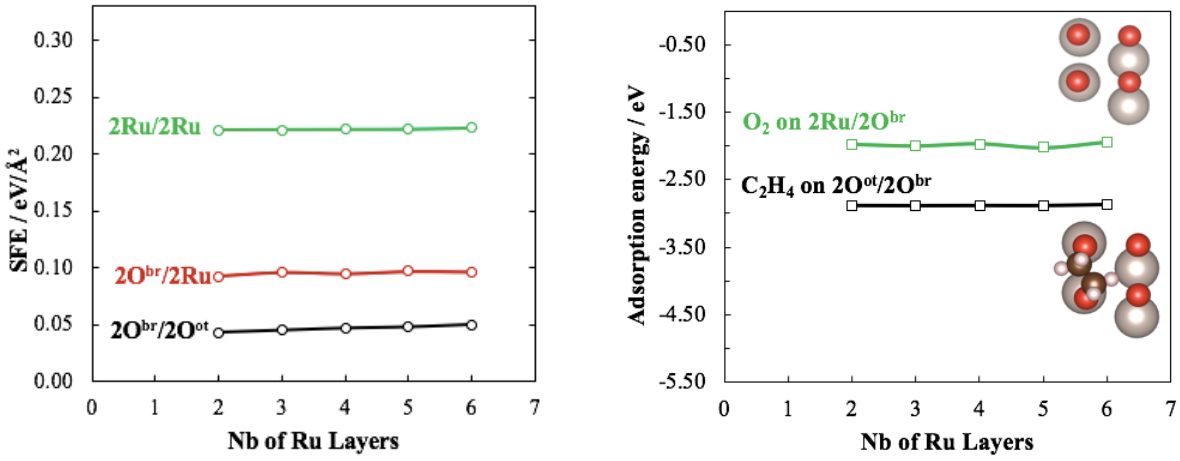

(a) (b)

Figure D 8: Effect of number of Ru layers on (a) the surface energy for $2O^{br}/2O^{ot}$, $2O^{br}/2Ru$ and 2Ru/2Ru surface termination of RuO_2 (110) surface and (b) on the adsorption energy of ethylene and oxygen molecules on the most stable position.

D 5.3 Vacuum effect test

Vacuum test was performed on the RuO_2 slab with $2O^{br}/2O^{ot}$, $2O^{br}/2Ru$ and 2Ru/2Ru surface termination by varying the vacuum in the range of 15 to 30 Å in z-direction. Figure D 9 demonstrates SFE under 15 and 30 Å only and it can be seen that there is an insignificant change in the SFE value as a function of vacuum length, which confirms the use of 15 Å of vacuum length in our calculations.

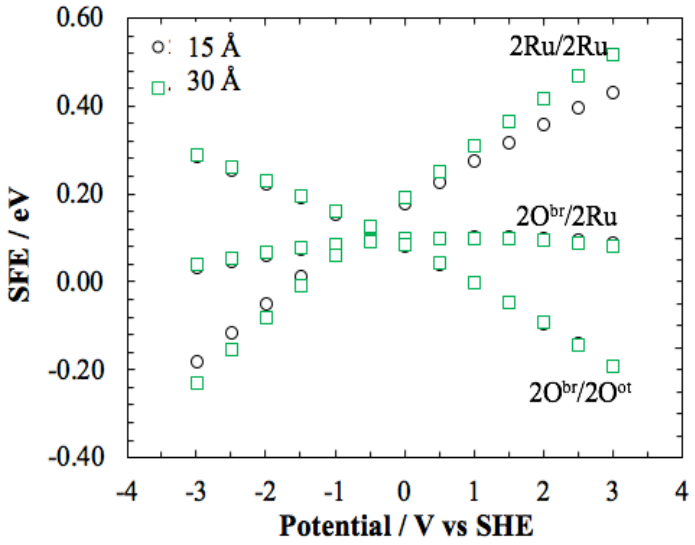

Figure D 9: Vacuum thickness effect on SFE value for $2O^{br}/2O^{ot}$, $2O^{br}/2Ru$ and 2Ru/2Ru surface termination of RuO_2 (110) surface.

D 5.4 Energy cut-off effect

The effect of energy cut-off on the variation of the slab energy is depicted in Figure D 10, showing that a value of 550 eV is large enough to converge the Fourier series set used in our DFT calculations.

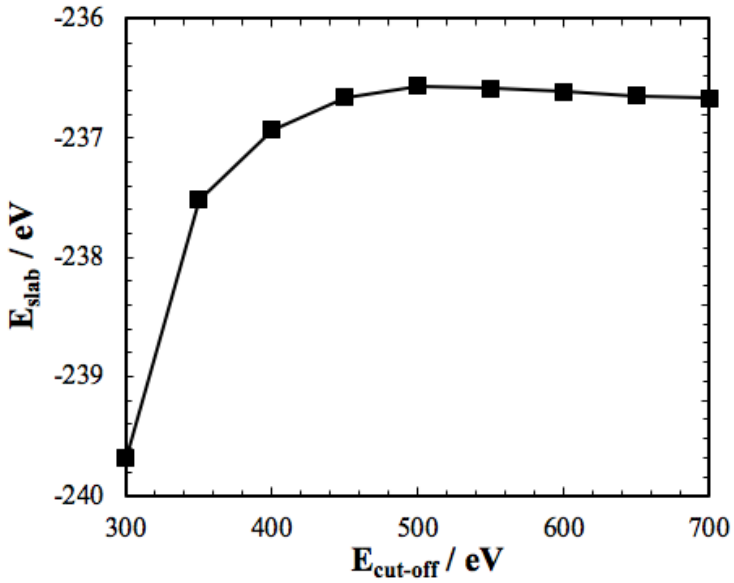

Figure D 10: Slab energy variation as a function of energy cut-off value, at K-points value of 6x6x1 for $2O^{br}/2O^{ot}$ surface termination of RuO_2 (110) surface.

D 5.5 Charge effect on potential and work function value

Figure D 11 serves as a confirmation to the charge addition/removal effect on the three systems' work function and corresponding potential. It can be seen that the removal of charges corresponds to an anodic behavior such as the potential value increases along with the work function value. In addition, there is an increasing work function value as a function of presence of more O^{ot} atoms when changing systems from 2Ru/2Ru to $2O^{br}$/2Ru to $2O^{br}/2O^{ot}$.

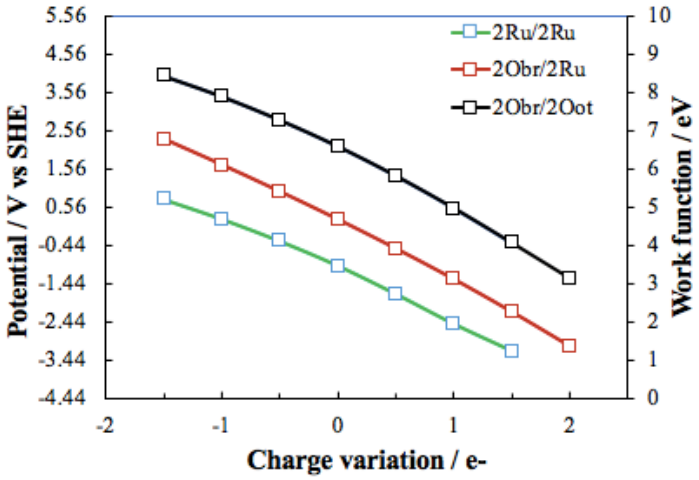

Figure D 11: Charge removal/addition effect on the potential value and work function value.

D 5.6 Relative permittivity test

Similarly, the relative permittivity test showed minimal variation in SFE as a function of the ε_r used, confirming the use of ε_r =79 corresponding to water solvent (Figure D 12).

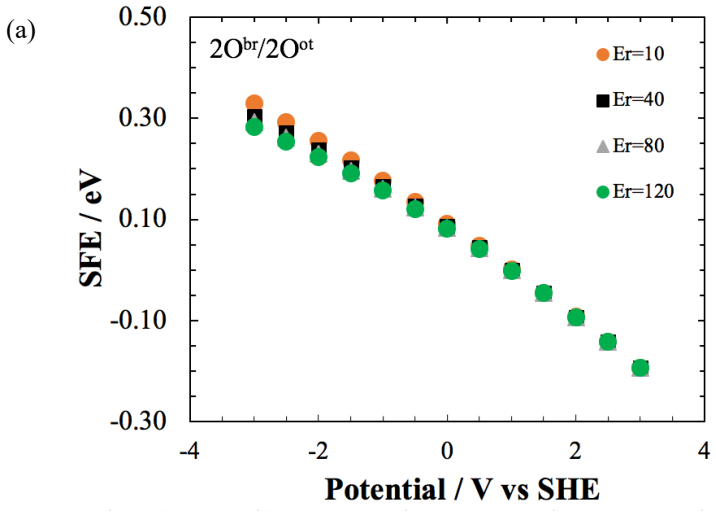

Figure D12 (Continued next page)

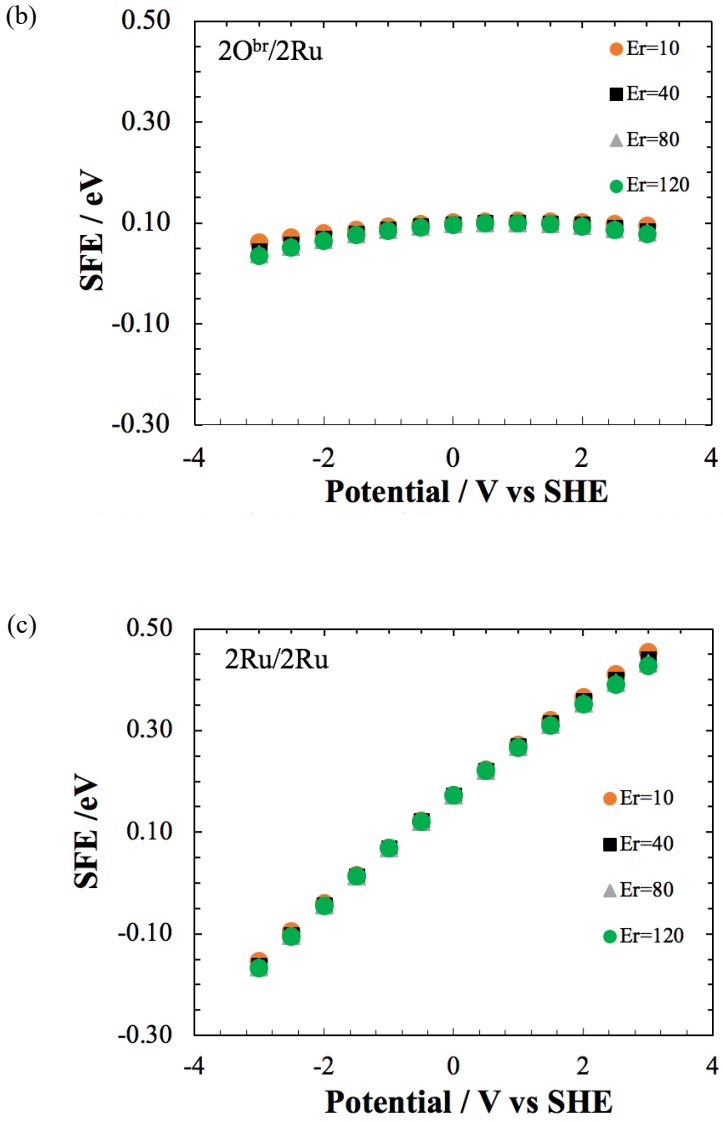

Figure D 12: Relative permittivity effect on surface free energy (SFE) of a)$2O^{br}/2O^{ot}$, b) $2O^{br}$/2Ru and c) 2Ru/2Ru surface termination of the RuO_2 (110) surface.

D 5.7 Cavity size test

Similarly, the cavity size test was performed on $2O^{br}/2O^{ot}$, $2O^{br}$/2Ru and 2Ru/2Ru surface termination of RuO_2 (110) surface and is depicted Figure D 13. The default value for cavity size is 0.0025 and it can be seen that a minimal variation in SFE value was detected, making the NC_K value used in our DFT calculation reliable.

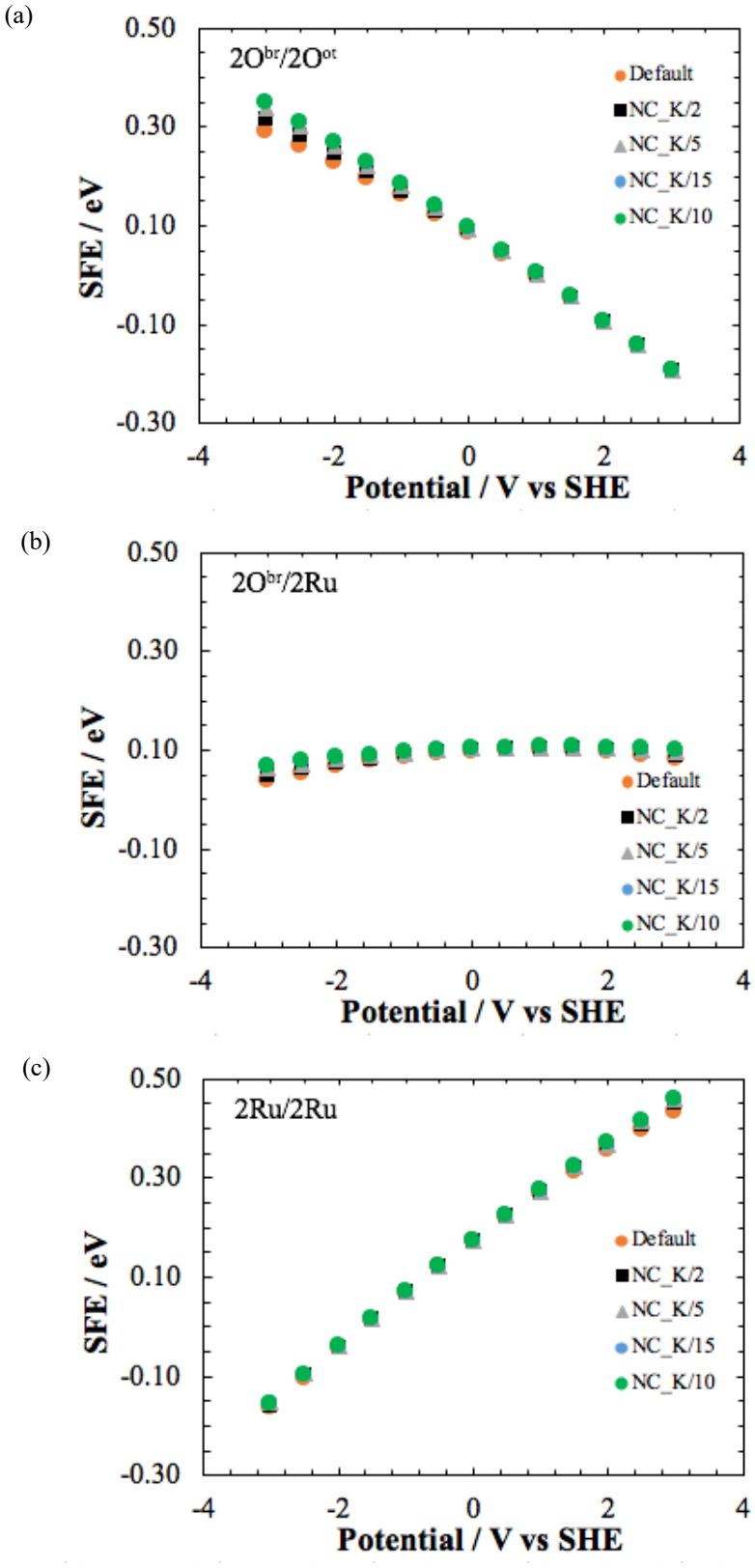

Figure D 13: Cavity size effect on surface free energy (SFE) of $2O^{br}/2O^{ot}$, $2O^{br}/2Ru$ and 2Ru/2Ru surface termination of the RuO_2 (110) surface.

D 5.8 Potential effect on atoms charge

The charge of bulk and surface Ru and O atoms was calculated and plotted as a function of potential applied. It can be seen that the Ru and O atoms in the bulk do not vary in charge as a function of potential applied. However, on the surface, Ru atoms increase their positive electron charge while O^{ot} and O^{br} 's charge value decrease (in absolute value) as a function of potential applied (Figure D 14).

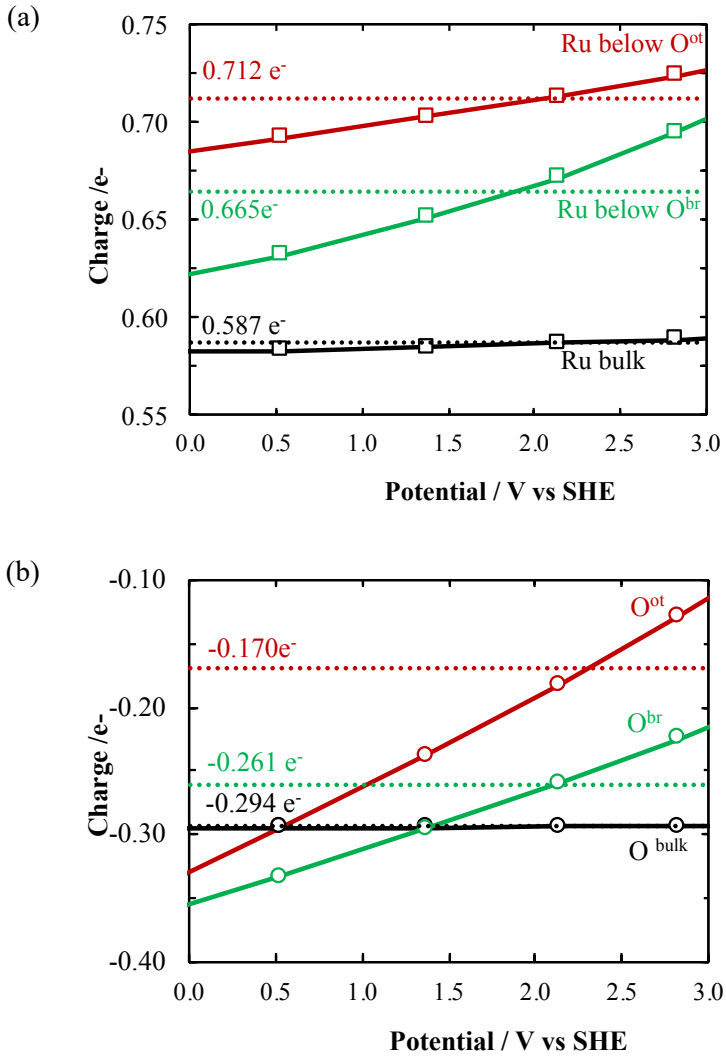

Figure D 14: Charge (e-) variation on Ru and O atoms as a function of potential for RuO_2 (110) surface with $2O^{br}/2O^{ot}$ termination

.

D 5.9 Gibb's energy calculation of the overall slab as a function of potential

In this section, we present the technical background behind the adsorption energy presented as a function of the potential in Eq.6. The relationship between the change in the electronic energy presented as Gibb's energy and the applied electrochemical potential was fitted to parabolas. Then, to find the adsorption energy as a function of potential, we subtracted from the Gibb's energy of the slab containing two ethylene molecules adsorbed symmetrically on the slab, the parabola of the energy of the bare slab and two times the constant ethylene energy that is independent of the potential applied. This value, when divided by two, accounts for the adsorption of one ethylene molecule (Figure D 15).

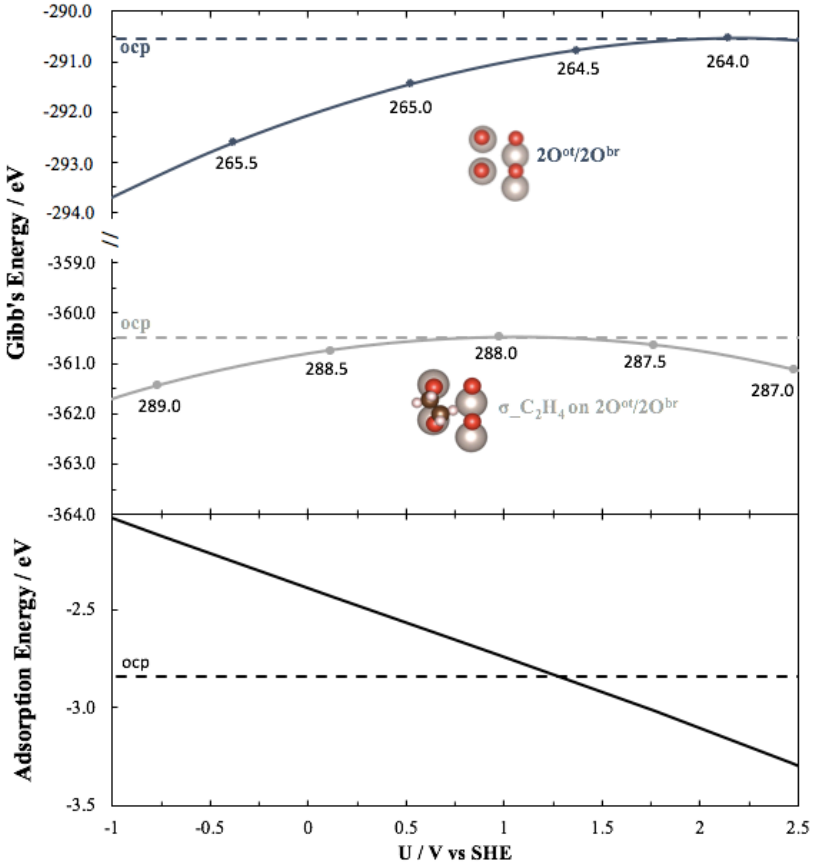

Figure D 15: Effect of potential applied on the Gibb's energy of the pre-adsorption slab and when C_2H_4 is adsorbed in the σ position on the $2O^{ot}$. The subtraction of the two energies is used to find the adsorption energies of the C_2H_4. The labeled points correspond to the computed values at a given surface charge. The half charge interval used for the bare surface is 265.5–264.0 electrons and 289.0–287.0 electrons for the surface with two adsorbed ethylene.

Similarly, the reaction energy is found from subtracting the Gibb's energy parabolas of the initial state from the final state, and the activation energy is found from subtracting that of the initial state from the energy of the transition state (Figure D 16).

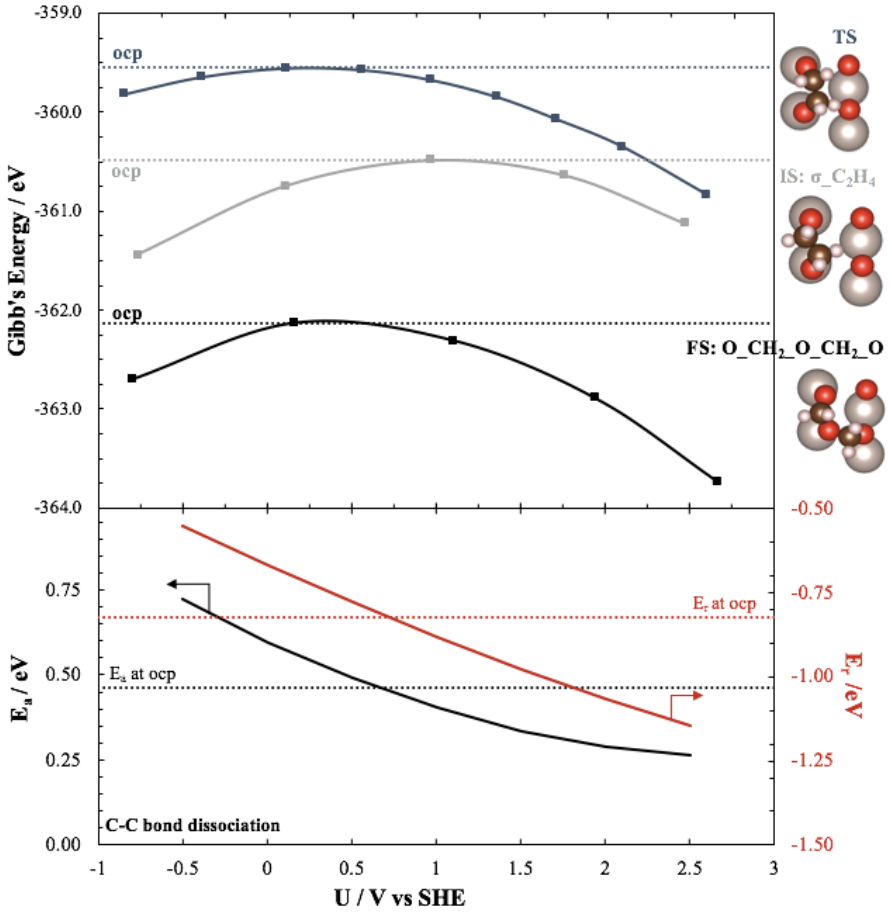

Figure D 16: Effect of potential applied on the Gibb's energy of the initial, transition and final states, used in activation and reaction energies calculations.

D 5.10 Effect of PBE and HSE functional on the work function of RuO2(110) surfaces

Additional computations at the HSE level of theory of the work function of the three main surfaces ($2O^{ot}/2O^{br}$, $2Ru/2O^{br}$ and 2Ru/2Ru) show that the PBE work function is in excellent agreement with experimental values (5.8 to 6.6 V) [11], while the HSE results are 0.5 V higher compared to PBE and reach 7.1 V for the $2O^{ot}/2O^{br}$ surface. The 0.5 V difference between HSE and PBE is small enough to ensure that the qualitative mechanistic insight gained in this study does not significantly depend on the theoretical level.

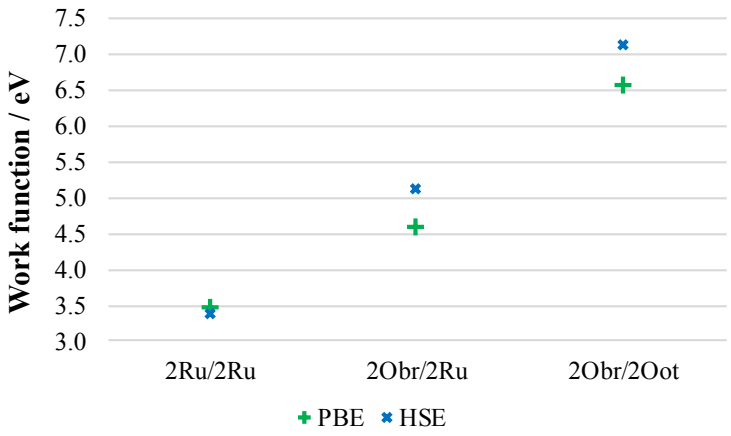

Figure D 17: Work function of the three main surface terminations of RuO_2 as computed with PBE and HSE. The experimental work function for RuO_2 in oxygen is 5.8 to 6.6 V according to [11].

D 6. Additional Energy Calculations

The potential effect on the adsorption of ethylene in different possible positions is shown in Figure D 18. The C_2H_4 on $2O^{br}/2O^{ot}$ is the most stable at all potential values.

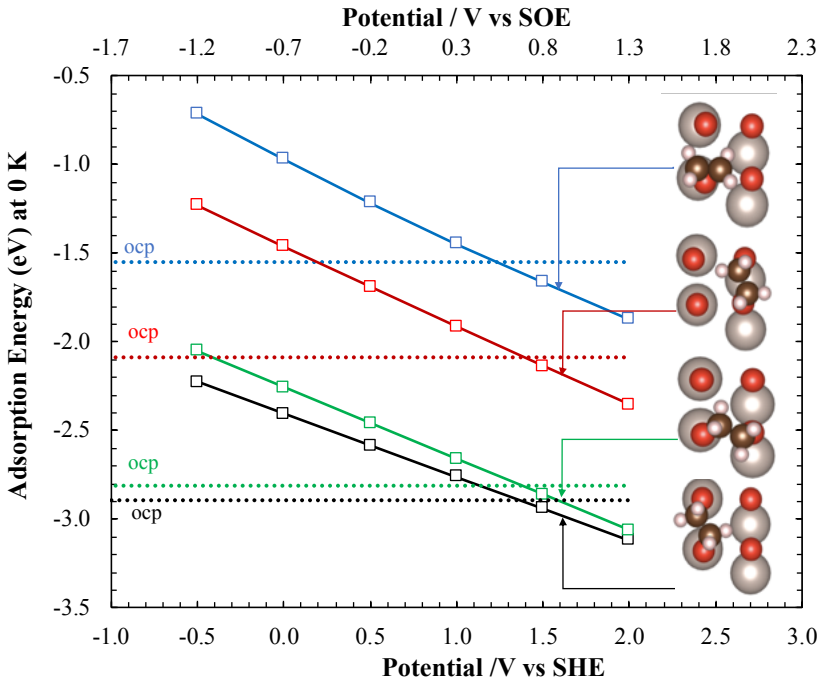

Figure D 18: C_2H_4 adsorption energy at different positions on RuO_2 (110) surface with $2O^{br}/2O^{ot}$ termination. Dotted line corresponds to ocp adsorption value, while the solid line corresponds to adsorption energy variation as a function of potential value.

The C-H dissociation is a possible alternative to C-C bond dissociation; however, its activation energy is slightly higher than that of C-C dissociation. This is shown in Figure D 19.

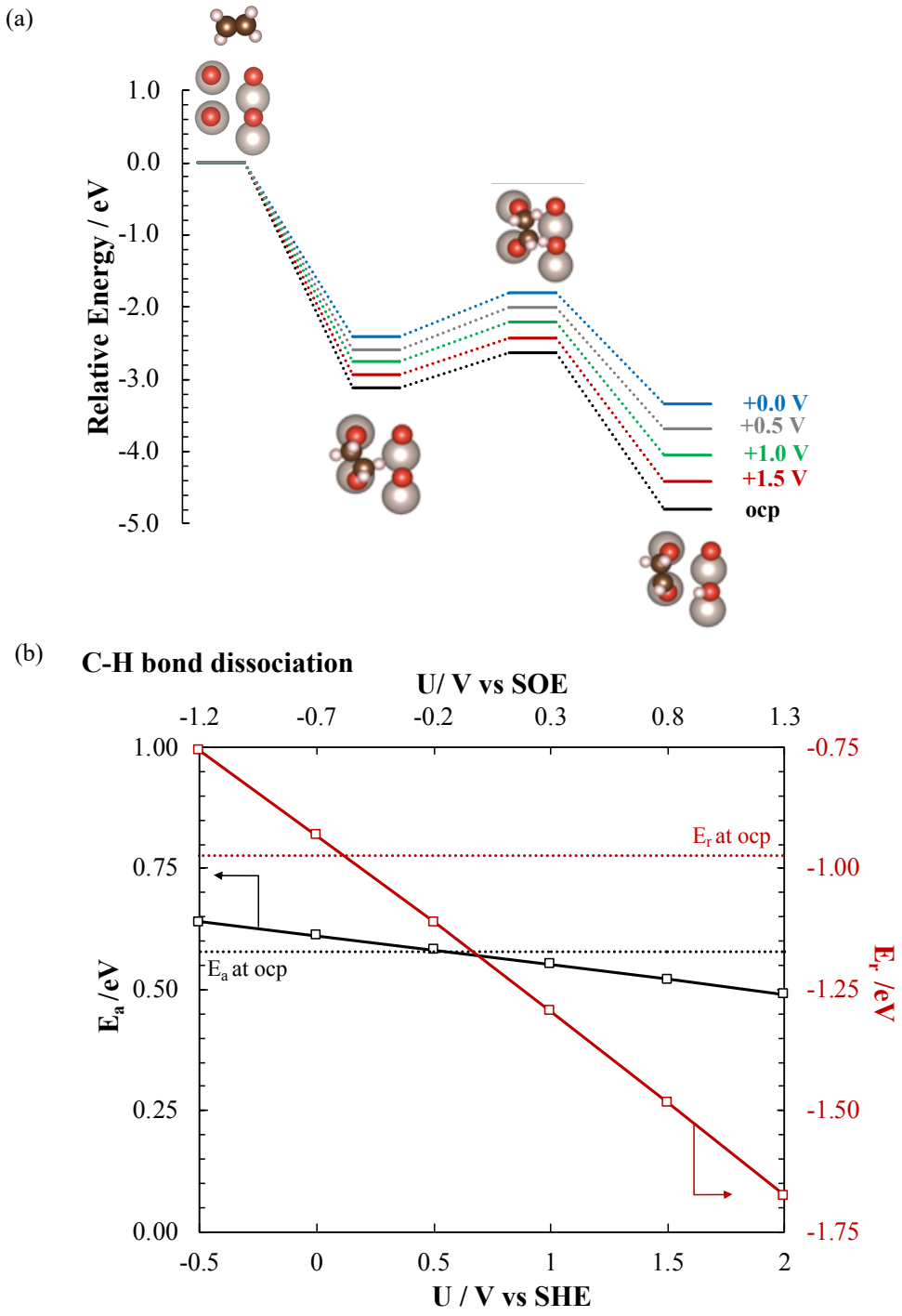

Figure D 19: (a) Energy diagram and (b) corresponding activation and reaction energies as a function of potential for C-H bond dissociation over $2O^{br}/2O^{ot}$ surface termination of RuO_2 (110).

The C-H bond cleavage showed an intermediate C-H bond length of 1.3 Å compared to the initial state of 1.1 Å and the final state of 3.1 Å (Figure D 20).

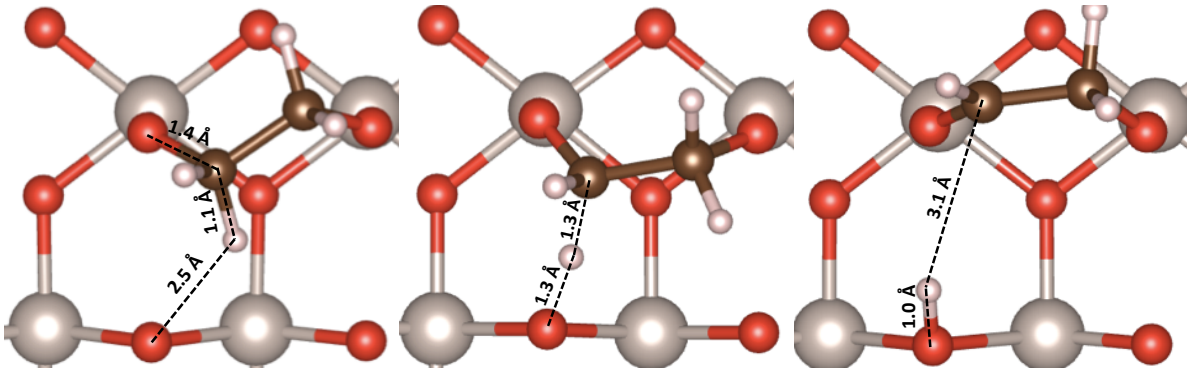

Figure D 20: Structure of the initial, transition and final state of C-H bond rupture on $2O^{br}/2O^{ot}$ RuO_2 (110) surface.

The geometries for oxygen dissociation are given in Figure D 21 where the stretching of the O-O bonds occurs from left to right, with the transition state being in the middle. The distance between the two oxygen stretched from an initial length of 1.4 Å to a final value of 3.1 Å, passing by 1.7 Å at the transition state.

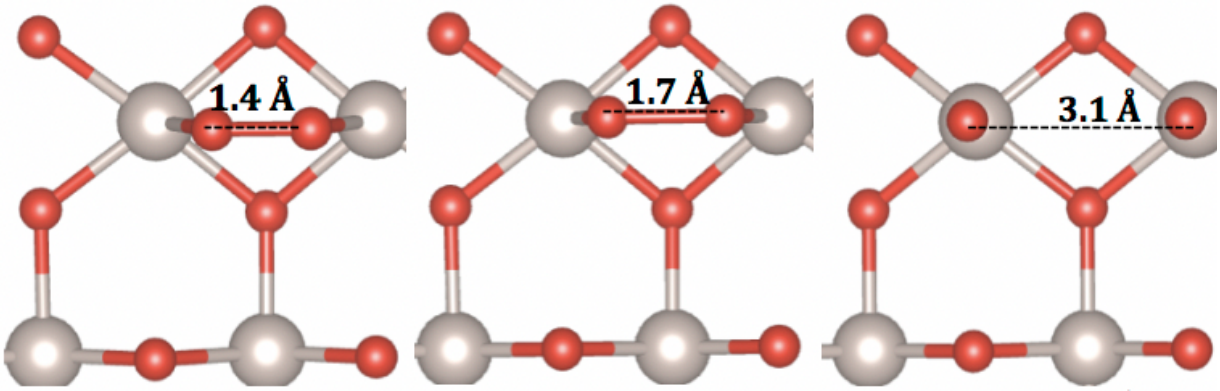

Figure D 21: Structure of the initial, transition and final state of (O-O) bond dissociation on $2O^{br}/2Ru$ RuO_2 (110) surface.

References

[1] K. Reuter, M. Scheffler, Composition, structure, and stability of RuO_2 (110) as a function of oxygen pressure, Phys. Rev. B. 65 (2001) 035406.

[2] J. Rossmeisl, A. Logadottir, J.K. Nørskov, Electrolysis of water on (oxidized) metal surfaces, Chem. Phys. 319 (2005) 178–184.

[3] C.W. Outhwaite, L.B. Bhuiyan, An improved modified Poisson-Boltzmann equation in electric-double-layer theory, J. Chem. Soc. Faraday Trans. 2 Mol. Chem. Phys. 79 (1983) 707–718.

[4] L.B. Bhuiyan, C.W. Outhwaite, D. Henderson, A modified Poisson-Boltzmann analysis of the capacitance behavior of the electric double layer at low temperatures, J. Chem. Phys. 123 (2005) 034704.

[5] VASPsol, (n.d.). https://github.com/henniggroup/VASPsol/blob/master/docs/USAGE.md.

[6] S.N. Steinmann, P. Sautet, Assessing a First-Principles Model of an Electrochemical Interface by Comparison, J. Phys. Chem. C. 120 (2016) 5619–5623.

[7] K. Mathew, R. Sundararaman, K. Letchworth-Weaver, T.A. Arias, R.G. Hennig, Implicit solvation model for density- functional study of nanocrystal surfaces and reaction pathways, J. Chem. Phys. 140 (2015) 084106.

[8] K. Mathew, R.G. Hennig, Implicit self-consistent description of electrolyte in plane-wave density-functional theory, ArXiv. (2016) 1–6.

[9] D. Tsiplakides, C.G. Vayenas, Electrode work function and absolute potential scale in solid-state electrochemistry, J. Electrochem. Soc. 148 (2001) E189–E202.

[10] S. Trasatti, The Absolute Electrode Potential: an Explanatory Note, Pure Appl. Chem. 58 (1986) 955–966.

[11] A. Böttcher, H. Niehus, Oxygen adsorbed on oxidized ru(0001), Phys. Rev. B - Condens. Matter Mater. Phys. 60 (1999) 14396–14404.

Appendix E: Scholarly Contributions

PUBLICATIONS

1. **Y. Hajar**, L. Treps, C. Michel, E.A. Baranova, S. N. Steinmann, Theoretical Insight into Origin of Electrochemical Promotion of Ethylene oxidation on Ruthenium Oxide, *Catal. Sci. & Tech.,* Accepted. doi: 10.1039/c9cy01421g.
2. **Y. Hajar, B**. Venkatesh, M.S.E. Houache, H. Liu, R. Safari, S. Prabhudev, G.A. Botton, E.A. Baranova, Electrochemical promotion of Bi-metallic Ni_9Pd core double-shell nanoparticles for complete methane oxidation, *J. of Catalysis*, 374 (**2019**) 127-135. doi.org/10.1016/j.jcat.2019.04.026.
3. **Y. Hajar**, B. Venkatesh, E. A. Baranova, Electrochemical promotion of nanostructured palladium catalyst for complete methane oxidation, *Catalysts,* **2019**, 9(1), 48; doi: 10.3390/catal9010048.
4. **Y. Hajar**, V. Di Palma, V. Kyriakou, M. A. Verheijen, E. A. Baranova, P. Vernoux, et al., Atomic layer deposition of highly dispersed Pt nanoparticles on a high surface area electrode backbone for electrochemical promotion of catalysis, *Electrochem. Commun.* 84 (**2017**) 40–44. doi: 10.1016/j.elecom.2017.09.023.
5. **Y. Hajar**, M. Houache, U. Tariq, E.A. Baranova, Nanoscopic Ni interfaced with oxygen conductive supports: Link between electrochemical and catalytic studies, *ECS Transactions*, 77 (10) 51-66 (**2017**). doi: 10.1149/07710.0051ecst.
6. **Y. Hajar**, K. Patel, U. Tariq, E.A. Baranova, Functional equivalence of electrochemical promotion and metal support interaction for Pt and RuO_2 nanoparticles, *J. of Catalysis*, 352 (**2017**) 42–51. doi: 10.1016/j.jcat.2017.05.001.
7. **Y. Hajar**, H. Dole, M. Couillard, E. Baranova, Investigation of Heterogeneous Catalysts by an Electrochemical Method: Ceria and Titania-Supported Iridium Nanoparticles for Ethylene Oxidation, *ECS Transactions*, **2016**, 72 (7) 161-172. doi: 10.1149/07207.0161ecst.

<u>In preparation</u>:

8. **Y. Hajar**, A. Boreave, A. Caravaca, P. Vernoux, E. Baranova, Isotopic oxygen exchange study to unravel noble metal oxide/support interactions, In preparation.
9. L. Treps, **Y. Hajar**, C. Michel, E. Baranova, S. Steinmann, Ab-initio elucidation of electric field effect on Pt for methane oxidation, In preparation.

CONFERENCES & MEETINGS

1. **Y. Hajar**, L. Treps, C. Michel, E. Baranova, Theoretical Insight into Origin of Electrochemical Promotion of Ethylene oxidation on Ruthenium Oxide, *Laboratoire International Associé (LIA) meeting* (Ottawa, Canada) (**2019**)
2. **Y. Hajar**, B. Venkatesh, E.A. Baranova, Non-Faradaic Enhancement of catalytic activity of core/shell PdNi for complete methane oxidation, 68th *Canadian Society for Chemical Engineering* (Toronto, Canada) (**2018**)
3. E.A. Baranova, **Y. Hajar**, C. Panaritis, *et al.*, Electrochemical Promotion of Bimetallic Nanoparticles with Low-Noble Metal Content Interfaced with Yttria-Stabilized Zirconia Solid-Electrolyte, *AiMES 2018 Meeting* (Cancun, Mexico) (**2018**)
4. **Y. Hajar**, C. Michel, E. Baranova, DFT modeling of NEMCA phenomenon on RuO_2 NPs for ethylene oxidation, *Laboratoire International Associé (LIA) meeting* (Lyon, France) (**2018**)
5. **Y. Hajar**, M. Houache, U. Tariq, P. Vernoux, E.A. Baranova, Nanoscopic Ni Interfaced with Oxygen Conductive Supports: Link between Electrochemical and Catalytic Studies, 231st Electrochemical Society Meeting (New Orleans, USA) (**2017)**
6. **Y. Hajar**, E. Baranova, A Comparison Study of Electrochemical Promotion and Metal-Support Interaction for Pt and RuO_2 Nanoparticles, *Ph.D. Day, ENS* (Lyon, France) (**2017**)
7. E.A. Baranova, H. Dole, **Y. Hajar**, Connecting Metal-Support Interaction and Electrochemical Promotion of Catalysis, *CARE - IRCELYON-Caractérisation et remédiation des pollutants dans l'air et l'eau,* (Lyon, France) (**2017**)
8. **Y. Hajar**, H. Dole, M. Couillard, E.A. Baranova, Investigation of Heterogeneous Catalysts by an Electrochemical Method: Ceria and Titania-Supported Iridium Nanoparticles for Ethylene Oxidation, *229th Electrochemical Society Meeting* (San Diego, USA) (**2016**)
9. **Y. Hajar**, E.A Baranova, Electrochemical Characterization of Ceria and Titania supported iridium nanoparticles for Gas Phase Ethylene Oxidation, *24th Canadian Symposium on Catalysis* (Ottawa, Canada) (**2016**)

POSTER PRESENTATIONS

1. Theoretical Modelling of Electrochemical Promotion of Catalysts for Ethylene Oxidation, *12th Engineering and Computer Science Faculty's Graduate Poster Competition*, *University of Ottawa* (Ottawa, Canada) (**2019**)
2. Electrochemical modification of methane oxidation on Pd and core-shell Pd/Ni, *Fall Symposium of the Canadian Section of the ECS* (Montréal, Canada) (**2018**)
3. Effect of Electrochemical Promotion of Methane Oxidation using $Nickel_{90}$-$Palladium_{10}$ Catalyst, *11th Engineering and Computer Science Faculty's Graduate Poster Competition*, *University of Ottawa* (Ottawa, Canada) (**2018**)
4. Electrochemical Promotion of Methane Oxidation on $Ni_{90}Pd_{10}$ Catalyst, *Fall Symposium of the Canadian Section of the ECS* (Kingston, Canada) (**2017**)
5. Nanostructure IrO_x Catalyst Supported on Ceria and Titania for Ethylene Oxidation, *9th Engineering and Computer Science Faculty's Graduate Poster Competition*, *University of Ottawa* (Ottawa, Canada) (**2016**)